UNIVERSITY OF CALIFORNIA SAN DIEGO

Plankton patchiness at mesoscale fronts and filaments: drivers, dynamics, and implications in the California Current System

A Dissertation submitted in partial satisfaction of the requirements
for the degree Doctor of Philosophy

in

Oceanography

by

Shailja Daphne Gangrade

Committee in charge:

Professor Peter J. S. Franks, Chair
Professor Katherine A. Barbeau
Professor Mark D. Ohman
Professor Eugene R. Pawlak

2024

The Dissertation of Shailja Daphne Gangrade is approved, and it is acceptable in quality and form for publication on microfilm and electronically.

University of California San Diego

2024

DEDICATION

To my Ah Pho, Ah Kung, Dadiji, and Dadaji
who gifted me with a love for
science, teaching, food, music, and family.

And to Jane Teranes as we continue her beautiful legacy.

TABLE OF CONTENTS

LIST OF FIGURES

LIST OF TABLES

LIST OF ABBREVIATIONS

ALF	Advanced Laser Fluorometer
BEUTI	Biologically Effective Upwelling Transport Index
CalCOFI	California Cooperative Oceanic Fisheries Investigations
CC	California Current
CCE	California Current Ecosystem
CCS	California Current System
Chl-a	Chlorophyll *a*
CTD	Conductivity, temperature, depth
CU	California Undercurrent
CUTI	Coastal Upwelling Transport Index
EBUS	Eastern Boundary Upwelling System
ESD	Equivalent spherical diameter
FSLE	Finite Size Lyapunov Exponent
HC	High chlorophyll
HS	High salinity
LC	Low chlorophyll
LOPC	Laser Optical Plankton Counter
LOWESS	Locally weighted scatterplot smoothing
LS	Low salinity
LTER	Long-Term Ecological Research
MOC	Maximum observed chlorophyll
MPC	Maximum potential chlorophyll

P1706	June 2017 CCE LTER Process Cruise
P1908	August 2019 CCE LTER Process Cruise
PPH	Pulsatile Patch Hypothesis
SPH	Stationary Patch Hypothesis
SSH	Sea surface height
SST	Sea surface temperature
T-S	Temperature-salinity

ACKNOWLEDGEMENTS

I will begin by thanking my adviser Peter Franks for his remarkable mentorship, kindness, generosity, and curiosity. As an ode to our mutual love for food, I must say: Peter brings an exquisite meal to the table—and I am leaving this PhD completely satisfied. It was Peter's guidance, which began even before graduate school, that helped me find my footing as a scientist, teacher, collaborator, and communicator. Also, Peter's wealth of ideas (e.g., his several tangents during a meeting) has always reminded me that the ocean presents us with endless enchanting mysteries, but our investigations—with a striking summary graphic and some "punchy" sentences—can communicate powerful stories. So, as Peter's last "recruited" PhD student (a label that has been tossed around for several years due to Peter's ability to spontaneously collect students), I am proud to carry the Franks Lab torch forever.

Next, I would like to thank my committee members: Kathy Barbeau, Mark Ohman, and Geno Pawlak. I met both Kathy and Mark on the *R/V Roger Revelle* when I was an undergraduate student volunteering on the 2017 CCE LTER Process Cruise. Little did I know, the people that helped bring me aboard that ship would be the ones to guide me throughout my PhD. I am grateful to have had Kathy as a committee member and co-author. I have learned so much from her leadership, and I strive to be just as witty and perceptive as she is one day. Her groundbreaking investigations of iron limitation have also completely changed the way I think about and evaluate planktonic ecosystem dynamics, and I hope to continue to shed light on the intricacies of these important processes. Speaking of plankton, our field would not be where it is today without Mark Ohman. Through his mentorship and unrelenting curiosity, I have learned to ask seriously good questions and consider phenomena I never thought to consider before. Mark is a luminary scientist, and I am lucky to have been trained by him. I will always cherish the

memory of sharing both science and a spanakopita on the back deck of the *R/V Sproul*. And, because of Mark, I will of course never forget the biology. But my committee would not have been the same without Geno. From the first day I reached out to him, he has been so kind and supportive. Every meeting, even when I struggled to explain my ideas, Geno always followed my thought process and asked insightful questions. I am in awe of his breadth of knowledge, as well as his pursuit to keep learning.

Next, I must abundantly thank my other co-authors, Kiefer Forsch and Inès Mangolte. While nothing will quite compare to banging on a 5-gallon-bucket drum while Kiefer plays the guitar on a ship, writing a paper with Kiefer sure comes close. Kiefer's wisdom and generosity are unparalleled, and every conversation we had added a special sparkle to my understanding of the ocean. Similarly, working with Inès has been such a gift. Throughout our months of meetings and banging our heads to rework our paper, I was so inspired by her. She is the cleverest person I have met, with the unique ability to absorb ideas like a sponge and then explain them in extraordinarily intelligent ways. She has made me a better writer, thinker, and scientist—and I am so proud of our work together.

There are also many people I need to thank for helping me get to graduate school in the first place. While there are too many to acknowledge individually, I must thank Jessica Garwood, Lilly McCormick, Lisa Levin, and Jane Teranes. During my SURF REU at SIO, I was questioning whether graduate school would even be a good option for me. Then, nurtured by Jessica and Lilly and guided by Lisa, I experienced the wonders of analyzing data and testing hypotheses. And I was ultimately convinced to apply to graduate school by Jane, who brick-by-brick built a community and program that supported, validated, comforted, and energized undergraduate students. I attribute my perseverance in oceanography and undergraduate teaching

to Jane, and I thank her—and her incredible fashion style—for really inspiring me to this day. I miss you, Jane.

I have also been fundamentally transformed by my friendships. I have the smartest, most talented, most creative, and kindest friends in the entire world. With these friends, I have traversed San Diego and beyond in pursuit of buttery pastries, cozy mystery books, reality TV gossip, jazzy speakeasies, trailer-park-themed dance floors, scenic mountaintops, powdery ski slopes, delicious waves, shark-infested waters, pots of tea, thrifted treasures, and fairy gardens—to mention just a few things. I have never felt so seen by a group of people who are so similar to me in so many ways. In particular, how often can a girl say she has an incredible coven of witches who would drop everything to write a spell with her?! I will cherish these friendships and memories forever.

Finally, I would like to thank my family. My parents are the reason I can enjoy any bit of this life I have. My mom is my inspiration, and her cooking—bowls of noodle soup and chicken curry—gave me strength. My dad is the kindest man you will ever meet, and his phone calls—dropping everything just to speak to me and my siblings—gave me support. My brother is my first best friend, and his visits—spontaneous adventures filled with tasty food—gave me joy. My sister is my eternal rock, and her advice—imbued with wisdom and fashion tips—gave me bravery. I am also so grateful for the life my Ah Pho, Ah Kung, Dadaji, and Dadiji have given me, and I hope to always make them proud. Lastly, to my partner Stephen, my "PhD spouse," my biggest supporter, and my absolute best friend: thank you. Our love has transcended all boundaries (and distances), and I could not have done this without you. I am so excited for the silly, cozy, yummy, and adventurous life we will continue to build together.

Chapter 1, in full, is a reprint of the material as it appears in *Journal of Geophysical Research: Oceans*. Gangrade, Shailja; Franks, Peter J. S., 2024. The dissertation author was the primary investigator and author of this paper.

Chapter 2, in full, is a reprint of the material as it appears in *Limnology & Oceanography*. Gangrade, Shailja; Mangolte, Inès, 2024. The dissertation author and Inès Mangolte were the primary investigators and first authors of this paper.

Chapter 3, in full, has been submitted for publication of the material as it may appear in *Limnology & Oceanography Letters*, 2024. Gangrade, Shailja; Franks, Peter J. S.; Forsch, Kiefer O.; Barbeau, Katherine A., 2024. The dissertation author was the primary researcher and author of this material.

Chapter 4, in part, is currently being prepared for submission for publication of the material. Gangrade, Shailja; Franks, Peter J. S., 2024. The dissertation author was the primary researcher and author of this material.

VITA

2019 Bachelor of Science in Marine Science, University of Delaware

2019 Bachelor of Environmental Engineering, University of Delaware

2021 Master of Science in Oceanography, Scripps Institution of Oceanography, University of California San Diego

2024 Doctor of Philosophy in Oceanography, Scripps Institution of Oceanography, University of California San Diego

PUBLICATIONS

Gangrade, S. & Mangolte, I. (2024), Patchiness of plankton communities at fronts explained by Lagrangian history of upwelled water parcels. Limnol Oceanogr, 69: 2123-2137. https://doi.org/10.1002/lno.12654

Gangrade, S., & Franks, P. J. S. (2023), Phytoplankton patches at oceanic fronts are linked to coastal upwelling pulses: Observations and implications in the California Current System. Journal of Geophysical Research: Oceans, 128, e2022JC019095. https://doi.org/10.1029/2022JC019095

McCormick, L.R., **Gangrade, S.,** Garwood, J.C., Oesch, N.W. & Levin, L.A. (2023), Oxygen and irradiance constraints on visual habitat in a changing ocean: The luminoxyscape. Limnol. Oceanogr. Lett, 8: 220-228. https://doi.org/10.1002/lol2.10296

Gangrade, S. (2020), Warmer Pacific Waters May Lead to Hungry Fish. Limnology and Oceanography Bulletin, 29: 93-93. https://doi.org/10.1002/lob.10387

ABSTRACT OF THE DISSERTATION

Plankton patchiness at mesoscale fronts and filaments: drivers, dynamics, and implications in the California Current System

by

Shailja Daphne Gangrade

Doctor of Philosophy in Oceanography

University of California San Diego, 2024

Professor Peter J. S. Franks, Chair

In the California Current System (CCS), mesoscale features such as fronts and filaments horizontally stir planktonic communities, generating heterogeneity in their spatial and temporal distributions, or "patchiness." Planktonic biomass and community structure have also been found to be nonuniform within the flow features themselves, often in correlation with water-mass properties such as temperature and salinity. But due to high horizontal velocities (50–80 km d^{-1})

along fronts and filaments, the transit times of waters within a flow feature (a few days) are shorter than the timescales required for significant biological community changes (several days to weeks). Given this strong lateral advection, mesoscale flow features must contain distinct plankton patches that propagate along their jets, and these patches must be predominantly structured by processes occurring at their upstream origins. However, few studies have investigated the underlying dynamics and upstream controls that lead to plankton patchiness at mesoscale fronts and filaments, and so this hypothesis remains largely untested.

In this dissertation, I used a diverse suite of hydrographic and biological measurements from satellite and field sampling to characterize spatiotemporal patterns in hydrographic and plankton patchiness at (across and along) mesoscale fronts and filaments in the CCS. I also developed and employed a Lagrangian particle backtracking method to investigate the relative contribution of physical and biological mechanisms in structuring the observed patchiness.

I found that mesoscale fronts and filaments are highly advective systems that act as conduits of different water masses with distinct planktonic communities. “Plankton patches” are entrained into fronts or filaments, where they can converge with other patches and advect along a jet. Distinct plankton patches, with nonuniform community structure and biomass, are shaped by fluctuations in upstream wind-driven upwelling intensity and source-water nutrient concentrations, as well as biological processes—such as growth, grazing, and iron limitation—that occur along Lagrangian trajectories. A combined Eulerian-Lagrangian approach is needed to appropriately characterize and interpret planktonic patchiness in mesoscale fronts and filaments, which are fundamentally non-steady-state systems. These findings help us to identify the physical-biological dynamics that structure biological productivity and diversity, ecological hotspots, and carbon export in Eastern Boundary Upwelling Systems.

INTRODUCTION

Upwelling and hydrography in the California Current System

In the California Current System (CCS), an Eastern Boundary Upwelling System (EBUS), wind-driven upwelling is temporally and spatially dynamic (Chelton, 1982). Coastal upwelling, driven by alongshore equatorward winds, occurs within a narrow (approximately 25-km wide) band along the coast (Huyer, 1983; Jacox & Edwards, 2012; Rykaczewski & Checkley, 2008), while regions of wind-stress curl upwelling can extend up to 200–300 km offshore (Pickett & Paduan, 2003). Upwelling intensifications and relaxations due to modulations in wind stress can result in fluctuations in coastal flow direction as well as shifts in biogeochemical properties, such as nutrient and phytoplankton concentrations, of coastal waters (Checkley & Barth, 2009; Melton et al., 2009; Rykaczewski & Checkley, 2008).

The CCS is composed of distinct water masses with different hydrographic and biogeochemical properties. These water masses originate from subarctic, subtropical, and tropical regions (Bograd et al., 2019; Thomson & Krassovski, 2010; Tomczak & Godfrey, 2003). While the regional-scale water-mass composition of the CCS can vary over several years (Bograd et al., 2015; Bograd et al., 2019), there is a persistent presence of two dominant water-mass features: the California Current (CC) and California Undercurrent (CU). The CC transports relatively fresh, nutrient-poor waters equatorward, while the CU transports relatively salty, nutrient-rich waters poleward (Lynn & Simpson, 1987). The CU is found inshore of the CC and its core is centered within 50–150 km of the coastline and at 50–200 m depth, varying seasonally (Gay & Chereskin, 2009; Lynn & Simpson, 1987; Rudnick et al., 2017; Todd et al., 2011; Zaba et al., 2018). During the upwelling season, waters can originate from source depths near the CU core (Chhak & Di Lorenzo, 2007; Meinvielle & Johnson, 2013).

Plankton patchiness: Characteristics and drivers

In the CCS, the distribution of planktonic communities is nonuniform in space and time; therefore, it is often described as "patchy." The biomass and community structure of phytoplankton —photosynthetic unicellular organisms forming the base of oceanic food webs— are often regulated by multiple physical, biological, and chemical forcings, and their interactions. Bottom-up effects such as the availability of temperature, light, and nutrients regulate phytoplankton growth and biomass (Goericke, 2011b; Tilman, 1977). Top-down processes such as grazing by zooplankton and forage fishes (e.g., sardine and anchovy) can decrease phytoplankton concentrations (Calbet & Landry, 2004; Rykaczewski & Checkley, 2008). In some cases, viruses can attack phytoplankton cells, leading to mortality (Kolody et al., 2019). These processes together enact biological controls on phytoplankton patchiness.

The spatiotemporal distribution of nutrients is a key bottom-up driver of phytoplankton patchiness. Phytoplankton rely on both macronutrients, such as nitrate (NO_3), and micronutrients, such as iron (Fe), to conduct the cellular and enzymatic processes critical for photosynthesis, respiration, and growth. While these nutrients are often supplied by the upwelling of nutrient-rich waters from depth into the euphotic zone where photosynthesis can take place, in some waters, these nutrients can also be limiting. For example, NO_3 is often depleted in well-lit surface waters and is also found in low concentrations in offshore regions of the CCS (King & Barbeau, 2011), due to rapid uptake by phytoplankton (Eppley & Renger, 1986). Moreover, dissolved Fe concentration constrains both phytoplankton growth and biomass and is generally low in the CCS (King & Barbeau, 2007; King & Barbeau, 2011). Supplies of Fe are predominantly modulated by continental shelf width, benthic boundary layer waters, and riverine inputs (Chase et al., 2007; Elrod et al., 2004). Furthermore, the availability of both macro- and micronutrients can depend on preformed concentrations within source water masses

that are advected into the region, reflecting the importance of upstream controls (Bograd et al., 2019; Fiechter & Moore, 2024; Forsch et al., 2023).

Both the supply and composition of nutrients have important implications for phytoplankton community composition and photophysiology. Cyanobacteria, primarily *Synechococcus* and *Prochlorococcus*, are small prokaryotes (cell diameter < 1.5 μm) that dominate communities in low-nutrient waters in this region (Goericke, 2011a, 2011b; Taylor et al., 2012). In contrast, diatoms are large (lengths ≥ 10–500 μm) and often chain-forming eukaryotes that dominate high-nutrient waters in this region (Goericke, 2011a, 2011b; Van Oostende et al., 2015). Other phytoplankton, such as prymnesiophytes (which include coccolithophorids) and dinoflagellates (a diverse taxon of often bloom-forming cells) make up heterogeneous communities throughout the CCS (Venrick, 2002). In their chloroplasts, these phytoplankton utilize protein complexes called photosystems with light-harvesting pigments such as chlorophyll *a* (Chl-a) to conduct photosynthesis. The functionality of these photosystems differs among taxa and is often sensitive to nutrient stress (Behrenfeld & Milligan, 2013; Campbell et al., 1998). Because Chl-a is the main light-harvesting pigment used by phytoplankton, Chl-a fluorescence and concentration are often used as proxies for phytoplankton biomass. The quantum yield of photosystem II can be estimated by the ratio of variable to maximal fluorescence (F_v/F_m) in cells and measured using fast repetition rate fluorometry techniques, yielding estimates of the photochemical efficiency and photophysiological status of phytoplankton cells (Falkowski et al., 2004; Gorbunov & Falkowski, 2022; Schuback et al., 2021).

Zooplankton, which include a wide range of unicellular and multicellular organisms with different reproductive and feeding strategies, are also found in patchy distributions, and this

patchiness is often driven by patchy food supplies. Copepods and euphausiids are important consumers of large phytoplankton and exhibit high abundances in waters with high phytoplankton concentration in this region (Lara-Lopez et al., 2012; Ohman et al., 2012). Some pelagic tunicates (e.g., salps and pyrosomes) are also prolific grazers of small phytoplankton and can be abundant in the CCS (Lavaniegos & Ohman, 2003; O'Loughlin et al., 2020). Zooplankton distributions thus often covary with phytoplankton distributions, though zooplankton are also patchy vertically. Many zooplankton exhibit diel vertical migration, in which organisms remain at depth during the day and migrate toward the surface during the night—mainly to avoid visual predators (Ohman, 1990). Vertical habitat use of zooplankton also varies with cross-shore distance in the CCS (Matthews & Ohman, 2023). Such variability in zooplankton vertical distribution can also affect their horizontal distributions. Zooplankton community composition and spatiotemporal distributions also depend on factors beyond food supply, including the combined effect of bottom-up and top-down forcing (i.e., wasp-waist dynamics), as well as climate conditions (Di Lorenzo & Ohman, 2013; Lilly & Ohman, 2021; Lindegren et al., 2018).

Horizontal stirring of plankton patches

While there are multiple interacting and co-occurring controls on plankton patchiness in this region, previous studies have shown that mesoscale (spatial scales of 10–100 km) and submesoscale (spatial scales of < 10 km) plankton patchiness is predominantly shaped by the coupling of biological processes and horizontal stirring (Lévy et al., 2018; Mahadevan, 2016; Martin, 2003). In the CCS, horizontal stirring is regulated by a mosaic of mesoscale physical features, such as fronts, filaments, and eddies. These stirring features typically persist and slowly evolve over weeks to months (Brink, 1992; Nagai et al., 2015; Strub et al., 1991; Zaba et al., 2021) and thus are robustly detected by both in situ sampling and satellite remote sensing (Barth et al., 2005; Ryan et al., 2005). Planktonic communities are transported within these features,

with different types of plankton sometimes dominating different features, generating an ecological landscape known as “fluid dynamical niches” (d'Ovidio et al., 2010). The types of plankton forming these niches are set by initial environmental conditions, and different flows containing different niches can be subsequently stirred together or apart by mesoscale turbulence (Lévy et al., 2015). Because these transient mesoscale flow features occur nonuniformly along the California coast (Marchesiello et al., 2003), they contribute to the patchy distribution of plankton, often generating conspicuous “tendrils” or “pockets” of high Chl-a (i.e., phytoplankton biomass) (Barth et al., 2005; Hood et al., 1990).

Plankton communities are also nonuniformly distributed within the stirring features themselves. Velocities along these flow features are often 50–80 km d^{-1} (Barth et al., 2000; Kosro & Huyer, 1986; Zaba et al., 2021). So, while these mesoscale features appear relatively stationary for weeks, sometimes with slight westward propagations, the waters they contain move through them rather quickly—usually within days. Given the short transit times of waters through relatively longer-lived hydrographic features, we would expect that plankton patches would similarly propagate along the jets of these features. Patchy distributions of plankton have indeed been observed in fronts, filaments, and eddies in the CCS (Chenillat et al., 2016; de Verneil et al., 2019; Keister et al., 2009). And so here, I describe the general physical and biological characteristics of fronts, filaments, and eddies and briefly explain how they might contribute to plankton patchiness.

Fronts

Fronts, defined as regions of high horizontal density gradients, can form at the boundaries of distinct water masses. In the CCS, mesoscale fronts often form at the interface between counter-rotating eddies (Ohman et al., 2013; Stukel et al., 2017) and at the abutment between mesotrophic upwelled waters and oligotrophic waters of offshore or equatorial origins (Landry et

al., 2009). Strong fronts also form at the boundaries between California Current and California Undercurrent waters (Zaba et al., 2021).

Distributions of biological communities at and across fronts exhibit several different patterns. In many cases, fronts are sites of locally enhanced biomass within the frontal zone distinguishing high-Chl-a frontal waters from relatively low-Chl-a surrounding waters (Claustre et al., 1994). Biological enhancement at these "peak fronts" (Mangolte et al., 2023) is thought to be driven by vertical fluxes of nutrients into the euphotic zone generated from strong horizontal frontal density gradients (Li et al., 2012). Such fronts have also been observed to attract higher trophic level predators (Belkin, 2021; Prants, 2022). In contrast, fronts can also act as boundaries between distinct biological communities associated with different biogeographical domains. These "transition fronts" (Mangolte et al., 2023) thus exhibit strong across-front gradients in planktonic community composition and organic matter (e.g., marine snow) (Gastauer & Ohman, 2024; Lara-Lopez et al., 2012; Ohman et al., 2012; Powell & Ohman, 2015). In some cases, biologically rich waters from remote locations can converge into frontal zones, in which primary production is additionally fueled by nutrient injections within the front (de Verneil et al., 2019) and structured by along-front processes (de Verneil & Franks, 2015).

Filaments

Filaments are also flow features characteristic of the CCS, and they can develop in a variety of ways. Submesoscale filaments, often defined as a central density maximum or minimum across the axis of flow, tend to rapidly develop between eddies and are usually elongated and weakly energetic, with widths ≤ 10 km (Lapeyre & Klein, 2006; McWilliams et al., 2009; McWilliams & Fox-Kemper, 2013). In the CCS, some slightly larger, mesoscale filaments (widths ~50 km) can develop as meanders from the broader California Current and are usually associated with the boundary between the current and a cyclonic eddy (Brink, 1992).

These types of filaments were extensively studied during the Coastal Transition Zone (CTZ) experiments conducted in the 1980s. With the advent of satellite technology to measure sea surface height, temperature, and chlorophyll, CTZ experiments explored waters in these filaments and distinguished them from inshore and offshore waters (Huyer et al., 1991; Strub et al., 1991), finding filaments to carry cold, high-chlorophyll waters offshore (Hood et al., 1991). Brink et al. (1992) concluded, however, that some "cold filaments" were not closely coupled to wind-driven coastal upwelling processes. However, filaments occurring close to the coast, inshore of the California Current, are indeed associated with upwelling. These upwelling filaments tend to form at coastal headlands (Abbott & Barksdale, 1991), during or shortly after upwelling events (Cravo et al., 2010). Upwelling filaments are associated with relatively cold sea-surface temperatures, high surface Chl-a concentrations, and high offshore-flowing velocities (Forsch et al., 2023; Zaba et al., 2021).

Eddies

Mesoscale eddies are circular current features that exist on horizontal scales of < 100 km and timescales of approximately a month. These eddies, which are primarily generated from baroclinic instabilities in the upwelling jet in the nearshore CCS, trap fluid parcels and transport them offshore (Chenillat et al., 2016; Chenillat et al., 2015; Marchesiello et al., 2003; Nagai et al., 2015). Cyclonic and anticyclonic eddies also tend to form at the offshore ends of filaments, limiting offshore transport within the filaments themselves; however, some filament waters can continue to move offshore in westward-propagating eddies (Strub et al., 1991). Eddy-driven upwelling, or eddy pumping, of nutrients into the euphotic zone leads to increased primary productivity associated with cyclonic eddies (McGillicuddy et al., 2003; McGillicuddy et al., 2007). In contrast, eddies can also contribute to a suppression of biological productivity,

particularly in coastal regions of EBUSs, through the lateral or downward transport of waters rich with unused nutrients (Chenillat et al., 2016; Damien et al., 2023; Gruber et al., 2011).

Ecological implications of patchiness

The strong lateral advection of biological material facilitated by mesoscale features can affect ecosystems in a variety of ways. Fronts, filaments, and eddies have been shown to transport organic carbon, which is a large component of living organisms and detritus, from nearshore to offshore regions (Amos et al., 2019; Chenillat et al., 2015; Kosro et al., 1991; Nagai et al., 2015). These features can also transport coastal species offshore, while advecting oceanic species nearshore (Mackas & Coyle, 2005). Furthermore, coastally sourced nutrients can be redistributed offshore, generating areas of localized production offshore (Legaard & Thomas, 2006) that can act as "hotspots" for higher trophic level organisms (Palacios et al., 2006). These modifications in the distribution of organic material by mesoscale features lead to persistent spatial patterns in productivity and export within pelagic and benthic ecosystems, as detailed below.

Spatial decoupling of new and export production

Long-term ecosystem monitoring in the CCS has facilitated the study of persistent, regional-scale ecological variability that is mediated by strong mesoscale advection. Observations and data from the California Current Ecosystem Long-Term Ecological Research (CCE LTER) program, as well as modeling experiments, have revealed that there is a spatial decoupling of coastal new production (production supported by nutrient inputs from outside the euphotic zone) and export production (production exported below the euphotic zone) (Chabert et al., 2021; Kelly et al., 2018; Stephens et al., 2018; Stukel et al., 2011). These studies have found low export production relative to new production in nearshore regions, leading to the hypothesis that mesoscale advective features not only structure biological patchiness but also transport new

production offshore, where the ratio of new production to export production is closer to one (Plattner et al., 2005). While we know filaments and eddies transport biologically rich waters away from the coast (Chenillat et al., 2015; Nagai et al., 2015), we do not fully understand how such across-shore flows mediate these productivity and export patterns, especially when waters transported along these flow features are potentially patchy in space and intermittent in time.

Ecological hotspots and climate implications

Characterizing the spatiotemporal patchiness of new and export production has important implications for both pelagic and benthic ecosystems, as well as oceanic carbon sinks. Knowing the spatial and temporal scales of phytoplankton patchiness at fronts, filaments, and eddies can help predict or diagnose ecological hotspots that may act as feeding grounds for commercially and ecologically important species of fishes (Ryther, 1969), seabirds (Ballance et al., 1997; Russell, 2024), and marine mammals (Barlow et al., 2008). Knowing the contributions of fronts, filaments, and eddies to carbon export can also help elucidate the spatial and temporal scales of ocean-mediated sinks of atmospheric carbon: inorganic CO_2 is converted into organic carbon by phytoplankton, and some fraction is eventually exported from the euphotic layer. This export has important impacts on deep-sea ecosystems and food webs (Tecchio et al., 2013). Sinking phytoplankton and fecal pellets are important food sources for benthic organisms (Rathburn et al., 2001; Smith et al., 1996; Turner, 2015). Characterizing the patchiness of this supply can help constrain models of benthopelagic coupling and further highlight how broad ecosystem patterns may be mediated from the bottom-up by phytoplankton patchiness in mesoscale stirring features.

Lagrangian approaches to investigate controls on patchiness

While static snapshots of the CCS clearly show spatiotemporal plankton patchiness, such measurements obtained using an Eulerian framework are not sufficient for describing how patchiness develops and how it may change in an advective flow field. Within such a stationary

sampling framework, questions remain as to the origins, pathways, and transformations of plankton patches. One powerful way to resolve these dynamics is to incorporate a Lagrangian framework, which follows the trajectories of individual fluid parcels in space and time (van Sebille et al., 2018), thus removing the contributions of physical advection to transformations of the planktonic communities being observed. The use of Lagrangian trajectories can also expand the spatiotemporal dimensions at which we can analyze physical and biogeochemical processes—beyond the coordinates of in situ sampling. Using Lagrangian frameworks, previous studies have estimated changes in biological variables as water masses age (Chabert et al., 2021) and are advected across shore (Messié & Chavez, 2017). By tracing biological processes in tandem with advection, ecological hotspots can be identified (Messié et al., 2022).

By taking a Lagrangian view of plankton patchiness, we can ask: What drives plankton patchiness within (across and along) a mesoscale flow feature (e.g., a front or filament)? Three main hypotheses stem from this question.

The first hypothesis—the "Boundary Condition Hypothesis"—is that differences in boundary conditions (e.g., upstream initial conditions) generate patches with different properties. This could result from time-dependent fluctuations in properties at a stationary boundary (or origin). This sub-hypothesis is referred to later in this dissertation as the "Pulsatile Patch Hypothesis." An additional sub-hypothesis is that differences in boundary conditions could result from spatial variability in properties along a boundary, which would lead to water parcels with different geographic origins having different initial conditions. In both cases, distinct patches, generated by fluctuating (at a point) or spatially distinct boundary conditions, converge and are advected along a flow feature, resulting in spatial gradients in

properties across and along the axis of flow. This concept is also known as the advection-reaction framework.

The second hypothesis—the "Lagrangian Reaction Hypothesis"—is that reactions occur within individual water parcels, or patches, resulting in the time-dependent evolution of plankton patches as they are advected. This would result in a changing concentrations of a hypothetical tracer *C* in a water parcel based on its net reaction rate (*r*), which includes both sources and sinks of *C*. Time-varying concentrations driven by internal dynamics within a patch that is advected would generate spatial patchiness along the axis of flow.

The third hypothesis—the "Stationary Patch Hypothesis"—is that a spatially stationary process or reaction (e.g., a nutrient injection) leads to the appearance of a spatially stationary patch. While tracer *C* (i.e., plankton) in water parcels are advected along a flow feature, the sources and sinks of *C*, described by the net reaction rate *r*, are stationary relative to this flow; therefore, the patch is stationary. Depending on how this patch is sampled in space and time, this process could generate the appearance of patchiness across and (or) along a flow feature.

Ultimately, patchy distributions of plankton result from all these hypothesized mechanisms, which occur contemporaneously. In this dissertation, we explore the relative contribution of these mechanisms to observed plankton patchiness in mesoscale fronts and filaments.

Objectives

The objectives of this dissertation are to:

1. Characterize the spatiotemporal patterns of hydrographic and plankton patchiness at mesoscale fronts and filaments in the California Current System.
    a. Quantify the temporal and spatial scales at which transport of phytoplankton through fronts and filaments is intermittent in time and patchy in space.

2. Investigate the relative contributions of physical and biological mechanisms in structuring plankton patchiness along and across fronts and filaments.
    a. Determine how the variability in nutrient and phytoplankton content of waters at the source of fronts and filaments varies with wind-driven coastal upwelling.
    b. Determine how along-front or along-filament advection contributes to variability in the spatial distribution and community structure of phytoplankton and zooplankton.
    c. Determine how planktonic communities evolve along Lagrangian trajectories.

Dissertation outline

Chapter 1 of this dissertation, "Phytoplankton patches at oceanic fronts are linked to coastal upwelling pulses: observations and implications in the California Current System," investigates phytoplankton patchiness along an eddy-associated front. Patches of elevated phytoplankton concentration were found to have developed at the coast during distinct wind-driven upwelling pulses and then advected into the frontal system, transiting along the front within 3–4 days. In this chapter, I employ an advection-reaction framework to demonstrate the dominant role of advection in structuring patchiness, relative to the weaker contribution of biological reactions such as phytoplankton growth and grazing.

Chapter 2 of this dissertation, "Patchiness of plankton communities at fronts explained by Lagrangian history of upwelled water parcels," is a study conducted with co-first-author Inès Mangolte. In this study, we show that water parcels with distinct planktonic community composition across an eddy-associated front in the CCS (same frontal system as Chapter 1), originated at the coast during episodic wind-driven upwelling events. Different water parcels followed widely different trajectories before converging temporarily at this front. Planktonic

communities in these water parcels transformed during their journeys into the front, with a succession of phytoplankton and zooplankton blooms. We emphasize the utility of Lagrangian approaches that allowed us to show that fine-scale spatial patchiness in planktonic communities can be driven by a patchwork of water parcels at different points in their biological histories.

Chapter 3 of this dissertation, "Salinity is diagnostic of maximum potential chlorophyll and phytoplankton community structure in an Eastern Boundary Upwelling System," derives an explanation for persistent relationships of phytoplankton community composition and Chl-a with salinity and nitrate in this region. In this chapter, I quantify the relationship between salinity and the maximum potential Chl-a (MPC) concentration of a water parcel, using nitrate concentration, a carbon to chlorophyll ratio, and the Redfield ratio. I explain cases in which the MPC is and is not reached, discussing scenarios in which Fe-limitation reduces observed Chl-a. I ultimately demonstrate that phytoplankton patchiness is fundamentally linked to hydrographic patchiness, through the correlation of nitrate with salinity. Therefore salinity, which is more easily measured than nutrients, is diagnostic of critical ecological dynamics.

Chapter 4 of this dissertation, "A salinity-age framework for describing variability in phytoplankton community structure and photophysiology within coastal upwelling filaments" describes spatiotemporal patterns in hydrographic and biological properties associated with coastal upwelling filaments in the CCS. In this chapter, I demonstrate that distinct phytoplankton communities within different water masses can converge in filaments, generating across-filament patchiness in phytoplankton community structure, photophysiology, and Chl-a. I also show that planktonic communities evolve along filaments, and changes in Chl-a and phytoplankton photochemical efficiency are consistent with growth-grazing dynamics and Fe-limitation. By tracking changes in Chl-a and photochemical efficiency in water of different salinities over time

(with age), I can predict the spatial and temporal scales at which export is likely occurring, thus diagnosing ecological conditions in the CCE using a replicable pseudo-Lagrangian strategy.

To conclude this dissertation, I describe how the main findings from each chapter fit within the Eulerian-Lagrangian framework of the controls on patchiness (i.e., Boundary Condition Hypothesis, Lagrangian Reaction Hypothesis, and Stationary Patch Hypothesis). I explore the ecological implications of the results and summarize how this dissertation could be used to characterize how planktonic ecosystems in EBUSs respond to changes in biological, chemical, physical, and climate forcings. Finally, I discuss future work that could be done to refine our understanding of biological patchiness in dynamics mesoscale flow fields of EBUSs.

Chapter 1: Phytoplankton patches at oceanic fronts are linked to coastal upwelling pulses: Observations and implications in the California Current System

1.1 Abstract

Locally enhanced biological production and increased carbon export are persistent features at oceanic density fronts. Studies often assume biological properties are uniform along fronts or hypothesize that along- and across-front gradients reflect physical-biological processes occurring in the front. However, the residence times of waters in fronts are often shorter than biological response times. Thus, an alternate—often untested—hypothesis is that observed biological patchiness originates upstream of a front. To test these two hypotheses, we explore an eddy- associated front in the California Current System sampled during two surveys, separated by 3 weeks. Patches of high phytoplankton biomass were found at the northern ends of both surveys, and phytoplankton biomass decreased along the front. While these patches occurred in similar locations, it was unclear whether the same patch was sampled twice, or whether the two patches were different. Using an advection-reaction framework combined with field and satellite data, we found that variations in along-front gradients in dissolved oxygen, particle biovolume, and salinity support the conclusion that the two phytoplankton patches were different. They were only coincidentally sampled in similar locations. Backward- and forward-in-time tracking of water parcels showed that these phytoplankton patches had distinct origins, associated with specific, strong coastal upwelling pulses upstream of the front. Phytoplankton grew in these recently upwelled waters as they advected into and along the frontal system. By considering both local and upstream physical-biological forcings, this approach enables better characterizations of critical physical and biogeochemical processes that occur at fronts across spatial and temporal scales.

1.2 Introduction

Oceanic density fronts, regions of high horizontal density gradient, are well-known to be sites of enhanced biological activity (Claustre et al., 1994; Franks, 1992; Marra et al., 1990; Yoder et al., 1994) and carbon export (Stukel et al., 2017). Recent studies of frontal systems in the California Current Ecosystem (CCE), a region forced by coastal wind-driven upwelling, have examined cross-frontal gradients of biological and hydrographic properties (Landry et al., 2012; Powell & Ohman, 2015; Stukel et al., 2017). These studies have shown that phytoplankton patchiness at fronts is often associated with enhanced nutrient fluxes along tilted isopycnals, which lead to local phytoplankton blooms as nutrient-rich waters enter the euphotic zone of the front (Levy et al., 2018; Li et al., 2012; Stolte et al., 1994). Patchiness of zooplankton and mesopelagic fish at and across fronts are often directly correlated with enhanced phytoplankton concentrations, and fronts can act as transitional boundaries of abundance and (or) community composition of organisms (Lara-Lopez et al., 2012; Ohman et al., 2012; Powell & Ohman, 2015). Plankton patchiness in the frontal zone is generally thought to be maintained by physical-biological processes occurring at the front, including bottom-up and top-down controls on phytoplankton communities (Li et al., 2012). For instance, Li et al. (2012) found that diapycnal nutrient fluxes combined with reduced microzooplankton grazing contributed to net growth and accumulation of phytoplankton at a frontal system in the CCE. Complex physical and biogeochemical processes are expected to occur at density fronts in the CCE, spanning a wide range of spatial and temporal scales. As a result, characterizing the active, passive, and reactive processes (Levy et al., 2018) that lead to biological patchiness at fronts is exceedingly difficult. In particular, these processes are seldom quantified—or even considered—in the along-front direction, despite strong along-front velocities (0.5–0.8 m s^{-1}) at fronts and other upwelling-

associated jets and filaments in the California Current System (Barth et al., 2000; Kosro & Huyer, 1986; Zaba et al., 2021).

Many studies of fronts have simplified frontal dynamics by assuming that (i) single or repeated cross-frontal transect(s) are representative of the physical-biological processes along the front, and that (ii) fronts can be interpreted as being in a steady state in the along-front direction. For instance, Franks and Walstad (1997) simulated phytoplankton patch formation at a model front due to transient wind events, aligned either along or against the frontal jet, that occurred over a few days. While they showed that physical processes—such as episodic wind events—may intensify phytoplankton patchiness at fronts, they did not consider any variation in properties along the axis of the front. Their simulation thus omitted any effects of along-front processes in driving patchiness at the front.

Because frontal features and their associated density gradients often appear stable and stationary over several days or weeks, some studies have implicitly assumed that planktonic communities are also stationary along the front. For example, Claustre et al. (1994) conducted repeated cross-frontal sampling, over one month, of a persistent front between Atlantic and Mediterranean waters in the strait of Gibraltar. They observed that cross-frontal physical and biological features were "identical and reproducible along the front." Curiously, however, they observed that a phytoplankton community that was seemingly identical at two frontal sites appeared to be in two different stages of a bloom. At one site, the community was at an early-bloom stage; at the other, the community was at an end-bloom stage. They reported that these unexpected differences within a supposedly uniform community warranted further investigation. Their assumption of along-front uniformity thus led them away from investigating how distinct plankton communities—which may have been at different stages of a bloom—can advect along

the front on short time scales relative to changes of the front itself. These examples show how applying steady-state boundary conditions or assumptions of along-front uniformity can potentially oversimplify frontal dynamics and lead to biased conclusions regarding physical-biological dynamics at the front. The residence times of water masses in fronts, and the spatial and temporal scales of transient forcings, must be considered when quantifying biogeochemical fluxes, such as carbon export, at fronts.

If residence times of waters in frontal features are short relative to the time scales of in situ biological reactions, fluctuations in biological and hydrographic properties entering through the upstream boundary may dominate the water mass structure observed at the front. One possible forcing mechanism in the CCE is wind-driven upwelling. Coastal wind-driven upwelling occurs within a narrow band along the coast (Rykaczewski & Checkley, 2008), though regions of wind-stress curl upwelling can extend up to 200–300 km offshore (Pickett & Paduan, 2003). Upwelling is temporally and spatially dynamic in this region (Chelton, 1982; Giddings et al., 2022; Rykaczewski & Checkley, 2008). Mesoscale stirring, driven by a patchwork of filaments and eddies, contributes to the lateral transport of biological productivity away from the upwelling zone (Amos et al., 2019; Nagai et al., 2015; Zaba et al., 2021). Thus, water parcels that originate at the coast in upwelling regions can be entrained into spatially and temporally dynamic mesoscale advective pathways. To understand the dynamics of along-front physical and biological gradients, we must understand the links between fronts, coastal upwelling, and cross-shelf mesoscale advection.

Here, we explored the physical and biological mechanisms associated with phytoplankton patchiness at an eddy-associated density front in the California Current Ecosystem. This front was sampled during two SeaSoar surveys, three to four weeks apart. Striking features of the two

surveys were patches of high phytoplankton biomass at the northern boundaries of each survey. We used an along-front advection-reaction equation (Cushman-Roisin & Beckers, 2011) to formalize two hypotheses that describe the presence of these patches: the stationary patch hypothesis (SPH) and the pulsatile patch hypothesis (PPH). The SPH assumes that gradients of biogeochemical properties are at steady state along the front: along-front advection of these gradients is balanced by in situ biological processes, leading to a geographically stationary patch. This SPH requires a constant flux of chlorophyll into the front at the northern boundary. On the other hand, the PPH assumes that along-front patchiness is driven by a time-varying flux of chlorophyll at the northern boundary. This leads to the along-front advection of distinct chlorophyll patches, with minimal modification by biological processes as they advect rapidly along the front. To test whether in situ biological processes maintained a stationary patch (SPH) or whether individual patches advected through the front (PPH), we calculated along-front gradients in chlorophyll, salinity, particle biovolume, and dissolved oxygen. We also tracked water parcels backward and forward in time to test whether the high-chlorophyll patches at the front could have originated from distinct pulses in coastal upwelling. Our analyses support reinterpretation of physical-biogeochemical dynamics at fronts and demonstrate the need for careful sampling in this region. We must consider the pulsatile nature of upwelling and the subsequent advection and transformation of plankton patches into and along fronts to understand critical biogeochemical processes and fluxes.

1.3 Data and methods

1.3.1 Cruise Sampling and SeaSoar Surveys

The California Current Ecosystem Long Term Ecological Research (CCE LTER) Process Cruise P1208 was conducted off the coast of California from July to August 2012 aboard R/V Melville. This cruise identified and sampled an eddy-associated front, dubbed the “E-Front.” The

sampling region spanned the area within 33.5–35.1˚N and 121.5–123.9˚W. Data were collected during two SeaSoar surveys (Figure 1.1). Survey 1 occurred from 30 July to 3 August, and Survey 2 occurred from 21 August (22 August in UTC) to 25 August. The two SeaSoar surveys spanned ~200 km and ~140 km, respectively, from the northernmost to southernmost transects. Survey 1 sampled in the south-to-north direction (against the along-front flow) (Figure 1.2a), while Survey 2 sampled north-to-south (with the along-front flow) (Figure 1.2b). Because of this, Survey 2 resampled some of the same waters as they advected along the front, while Survey 1 did not (de Verneil & Franks, 2015). The towed SeaSoar acquired data from the surface to approximately 300 m depth. The equipment mounted on the SeaSoar included two CTD sensors, a Chl-a fluorometer, a dissolved oxygen sensor, and a Laser Optical Plankton Counter (LOPC) (Herman et al., 2004). Temperature, salinity, and fluorescence data were averaged into 5-m depth bins; particle counts, particle sizes, and particle biovolumes derived from the LOPC were averaged into 3-m depth bins. Only biovolumes from particles with an equivalent spherical diameter (ESD) of 105–510 μm (~0.1–0.5 mm) were used in this study. This size class contains microzooplankton, such as large ciliates (Dolan, 2010), and mesozooplankton, such as small copepods and pteropods (Brandao et al., 2021; Lopez & Anadon, 2008). Fecal pellets, such as those from copepods, are also within this size range (Feinberg & Dam, 1998). We also used surface chlorophyll concentrations derived from underway measurements by an advanced laser fluorometer (ALF) (Chekalyuk & Hafez, 2008). Persistent cloud cover in this region during the time of sampling precluded the use of satellite-derived sea-surface temperature and chlorophyll in assessing the variability of biological and hydrographic patchiness.

1.3.2 Objective Mapping

SeaSoar data were objectively mapped on depth surfaces to create two-dimensional interpolated fields for both surveys, as in de Verneil and Franks (2015). The along-track and

across-track sampling resolution was ~1 km and ~15–17 km, respectively. Assuming a Gaussian autocovariance and a noise-to-signal ratio of 0.05, we applied decorrelation length scales of 27 km in the along-track direction and 34 km in the across-track direction for salinity, temperature, particle biovolume, oxygen, and density. For chlorophyll, we used length scales of 15 km along-track and 30 km across-track. We applied an error threshold of 0.3 to all maps and selected the depth surface at 27.5 m (25–30 m depth bin) for our analyses, as this eliminated poor-quality surface data (the upper 3–4 bins) while ensuring that the data were collected within the euphotic zone. Euphotic depth ranged from ~40–90 m at the front (Stukel et al., 2017). We also mapped SeaSoar data on isopycnal surfaces. However, many isopycnals in each SeaSoar transect did not remain in the euphotic zone across the front, confounding chlorophyll-oxygen-salinity relationships on density surfaces (Supplemental Figures 1.1 and 1.2).

1.3.3 Horizontal Density Gradient

We defined the front in the two-dimensional objective maps using the region of maximum horizontal density gradient (Supplemental Figure 1.3). Density-gradient contours are symmetric around the maximum gradient; we found that the along-front axis was best described by the eastern 0.04 kg m^{-4} gradient contour for Survey 1 and the eastern 0.02 kg m^{-4} gradient contour for Survey 2. In Survey 2, regions of high horizontal density gradient appear to fork at the northern boundary (Supplemental Figure 1.3). However, we chose the easternmost contour to define the along-front axis because it was the only continuous contour line that aligned with the high-chlorophyll patch; furthermore, the temperature-salinity properties of waters along this line were consistent with those along the frontal axis in Survey 1.

1.3.4 Finite Size Lyapunov Exponents (FSLEs) and Geostrophic Currents

The context of the mesoscale flow in and around E-Front from July to August 2012 was provided by altimetry-derived geostrophic velocities and FSLEs. The geostrophic velocities were

obtained from the Archiving, Validation, and Interpretation of Satellite Oceanography (AVISO) gridded product with 0.25º resolution, provided by Copernicus Marine Environment Monitoring Service (https://marine.copernicus.eu/). FSLE intensities, at a spatial resolution of 0.04º, are calculated based on d'Ovidio et al. (2004) and were downloaded from the AVISO website (https://www.aviso.altimetry.fr/). These backward-in-time FSLEs are derived from backward advection and thus represent rates of convergence of fluid parcels in forward time. FSLE values are inversely proportional to the time it takes for particles to reach a target separation. Therefore, more negative values of FSLEs represent regions of faster convergence. FSLEs often form continuous lines, or ridges, that outline regions of high convergence of fluid parcels. These ridges can therefore represent convergence zones along which waters travel, and we can trace them in space upstream from the front to identify possible source regions of waters found in the front. We also used the altimetry-derived geostrophic currents to obtain streamlines of flow; these were found to align with the FSLE ridges.

We explored velocity products that included both geostrophic currents and wind-driven Ekman currents (at 0 m and 15 m) modelled using European Centre for Medium-Range Weather Forecasts (ECMWF) ERA5 wind stress (Rio et al., 2014). We ultimately selected geostrophic current velocities for our water-parcel trajectories (Section 1.3.5). Although the data products including the geostrophic and Ekman velocities are important for estimating surface currents, in this study, we primarily explore patterns and trajectories of sub-surface (25–30 m) patchiness at the front. The Ekman velocities did not significantly alter our water-parcel trajectory analyses. Because the reliability of satellite data decreases close to shore, we used daily averaged high-frequency (HF) radar velocities (6-km, hourly resolution) provided by the Southern California Coastal Ocean Observing System to complement the geostrophic velocity products (not shown).

These surface currents include potential ageostrophic components of flow, such as wind-driven Ekman currents, but provided particle trajectories that were similar to those generated from the coastal geostrophic velocities. This process further validated the use of the geostrophic velocities to compute water-parcel trajectories for narrow regions close to the coast.

1.3.5 Water-Parcel Trajectories

To explore advection between coastal upwelling regions and the front, we employed the geostrophic velocity fields described above to generate water-parcel trajectories. Given initial water-parcel locations ($x(t)$, $y(t)$) at time *t*, we applied the first-order Euler method to find new parcel locations:

$$x(t + \Delta t) = x(t) + u(x, y, t) \times \Delta t \quad (1.1)$$

$$y(t + \Delta t) = y(t) + \ v(x, y, t) \times \Delta t \quad (1.2)$$

Water-parcel trajectories were analyzed in two different ways (using a Δt = 1 d): backward in time, with particles seeded in the frontal region, or forward in time, with particles seeded in a defined coastal region. Particles initialized at the frontal region were selected based on the latitude-longitude locations of water parcels with Chl-a > 0.25 volts in the objective map surfaces. To maintain focus on the upwelling-driven trajectories, only coastally associated parcels were shown; any parcels that originated (on 21 July for Survey 1 or 6 August for Survey 2) west of 122.8˚W for Survey 1 or 123˚W for Survey 2 were not plotted. For forward-time tracking of parcels, the region bounds (diagonal corners) selected for particle seeding (n=100) were (36.1˚N, 121.89˚W) and (36.2˚N, 122.0˚W). This selection was based on trial and error; we sought to reduce the number of particles that recirculated in the seeding region and therefore selected a narrow coastal region from which all seeded particles traveled into the frontal region.

1.3.6 Upwelling Index

The Coastal Upwelling Transport Index (CUTI) combines in situ and satellite data to provide estimates of upwelling and downwelling at the coast (Jacox et al., 2018). We assembled a time series of daily indices for the 36ºN region to identify the timing of strong upwelling pulses (CUTI > 0.75 $m^2\ s^{-1}$). To isolate a narrow timing window for each pulse and to differentiate between water-parcel trajectories from consecutive pulses, various index threshold values were evaluated to identify "strong" upwelling pulses (not shown) before selecting 0.75 $m^2\ s^{-1}$.

1.3.7 Water Mass Classification

To identify and categorize water masses at the front, waters with particular temperature-salinity (T-S) properties (Supplemental Figure 1.4) were designated as California Current (CC) or California Undercurrent (CU) waters. Previous literature (Bograd et al., 2015; Lynn & Simpson, 1987; Zaba et al., 2021) has identified similar T-S values for CC and CU water masses. These are the two endmembers of the sampled waters found in T-S diagrams. Waters that fell in between the CC or CU regions on the T-S diagram were considered "mixed."

1.3.8 Diagnosing Along-Front Patch Dynamics

To describe the temporal and spatial gradients in a reactive tracer *C* (in this case, chlorophyll), we applied the three-dimensional advection-diffusion-reaction equation (Cushman-Roisin & Beckers, 2011):

$$\frac{\partial C}{\partial t} + \frac{\partial uC}{\partial x} + \frac{\partial vC}{\partial y} + \frac{\partial wC}{\partial z} = \frac{\partial}{\partial x}\left(K_x \frac{\partial C}{\partial x}\right) + \frac{\partial}{\partial y}\left(K_y \frac{\partial C}{\partial y}\right) + \frac{\partial}{\partial z}\left(K_z \frac{\partial C}{\partial z}\right) + rC \tag{1.3}$$

In this equation, the local rate of change of *C* is determined by advection, diffusion, and a net source/sink rate *r.* This net rate *r* could represent a balance of growth and grazing, or physically mediated sources and sinks, such as local nutrient injections and subduction. To make this equation more tractable, we assumed that diffusion, cross-frontal flows (*y*-direction), and vertical

flows (z-direction) are small relative to local rates of change, along-front (x-direction) advection, and source/sink rates. We set the northern boundary of the frontal survey at $x = 0$. With these assumptions, Equation 1.3 simplifies to:

$$\frac{\partial C}{\partial t} + u\frac{\partial C}{\partial x} = rC \tag{1.4}$$

With this simplified along-front advection-reaction equation, we derived equations describing two potential hypotheses to explain biological patchiness in the advective field at the front.

1.3.8.1. The Stationary Patch Hypothesis

Here, we assume the tracer C is at steady state ($\frac{\partial C}{\partial t} = 0$), so that C is stationary in time and space. Along-front gradients of C must be maintained by a constant flux of chlorophyll into the northern boundary ($x = 0$) and a downstream source/sink. Given these assumptions, Equation 1.4 becomes:

$$u\frac{\partial C}{\partial x} = rC, \qquad C(0,t) = C_0 \tag{1.5}$$

1.3.8.2. The Pulsatile Patch Hypothesis Equation

Here, we do not assume that the tracer C is at steady state; instead, we include a time-varying flux of C at the northern boundary ($x = 0$), and no downstream source/sink. The fluctuations of C at the boundary are simply advected into and along the front. Given these assumptions, Equation 1.4 becomes:

$$\frac{\partial C}{\partial t} = -u\frac{\partial C}{\partial x}, \qquad C(0,t) = C(t) \tag{1.6}$$

1.4 Results

1.4.1 Horizontal and Vertical Structure of Front

E-Front, located offshore of Point Conception, California, was positioned between an anticyclonic eddy (positive sea level anomaly) to the west and a cyclonic eddy (negative sea

level anomaly) to the east (Figure 1.1). During the month between the beginning and end of the two SeaSoar surveys, the front was relatively stationary, with a slight westward propagation. However, the flow field surrounding the front evolved over time, with more distinct eddies forming to the north and east of the frontal region (Figure 1.1). Geostrophic currents showed an along-front jet flowing from north to south with a mean along-front speed of 0.47 m s^{-1} (~40.6 km d^{-1}) (Figure 1.1).

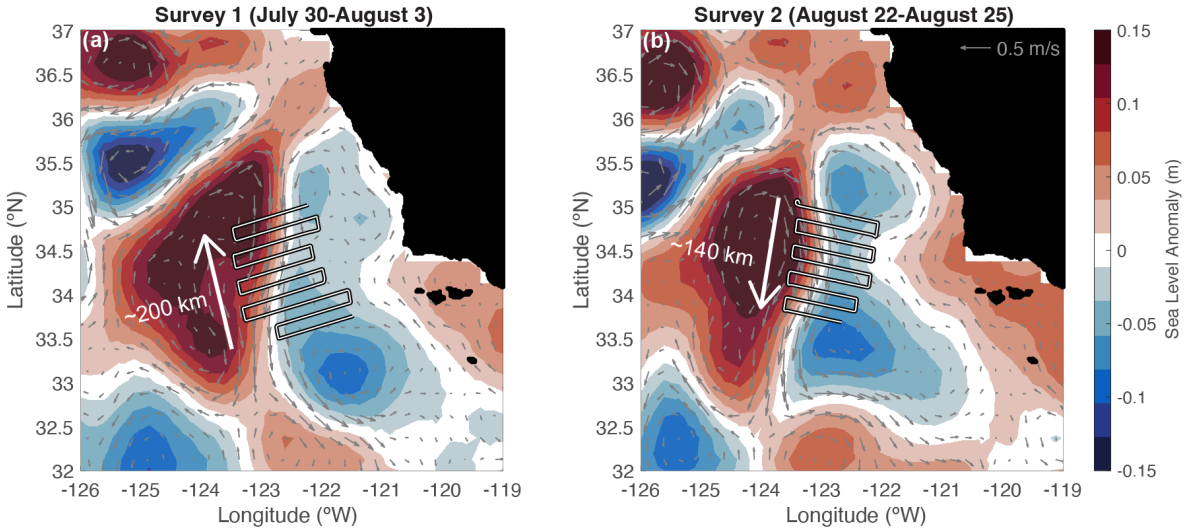

Figure 1.1: Average altimetry-derived sea level anomaly (colors) and geostrophic velocity vectors with cross-frontal survey tracks for (a) SeaSoar Survey 1 (30 July–3 August 2012) and (b) SeaSoar Survey 2 (22–25 August 2012) sampled during the 2012 CCE LTER Process Cruise. Positive (negative) sea level anomaly indicates an anticyclonic (cyclonic) eddy to the west (east) of the front. White arrows show the SeaSoar sampling directions.

The front was defined as the region where the horizontal gradient in density was highest (see Methods). The cross-frontal density structure revealed sloping isopycnals that shoaled from west to east (offshore to inshore), and isopycnals $\sigma < 25.2$ kg m^{-3} outcropping at the surface at the front (Supplemental Figures 1.1 and 1.2). The front was located at the interface of fresher California Current waters to the west, and saltier California Undercurrent waters to the east (Supplemental Figure 1.4). Cross-frontal transects from each SeaSoar survey showed vertically

and horizontally layered chlorophyll patches that were associated with fine-scale salinity structures and FSLEs at the front (de Verneil et al., 2019).

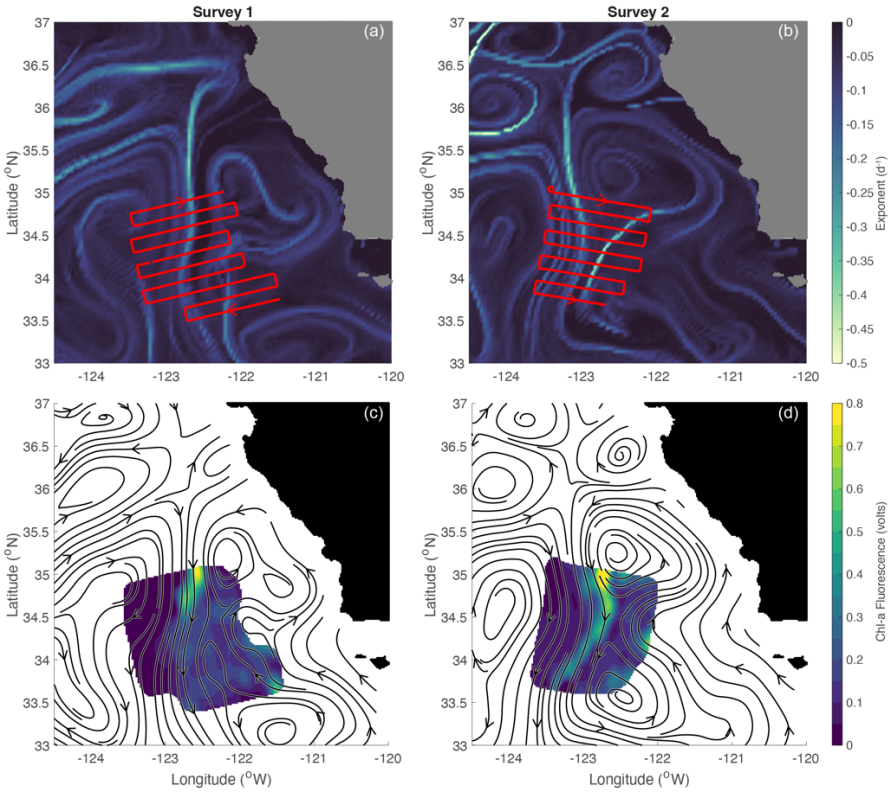

Figure 1.2: Satellite-derived FSLE fields, averaged over the duration of each survey, with SeaSoar tracks for (a) Survey 1 and (b) Survey 2. Altimetry-derived streamlines, averaged over the duration of each survey, over objectively mapped surfaces of Chl-a at 27.5 m (color) for (c) Survey 1 and (d) Survey 2. Both FSLE ridges and streamlines connect the eastern waters of E-Front to potential coastal upwelling regions, near 36ºN.

1.4.2 Along-Front Patchiness

During both surveys, both biological and hydrographic gradients were found along the front; these included along-front variability in chlorophyll, salinity, dissolved oxygen (both concentration and % saturation, not shown), and particle biovolume on the 27.5 m depth surface (Figures 1.3 and 1.4). Both surveys showed a high-chlorophyll (HC) patch positioned at the northern survey boundary; chlorophyll generally decreased from this patch along the front (Figures 1.3e and 1.4e). The along-front decrease in chlorophyll was sharper for Survey 1 than for Survey 2 (Figures 1.3e and 1.4e).

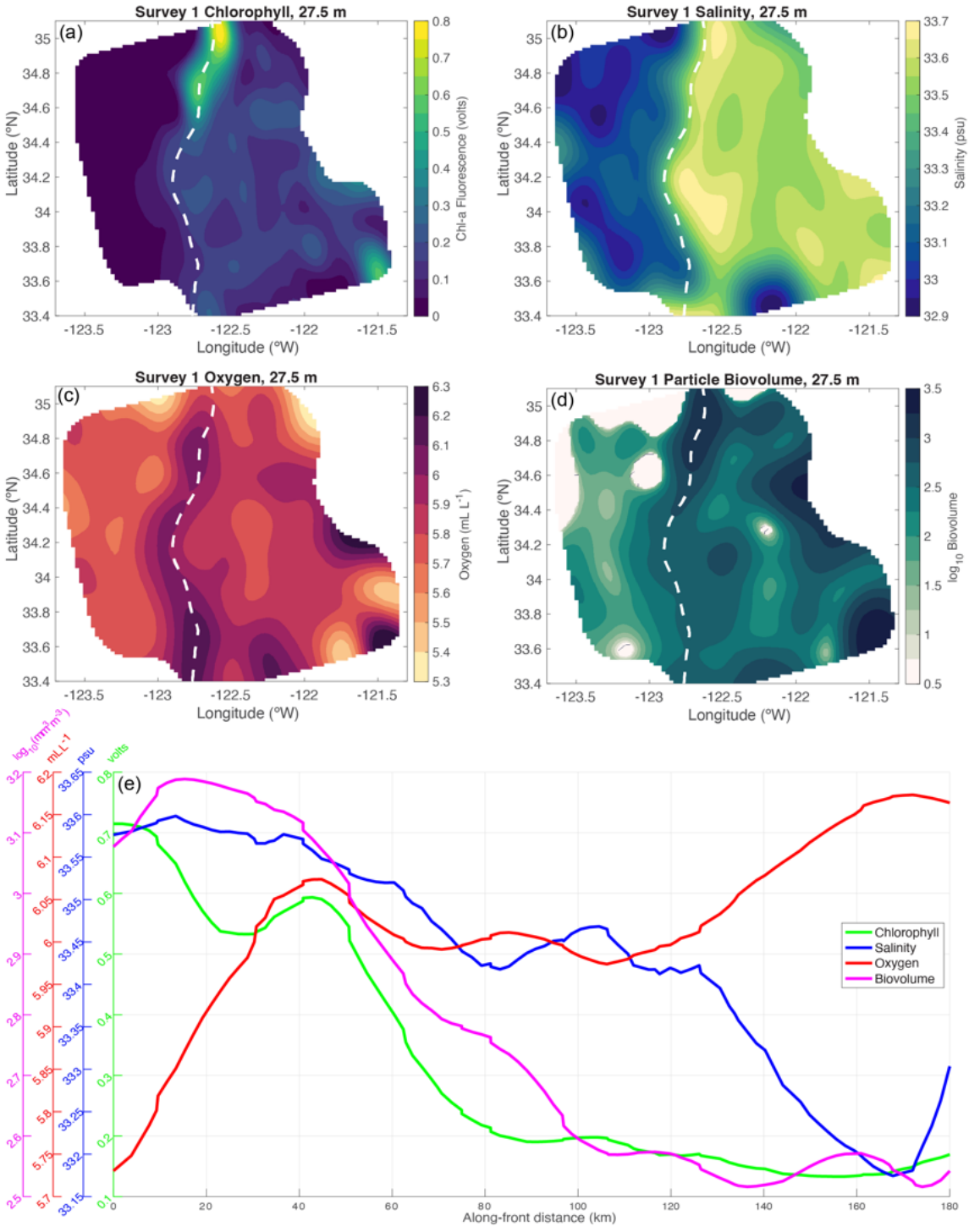

Figure 1.3: Survey 1 objective maps on the 27.5 m depth surface of (a) Chl-a fluorescence, (b) salinity, (c) dissolved oxygen, and (d) particle biovolume (ESD 0.1-0.5 mm). Contour of the horizontal density gradient (white dashed line) shows the along-front axis, from north to south. (e) Along-front fluctuations of Chl-a fluorescence, salinity, dissolved oxygen, and particle biovolume.

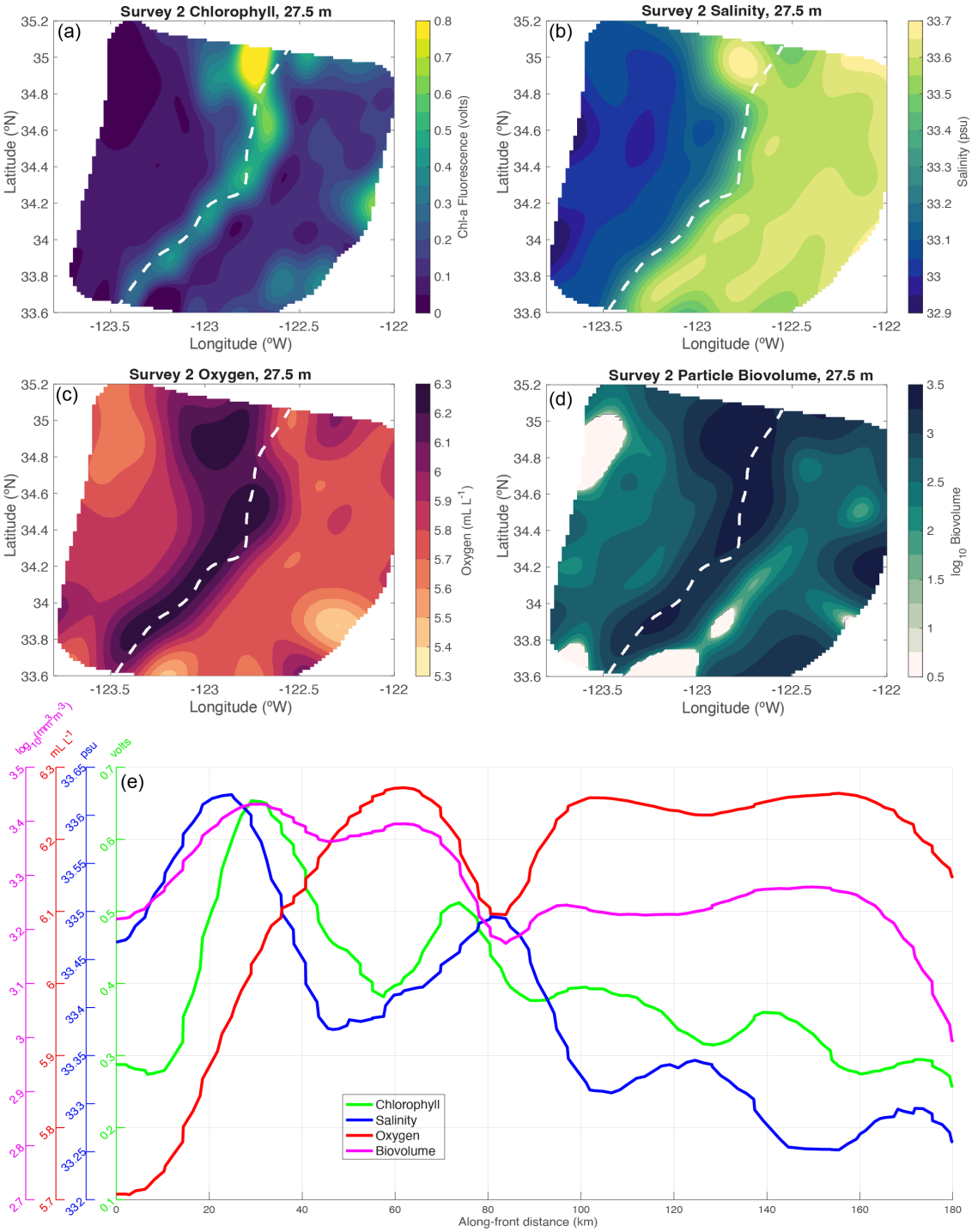

Figure 1.4: Survey 2 objective maps on the 27.5 m depth surface of (a) Chl-a fluorescence, (b) salinity, (c) dissolved oxygen, and (d) particle biovolume (ESD 0.1–0.5 mm). Contour of the horizontal density gradient (white dashed line) shows the along-front axis, from north to south. (e) Along-front fluctuations of Chl-a fluorescence, salinity, dissolved oxygen, and particle biovolume.

During both surveys, high chlorophyll at the northern boundary was also associated with high salinity and high particle biovolume, but low dissolved oxygen (Figures 1.3 and 1.4). During Survey 1, there were two high-salinity (> 33.6 psu) features (Figure 1.3b): one positioned at the northern boundary associated with the high chlorophyll patch and another just south, not associated with high chlorophyll. Similarly, during Survey 2, the highest chlorophyll was associated with the highest salinity (and low oxygen) at the northern boundary (Figures 1.4a and 1.4b). While the along-front axis did not clearly intersect this northern patch, it still aligned with some high-chlorophyll, high-salinity (HC-HS) waters to the north that appeared to mix with low-chlorophyll, low-salinity waters (LC-LS) to the west as they advected downstream (Figure 1.4b). Fluctuations and a general decrease in chlorophyll along the front were mirrored by fluctuations and decreases in both salinity and particle biovolume (Figures 1.3e and 1.4e). In contrast, oxygen remained relatively constant or increased along the front. In Survey 1, the highest oxygen concentration was found at the southern end of the survey region where chlorophyll was lowest. The negative mean along-front gradients in chlorophyll, salinity, and particle biovolume thus contrasted with positive mean along-front gradients in oxygen in both surveys. Superimposed on the mean along-front gradients were fluctuations at 10–20 km scales (Figures 1.3e and 1.4e); these smaller-scale fluctuations in biological properties (chlorophyll, particle biovolume, oxygen) were usually aligned spatially with fluctuations in salinity.

Based on this biological and hydrographic structure on the 27.5 m depth surface, we observed that HC-HS waters flowed into the front at the northern boundary and were sampled about three weeks apart during surveys carried out in two different directions: south to north (against the along-front flow, Survey 1), and north to south (with the along-front flow, Survey 2).

1.4.3 Thermohaline Characteristics of Patchy Waters

We identified endmember water masses in the T-S diagrams as low-salinity, low-chlorophyll California Current waters, and high-salinity, high-chlorophyll California Undercurrent waters (Figure 1.5 and Supplemental Figure 1.4). These water-mass patterns have been seen in other upwelling features in the CCE, such as coastal upwelling filaments (Zaba et al., 2021). The highest chlorophyll (> 0.7 volts) at the front in both surveys fell within a narrow band of high salinity: 33.6–33.7 psu for Survey 1, and 33.5–33.7 psu for Survey 2 (Figure 1.5). On the T-S diagram, these HC-HS waters also appeared within a narrow temperature range for Survey 1, but a broader temperature range for Survey 2 (Figures 1.5c and 1.5d). This broader temperature range was driven by higher temperatures due to radiant heating of the surface.

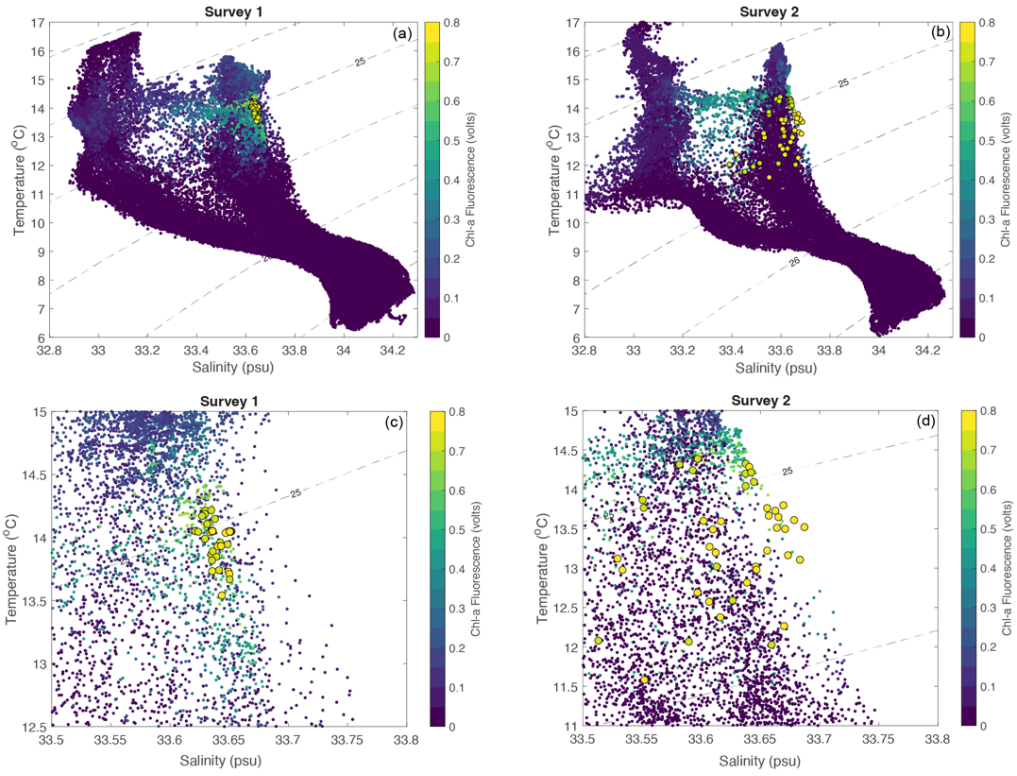

Figure 1.5: Temperature-salinity diagrams of all measurements in (a) Survey 1 and (b) Survey 2. Zoomed-in views show the high chlorophyll associated with narrow salinity ranges of 33.6–33.7 psu in (c) Survey 1, and with salinity ranges of 33.5–33.7 psu in (d) Survey 2.

1.4.4 Mesoscale Flow Context Links Patchiness to Coast

Chlorophyll patchiness at this front has previously been linked to both coastal and offshore waters through FSLEs (de Verneil et al., 2019). There were three main FSLE ridges contributing to the along-front jet in Survey 1, with the easternmost frontal ridge connecting to the inshore coastal region (Figures 1.2a and 1.2c). In Survey 2, these three FSLE ridges had shifted to the west, and a cyclonic eddy had formed on the eastern (inshore) side of the front, circulating coastal waters into the front. The streamlines of flow indicate that waters flowing into the front and containing the HC-HS patch at the northern boundary of Survey 1 likely originated at the coast around 36 ºN. Waters forming the HC-HS patch concentrated at the northern end of Survey 2 originated in a broader coastal region connected to the frontal system by the coastal streamlines centered around 36 ºN as well as the cyclonic eddy on the eastern side of the front (Figures 1.2b and 1.2d).

1.5 Discussion

We observed pronounced patches of high phytoplankton biomass at the northern boundaries of both SeaSoar surveys, and phytoplankton biomass decreased along the front (north-to-south). These features were sampled three to four weeks apart and appeared relatively geographically stationary in the face of constant advection along the front. To diagnose the dynamics that created these strong along-front biological gradients, we tested both the stationary patch hypothesis (SPH) and pulsatile patch hypothesis (PPH).

Our analyses showed that even though the front was relatively geographically stationary over the entire month-long sampling period, waters were only resident in the front for a few days. We found that the front was not in a biological steady state, which rejects the SPH. Instead, hydrographic and biological patches advected along the front with relatively little change,

supporting the PPH. Backward- and forward-in-time advection showed that these patches originated from distinct pulses in coastal upwelling, which occurred upstream of the front.

To highlight how the SPH-PPH hypothesis framework can influence estimates of carbon export and how our novel characterization of along-front gradients can improve our understanding of E-Front, we begin by discussing assumptions that have been made in previous analyses of this frontal system.

1.5.1 Previous Interpretations of E-Front Dynamics

Chronologically, over the month-long study, sampling included SeaSoar Survey 1, a Moving Vessel Profiler survey, two cross-frontal transects separated by five Lagrangian "cycles", and SeaSoar Survey 2. Other studies of this frontal system interpreted the decreasing phytoplankton biomass along the front as driven by an in situ biological sink (de Verneil & Franks, 2015) or vertical export along the front (Stukel et al., 2017). These studies assumed that the productive waters at the front either had a "similar source" (de Verneil & Franks, 2015) or were geographically stationary and at steady state between the various sampling campaigns conducted (Stukel et al., 2017). These interpretations are consistent with the assumptions of the SPH.

Using a pseudo-Lagrangian tracer-rate analysis, de Verneil and Franks (2015) quantified the loss rate of chlorophyll in Survey 2 (the survey in the direction of the frontal flow that resampled some water masses) to be $r = -0.17$ d^{-1}. Stukel et al. (2017) used sediment traps and a steady-state ^{238}U–^{234}Th disequilibrium model to estimate carbon export rates of 437 mg C m^{-2} d^{-1} and 145 mg C m^{-2} d^{-1}, respectively. These export processes were presumed to have been driven by sinking particle fluxes and increased mesozooplankton grazing along the front. This study noted that potential error in calculating these export rates could have arisen from the fact that the half-life of Thorium-234 (24.1 d) was much longer than the residence time of waters in the front

(3–4 d). Also, the export rates measured from cross-frontal transects in this study averaged across several distinct high-chlorophyll, high-particle-load layers at the front, as described by de Verneil et al. (2019). This may have also invalidated some of the assumptions underlying Stukel et al.'s (2017) calculations.

Neither of these studies considered changes in the biological patterns over the month-long sampling period outside of a steady-state framework. In other words, these two studies implicitly assumed the SPH, but did not consider or test the PPH. Applying only the SPH could lead to overestimates of carbon export, forced by biological processes. On the other hand, assuming only along-front advection in the PPH could lead to underestimates of biological processes or vertical particle fluxes. In the next section, we outline predictions associated with both the SPH and PPH and evaluate evidence that either supports or rejects each hypothesis.

1.5.2 Testing the SPH and PPH

The SPH posits that the phytoplankton patch was geographically and temporally stationary in the face of strong along-front advection. To keep such a patch stationary, the along-front advection of high chlorophyll concentrations from the north would have to be balanced by a loss of chlorophyll along the front. In contrast, the PPH posits that the chlorophyll patchiness at the front resulted from fluctuations in chlorophyll at the northern boundary, rather than an in situ sink. Here, we outline a set of predictions for each hypothesis, followed by a test of the predictions based on the data.

SPH Prediction 1: There was an along-front loss of chlorophyll driven by grazing and sinking; the respiration associated with grazing should cause a decrease in dissolved oxygen along the front. Furthermore, the elevated presence of grazers and/or detritus associated with the decreasing phytoplankton should appear as an increase in particle biovolume (both grazers and detritus) along the front.

PPH Prediction 1: There was no significant grazing loss or export of chlorophyll maintaining the along-front chlorophyll gradient in either survey. Along-front variations in oxygen and particle biovolume were associated with the fluctuating water masses that entered the front at the northern boundary and subsequently advected along the front.

Test 1: Dissolved oxygen concentration on the 27.5 m depth surface in both surveys *increased* from north to south, along the front, non-monotonically (Figure 1.3e). The lowest oxygen was found at the northern end in waters associated with the highest chlorophyll, while the highest oxygen was found downstream in regions of much lower chlorophyll (Figure 1.3c)—exactly the opposite of the prediction from the SPH. Particle biovolume peaked at the northern boundary, decreasing along the front (Figures 1.3e and 1.4e)—again, the opposite of the prediction of the SPH. These trends, however, are consistent with the predictions of the PPH, which predicts that changes in properties along the front reflect the properties of different water masses advecting along the front.

SPH Prediction 2: Water mass properties were relatively uniform along the front; salinity variations along the front were minimal and unrelated to variability in biological and chemical properties.

PPH Prediction 2: Variations in chlorophyll, dissolved oxygen, and particle biovolume were associated with the differing water masses entering the front through the northern boundary and were correlated with variations in salinity (an indicator of water mass).

Test 2: In both surveys, salinity fluctuated along the front, and along-front fluctuations in chlorophyll were associated with these fluctuations in salinity (Figures 1.3e, 1.4e, and Supplemental Figure 1.5). Most waters within certain high-salinity ranges (~33.5–33.7 psu) also had higher chlorophyll (Figure 1.5). Oxygen had a nonlinear and mostly negative relationship

with salinity (Supplemental Figure 1.5): while salinity generally decreased along the front, oxygen increased (Figures 1.3e and 1.4e). Particle biovolume had a nonlinear and positive relationship with salinity for most points along the front (Supplemental Figure 1.5). There were regions along the frontal axis, particularly in Survey 2, where biovolume and salinity were not positively associated, but these occurred at spatial scales < 10 km, which are smaller than the across-track sampling resolution (15–17 km). Thus, these small-scale patterns could represent unresolved submesoscale biological and hydrographic patchiness, but we cannot resolve the contributing processes at those spatial scales. Overall, the along-front relationships between salinity, chlorophyll, oxygen, and particle biovolume are inconsistent with the SPH, but strongly support the PPH predictions.

1.5.3 The Potential Influences of Vertical Processes in the Front

Modulations in chlorophyll along the front could occur due to local vertical fluxes, such as nutrient injections, subduction, and sinking. In our advection-reaction framework, these processes are implicitly included in the net rate *r*. However, our data do not allow us to resolve the relative influence of each process within the net rate term.

Nutrient fluxes within the front, especially those that may be regulated by the cyclonic eddy east of the front, may contribute to phytoplankton growth—particularly at Survey 2—as cold, nutrient-rich waters upwelled at the edges of eddies stratify and are exposed to more light (Mahadevan, 2016). The stratification of waters by eddy-associated processes may lead to inhomogeneous and patchy phytoplankton distributions (Mahadevan et al., 2012). While we cannot test the degree to which eddy restratification influenced the timing and intensity of phytoplankton growth upstream of or along the front, we found that the along-front variability in chlorophyll was tightly coupled to the along-front variability in salinity. This is consistent with

the patches of chlorophyll being predominantly driven by the advection of distinct water masses along the front.

An along-front loss of chlorophyll could result from subduction or sinking; however, these processes do not appear particularly strong at the front. On the time scales of sampling at this front (10–12 hours between individual transects), both subduction and sinking would lead to unusually high concentrations of chlorophyll below the euphotic zone, but this was not observed at the front (Supplemental Figures 1.6 and 1.7). There is no unusually high chlorophyll fluorescence any deeper than the subsurface chlorophyll maximum found on the western side of the front (Supplemental Figure 1.1). This suggests that if subduction or sinking of the phytoplankton patches occurred, it was weak over the spatial and temporal scales of sampling at the front.

While vertical fluxes and stratification processes are relevant to this frontal system, we cannot currently separately estimate the sources and sinks related to each physically mediated horizontal or vertical process. However, our analyses show that the spatial and temporal patterns of chlorophyll, oxygen, particle biovolume, and salinity are better explained by the PPH and SPH.

1.5.4 Evidence Supports the PPH

Our analyses show that the survey data are more consistent with the PPH than the SPH. Increases in oxygen and decreases in particle biovolume along the front indicate that the losses of chlorophyll were not solely a reflection of biological processes. Oxygen was lowest where the SPH would predict it to be greatest: in waters associated with the chlorophyll patch. Oxygen increased downstream, inconsistent with the respiration required to drive a loss of phytoplankton (SPH). Moreover, particle biovolume decreased downstream where we expected to have a high grazing and export signal, according to the sink of the SPH. Furthermore, particle biovolume,

dissolved oxygen, and chlorophyll all varied in association with salinity—a water mass tracer—along the front. From this, we conclude that the chlorophyll patches in the two surveys must have been entirely different: it was only by coincidence that the patches were sampled in similar geographic locations in the front. We now investigate the PPH in more detail, exploring the sources of the water-mass fluctuations at the northern boundary of the front.

1.5.5 Relating PPH Predictions to Upwelling Dynamics

The PPH posits that the along-front gradients in chlorophyll varied in time and space and were not predominantly mediated by biological processes. Instead, given that the residence time of waters at the front was only 3–4 days, patches of high-chlorophyll, high-salinity, and low-oxygen water must have entered the survey region at the northern boundary and advected along the front. Thus, differences in the upstream origins and advective pathways of these patches may explain the coincidental observation of the two patches at similar locations. The high chlorophyll concentrations at the front suggest a prior influx of nutrients into the water mass that supported the phytoplankton growth. A likely source of high nutrient concentrations in the euphotic zone is coastal wind-driven upwelling.

The easternmost FSLEs and streamlines in the front (Figure 1.2) showed a clear upstream connection of the front to coastal regions to the east. We therefore investigated the potential for advection of chlorophyll/salinity patches into the front from the coast, where wind-driven upwelling occurs. In particular, we tested whether the chlorophyll/salinity patches found at the front in the two surveys could have been linked to distinct upwelling pulses. To assess this, we used satellite-derived geostrophic velocities to calculate water-parcel trajectories backward-in-time from the front to potential source regions, and forward-in-time from potential coastal upwelling source regions to the front.

These trajectories, which tended to align with the coastally associated FSLE ridges or streamlines, revealed the patterns of the mesoscale flow field surrounding the relatively physically stationary front. These FSLE ridges and streamlines showed the flow of water into the front and displayed how these flows were connected to coastal upwelling regions. Understanding the spatial and temporal dynamics of coastal upwelling and the pathways for upwelled water to enter the front will allow us to explore links between these flow pathways, and the spatial and temporal variability of biological and chemical properties measured at the front.

1.5.5.1 Patch Source Dynamics: Geographic

We tracked the water parcels that formed the high-chlorophyll patches (locations where Chl-a > 0.25 volts on 27.5 m depth surfaces) backward-in-time to identify potential source locations. These analyses showed that the high-chlorophyll waters in Survey 1 likely originated within a narrow region centered at ~36˚N and 121.75˚W (Figure 1.6). The high-chlorophyll patch in Survey 2 was also linked to a coastal source region; however, this region was broader than that in Survey 1, encompassing both waters at the coast, and waters circulating around a cyclonic eddy just east of the frontal region (Figure 1.7). A coastal filament that wrapped around the northern edge of this eddy carried coastal waters into the frontal sampling region. This cyclonic eddy appeared to be the dominant mechanism by which coastal, high-chlorophyll waters were entrained and transported into the front before being sampled during Survey 2. Vertical nutrient fluxes and stratification, regulated by this cyclonic eddy, likely contributed to the growth of phytoplankton in nutrient-rich waters exposed to the euphotic zone upstream of the front (Chenillat et al., 2016; Mahadevan, 2016). In addition, the entrapment and retention of some upwelling-associated waters within this eddy over the shelf could have also enhanced local phytoplankton growth as well (Chenillat et al., 2016; Chenillat et al., 2015).

These parcel trajectories demonstrated that the high-chlorophyll waters flowing into the northern boundary of the front originated at the coast. However, the patch observed during Survey 1 had different spatial origins (narrow region at ~36ºN) than the patch observed during Survey 2 (broader coastal region around 36ºN and driven by a cyclonic eddy inshore of the front).

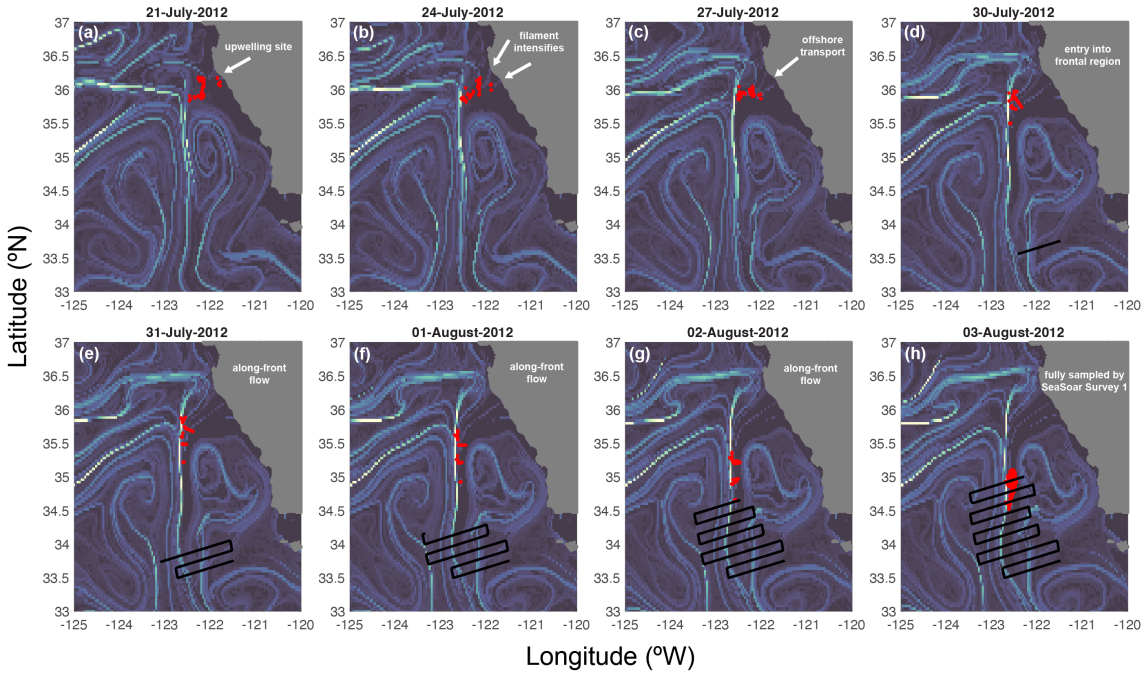

Figure 1.6: Daily FSLE field with snapshots of water parcel locations (red filled circles) of the high-chlorophyll patch sampled in Survey 1 (black lines) from 21, 24, 27 and 30 July (a-d) and 31 July to 3 August (e-h). Water-parcel trajectories are shown on the day of estimated origin (a), on subsequent days as a filament that connects the coast to the front (b-g) and the day the patch was sampled (h).

1.5.5.2 Patch Source Dynamics: Temporal

The backward-in-time water-parcel trajectories showed that the waters sampled in Survey 1 originated at the coast around 20–21 July (Figure 1.6). A filament carrying these water parcels developed at the coast from approximately 20 July to 30 July, eventually connecting the parcels to the frontal survey region by 2 August. This resulted in a time window of 12–14 days after

upwelling, during which phytoplankton biomass could have increased as the water mass transited from the coast to the front before being sampled by Survey 1 from south to north.

The waters sampled at the front during Survey 2 originated later than Survey 1 waters and were likely upwelled around 6 August and subsequently advected into the frontal region, where they were sampled beginning 22 August (Figure 1.7). Some of these waters were then resampled along the front during Survey 2, which progressed from north to south in the direction of the along-front flow. This resampling of the advecting patch would make it appear longer (along the front) than the patch in Survey 1, which was sampled against the direction of the flow. The different along-front chlorophyll gradients are consistent with the PPH and the sampling direction of the two surveys: strong gradients when sampled against the flow, weak gradients when sampling with the flow. This further underscores the need to account for sampling strategy and flow directions when interpreting spatial patchiness at fronts.

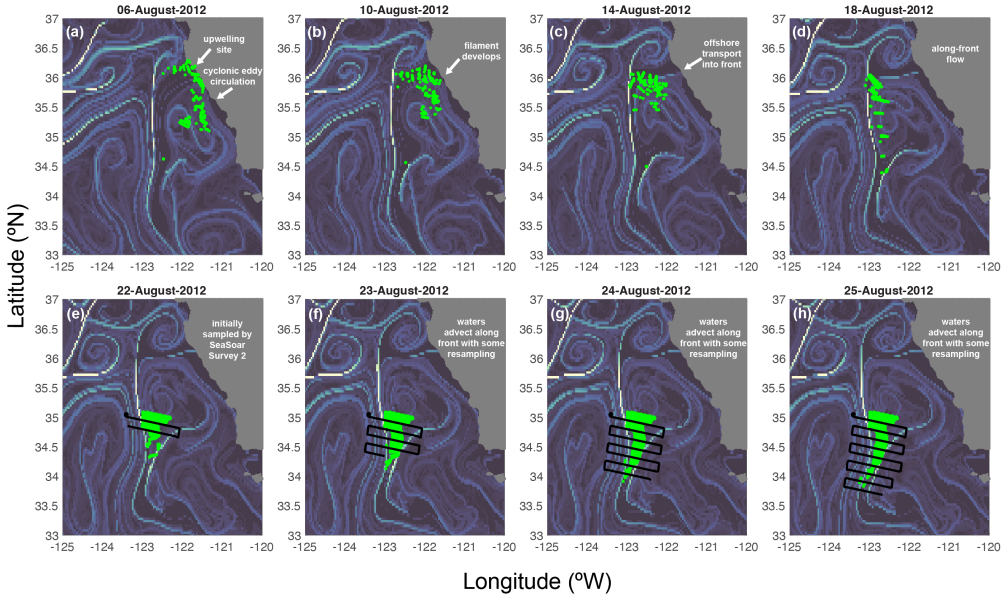

Figure 1.7: Daily FSLE field with snapshots of water parcel locations (green filled circles) of the high-chlorophyll patch sampled in Survey 2 (black lines) from 6, 10, 14 and 18 August (a–d) and 22 August to 25 August (e–h). Water-parcel trajectories shown on the day of estimated origin (a), and on subsequent days as an eddy located east of the front, and coastal upwelling circulate water into the front (b–d) to be sampled by the SeaSoar (e–h).

We used records of the daily CUTI (Jacox et al., 2018) at 36ºN to investigate whether particular upwelling pulses might have led to the high-chlorophyll water masses found in the front during the surveys. Seeding water parcels within a narrow region (0.1º latitude x 0.1º longitude) at ~36ºN during strong upwelling pulses (Figure 1.8) gave us forward-in-time trajectories (Figure 1.9) showing the timings and trajectories of water parcels entering the surveyed frontal region. We compared those to the timings approximated from the backward-in-time trajectories (Figures 1.6 and 1.7).

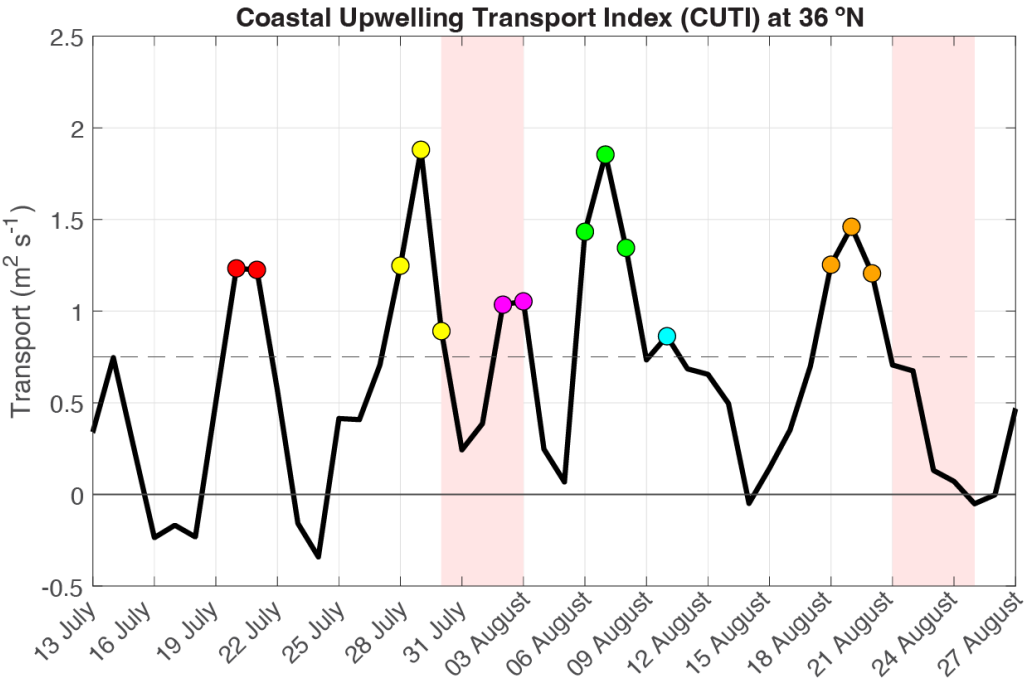

Figure 1.8: Coastal upwelling transport index (CUTI, black line) at 36˚N for 13 July to 27 August 2012. Index values above 0.75 m^2 s^{-1} (dashed line) were identified as "strong pulses" and were considered in forward-tracking water-parcel trajectories with colors of filled circles corresponding to specific upwelling pulses. Red-shaded regions indicate the SeaSoar survey periods.

Our analyses support the hypothesis that the phytoplankton patches observed in the frontal SeaSoar surveys originated from distinct upwelling pulses that preceded our sampling by about 11 to 16 days (Figure 1.8). The high-chlorophyll waters sampled in Survey 1 on 2-3

August were formed by the 21–22 July upwelling pulse; at that time, a filament connected the coast directly to the front (red dots in Figures 1.8 and 1.9). Strong upwelling pulses prior to this date did not feed into the frontal region (not shown). The high-chlorophyll waters sampled in Survey 2 on 21–22 August originated partially from the 6–7 August upwelling pulse (green dots in Figures 1.8 and 1.9). At that time, there was still a filament directly connecting the coast to the front, as well as a developing cyclonic eddy circulation seen in the FSLE field (Figure 1.9e-h).

These results from the forward-tracking analyses are also consistent with the spatial origins we detected in the backward tracking. These results underscore the hypothesis that the high-chlorophyll patch in Survey 1 originated from a narrow region at the coast ~36ºN, while the patch in Survey 2 originated from a broader coastal region, near 36ºN, that was also directly associated with the cyclonic eddy inshore of the front. Notably some of the waters sampled by Survey 2 in the forward-tracking (green dots in Figure 1.9) were located slightly west of those identified in the backward-tracking (green dots in Figure 1.7), highlighting how waters in the interior of the cyclonic eddy inshore of the front may have contributed to the high-chlorophyll patch in Survey 2. Indeed, the backward tracking (Figure 1.7) confirms that waters from the 6–7 August upwelling pulse that developed at the coast ~36ºN—*as well as* the interior eddy waters—contributed to high chlorophyll at the northern end of Survey 2 and subsequently along the front (Figure 1.7). In summary, both backward-tracking and forward-tracking of the water parcels to and from the coast, respectively, identified the same temporal windows of origin that corresponded to distinct and intense upwelling pulses: 21–22 July for Survey 1 and 6–7 August for Survey 2.

Given the time scale of 11 to 16 days to advect from the coast to the sampled frontal patches, we can use the increase in chlorophyll along the water parcel's trajectory to calculate phytoplankton net growth rates (r). Assuming a constant growth rate, we can calculate r as:

$$r = \frac{1}{\Delta t} ln \frac{C(t)}{C_0} \quad (7)$$

With an assumed initial chlorophyll concentration C_0 = 0.1 μg L^{-1} in recently upwelled waters at the coast (Kahru et al., 2012; Zaba et al., 2021) and maximum surface chlorophyll values of 7.9 μg L^{-1} (Survey 1) and 8.7 μg L^{-1} (Survey 2) as the final concentrations, r ranged from 0.28 to 0.40 d^{-1} for Δt = 11 to 16 days, respectively. These rates are consistent with those previously measured during CCE process studies (Landry et al., 2012; Landry et al., 2009; Li et al., 2012). This provides support for the hypothesis that the nutrient-rich waters that led to the chlorophyll patches in the front originated during upwelling at the coast, approximately two weeks prior to sampling.

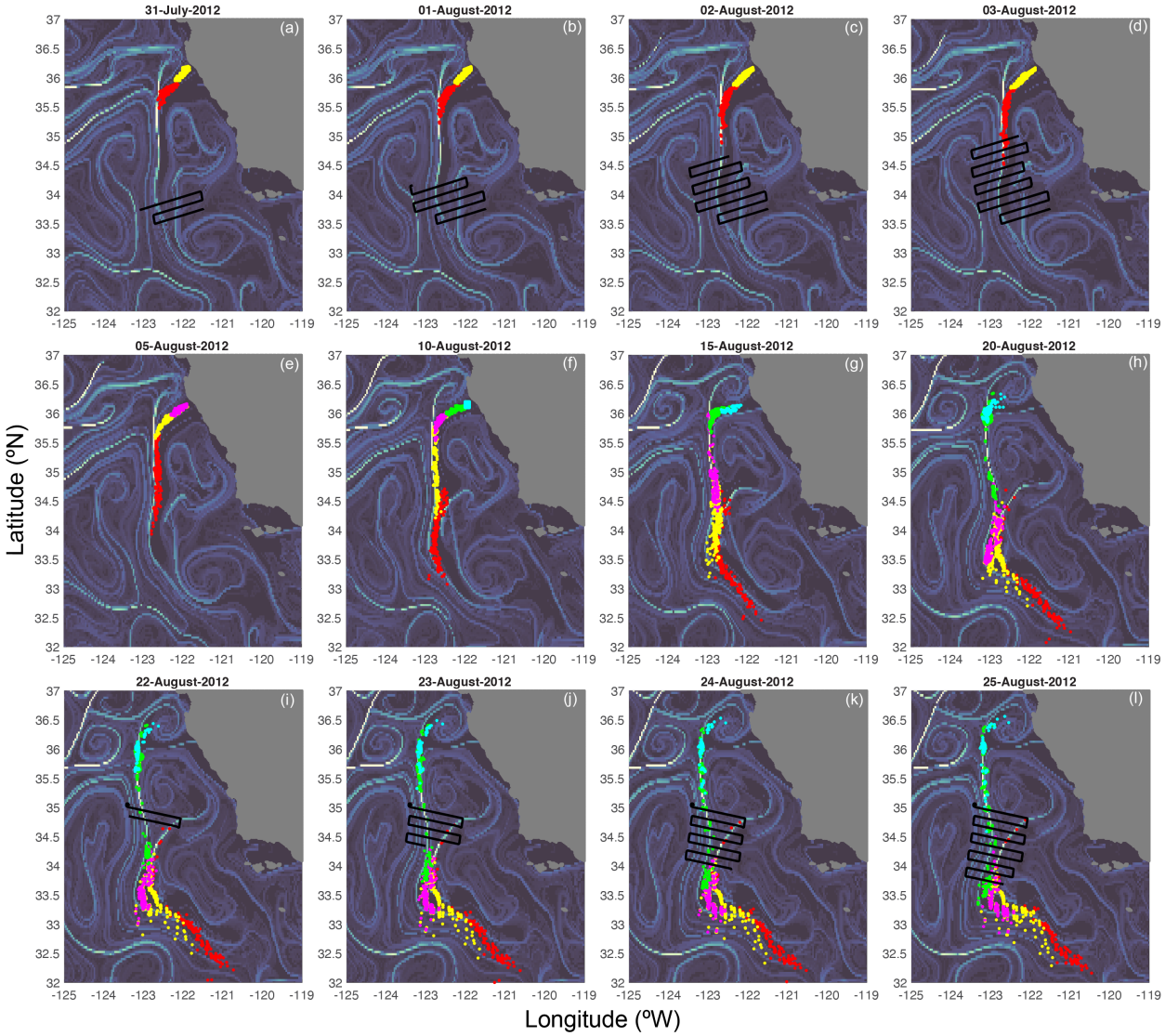

Figure 1.9: Daily FSLE fields (background) and forward-tracking water parcel locations from 36˚N for the duration of Survey 1 (a–d), every 5 days in between the two surveys (e–h), and Survey 2 (i–l). Colors of parcel locations correspond to the upwelling pulses in Figure 1.8.

1.5.5.3 Patch Source Dynamics: Depth

Temporal variations in upwelling intensity will influence the biogeochemical properties of the upwelled waters. Modeling experiments have shown that the intensity of wind stress at the coast determines the magnitude of vertical transport, and thus the source depth from which upwelled waters originate (Jacox & Edwards, 2012). Increased stratification is associated with shallower upwelling source depths (Bograd & Lynn, 2003; He & Mahadevan, 2021), with

reduced nutrient supply to the euphotic zone and subsequently smaller increases in phytoplankton biomass (McGowan et al., 2003). We qualitatively linked these upwelling intensity-depth-nutrient relationships to the chlorophyll-salinity-oxygen relationships we examined at the front. In this region, California Undercurrent waters have been found to upwell into the euphotic zone and to generate elevated phytoplankton concentrations (Zaba et al., 2021). Here, we hypothesize that as the source depth of upwelling increases, the upwelled waters are higher in nutrients, but lower in oxygen—even within California Undercurrent waters. The nutrient concentrations set the subsequent phytoplankton concentrations of the upwelled waters.

Most high-chlorophyll waters at the front were associated with California Undercurrent waters within a narrow salinity band of 33.5–33.7 psu (Figure 1.5). These HC-HS waters likely originated from a source depth below the euphotic zone, where nutrient concentrations were higher than in the euphotic zone. Once upwelled into the euphotic zone, these nutrient-rich waters would fuel subsequent phytoplankton growth. Some waters found at the front were within this 33.5–33.7 psu salinity range yet had low chlorophyll concentrations (Figures 1.5c and 1.5d). We hypothesize that these LC-HS waters either (i) were not recently upwelled, (ii) did not have high enough nutrients and/or irradiance to support enhanced phytoplankton growth after upwelling, or (iii) experienced grazing losses that offset phytoplankton growth.

We used our water-parcel trajectories to trace the spatial origins of both the HC-HS patch and the LC-HS patches (Figures 1.3 and Supplemental Figure 1.8) in Survey 1. The LC-HS patch seems to have originated before the HC-HS patch (before 21–22 July), and slightly south of 36ºN where the HC-HS originated. CUTI values at both 35ºN (not shown) and 36ºN (Figure 1.8) were relatively weak (< 0.75 m^2 s^{-1}) during the week prior to 20 July when the LC-HS patch likely formed. These upwelling intensities are weaker than the pulses that we believe generated the

HC-HS patches in Survey 1 and Survey 2 (CUTI > 0.75 m^2 s^{-1} during 21–22 July and 6–7 August). Therefore, the LC-HS signature could have resulted from a weaker upwelling pulse, which could have been associated with a shallower source depth and thus lower initial nutrient concentrations.

We also tested the influence of upwelling source depth on the chemical properties of frontal waters by using dissolved oxygen as a water mass tracer. In the California Undercurrent (Supplemental Figure 1.4), around the base of the euphotic zone, deeper waters have lower oxygen concentrations than shallower waters (Supplemental Figure 1.2), as oxygen respired during the remineralization of organic matter outweighs any potential photosynthetic production. On the 27.5 m depth surface, the mean [O_2] was 5.84 mL L^{-1} for the HC-HS patch and 5.86 mL L^{-1} for the LC-HS patch (Figure 1.3c). This 0.02 mL L^{-1} difference is small but consistent with the hypothesis that the higher-oxygen LC-HS waters were upwelled during a weaker upwelling pulse and hence originated from a shallower source depth.

These analyses are consistent with the temporal variability in intensity of wind-driven upwelling at the coast accessing different source depths with different hydrographic and biogeochemical properties. Waters originating at the coast in upwelling pulses can be transported offshore by narrow but geographically and temporally persistent filaments. Fluctuations in wind stress will change the source depths of upwelled waters: deeper source waters will be higher in nutrient concentrations, with the capability of stimulating intense phytoplankton blooms when brought into the euphotic zone (Figure 1.10). Therefore, it is likely that the phytoplankton patches at this front resulted from specific combinations of wind, upwelling, nutrients, irradiance, and advection conditions.

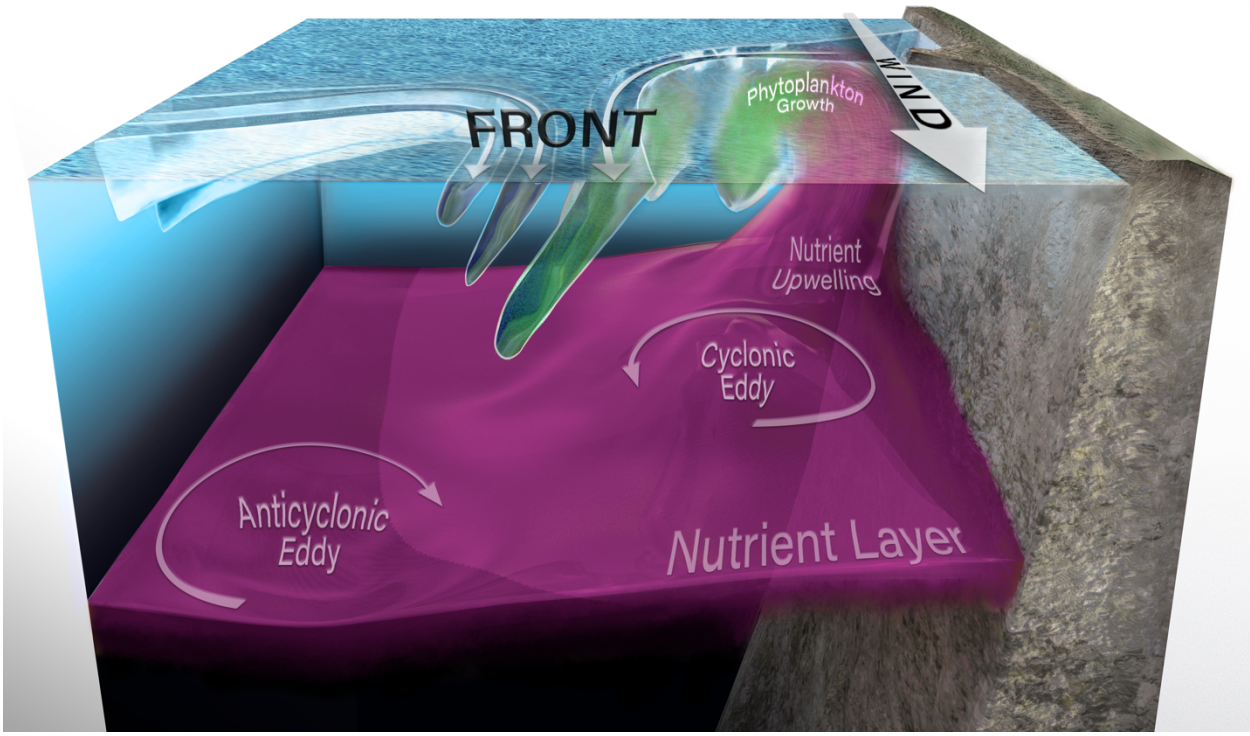

Figure 1.10: A 3-D illustration of the origins and advection of phytoplankton patches at a density front in the California Current System. The front, which formed between a cyclonic and anticyclonic eddy, contained streams of water with both offshore and inshore origins. These streams formed tilted layers of hydrographic and biological properties within the front. Two streams originated offshore, while the most productive stream originated at the coast. There, strong alongshore winds drove local upwelling of nutrients from the aphotic zone to the euphotic zone. Phytoplankton grew in these upwelled waters, forming distinct patches that advected into and along the front. The small spatial-scale and short time-scale fluctuations of phytoplankton in this front were thus largely controlled by upstream processes. Illustration: Freya Hammar.

All of our analyses are consistent with the PPH: water-parcel trajectories, the timing of upwelling events, the intensities of upwelling, and the vertical gradients in source-water properties all support the hypothesis that the HC-HS patches measured in the SeaSoar surveys originated during strong upwelling pulses at the coast (Figure 1.10). Phytoplankton biomass increased in the upwelled waters during the roughly two-week transit from the coast to the front and then did not change much during the 3- to 4-day transit along the front. Weaker upwelling

pulses did not penetrate the high-nutrient, sub-euphotic waters at the coast; therefore, they did not generate phytoplankton patches, though they did create patches of higher salinity and higher oxygen that were later found in the front. All of these patches subsequently advected along the front, with relatively short residence times in the front.

1.6 Conclusion

This study has reinterpreted the physical-biological dynamics at a density front in the California Current System by applying a new framework to understand the origins of the observed biological and hydrographic patchiness. By employing an advection-reaction equation, we explicitly stated the assumptions regarding the physical and biological gradients at the front, generating two alternate hypotheses: the stationary patch hypothesis (SPH) and the pulsatile patch hypothesis (PPH).

Our data suggest that the PPH is more strongly supported: biogeochemical patchiness in the front was regulated by upstream upwelling processes and the advection of biological properties along the front, rather than solely processes in the front. Chlorophyll, dissolved oxygen, and particle biovolume were likely not at steady state in the front due to strong-along front advection. The sources and sinks of these properties were small relative to their fluctuations at the upstream boundary of the front. While vertical fluxes and mesozooplankton grazing, for example, likely contributed somewhat to sources and sinks of phytoplankton biomass in the front, these processes did not fully explain the observed patchiness. Therefore, the most realistic advection-reaction equations to describe the front would have both non-zero $\partial C/\partial t$ (local time rate of change) and rC (biological source/sink) terms. This study did not seek to define the magnitudes of each term; instead, we set up a framework to evaluate the relative importance of each in conjunction with spatiotemporal along-front gradients. Equilibrium and steady-state assumptions, while suitable for some interpretations, do not capture the biological and

hydrographic properties of this front that varied on relatively small spatial and temporal scales: tens of kilometers and days to weeks.

Fronts are dynamic and patchy environments; therefore, sampling and modeling them remains complex. A single transect across a front cannot be considered representative of the entire frontal system. While Lagrangian or pseudo-Lagrangian sampling at fronts have provided promising measurements of gradients with the flow, there are still potential shortcomings of these sampling methods due to the across- and along-frontal patchiness that potentially varies over 5–10 km and over 3–4 days, as seen at E-Front. While steady-state and equilibrium assumptions simplify analyses of the physical and biological dynamics at upwelling-associated fronts, they may also overlook or oversimplify the time- and space-dependent dynamics of frontal source waters. Therefore, in this highly dynamic upwelling system, while eddies and fronts may appear physically stationary over days or weeks, the waters and the biological gradients associated with them may vary rapidly, potentially in a pulsatile way.

To further support the results presented in this study, measurements of plankton community composition over the month-long period of sampling at E-Front would be useful in characterizing the biological patchiness and differentiating the pulsatile upwelled waters at the front. Despite its along-front variability, the E-Front was still a site of elevated plankton biomass and export over the time it was sampled. But the along-front spatial and temporal variability is strikingly important, and this study provides an effective framework for investigating more fine-scale spatial and temporal variations in these ecologically important patterns given different, and often opposing, assumptions.

Open Research

All cruise and SeaSoar data sets are available on the CCE LTER Datazoo website (https://oceaninformatics.ucsd.edu/datazoo). Satellite altimetry and FSLE data are available on

the AVISO+ website (https://www.aviso.altimetry.fr/en/home.html). Data for geostrophic and wind-driven currents are available from CMEMS (https://marine.copernicus.eu/; product identifiers: "SEALEVEL_GLO_PHY_L4_MY_008_047" and "MULTIOBS_GLO_PHY_REP_015_004"). HF radar data are available using the NOAA ERDDAP griddap tool ("Currents, HF Radar, US West Coast, RTV, Near-Real Time, 2012-present, Hourly, 6km, Lon0360"). Upwelling indices are also available online (https://mjacox.com/upwelling-indices/).

Acknowledgments

The authors thank the team aboard the R/V Melville on P1208, Carl Mattson for SeaSoar operations, David Jensen and Mark Ohman for guidance on SeaSoar/LOPC data sets, Alain de Verneil for guidance on FSLEs, Pierre Chabert for guidance on velocities, Freya Hammar for the schematic illustration, and the Franks Lab and three anonymous reviewers for feedback that improved the manuscript. SG was supported by the NSF GRFP. This work was supported by NSF/OCE-2220258 and CCE LTER (NSF/OCE-10-26607 and NSF/OCE-16-37632).

Chapter 1, in full, is a reprint of the material as it appears in *Journal of Geophysical Research: Oceans*. Gangrade, Shailja; Franks, Peter J. S., 2024. The dissertation author was the primary investigator and author of this paper.

Supplemental Information

Here, we provide depth-dependent sections, from selected transects from the two SeaSoar surveys across E-Front, of biological, chemical, and hydrographic properties (Supplemental Figures 1.1 and 1.2). These sections show the fine-scale, layered structure of tongues of high salinity and chlorophyll at the front (de Verneil et al., 2019) as well as the interweaving of low oxygen, high- particle load waters. To calculate along-front gradients in biological and chemical properties, the along-front axis was determined from contours of the horizontal density gradient, objectively mapped onto the 27.5 m depth surface (Supplemental Figure 1.3). The relationship between temperature, salinity, and California Current and California Undercurrent water masses were also explored (Supplemental Figure 1.4) at E-Front, revealing how many of the high-salinity, high-chlorophyll waters on the eastern (inshore) side of the front are associated with the California Undercurrent. The chlorophyll, dissolved oxygen, and particle biovolume concentrations of waters along the front had nonlinear associations with salinity, a water mass tracer (Supplemental Figure 1.5). The depth-dependent, cross-frontal transects of chlorophyll from each SeaSoar survey (Supplemental Figures 1.6 and 1.7) revealed patches of chlorophyll at the northern boundary and decreases in chlorophyll from north to south (in the direction of the frontal jet) without a strong signal of subduction along the frontal jet. The origins of high-salinity patches (one with higher chlorophyll, one with lower chlorophyll) at the E-Front were also investigated using water-parcel trajectories (Supplemental Figure 1.8). Backward- tracking revealed that these patches had different temporal origins, and slightly different geographic origins. The temporal origins may be associated with different upwelling pulses, with the stronger episode aligning with the high-chlorophyll, high-salinity patch.

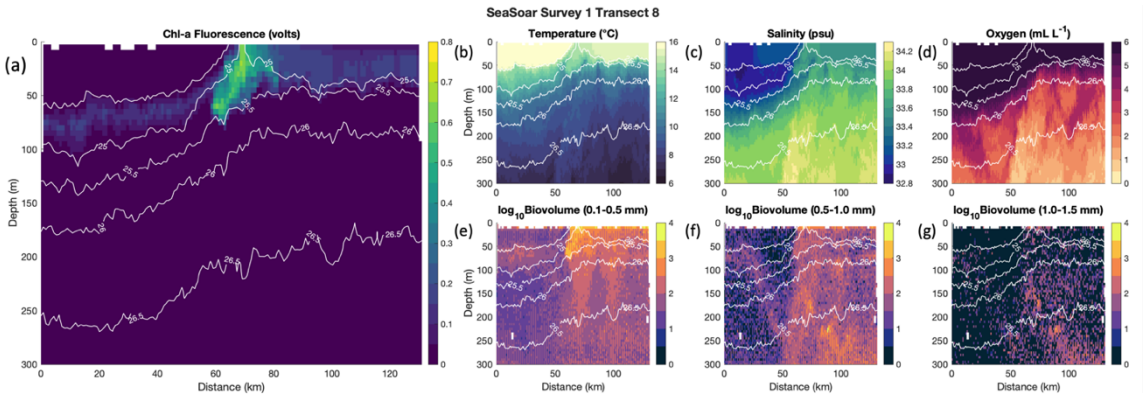

Supplemental Figure 1.1: Survey 1 depth transects (from Transect 8) of with isopycnals (white lines) for (a) Chl-*a* fluorescence, (b) temperature, (c) salinity, (d) dissolved oxygen, (e) particle biovolume for ESD 0.1–0.5 mm, (f) particle biovolume for ESD 0.5–1.0 mm, and (g) particle biovolume for ESD 1.0–1.5 mm.

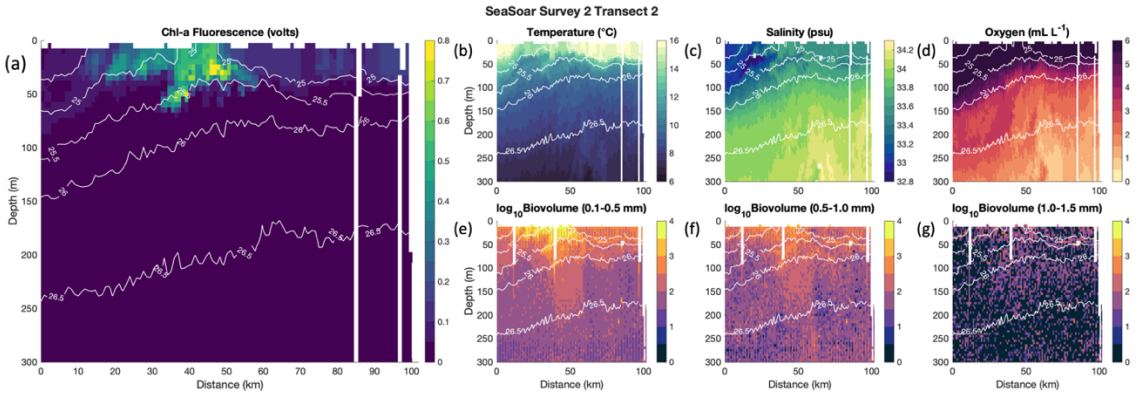

Supplemental Figure 1.2: Survey 2 depth transects (from Transect 2) of with isopycnals (white lines) for (a) Chl-*a* fluorescence, (b) temperature, (c) salinity, (d) dissolved oxygen, (e) particle biovolume (in $\log_{10}$ mm^3 m^{-3}) for ESD 0.1–0.5 mm, (f) particle biovolume for ESD 0.5–1.0 mm, and (g) particle biovolume for ESD 1.0–1.5 mm.

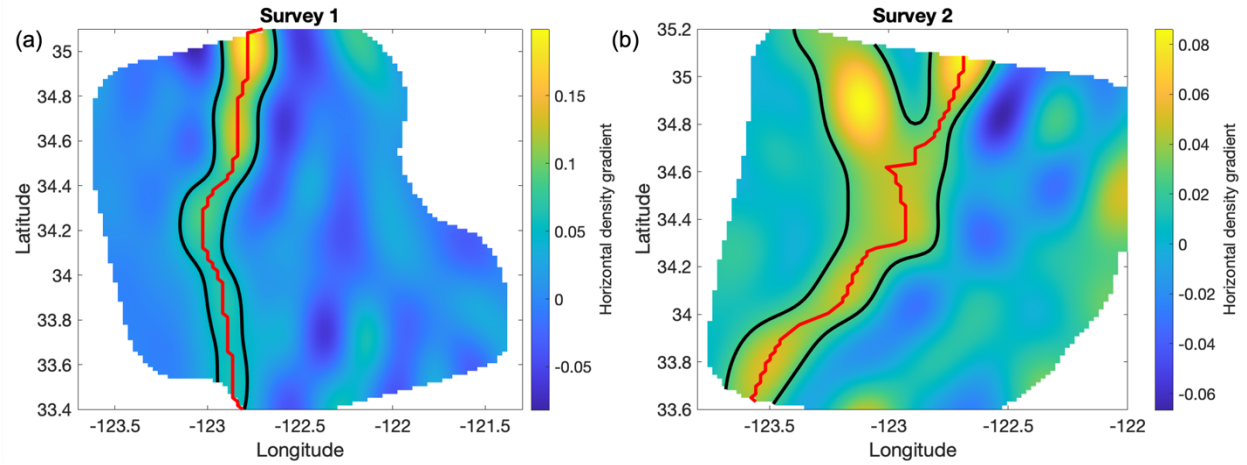

Supplemental Figure 1.3: Horizontal density gradient (in kg m^{-4}) for (a) Survey 1 and (b) Survey 2 with maximum density gradient (red line) and contours of 0.04 kg m^{-4} and 0.02 kg m^{-4} (black lines), for Survey 1 and 2 respectively.

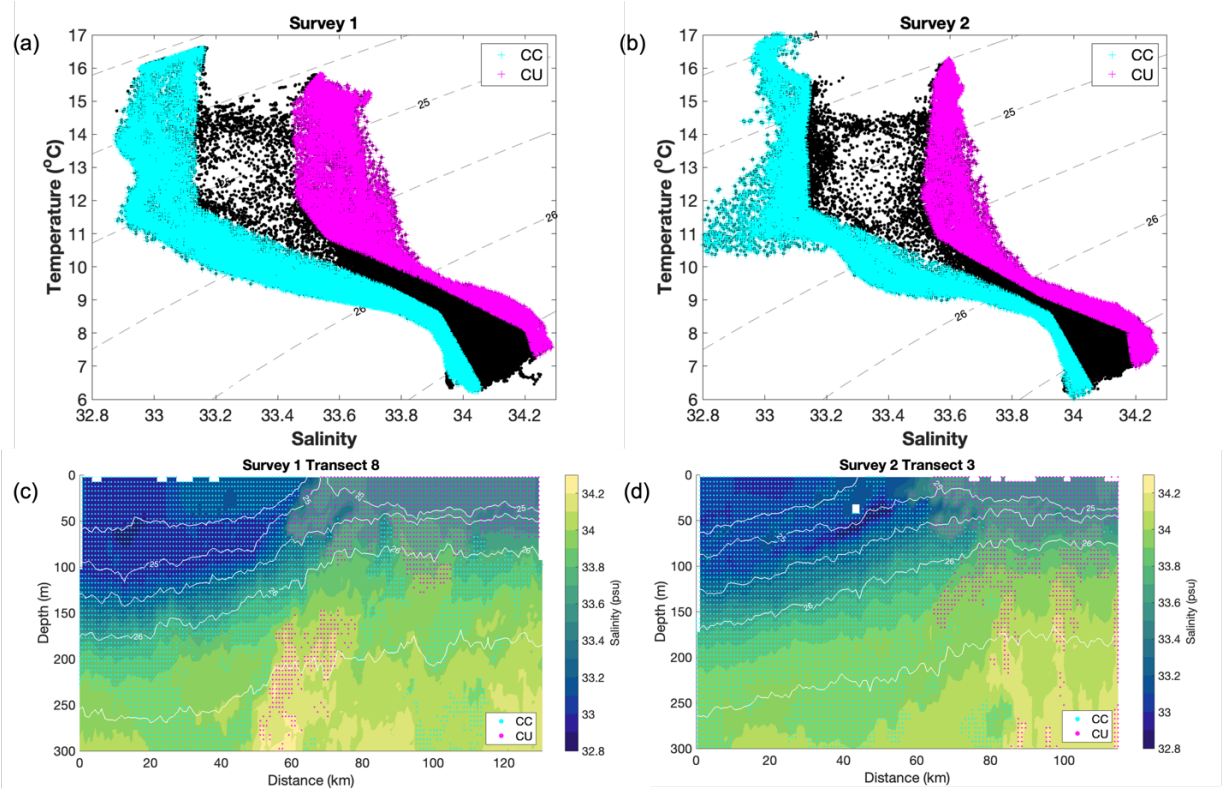

Supplemental Figure 1.4: Temperature-salinity diagrams of all waters sampled during (a) Survey 1 and (b) Survey 2, with California Current (CC, cyan markers) and California Undercurrent (CU, magenta markers) water masses highlighted. Transect of salinity with depth from (c) Survey 1 and (d) Survey 2 with isopycnals (white lines). Waters classified as CC (cyan markers) primarily make on the western side of the front, while waters classified as CU (magenta markers) make up the eastern side of the front.

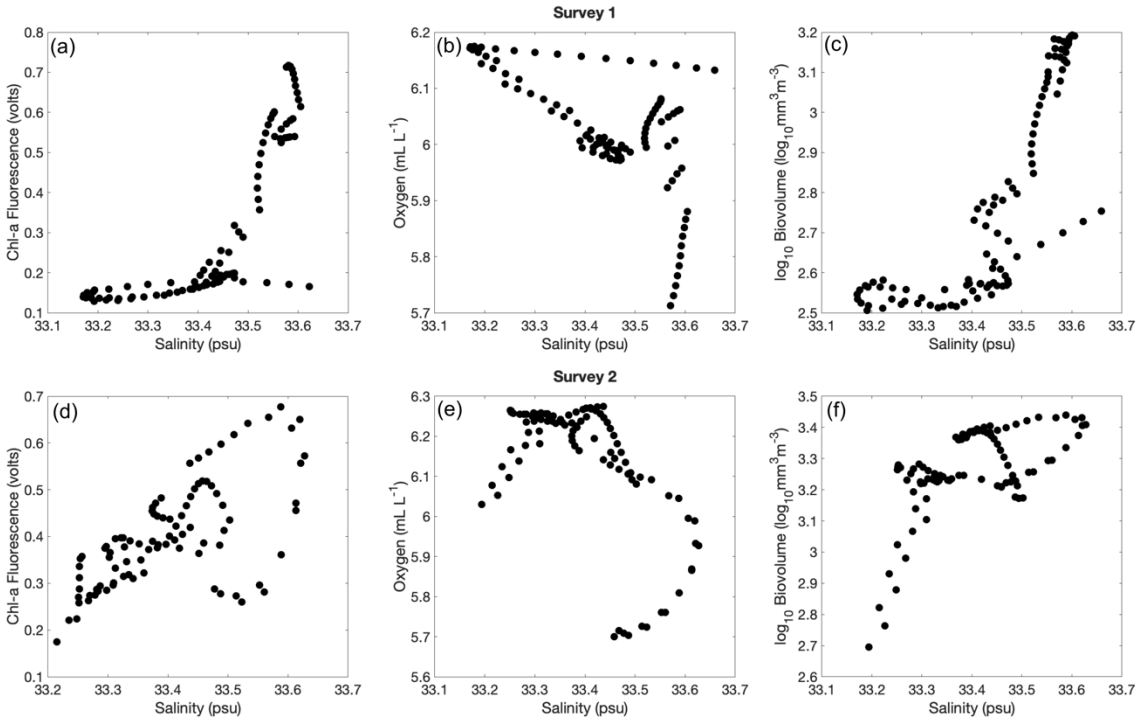

Supplemental Figure 1.5: Nonlinear relationships between along-front salinity and along-front chlorophyll, oxygen, and particle biovolume for (a-c) Survey 1 and (d-f) Survey 2.

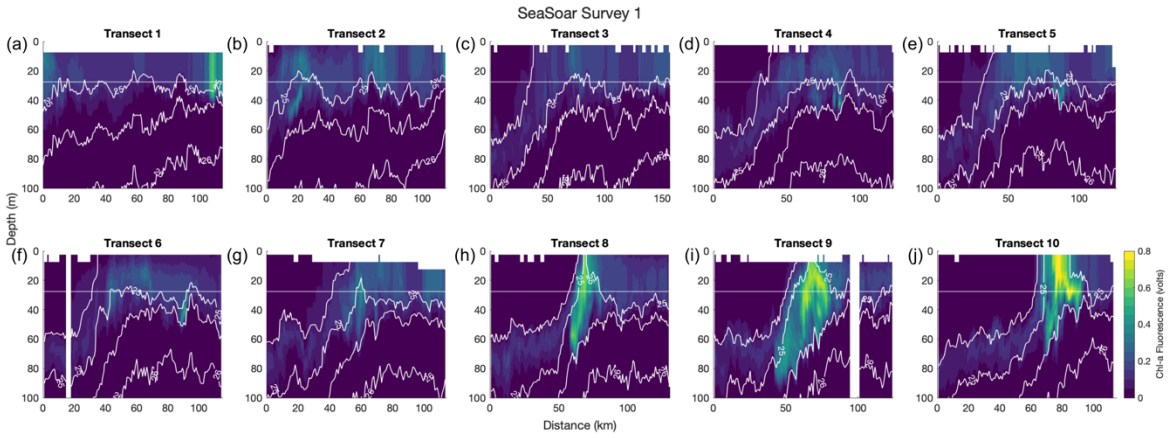

Supplemental Figure 1.6: Depth-dependent transects of chlorophyll from Survey 1 (south-to-north direction). Horizontal white line is the 27.5 m depth used in objective maps. White contours are isopycnals.

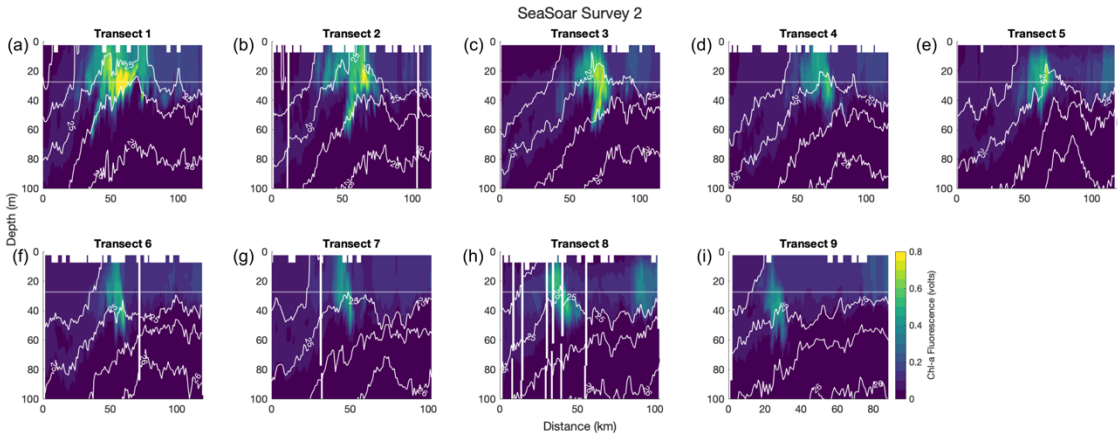

Supplemental Figure 1.7: Depth-dependent transects of chlorophyll from Survey 2 (north-to-south direction). Horizontal white line is the 27.5 m depth used in objective maps. White contours are isopycnals.

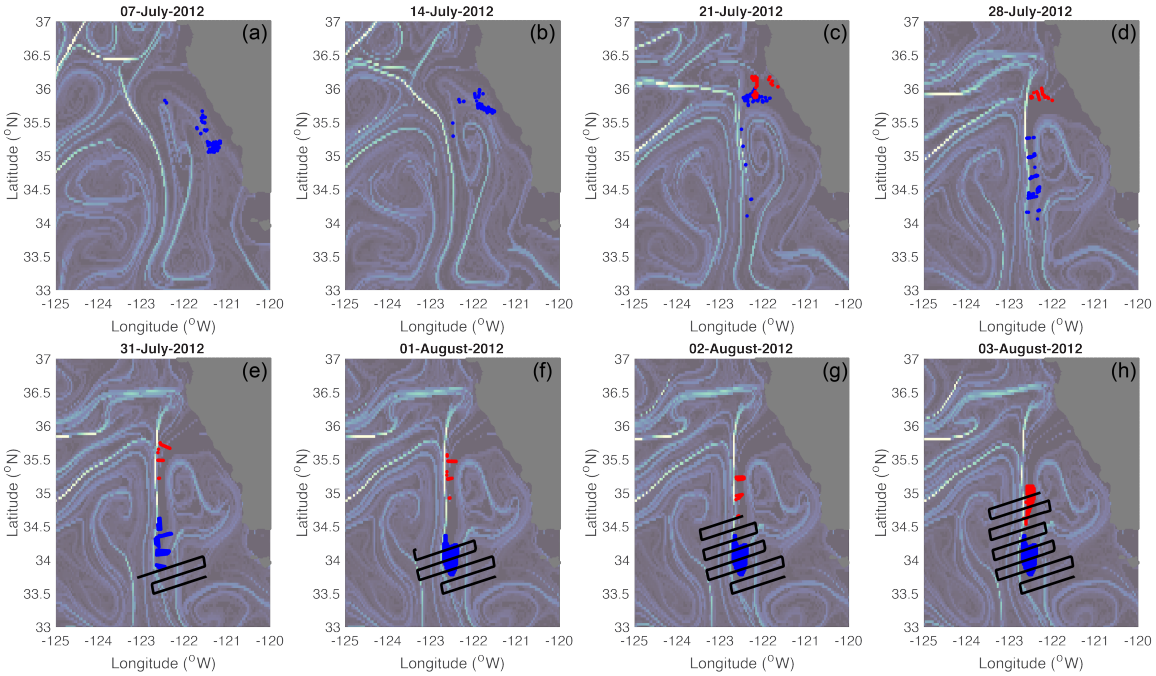

Supplemental Figure 1.8: Snapshots, shown forward in time, from eight different days (a–f) of a backward-tracking of two high-salinity patches (only parcels with inshore origins), from the 27.5 m depth, sampled in Survey 1. Red circles were seeded at locations of Survey 1 HC-HS water parcels and run backward, and their locations are shown here from 21 July to 3 August. Blue circles were seeded at locations of Survey 1 LC-HS water parcels, and their locations are shown here from 7 July to 3 August. Survey 1 tracks (black lines) appear from 30 July to 3 August.

Chapter 2: Patchiness of plankton communities at fronts explained by Lagrangian history of upwelled water parcels

2.1 Abstract

The transport of plankton by highly dynamic (sub)mesoscale currents—often associated with fronts and eddies—shapes the structure of plankton communities on the same time scales as biotic processes, such as growth and predation (days–weeks). The resulting bio-physical couplings generate heterogeneities in their finescale distributions (1–10 km), or "patchiness." Here, we test the hypothesis that cross-frontal plankton patchiness at a front found 200–250 km offshore in the California Current System was influenced by wind-driven upwelling conditions upstream of the front. We show that in situ Eulerian measurements (cross-frontal transects) can be interpreted in a Lagrangian framework by using satellite-derived current velocities to trace water parcels backward in time to their coastal origins. We find that the majority of the water parcels sampled at this front originated along the central California coast during different episodic wind-driven upwelling pulses and followed various trajectories before converging temporarily at the front. In response to nutrient injections at the coast, plankton communities transformed during their journeys from the coast to the sampling zone, with a succession of phytoplankton and zooplankton blooms. The cross-frontal sampling captured the convergence of these distinct water parcels at different points in their biological histories, which resulted in the observed spatial patchiness. Our results suggest that identifying the processes controlling frontal plankton communities requires understanding them in the context of their spatial and temporal histories. In particular, Lagrangian approaches should be more widely applied to understand critical ecological patterns in highly dynamic systems.

2.2 Introduction

Marine plankton are passively drifting organisms of immense ecological and biogeochemical importance in the functioning of ocean ecosystems. Plankton spatial distributions are profoundly impacted by ocean currents, particularly in regions of highly energetic mesoscale stirring. In stirring features, such as fronts and eddies, horizontal current velocities can reach up to 50–80 km/day (Barth et al., 2000; McWilliams, 2016; Zaba et al., 2021), resulting in transport over long distances within a few days to weeks. Importantly, biological processes, such as growth, competition, or predation, occur on similar time scales. Phytoplankton blooms, for instance, can develop within a few days given adequate light and nutrient availability, such as during spring blooms (Lewandowska et al., 2015) or in upwelling filaments (Zaba et al., 2021). Most mesozooplankton can complete a reproduction cycle in a few weeks (Deibel & Lowen, 2012; Eiane & Ohman, 2004).

As a result, physical and biological processes are highly coupled, often resulting in a high level of heterogeneity in biological properties on small spatial scales (1–10 km), or "patchiness." Disentangling the interacting roles of physics and biology in driving plankton patchiness has been a central question in ecology for many decades (Levin & Segel, 1976; Martin, 2003; McGillicuddy & Franks, 2019). The processes driving plankton diversity and community structure have similarly been examined, with many studies showing the influence of bottom-up and top-down trophic interactions (Allen et al., 2005; Dugenne et al., 2021), transport (Wilkins et al., 2013), or a combination of all of these processes (Clayton et al., 2013; Schmid et al., 2023). Lagrangian studies have also explored how water parcels are connected between remote regions (i.e., their "connectivity") across differing spatial scales—from a single basin to the global ocean—and how this connectivity influences various biological processes, such as genetic similarity or larval dispersal (Jönsson & Watson, 2016; Rossi et al., 2014; Wilkins et al., 2013).

Recently, many studies have employed Lagrangian approaches to describe how plankton communities transform as they are transported, sometimes hundreds of kilometers in a matter of days (Lehahn et al., 2018; Messié et al., 2022; Messié & Chavez, 2017). These approaches have shown that the abundance of plankton is not only determined by their immediate environment (e.g., temperature and nutrient concentration (Haberlin et al., 2019; Mousing et al., 2016; Tzortzis et al., 2021)) but is also shaped by the conditions experienced during the previous weeks at different locations (d'Ovidio et al., 2010; Gangrade & Franks, 2023; Hernández-Carrasco et al., 2023). The first view—local environmental conditions determine species abundance—can be likened to the classic Eulerian concept of an "ecological niche." This concept was originally developed for terrestrial ecosystems and successfully applied to the ocean on large scales (e.g., biogeochemical provinces as in Longhurst (2007)). The second view—transport history shapes species distributions—is a Lagrangian concept, relevant to small scales and specific to passively drifting marine plankton. This concept has been described as "fluid dynamical niches" (d'Ovidio et al., 2010): finescale plankton patchiness is a moving mosaic of water parcels carrying different plankton communities.

Here, we investigate the processes generating finescale cross-frontal patchiness in plankton community structure in an upwelling system, the California Current System (CCS). In an Eastern Boundary Upwelling System (EBUS) such as the CCS, wind-driven vertical nutrient injections at the coast modulate biological variability at time scales ranging from days to decades (Jacox et al., 2018; Messié et al., 2023), while horizontal currents structure the ecosystem spatially by advecting recently upwelled waters in filaments from the coast to offshore (Chelton et al., 2011; Rossi et al., 2013; Zaba et al., 2021). The California Current System is thus structured by a cross-shore gradient: new production (primary production resulting from nutrient

inputs from outside the euphotic zone, such as coastal upwelling) generally takes place inshore while export takes place further offshore (Chabert et al., 2021; Stukel et al., 2011). In addition to the small-scale circulation (filaments and eddies), the California Current System is composed of two main flow features: the California Current (CC), an equatorward-flowing current of subarctic origin, and the California Undercurrent (CU), a subsurface poleward-flowing current of equatorial origin (Bograd et al., 2019; Lynn and Simpson, 1987).

We use the case study of a front in the southern California Current System, characterized by an intense frontal jet and horizontally converging flow (de Verneil et al., 2019), to explore how coastal upwelling pulses propagate offshore (Gangrade and Franks, 2023) and generate plankton patchiness (Mangolte et al., 2023) on time scales of a few weeks. We evaluate the relationship between plank- ton distributions and the characteristics of water parcels based on two different frameworks. First, we describe the water parcels by their in situ hydrographic properties (the *regional water-mass types* derived from temperature and salinity: CC or CU). Second, we describe the water parcels based on their Lagrangian trajectories since upwelling (the *water-mass history*, derived from a backtracking analysis). Our results show that both frameworks give insights into the drivers of plankton com- munity structure; however, the Lagrangian method provides a more detailed understanding of the mechanisms generating local finescale patchiness.

2.3 Data and methods

2.3.1 Cruise data

Biological and hydrographic measurements were collected during the California Current Ecosystem Long-Term Ecological Research (CCE LTER) Process Cruise P1208 in August 2012. This cruise sampled an eddy-associated front, dubbed "E-Front," located approximately 200–250 km offshore of Point Conception, California. This front was positioned between an anticyclonic

eddy to the west (offshore) and a cyclonic eddy to the east (inshore) (de Verneil and Franks, 2015; Stukel et al., 2017). The cross-frontal sampling included 2 transects (E1 and E2) with high horizontal resolution (3–5 km between consecutive stations), conducted on 4–5 August 2012 and 20–21 August 2012 respectively (Figure 2.1).

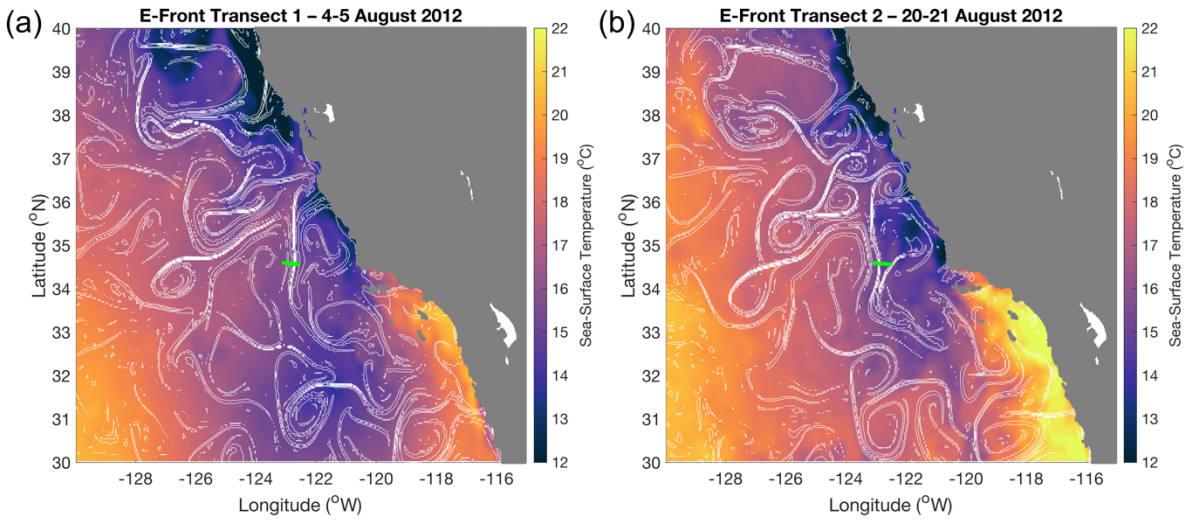

Figure 2.1: Maps of sea-surface temperature (SST in $°C$, color scale) and Finite Size Lyapunov Exponents (FSLEs in d^{-1}, white contours) averaged over the duration of E-Front Transect E1 (a), and Transect E2 (b). We used FSLEs to visualize the transport patterns creating convergent flow structures such as fronts. FSLE contours represent values from to 0 d^{-1} to -0.3 d^{-1}, in increments of 0.1 d^{-1}. Green markers indicate the locations of the sampling stations in each transect. Filaments of recently upwelled cold water were advected offshore via mesoscale stirring features (outlined by the FSLE contours) at various locations along the coast (e.g., at 38°N in Transect E2).

At each transect station, a CTD (conductivity, temperature, depth) vertical profile was recorded down to 350 m and binned to 1-m vertical resolution, and water samples were collected in Niskin bottles at discrete depths (5–6 levels between 0 and 100 m) on the ascent. The CTD rosette included a fluorometer which measured in vivo chlorophyll-a fluorescence. After the CTD cast, zooplankton samples were collected with a 0.71-m diameter, 202-µm mesh vertical Bongo net tow from 0 to 100 m. The plankton samples were later analyzed using three different methods; the full dataset was described in detail in Mangolte et al. (2023) (see their Figure 2) and is summarized here (Supplemental Table 2.1). Flow cytometry was performed on the Niskin

bottle water samples (0–100 m), producing the abundance (number of cells/L) of 4 taxa of pico-plankton (< 2 μm) identified by their light-scattering properties. High-performance liquid chromatography (HPLC) was performed on the surface Niskin bottle samples; the concentrations of chlorophyll *a* and accessory pigments were measured and used to determine the contributions (percentage) of 8 phytoplankton taxa relative to the total chlorophyll (Goericke & Montoya, 1998). Zooplankton samples, collected from vertical Bongo nets, were preserved in 1.8% buffered formaldehyde, and organisms were then identified in the lab using the ZooScan semi-automated imaging system (Ohman et al., 2012) with 100% manual validation, producing the vertically integrated abundance (number of organisms m^{-2}) of 15 groups of mesozooplankton.

2.3.2 Water-mass classification

We classified the waters sampled by the CTD as California Current (CC) or California Undercurrent (CU) based on their salinity and temperature values. We used criteria that were defined by Zaba et al. (2021) using climatological measurements from the California Underwater Glider Network. They first identified the currents by their velocities (poleward for the CU vs. equatorward for the CC) and then determined the corresponding boundaries in temperature-salinity space. Thus, waters saltier and warmer than the CU threshold were classified as CU, while waters fresher and colder than the CC threshold were classified as CC. Waters with intermediate salinity and temperature values were assumed to be composed of a mixture of CC and CU water and were classified as MIX (Supplemental Figure 2.1).

2.3.3 Statistical analysis of water-mass type and abundance association

We combined the information on hydrographic classifications (CC, CU, or MIX) and plankton abundances to determine whether plankton were preferentially associated with a certain water mass. For phytoplankton and bacteria, we used abundances and water-mass type classification at each Niskin bottle depth. Because the Bongo nets generate vertically integrated

zooplankton abundances, we found it most informative to relate the zooplankton distributions to the dominant water-mass type in the sampled water column (0–100 m). We defined this dominant water type as CC or CU if more than 50% of the vertical bins were classified as such, and MIX in other cases. The abundances of bacteria, phytoplankton, and zooplankton in each water-mass type were first examined qualitatively (Supplemental Figures 2.2–2.5) and Kruskal-Wallis tests were then used to determine whether abundances among the three water-mass types were statistically different.

2.3.4 Water-parcel tracking

We advected the water parcels backward in time from initial locations (i.e., each transect station), using the following equations:

$$x(t + \Delta t) = x(t) + u(x, y, t) \times \Delta t \quad (2.1)$$

$$y(t + \Delta t) = y(t) + v(x, y, t) \times \Delta t \quad (2.2)$$

Instead of a positive Δt, we applied a $\Delta t = -1$ day and iteratively computed x and y for the 2 months (66 days) preceding the transect date. We limited the backtracking to 2 months because the contribution of stirring and mixing to water-mass property changes is likely to be smaller than the contribution of advection for this duration. We used a 2-D advection scheme with surface velocities because upwelled waters parcels are likely to stay near the surface for this duration. We used the "GLOBCURRENT" velocity product from the Copernicus Marine Environment Monitoring Service (CMEMS; https://doi.org/10.48670/mds-00327), which consists of surface zonal and meridional velocities ($u(x, y, t)$, $v(x, y, t)$) with a 1-day temporal resolution and a 0.25-degree horizontal resolution. When water-parcel locations (x, y) fell between grid points, we linearly interpolated the GLOBCURRENT gridded velocity product to obtain ($u(x, y, t)$, $v(x, y, t)$) at each location along the trajectory. The velocities include a

geostrophic component (derived from satellite altimeter measurements) and a wind-driven Ekman component at 0 m and 15 m depth, derived from the wind stress from the ERA reanalysis (Rio et al., 2014). We selected the 15-m Ekman component because it is more representative of the movement of the euphotic layer, which was measured to be 60–70 m during this same cruise (Stukel et al., 2017), than the 0-m component. Additionally, we used backward-in-time finite-size Lyapunov exponents (FSLEs) to visualize transport patterns creating convergent flow structures such as fronts. The FSLEs represent the exponential rate of separation (when calculated forward-in-time) or convergence (when calculated backward-in-time) of water-parcel trajectories. The FSLEs, obtained from Aviso+ (https://doi.org/10.24400/527896/a01-2022. 002), were calculated with a final separation distance of 0.6 degrees and advected by altimetry-derived velocities (d'Ovidio et al., 2004).

2.3.5 Random parcel seeding

To estimate the uncertainty associated with these trajectories (primarily caused by the coarse 0.25-degree spatial resolution of the velocities, representing approximately two velocity data points in each 50 km transect), we performed the backtracking for 100 parcels seeded randomly within a 0.0625° (approximately 5 km) radius around each transect station. The distance between stations ranged between 1 and 10 km, with an average of about 5 km. We then described the presumed upwelling conditions experienced by the waters sampled at each station based on this ensemble of possible trajectories.

2.3.6 Upwelling pulses

Wind-driven upwelling pulses were determined from the Coastal Upwelling Transport Index (CUTI; Jacox et al. 2018), which is defined in 1° latitudinal bands. We defined anomalies relative to the temporal average of the CUTI during the study period (June to August 2012). Upwelling pulses were defined as short periods (typically a few days) of positive CUTI

anomalies. Large positive anomaly values indicate strong upwelling pulses that are expected to upwell high-nutrient waters from below the euphotic zone and generate a strong biological response.

2.3.7 Upwelling conditions upstream of the front

We used the backward-in-time trajectories and Coastal Upwelling Transport Index (CUTI) values along the California coast to determine how many days before being sampled at the front a water parcel had experienced an upwelling pulse, and the intensity of that pulse. First, we determined whether each sampled water parcel was in the coastal region influenced by wind-driven upwelling (i.e., within 25 km of the coastline [Huyer, 1983]) in the two months before sampling. Next, for parcels with coastal origins, we determined whether the parcel experienced an upwelling pulse. If it did, we recorded the location (latitude, longitude, and date) of the water parcel when it was last at the coast during an upwelling pulse; these coordinates thus represented the parcel's temporal and spatial origin. Finally, we characterized a parcel's upwelling pulse using two criteria: (1) the intensity of the upwelling pulse (Coastal Upwelling Transport Index anomaly) at the parcel's origin, and (2) the water parcel age since the upwelling pulse (i.e., the time elapsed between the origin date and the frontal sampling date, in days). We followed this procedure for all 100 points seeded around each transect station.

2.4 Results

2.4.1 Distribution of water masses and chlorophyll a across the front

In the upper 100 m, the eastern (inshore) side of the front was composed of primarily CU waters while the western (offshore) side was composed of primarily CC waters (Figure 2.2). The interface between the water masses, where water-mass mixing occurred, was composed of a 2–15 km wide layer of MIX waters. While this MIX layer persisted for at least the duration of the cruise (approximately 1 month), its geometry changed between the two transects, which were

sampled two weeks apart. During the first transect (E1, Figure 2.2a), the MIX water layer between the CC and CU water masses was tilted across the front, with CU waters extending offshore below the CC waters (and vice versa: CC waters extending inshore above CU waters). During the second transect (E2, Figure 2.2b), the MIX layer was mostly vertical, with the exception of an intrusion of offshore CC waters into inshore CU waters below the surface (30–70 m).

The distribution of Chl-a fluorescence (Figure 2.2, hatched contours) across the front was closely related to the distribution of the water masses. Generally, CC waters contained less Chl-a than CU waters. Most strikingly, small patches of high Chl-a were associated with MIX waters at the interface between CC and CU waters. This visual pattern was then confirmed by the results of a Kruskal-Wallis statistical test summarized in Table 2.1, where statistically significant associations are indicated by "X", and taxa with a weak association with a water mass (identified qualitatively, but without passing the Kruskal-Wallis tests) with "x." The geometry of the Chl-a patches was closely aligned with the boundaries between the water masses, consistent with a coupling of hydrographic and biological properties. In the next section, we investigate this coupling in more detail by looking at the individual phytoplankton and zooplankton taxa.

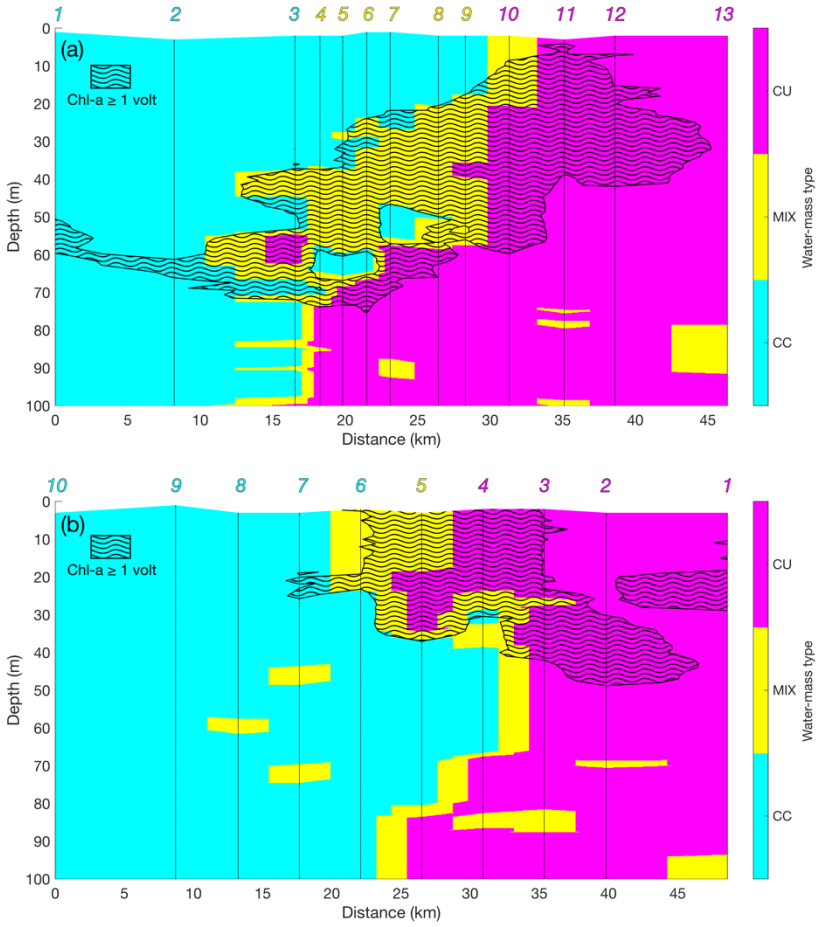

Figure 2.2: Vertical sections (0–100 m) across the front from west (offshore, on the left) to east (in-shore, on the right) of water masses for Transect E1 (a) and Transect E2 (b). Cyan, magenta, and yellow colors indicate California Current (CC), California Undercurrent (CU), and Mixed (MIX) waters, respectively. Here, the frontal interface coincided with the MIX waters (yellow). Hatches show the position of chlorophyll-a patches (fluorescence $\geq 1\ V$). Vertical black lines indicate the position of the CTD stations, with the station number colored by the majority water-mass type on the top x-axis.

2.4.2 Distribution of plankton taxa across the front

We analyzed the spatial distribution of 23 plankton taxa (including bacteria, phytoplankton and zooplankton) across the front to characterize their relationship with water-mass type. We found that spatial distribution across the front varied by taxon; bacteria, phytoplankton, and zooplankton were not necessarily co-located in space in terms of abundance (Figure 2.3). This cross-frontal patchiness and variability both within and across transects prompted us to investigate the association of each taxon with water-mass type.

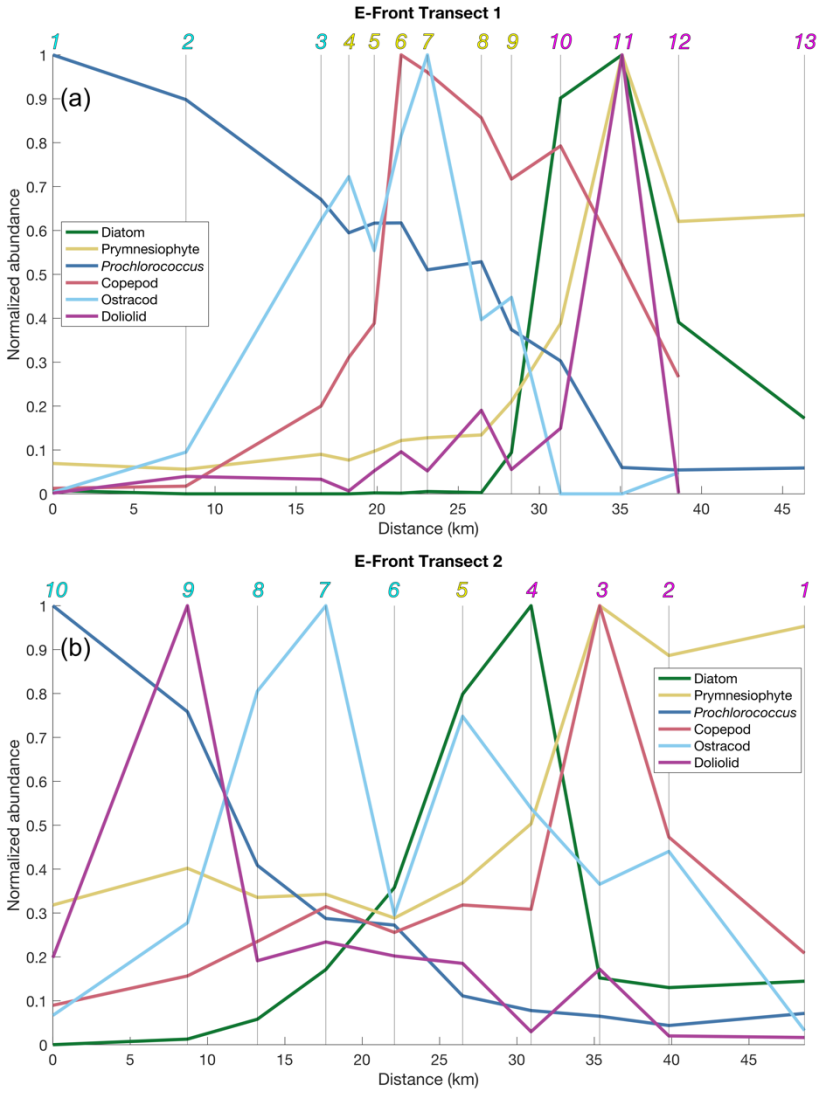

Figure 2.3: Cross-frontal abundances, normalized by the maximum abundance for each taxon in each transect, of select bacteria, phytoplankton, and zooplankton taxa in Transect E1 (a) and Transect E2 (b). Top x-axis and vertical black lines indicate locations of the stations for each transect, and coloring of transect station numbers correspond to water-mass type as defined in Figure 2.2 (cyan for CC, magenta for CU, and yellow for MIX). The color of each plotted line represents a specific taxon.

We considered that a given taxon was consistently associated with CC or CU if it had a significantly higher abundance in that water-mass type for the two transects conducted two weeks apart during the cruise. We found that 8 taxa (chlorophytes, cryptophytes, dinoflagellates, pelagophytes, prymnesiophytes, heterotrophic bacteria, rhizaria, and pteropods) were

consistently associated with CU waters, and 1 taxon (*Prochlorococcus*) was consistently associated with CC waters in both transects (Table 2.1, upper rows).

Table 2.1: Association between plankton taxa and water-mass types. Different market indicate different associations: X = statistically significant association; x = minor association; - = no association. The upper rows (Chlorophytes to *Prochlorococcus*) indicate taxa that were consistently associated with a single water-mass type (CC or CU), while the bottom rows (Chlorophyll-a fluorescence to Other crustaceans) indicate taxa that were not consistently associated with a single water-mass type. The full results of the Kruskal-Wallis tests are provided in Supplemental Table 2.2 and Supplemental Table 2.3.

	CC		MIX		CU	
Taxa	***E*1**	***E*2**	***E*1**	***E*2**	***E*1**	***E*2**
Chlorophytes	—	—	—	—	X	X
Cryptophytes	—	—	—	—	X	X
Dinoflagellates	—	—	—	—	X	x
Pelagophytes	—	—	—	—	X	x
Prymnnesiophytes	—	—	—	—	X	x
Heterotrophic bacteria	—	—	—	—	X	X
Rhizaria	—	—	—	—	x	X
Pteropods	—	—	—	—	X	X
Prochlorococcus	X	X	—	—	—	—
Chlorophyll *a* fluorescence (0–100 m)	—	—	X	X	—	—
Ostracods	—	—	x	x	—	—
Diatoms	—	—	—	x	—	—
Synechococcus	—	—	X	—	—	—
Pico-eukaryotes	—	—	X	—	—	—
Appendicularians	—	—	x	—	—	—
Chaetognaths	—	—	x	—	—	—
Cnidarians	—	—	x	—	—	—
Doliolids	—	X	—	—	x	—
Copepods (Calanoids, Oithona, others)	—	—	x	—	—	x
Polychaetes	—	—	X	—	—	x
Euphausiids	—	—	x	—	—	x
Other crustaceans	—	—	x	—	—	x

CC, California Current; CU, California Undercurrent; MIX, Mixed.

The remaining taxa (n=14) did not have a consistent association with a single water-mass type (CC or CU) and displayed a range of patterns (Table 2.1, bottom rows). Ostracods were associated with MIX waters in both transects, while the 13 other taxa exhibited time-dependent water-mass associations. Doliolids were associated with CU waters in E1, but CC waters in E2;

three copepod taxa, polychaetes, euphausiids, and other crustaceans were associated with MIX waters in E1, but with CU waters in E2. The remaining taxa were associated with a particular water mass in only one transect, with no statistically significant association in the other: pico-eukaryotes, *Synechococcus*, chaetognaths, cnidarians, and appendicularians were associated with MIX waters in E1 only; diatoms were associated with MIX waters in E2 only (Supplemental Table 2.2 and Table 2.3). While the distributions of some plankton taxa were explained by the local water mass type (consistent association with either CC or CU), the majority were not. In the next sections, we explore the possibility that the water-mass history (through a Lagrangian approach) could provide an alternative explanation.

2.4.3 Horizontal convergence of water masses at the front

Here, we examine the origins of the water parcels sampled across the front to investigate how wind-driven coastal upwelling upstream of the front drove temporal and spatial biological variability across the front.

2.4.3.1 Geographic origins

Our backward-in-time tracking showed that waters sampled during both E1 and E2 had variable geographic origins (Figure 2.4). While almost all the stations contained waters that originated at the coast in the two months before sampling (Supplemental Table 2.4), the origin locations varied. Waters sampled in E1 originated from a broad stretch of the coast (from 34°N to 39°N, about 500 km), while the waters sampled in E2 originated in a narrower region (34°N to 36°N, about 200 km). Thus, for both transects, water parcels sampled within 25 km of each other at the front were hundreds of kilometers apart two months earlier. The lengths and geometries of parcel trajectories from the coast to the transect locations were also variable: water parcels sampled on the offshore side of the transects generally had long, meandering trajectories, while

water parcels sampled on the inshore side of the transects generally had shorter, more direct trajectories to the front (Figure 2.4).

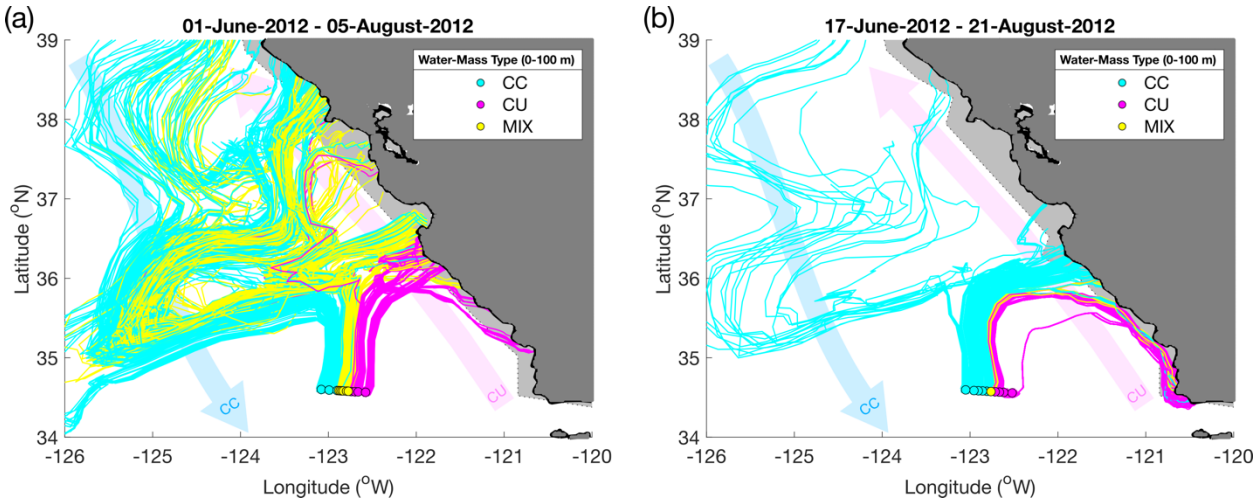

Figure 2.4: Trajectories of water parcels sampled across E-Front Transect E1 (a) and Transect E2 (b) in the two months before sampling. Trajectories were computed from backward-in-time advection, using a velocity field that includes a geostrophic and a 15-m depth Ekman component. Filled circles show the locations of the sampled stations, with each station consisting of a CTD cast and a Bongo net tow. For each station, the back-trajectories of 100 points, randomly seeded in a 5-km radius around the actual station, were computed. The colors of each circle and trajectory pathline correspond to the dominant water-mass type of the water parcel when it was sampled (as defined in Figure 2.1). The light gray region outlined by the dotted line indicates the coastal upwelling region, which encompasses the coastal region within approximately 25 km of the coastline. The blue and magenta arrows show the approximate position and direction of the CC and CU, respectively.

2.4.3.2 Temporal origins: Upwelling pulses

Water parcels sampled at the frontal transect sites also originated at the coast at different times. For simplicity, we assumed that water parcels originating in the coastal region during an upwelling pulse were upwelled from depth. Remarkably, despite the fact that upwelling pulses only occurred 40–50% of the time (Figure 2.5), our backtracking analysis revealed that almost all the water parcels sampled during the cruise originated at the coast during an upwelling pulse (Supplemental Table 2.4). Some of the sampled parcels were upwelled much more recently than others: the median ages (times since upwelling) ranged from 8 to 51 days for Transect E1, and from 11 to 43 days for Transect E2 (Figure 2.6). For E1, the inshore stations tended to contain

more recently upwelled water than the offshore stations (Figure 2.6a). However, counter-intuitively, for E2, the oldest waters (median age = 43 days) were found at the two most inshore stations (E2 Stations 1 and 2), while the other stations contained more recently upwelled water with median ages ranging from 11 to 15 days (Figure 2.6b). We discuss this apparent discrepancy further in the next section. Finally, we found that the intensities of the upwelling pulses were variable along the coast, with the Coastal Upwelling Transport Index anomaly ranging from approximately 0 to 1.8 $m^2\ s^{-1}$ (Figures 2.5–2.6).

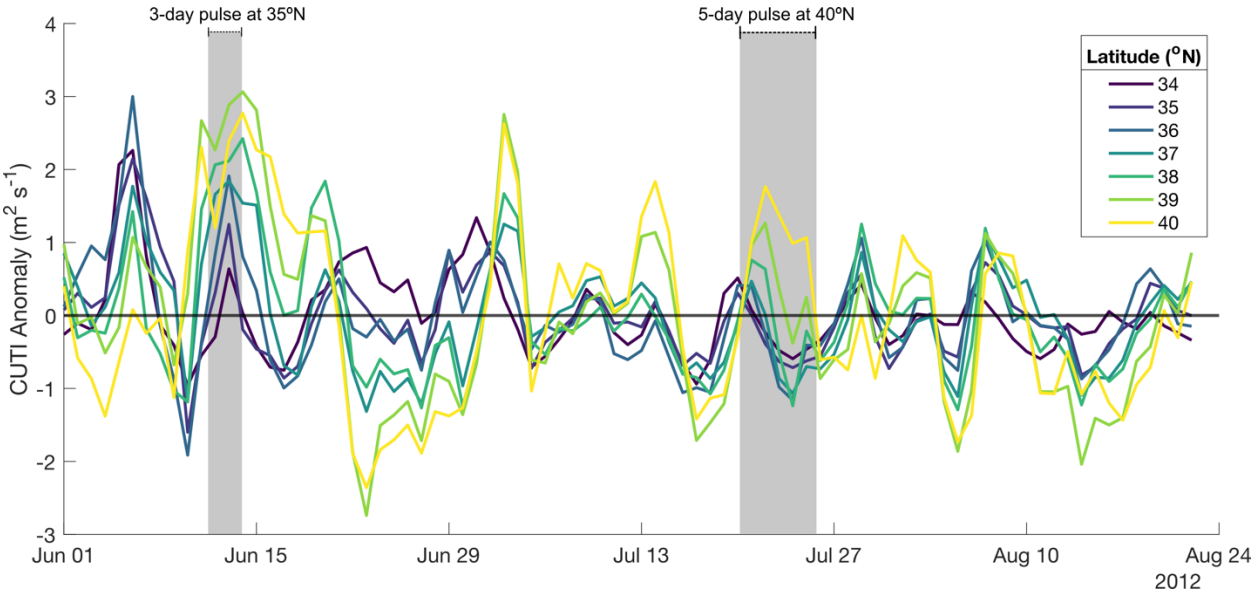

Figure 2.5: Time series of the Coastal Upwelling Transport Index (CUTI) anomaly from 1 June to 24 August 2012 for different latitudinal bands (colors) in the California Current System. Two contrasting upwelling pulses are highlighted (gray shaded regions), illustrating upwelling variability in terms of location, timing, duration, and intensity.

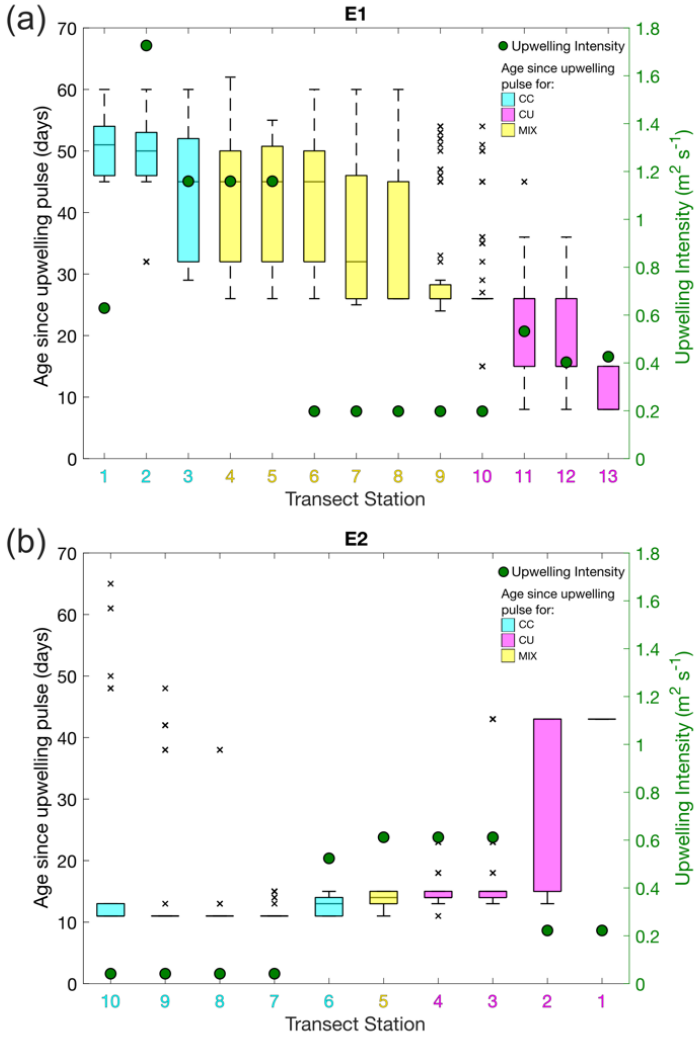

Figure 2.6: Upwelling conditions experienced by the ensemble of trajectories for each sampled station of Transect E1 (a) and Transect E2 (b). Box plots show the interquartile range of age since upwelling pulse in days (left y-axis, with outliers indicated by black x-markers). Box plots and transect station numbers are colored by the majority water-mass type at each station. Green filled circles indicate the median upwelling intensity, calculated as the Coastal Upwelling Transport Index (CUTI) anomaly, when parcels were at the coast (right y-axis in green).

2.4.3.3 Relationship between upwelling and water masses

The distributions of CC and CU waters across the front were related to their geographic and temporal origins during upwelling pulses. The data collected during the Transect E1 supported the typical scenario of subsurface nearshore CU waters being entrained first upward (into the euphotic zone by upwelling) and then offshore by transport (Zaba et al., 2018). The

water parcels with short, direct trajectories between coastal upwelling sites and the transect location (E1 Stations 10–13) retained a CU temperature-salinity signature, while parcels with long, meandering, offshore trajectories (E1 Stations 1–9) mixed with CC waters, leading to their classification as MIX, and CC for the oldest water parcels (Figures 2.2 and 2.4).

Data from E2, however, indicates a more complicated scenario. E2 included recently upwelled water parcels (with very short and direct trajectories from the coast) that were classified as CC (E2 Stations 5–10). Conversely, some older water parcels with long meandering trajectories were classified as CU (E2 Stations 1–2, Figures 2.4 and 2.6). Some trajectories can be seen meandering strongly between offshore and coastal regions (Figure 2.4); this suggests that CC waters may have first been brought from offshore into the coastal regions and then were advected offshore again along with newly upwelled waters.

2.4.4 Biological history along water-parcel trajectories

We investigated the relationship between the age of an upwelled water parcel and the plankton community found within this water parcel. We defined the "biological history" of a water parcel as the relationship between its age (defined as time since upwelling) and abundances of key planktonic taxa within that water parcel. By combining the trajectories of water parcels of different ages, we reconstructed the biological histories of these water parcels between the upwelling pulse (at the coast) and sampling (at the transects). Since we found no relationship between plankton abundance and upwelling pulse intensity (Supplemental Figures 2.6–2.8), we assumed that all upwelling pulses generated a similar biological response.

We found that the abundances of diatoms and copepods exhibited the clearest relationship with age since upwelling, with peaks at about 15 days and 30 days, respectively, after a water parcel experienced an upwelling pulse (Figure 2.7). This succession is consistent with the well-known trophic dynamics of these two taxa. In this region, diatom doubling times

are only a few days under nutrient- rich conditions (Sarthou et al., 2005), though times may vary depending on the exact nutrient and diatom species present. Copepods, which are among the main predators of diatoms, can complete a reproduction cycle in 28 days (Eiane and Ohman, 2004). Thus, we interpreted this succession of abundance peaks as a diatom bloom in response to the upwelling pulse, followed by a copepod bloom in response to the increase of their food supply. The other taxa showed more complex relationships between abundance and age, which, due to higher uncertainties regarding their food-web dynamics and growth rates, prevented us from deriving robust interpretations of the influence of the upwelling pulses (see Supplemental Information: Biological responses of non-diatom and non-copepod taxa, and Supplemental Figures 2.6–2.8).

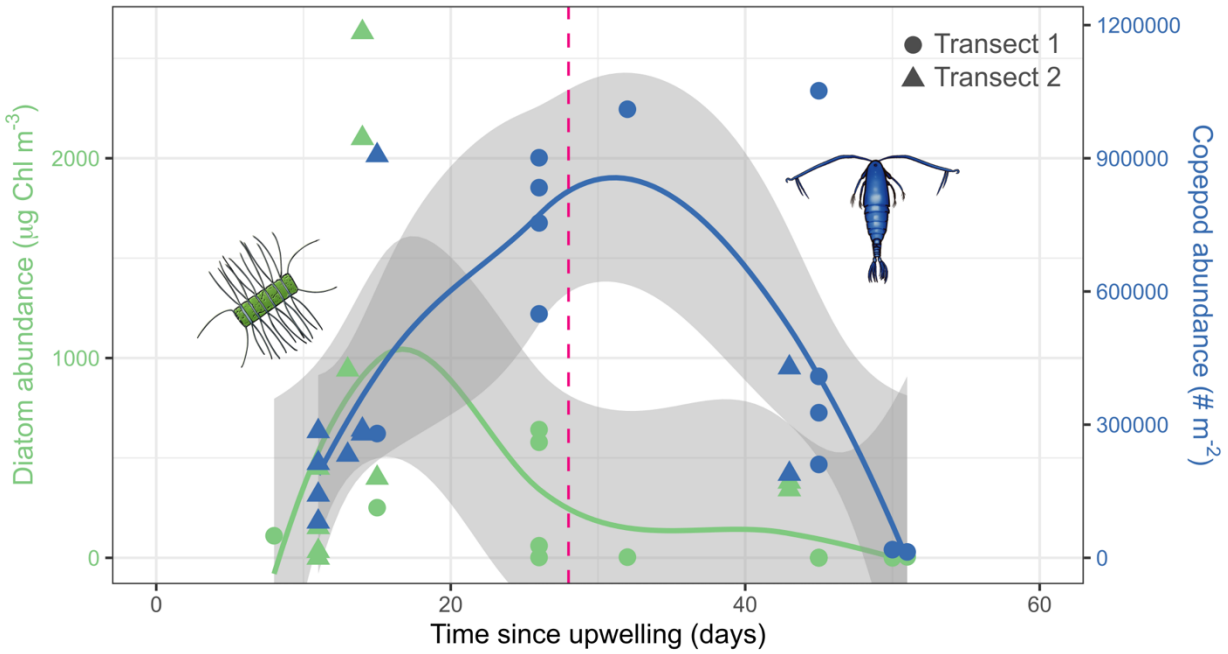

Figure 2.7: Relationship between plankton abundance and time since upwelling for diatoms (prey) in green and copepods (predator) in blue. Each marker represents one station (triangles for Transect E1, circles for Transect E2). The green and blue lines represent the locally weighted scatterplot smoothing (LOWESS) fits (f = 0.75) for the diatom and copepod abundances respectively. The gray shaded regions indicate the 95% confidence interval for each LOWESS fit. The vertical dashed line in magenta indicates the typical copepod generation time (28 days). Plankton illustrations: Freya Hammar.

2.5 Discussion

In this study, we sought to investigate the influence of wind-driven coastal upwelling on the finescale plankton community structure observed across a front. We first attempted to relate the ecosystem structure to the hydrographic properties of water (the water mass-type, CC or CU), relying on previous literature that established that CU waters are generally recently upwelled while CC waters are found offshore. However, we found that the explanatory power of this approach was limited: many plankton taxa were either found at the interface between the two water masses, or they did not have a consistent association with a particular water-mass type.

We then used a Lagrangian approach to describe the history of the water parcels by backtracking each parcel to its origin. Our results from this approach demonstrated a consistent story (Figure 2.8). Intermittent increases in alongshore wind generated short upwelling pulses every week or so, transporting deep, nutrient-rich waters into the euphotic zone in the coastal region. These water parcels were then advected offshore, following distinct trajectories until they reached the front where they were sampled. During this advection, the plankton community carried by each water parcel transformed in response to nutrient injections, experiencing a succession of phytoplankton and zooplankton blooms. Eventually, various distinct water parcels were brought together by the horizontally convergent flow at E-Front. Because the water parcels were generated by different upwelling pulses (i.e., at different dates and locations along the coast), they contained plankton communities at different stages of maturity since upwelling (i.e., young parcels were dominated by phytoplankton, and older parcels dominated by zooplankton). However, because they converged at the front, they were located very close to one another in space (within the 25 km sampled by an in situ transect). Thus, the horizontal convergence of water parcels of different ages since upwelling (and thus different plankton communities) created

finescale variations in the distribution of plankton abundances across the front, thus the generation of cross-frontal plankton patchiness.

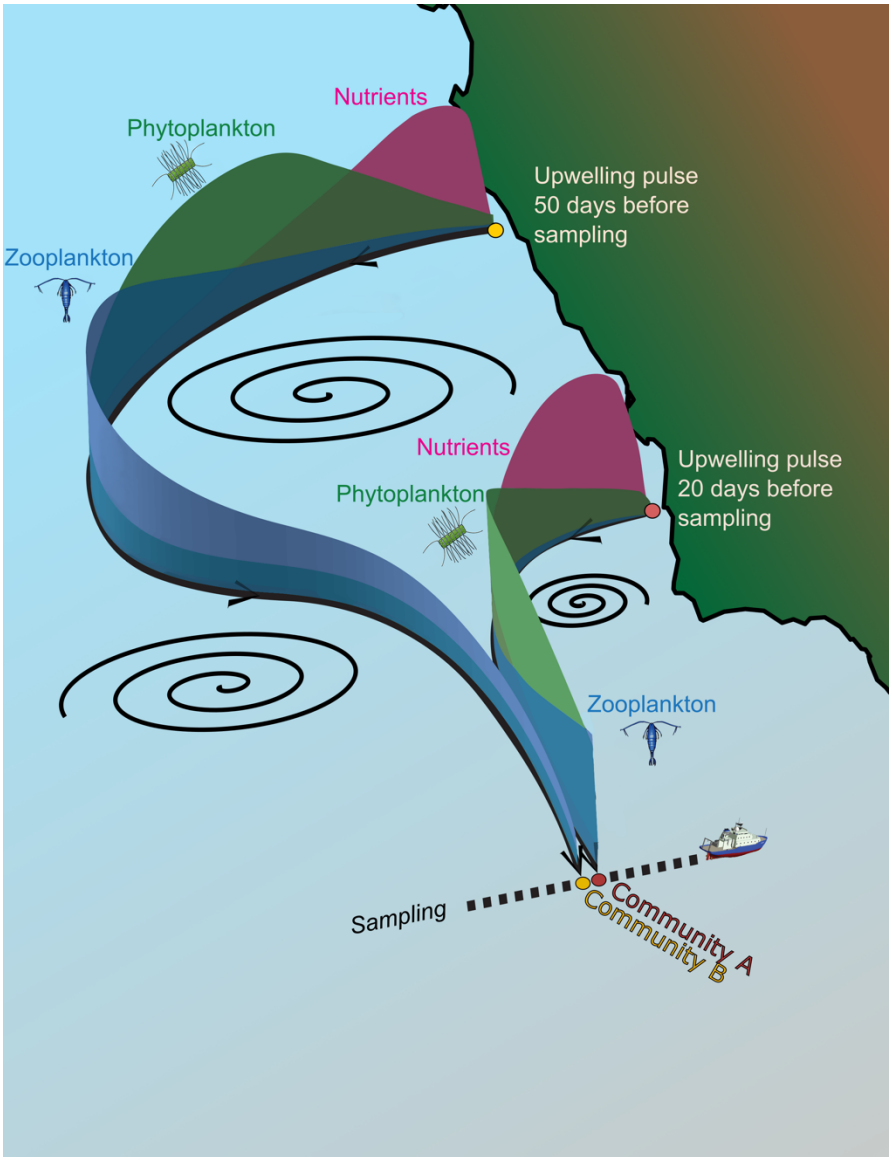

Figure 2.8: Schematic representation of the biological transformation taking place in upwelled water parcels and their subsequent convergence at a front. The longer trajectory (left) originates in the north during an upwelling pulse that occurs 50 days before sampling, and the shorter trajectory (right) originates in the south during an upwelling pulse that occurs 20 days before sampling. Along each trajectory, nutrients, phytoplankton, and zooplankton concentrations peak in succession, resulting in two very different communities sampled during the cross-frontal transect. Illustration: Peter J.S. Franks and Freya Hammar. Icons: Freya Hammar (plankton) and Woods Hole Oceanographic Institution (ship).

The critical mechanisms underlying cross-frontal plankton patchiness have been previously discussed in other studies; however, they are often treated—and analyzed—separately. These key concepts can be summarized by the following three points: (1) a front is a mosaic of distinct water parcels brought together by convergence; (2) plankton patchiness can be explained to only a limited extent by hydrographic properties; and (3) plankton communities transform while they are advected by currents, particularly in response to nutrient injections. Below, we discuss how these ideas have been applied in previous literature and conclude that combining these concepts within a Lagrangian framework provides us with a more holistic view of physical-biological interactions at ocean fronts.

4.5.1 Refining our view of finescale patchiness at ocean fronts

We found that E-Front was very patchy on small spatial scales (approximately 1–5 km). The front was composed of a mosaic of water parcels contrasting in terms of biology (i.e., the plankton community), hydrography (i.e., the water-mass type derived from temperature and salinity), and history (i.e., the origin and trajectory).

Our conclusion thus extends and complements previous findings about fronts in the California Current System. For instance, Mangolte et al. (2023) demonstrated the existence of sub-frontal-scale plankton patchiness at multiple fronts in the CCE, including E-Front. Furthermore, de Verneil et al. (2019), by inferring water-mass histories from finite size Lyapunov exponents, showed that water parcels with different biological and hydrographic signatures converged at E-Front. By integrating both the approaches and data presented in Mangolte et al. (2023) and de Verneil et al. (2019) for E-Front, we have shown that cross-frontal plankton community structure was well explained by upstream and along-trajectory factors.

These results challenge the traditional representation of a front as either a well-defined, localized boundary between two distinct biogeochemical provinces (Mousing et al., 2016;

Tzortzis et al., 2021), or as a homogeneous patch of enhanced productivity that emerges from a (typically) less productive background (Allen et al., 2005; Mangolte et al., 2022; Taylor et al., 2012). These views are generally associated with a focus on the local processes that control plankton community structure: in the first view, the two provinces contain different plankton communities because of the different environmental conditions (e.g., temperature, nutrients, light, etc.), while in the second view the productive patches are explained as a response to vertical processes, such as an enhanced nutrient supply or an increased exposure to light due to restratification (Lévy et al., 2018; Mahadevan, 2016). In the California Current System, which already has very shallow mixed layers (Franks, 2014), the restratification mechanism is unlikely to play a role. While the contribution of frontal nutrient supply is impossible to quantify without dedicated measurements, we emphasize the role of the horizontal circulation that brings together plankton communities with distinct origins, and influenced by earlier conditions. We were thus able to explain the observed plankton patchiness by invoking only upwelling dynamics and Lagrangian backtracking. It should be noted that the California Current System contains additional sources of nutrients farther offshore, mainly generated by finescale processes (such as the frontal circulation (Kessouri et al., 2020; Li et al., 2012), or eddy pumping (Chenillat et al., 2015; Gaube et al., 2013). However, these sources appear to have influenced plankton patchiness at E-Front to a much smaller extent than horizontal transport from the coastal upwelling zone.

4.5.2 Integrating local hydrographic properties and Lagrangian dynamics

In a coastal upwelling system, ecosystem variability can often be explained by the variability in upwelling itself; this hinges on the idea that vertical transport of nutrient-rich waters at the coast stimulates primary production, which in turn fuels biomass of higher trophic levels (Chavez & Messié, 2009; Checkley & Barth, 2009). However, the pathways through which wind-driven upwelling influences the ecosystem involve both physical (particularly,

horizontal currents) and biological (growth and predation) processes that are often difficult to disentangle. In this study, we attempted to explain the underlying drivers of plankton community structure using two approaches that connected a given water parcel to wind-driven coastal upwelling.

In the first approach (applying a water-mass type association), we based the connection between biology and hydrography on the following assumption: water parcels with a CU signature were likely more recently upwelled than water parcels with a CC signature, and thus CU waters likely contained higher nutrient concentrations more recently than CC waters. However, our results showed that the assumptions underlying this first approach were too simplistic, especially at very small spatial scales. For example, recently upwelled water may have acquired a CC signature by mixing with offshore waters that had recirculated inshore. Thus, we learned that we needed to understand the Lagrangian trajectories of each individual water parcel to better analyze the relationship between their hydrographic and biological signatures.

Therefore, in the second approach, we used a Lagrangian backtracking analysis to explicitly describe the upwelling conditions experienced by a given water parcel. We found that the timing and location of upwelling influenced the biological history of each water parcel, and that qualitatively describing a water parcel as "recently upwelled" (as was the case with the first approach) was not precise enough to explain biological patterns. For example, we found that two CU water parcels may have been accurately described as "recently upwelled," but if 20 days had elapsed since upwelling for the first one and 50 days for the second, they would have had very different plankton communities (Figure 2.8). The location and intensity of upwelling may have also affected the concentration and composition of nutrients available (Jacox et al., 2018). For example, dissolved iron supply, which exerts a bottom-up control on phytoplankton biomass,

varies spatially along the coast, depending on factors such as shelf width, degree of sediment resuspension, and riverine inputs (Forsch et al., 2023; Till et al., 2019). These processes may drive some biological patchiness, which has been seen with diatoms across fronts (Brzezinski et al., 2015). Indeed, investigating the effects of initial nutrient concentrations and composition would require dedicated analyses that, while beyond the scope of this study, should receive further attention.

Overall, our results showed that in order to understand the drivers of plankton structure in a highly dynamic system, a local, hydrographic description of the water masses is not sufficient: all CU waters are not biologically equivalent, and sometimes CU water parcels can have more in common (in terms of biology) with a CC water parcel than another CU water parcel. The division of ocean basins into water masses, or biogeochemical provinces, is a powerful tool to understand large scale patterns of biodiversity (Longhurst, 2007). However, at smaller spatiotemporal scales, this question is more appropriately addressed through a Lagrangian approach that describes the history of the water parcels.

4.5.3 The Lagrangian history: a powerful framework to understand plankton community structure

In this study, we found that the spatial structure of plankton communities is better explained by a Lagrangian metric like time since upwelling than by the hydrographic properties of the water parcel. Thus, analyzing the Lagrangian history of biological data allows for a more comprehensive view of plankton ecosystem dynamics.

Many studies, using a variety of approaches, have similarly investigated how plankton communities carried by horizontal currents transform in response to an initial nutrient injection, driven by coastal upwelling or by other processes. For instance, empirical studies have taken advantage of iron fertilization experiments to explore how phytoplankton blooms develop in

response to a natural or artificial iron source (Boyd et al., 2007; d'Ovidio et al., 2015; Robinson et al., 2014), while retentive eddies give a unique glimpse into the transformation of a virtually isolated plankton community over a few weeks or even months (Chenillat et al., 2015; Lehahn et al., 2011).

Other studies have used growth-advection models—validated by in situ observations—to describe how chlorophyll and zooplankton patches are generated downstream of a nutrient source (Lehahn et al., 2017; Messié & Chavez, 2017; Ser-Giacomi et al., 2023). Lagrangian approaches can also help elucidate the physical mechanisms driving phytoplankton blooms, such as nutrient injections driven by finescale turbulence (Hernández-Carrasco et al., 2023), or iron enrichment driven by interactions with islands (Della Penna et al., 2018) or seamounts (Sergi et al., 2020).

2.6 Conclusion

In this study, we employed a novel Lagrangian framework based on empirical data (in situ sampling and satellite observations) and water-parcel backtracking to demonstrate that the observed plankton patchiness across a front in the California upwelling region can be explained by distinct biological histories along converging trajectories.

This framework allows us to explicitly employ the dimension of time, thus challenging the static view of fronts and underscoring the notion that in order to identify the processes driving frontal plankton communities, we must view them as responses to their spatial and temporal histories rather than solely resulting from local frontal dynamics. For instance, the many frontal studies in the California Current System (including the present study and others referenced above) show that even superficially similar fronts located in the same region can be driven by completely different processes (e.g., nutrient injections by the frontal vertical

circulation or horizontal transport from the coastal upwelling), and that more effort should be directed toward identifying these processes.

Thus, we encourage the widespread adoption of Lagrangian approaches such as satellite-based backtracking analyses, modeling studies, or dedicated in situ sampling strategies aimed at collecting data along water-parcel trajectories. The inclusion of these Lagrangian approaches will be beneficial to research efforts aimed at gaining a better understand of the mechanisms generating and maintaining biodiversity in the ocean, especially at small scales.

Data Availability

The satellite-derived data used for our analyses and/or figures can be downloaded from the CMEMS website (https://marine.copernicus.eu/) and the Aviso+ website (https://www.aviso.altimetry.fr/en/home.html). The velocity data set is cataloged here: https://doi.org/10.48670/mds-00327. The sea-surface temperature data set is cataloged here: https://doi.org/10.48670/moi-00169. The Finite Size Lyapunov Exponent (FSLE) data set is cataloged here: https://doi.org/10.24400/527896/ a01-2022.002. The P1208 cruise data are available on the CCE LTER Datazoo website (https://oceaninformatics.ucsd.edu/datazoo/catalogs/ccelter/datasets) or from the Environmental Data Initiative (searchable through the ezCatalog: https://ccelter.ucsd.edu/data/). The Coastal Upwelling Transport Index data are available here: https://mjacox.com/upwelling-indices/.

Acknowledgments

The authors would like to warmly thank Peter J. S. Franks, Marina Lévy, Mark Ohman, Ralf Goericke, Pierre Chabert, Katherine Zaba, and Michael Stukel for providing data, guidance, and/or feedback. The authors are also grateful to Peter J. S. Franks (schematic) and Freya Hammar (schematic and icons) for their illustrations, and the ship/science crews on the R/V Melville in August 2012. SG was funded by the NSF GRFP and Scripps Institution of

Oceanography. IM was funded by an ENS/Sorbonne Université PhD grant, a Fulbright scholarship, and CNES. Support for CCE LTER was provided by NSF OCE-1637632/OCE-1026607/OCE-2224726.

Chapter 2, in full, is a reprint of the material as it appears in *Limnology & Oceanography*. Gangrade, Shailja; Mangolte, Inès, 2024. The dissertation author and Inès Mangolte were the primary investigators and first authors of this paper.

Supplemental Information

Biological responses of non-diatom and non-copepod taxa

The diatom-copepod food chain, despite its importance (both in terms of quantity and in ecological and biogeochemical consequences), is one dimension of a very complex plankton ecosystem. On the one hand, many other grazing zooplankton taxa also consume diatoms (particularly filter-feeding tunicates); on the other hand, the diet of copepods can include a variety of sources including other phytoplankton, zooplankton, or detritus (Whitmore & Ohman, 2021).

Many factors might explain why the collected data only showed a significant biological response for diatoms and copepods. In the case of non-diatom phytoplankton (Supplemental Figure 2.6), it is possible that a bloom developed at the subsurface only and was thus not measured in our surface measurements. Or, it is also possible that—unlike diatoms—the other phytoplankton taxa were unable to escape grazing pressure due to their slower growth rates (Inomura et al., 2023). In the case of carnivorous zooplankton (Supplemental Figure 2.7), it is likely that the duration of our backtracking analysis (two months) was too short relative to their reproduction rates. We would expect large changes in their abundances to be visible after several months or even years. For instance, Messié et al. (2023) described a "damping effect" in the California upwelling region by which metazoan organisms with longer lifespans or those located deeper in the water column (i.e., mesopelagic or benthic) respond slower to environmental forcings than phytoplankton or micro-zooplankton: the response time scales may be months to years as opposed to days to weeks.

Moreover, some taxa showed multiple peaks in abundance within water parcels of different ages, which could indicate more complex trophic interactions. For instance, appendicularians (Supplemental Figure 2.8a) showed an initial peak at about 10 days, consistent

with their fast growth rate in response to the diatom bloom (Capitanio & Esnal, 1998), followed by a second peak at about 30 days, which could be generated by the consumption of copepod fecal pellets.

The only taxon other than diatoms and copepods that showed a clear relationship with age since upwelling pulse was rhizarians. The abundance of rhizarians peaked at approximately 30 days (Supplemental Figure 2.8b). While the feeding strategies and growth rates of rhizarian organisms are extremely diverse (Biard, 2015; Biard & Ohman, 2020), the time scale of this increase in abundance is consistent with a growth response to an increase in the availability of their nutrition source (whether they are photosynthetic, eat inorganic nutrients, diatoms, or detritus).

Supplemental Table 2.1: List of plankton taxa sampled during the E-Front transects, the methodologies used (sampling and identification methods), and the vertical resolution.

Sample	Instrument	Taxa included	Depth
Niskin bottle	Flow Cytometry	Heterotrophic bacteria, *Prochlorococcus* (PRO), *Synechococcus* (SYN), pico-eukaryotes	Discrete levels 0-120 m
Niskin bottle	HPLC	Diatoms, dinoflagellates, coccolithophores, pelagophytes, chlorophytes, cryptophytes	Surface
Bongo net	ZooScan	3 copepod groups (calanoids, oithonoids, and others), pteropods, euphausiids, other crustaceans, rhizarians, doliolids, appendicularians, salps, pyrosomes, cnidarians+ctenophores, polychaetes, chaetognaths, ostracods	Vertically averaged 0-100 m

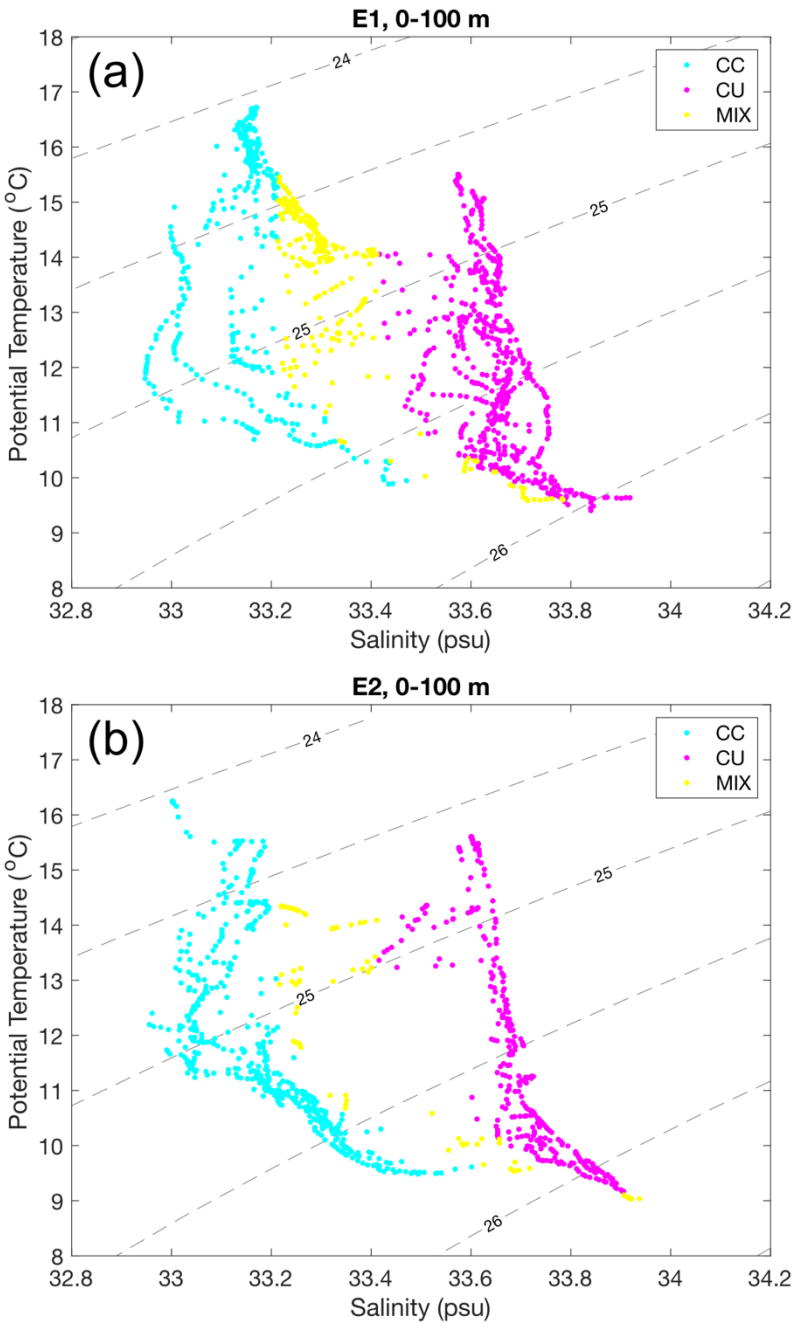

Supplemental Figure 2.1: Salinity-temperature plots for E-Front Transect E1 (a) and Transect E2 (b) from CTD vertical profiles (0–100 m). Dashed gray lines indicate the density (σ_θ) isolines. Points are colored according to their water-mass type classification: California Current (CC, cyan), California Undercurrent (CU, magenta) and MIX (yellow).

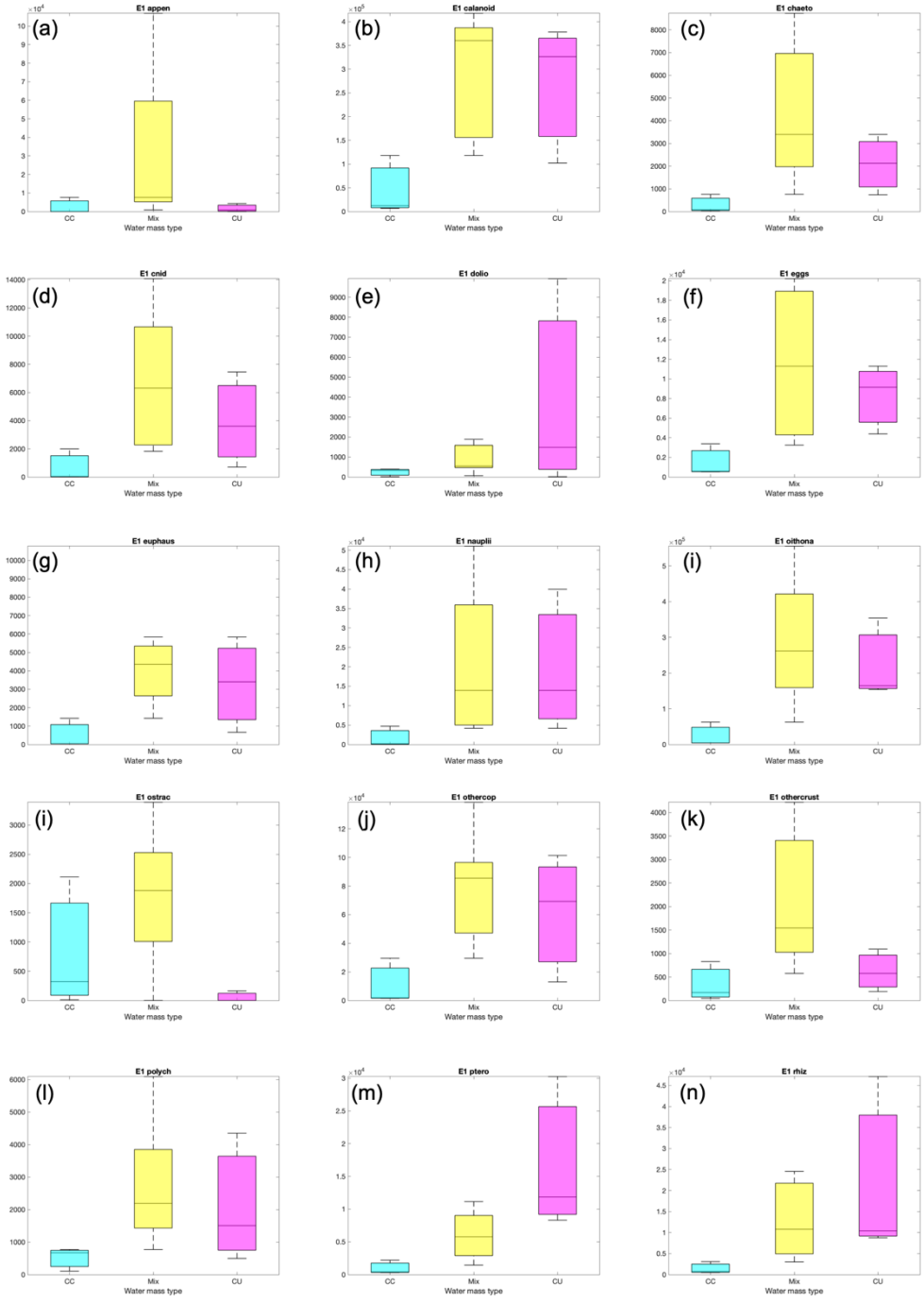

Supplemental Figure 2.2: Distribution of zooplankton abundance ($no./m^2$) in each majority water-mass type for E-Front Transect E1. Box plots indicate the median and interquartile ranges of abundance and are colored by the corresponding water-mass type (cyan for CC, yellow for MIX, and magenta for CU). Zooplankton abundances were vertically integrated (0–100m), and the majority water-mass type in the vertical water-column profile was used (see Chapter 2 Data and Methods).

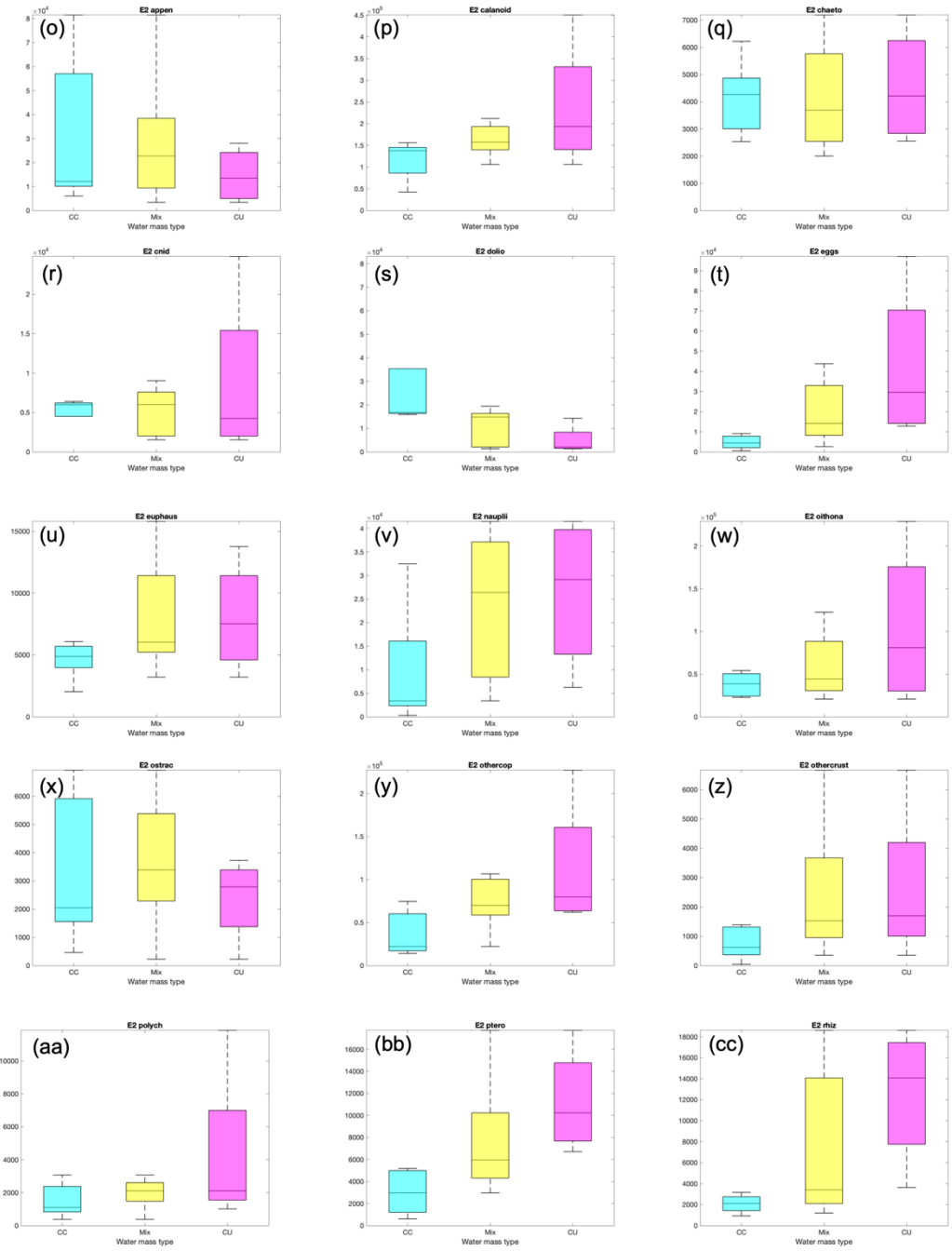

Supplemental Figure 2.3: Same as Supplemental Figure 2.2 above, but for E-Front Transect E2.

Supplemental Figure 2.4: Distribution of picoplankton and phytoplankton abundance in each majority water-mass type for E-Front Transect E1. Box plots indicate the median and interquartile ranges of abundance and are colored by corresponding water-mass type (cyan for CC, yellow for MIX, and magenta for CU). Picoplankton abundance (*Prochlorococcus*, *Synechococcus*, picoeukaryotes, and heterotrophic bacteria, in $cells/L$) were measured with flow cytometry at each vertical level. Phytoplankton (μg Chl/m^3) were measured with HPLC for the surface sample only. The water-mass types were taken at the vertical level corresponding to each sample.

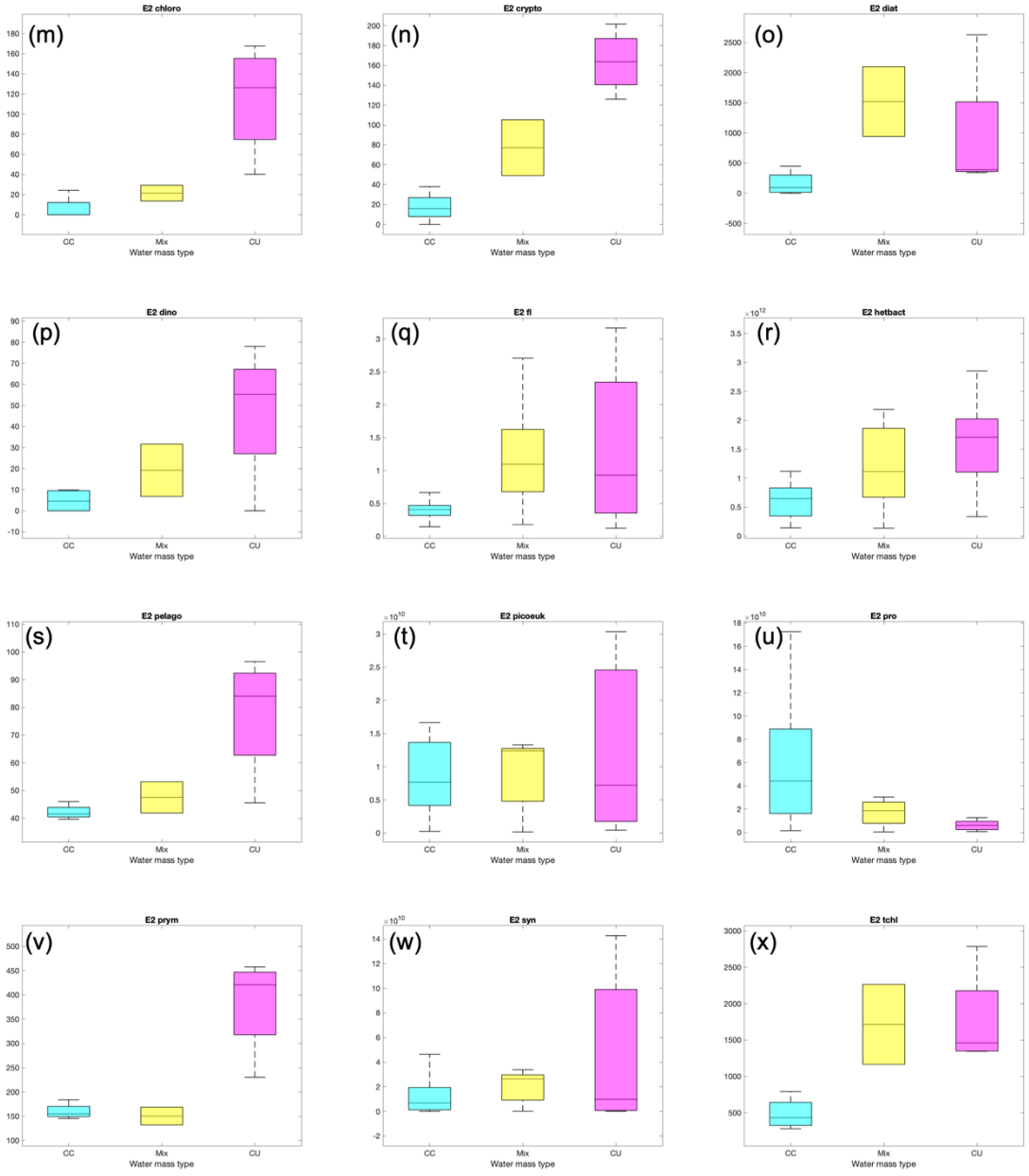

Supplemental Figure 2.5: Same as Supplemental Figure 2.4 above, but for E-Front Transect E2.

Supplemental Table 2.2: Results from Kruskal-Wallis statistical tests comparing the distributions of plankton abundances in pairs of water-mass types (CC vs. CU, CC vs. MIX and CC vs. MIX) for E-Front Transect E1. High *p*-values (> 0.05) indicate that the distributions are not statistically different (i.e., the null hypothesis—that the data originate from the same distributions—is not rejected). In contrast, low *p*-values ≤ 0.01 (yellow) and 0.01 < *p*-value < 0.05 (orange) indicate that the distributions are statistically different (null hypothesis is rejected).

Taxon/Group*	CC vs. MIX	CC vs. CU	MIX vs. CU
chloro	0.558	0.0109	0.7485
crypto	0.3817	0.0095	0.8791
diat	0.1996	0.0377	0.9878
dino	0.4415	0.019	0.8965
fl	0	0.005	0.0111
hetbact	0	0	0.9098
pelago	0.2032	0.0391	0.988
picoeuk	0.0254	0.9393	0.0095
pro	0.01	0	0.0001
prym	0.4425	0.0192	0.8967
syn	0.0029	0.8109	0.0138
tchl	0.4425	0.0192	0.8967
appen	0.1775	0.9715	0.0989
calanoid	0.0329	0.3312	0.7239
chaeto	0.0268	0.4321	0.5359
cnid	0.0487	0.3800	0.7465
dolio	0.1981	0.2860	0.9906
eggs	0.0401	0.2448	0.8867
euphaus	0.0401	0.2448	0.8867
nauplii	0.0704	0.2077	0.9906
oithona	0.0268	0.2077	0.8692
ostrac	0.8389	0.4818	0.1181
othercop	0.0401	0.2448	0.8867
othercrust	0.0364	0.8228	0.1912
polych	0.0487	0.3800	0.7465
ptero	0.1267	0.0145	0.3025
pyro	NaN	NaN	NaN
rhiz	0.0643	0.0984	0.9576
salp	NaN	NaN	NaN
totvintfl	0.3267	0.4779	0.9953
totvintdiat	0.3267	0.4779	0.9953

Supplemental Table 2.3: Same as Supplemental Table 2.2 above, but for E-Front Transect E2.

Taxon/Group*	CC vs. MIX	CC vs. CU	MIX vs. CU
chloro	0.6601	0.0180	0.3668
crypto	0.4869	0.0140	0.4869
diat	0.1116	0.3402	0.6667
dino	0.7777	0.2227	0.7777
fl	0.0224	0.0050	0.8300
hetbact	0.0841	0.0000	0.4874
pelago	0.6064	0.0510	0.6064
picoeuk	0.9666	0.9662	0.9963
pro	0.1458	0.0000	0.1926
prym	0.9559	0.0680	0.0903
syn	0.6079	0.7643	0.8802
tchl	0.1991	0.0378	0.9559
appen	0.9976	0.7389	0.6575
calanoid	0.1935	0.1193	0.8475
chaeto	0.9710	0.9615	0.8677
cnid	0.9995	0.9827	0.9729
dolio	0.1446	0.0175	0.4306
eggs	0.0940	0.0227	0.6060
euphaus	0.2725	0.4010	0.9998
nauplii	0.1781	0.1394	0.9047
oithona	0.8621	0.7300	0.9365
ostrac	0.9024	0.9326	0.7082
othercop	0.1228	0.0918	0.8868
othercrust	0.2308	0.2327	0.9623
polych	0.7775	0.7389	0.9818
ptero	0.1446	0.0175	0.4306
pyro	NaN	NaN	NaN
rhiz	0.2725	0.0290	0.3621
salp	NaN	NaN	NaN
totvintfl	0.0585	0.0290	0.7810
totvintdiat	0.0585	0.0290	0.7810

Supplemental Table 2.4: Description of water-parcel origins for each E-Front transect station based on an ensemble of back-trajectories (100 parcels seeded randomly in a 5-km radius around each station). A water parcel was considered to have originated from the coast (6th column) if its trajectory location was within 25 km of the coastline at any point during the 2-month backtracking. A water parcel was assumed to have been upwelled (last column) if it was at the coast during an upwelling pulse (positive CUTI anomaly). The median age since upwelling and pulse intensity were computed only for upwelled water parcels.

Transect	Station	Median age since upwelling (days)	Median CUTI (m^2/s)	Median CUTI anomaly (m^2/s)	Fraction of parcels from coast	Fraction of upwelled parcels
1	1	51	1.618	0.629	0.68	0.68
1	2	50	2.787	1.727	0.80	0.80
1	3	45	2.130	1.159	0.95	0.95
1	4	45	2.130	1.159	0.91	0.91
1	5	45	2.130	1.159	0.92	0.91
1	6	45	1.020	0.198	0.94	0.94
1	7	32	1.020	0.198	0.95	0.95
1	8	26	1.020	0.198	0.92	0.92
1	9	26	1.020	0.198	0.95	0.95
1	10	26	1.020	0.198	1	1
1	11	26	1.503	0.532	1	1
1	12	15	1.225	0.403	1	0.96
1	13	8	1.248	0.426	1	0.89
2	1	43	0.909	0.222	1	1
2	2	43	0.909	0.222	1	1
2	3	15	1.433	0.612	1	1
2	4	14	1.433	0.612	1	1
2	5	14	1.433	0.612	1	1
2	6	13	1.345	0.524	1	1
2	7	11	0.863	0.042	1	1
2	8	11	0.863	0.042	1	1
2	9	11	0.863	0.042	1	0.91
2	10	11	0.863	0.042	0.96	0.91

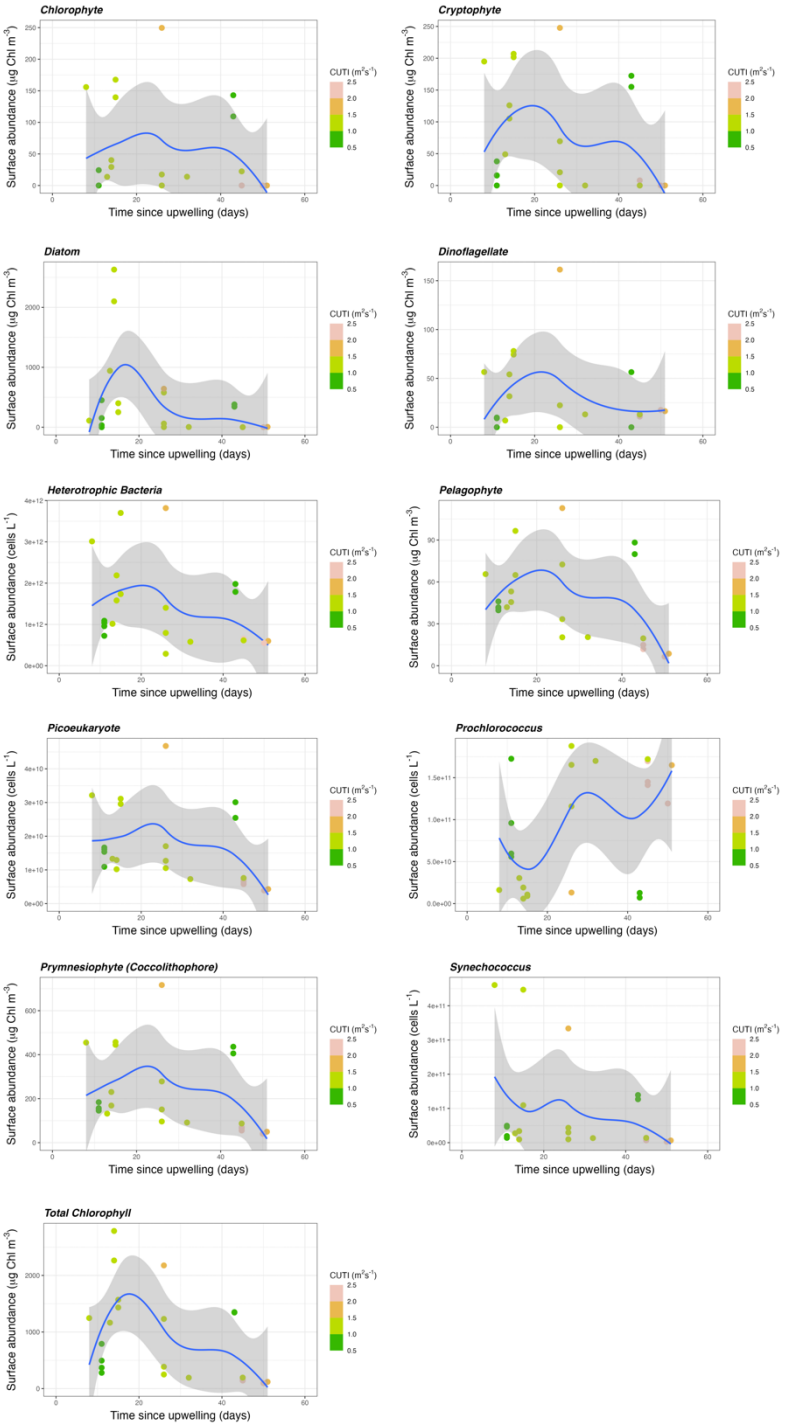

Supplemental Figure 2.6: Relationship between phytoplankton and bacteria abundance and age (time) since upwelling, in days. Each marker represents one station; the points include data from both transects. Blue lines represent the lowess fits (f=0.75) of time vs. abundance, with gray shaded regions indicating the 95% confidence interval. The color of the points indicate the median upwelling pulse intensity calculated from the magnitude of CUTI when parcels were at the coast.

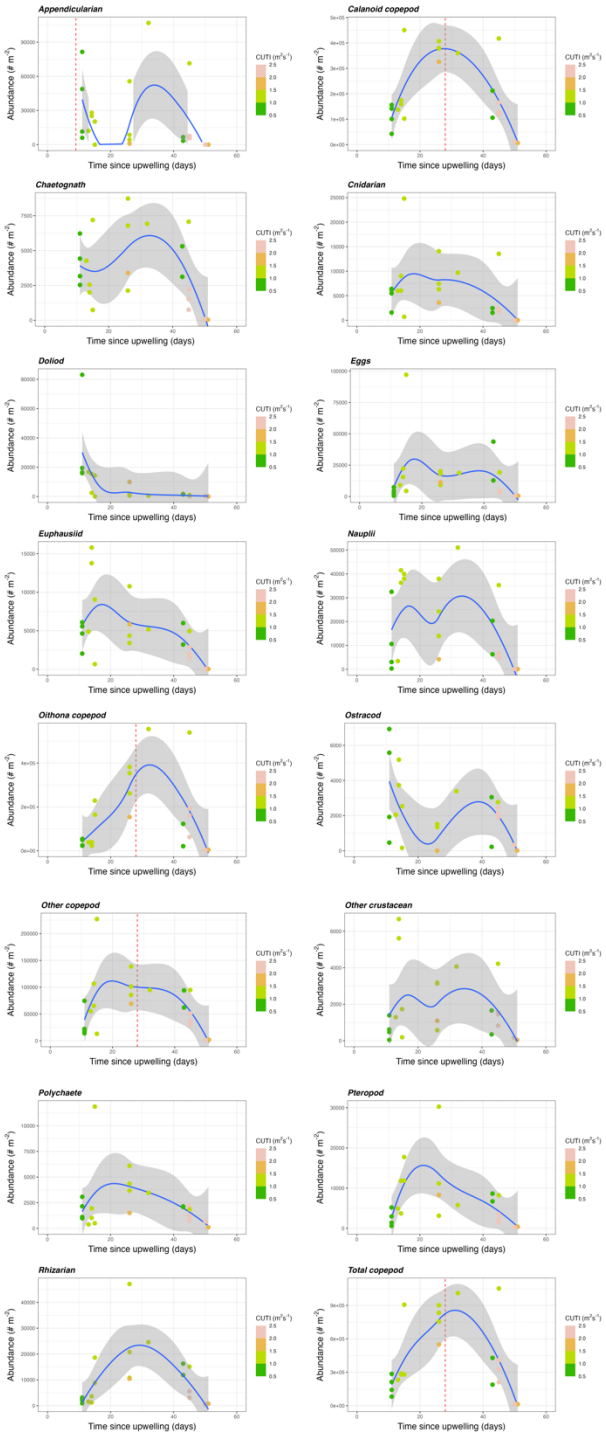

Supplemental Figure 2.7: Relationship between zooplankton (and related taxa) abundances and age (time) since upwelling. Each marker represents one station; the points include data from both transects. Blue lines represent the lowess fits (f=0.75) of time vs. abundance, with gray shaded regions indicating the 95% confidence interval. The color of the points indicate the median upwelling pulse intensity calculated from the magnitude of CUTI when parcels were at the coast. Vertical dashed lines in red, when plotted, indicate the estimated generation time of the taxon (e.g., 28 days for copepods).

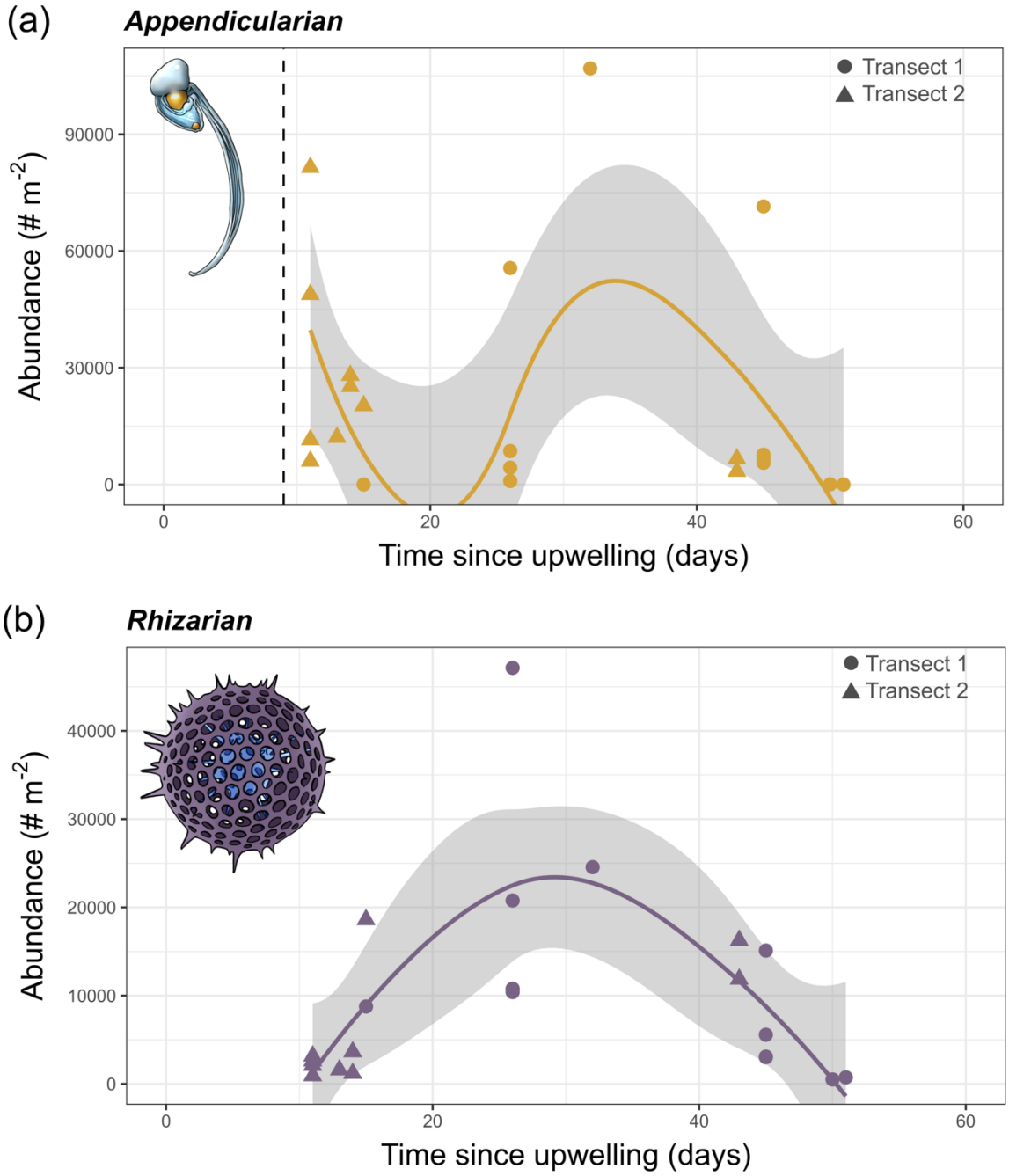

Supplemental Figure 2.8: Relationship between plankton abundance and age (time) since upwelling for (a) appendicularians and (b) rhizarians. Each marker represents one station (triangles for Transect E1, circles for Transect E2). The orange and purple lines represent the lowess fits (f=0.75) of time vs. abundance for appendicularians and rhizarians respectively. Gray shaded regions indicate the 95% confidence interval of the lowess fits. The vertical dashed line in (a) shows the typical appendicularian generation time (9 days). Plankton illustrations: Freya Hammar.

Chapter 3: Salinity is diagnostic of maximum potential chlorophyll and phytoplankton community structure in an Eastern Boundary Upwelling System

3.1 Abstract

Coastal upwelling ecosystems associated with strong physical stirring exhibit significant mesoscale hydrographic and biological patchiness. Though many studies have found broad correlations between hydrographic properties (e.g., temperature and salinity) and phytoplankton biomass, we lack a detailed understanding of the mechanisms underlying these correlations. Here, using observational data from coastal waters in the California Current System, we demonstrate that the maximum observed chlorophyll in a water parcel increases with salinity—a conservative water-mass tracer. This relationship arises from the correlations of vertical salinity and sub-euphotic zone nitrate profiles. This allows us to define the maximum potential chlorophyll as a function of salinity, and thus nitrate. We show that variations in salinity explain patterns in phytoplankton community structure, and discuss how growth, grazing, and light and micronutrient limitation can generate chlorophyll values below the maximum potential. Our mechanistic explanation provides a novel framework for diagnosing biological patchiness solely using salinity observations.

3.2 Introduction

Within Eastern Boundary Upwelling Systems (EBUSs), equatorward alongshore winds drive the upwelling of cold, nutrient-rich waters at the coast. These waters, once upwelled into the euphotic zone, promote phytoplankton growth and fuel secondary production of zooplankton and fishes, many of which contribute to important commercial fisheries (Chavez & Messié, 2009; Pauly & Christensen, 1995).

The California Current System (CCS), an EBUS in the Northeast Pacific, is a confluence of hydrographically and biogeochemically distinct waters transported within two main flow

features: the equatorward-flowing, relatively fresh, nutrient-poor California Current (CC); and the coastal, poleward-flowing, relatively salty, nutrient-rich California Undercurrent (CU) (Bograd et al., 2015; Bograd et al., 2019; Lynn & Simpson, 1987).

In the CCS, coastal-upwelling-associated filaments can rapidly transport phytoplankton-rich California Undercurrent waters offshore (Zaba et al., 2021). Within these broad, high-velocity but slowly-varying mesoscale features, there are strong biological gradients at small spatial scales (tens of kilometers) and short time scales (days to weeks) (de Verneil & Franks, 2015; Gangrade & Franks, 2023; Mangolte et al., 2023). Such gradients are often associated with hydrographic (as opposed to velocity) properties. In particular, fine-scale variability in chlorophyll *a* (Chl), a proxy for phytoplankton biomass, is often associated with salinity gradients: high nutrient and Chl concentrations are found in high-salinity waters (Strub et al., 1991; Zaba et al., 2021). This relationship between biological variables and water-mass properties has been well-investigated in estuarine systems, where gradients in phytoplankton biomass have been linked to salinity gradients (Cloern et al., 2017). In estuaries, low-salinity waters are correlated with high nutrient concentrations (Conomos et al., 1979) and high phytoplankton abundance (Peterson et al., 1975).

Here, we similarly investigate the relationship between salinity, a commonly measured conservative water-mass tracer, and Chl in the coastal waters of the CCS—a region with relatively little riverine freshwater input. We use high-resolution observations from two cruises that sampled the California coastal region in 2017 and 2019. We demonstrate a systematic relationship between the maximum observed Chl (MOC) in a water parcel and its salinity. We then derive a nitrate-based estimate of the maximum potential Chl (MPC) that can be achieved in a water parcel, given its salinity. We also show that phytoplankton community structure varies

systematically with salinity, and we explain how sub-euphotic zone nitrate concentrations drive these salinity-based relationships. Finally, we explore cases in which the MPC of a water parcel is not achieved, due to timing of phytoplankton growth and grazing losses, as well as micronutrient and (or) light limitation. Fundamentally, we emphasize how a simple salinity-based framework can provide an estimate of the MPC that can be applied to upwelling ecosystems, even when nutrient measurements are lacking. The MPC framework also allows for the identification of when, where, and why the MPC may not be reached, elucidating important ecological dynamics that potentially mediate biological productivity, energy transfers to higher trophic levels, and carbon export in the CCS.

3.3 Methods

3.3.1 Hydrographic and biogeochemical data

Data were collected during two California Current Ecosystem Long-Term Ecological Research (CCE LTER) cruises. The P1706 cruise (June 1–July 2, 2017) sampled the coastal region surrounding a westward-flowing upwelling filament offshore of Morro Bay, California (the "Morro Bay filament"). The P1908 cruise (August 5–September 6, 2019) sampled the region surrounding a southwestward-flowing upwelling filament offshore of Pt. Sur, California (the "Pt. Sur filament"). We analyzed measurements of Chl, salinity, temperature, and depth from a towed SeaSoar that undulated between 0–250 m depth. We used data from the first SeaSoar survey of each cruise (Figure 3.1). As in Zaba et al. (2021), we objectively mapped SeaSoar profiles by assuming a Gaussian covariance with a horizontal decorrelation length scale of 15 km and noise-to-signal ratio of 0.1. This generated maps with 5 km along-track and 5 m vertical resolution of salinity and Chl; we omitted points with normalized mean squared error greater than 0.3.

We also used data from cross-filament CTD-rosette transects (3 per cruise), with 3–8 km horizontal resolution and 1 m vertical resolution down to 300 m. We obtained measurements of

Chl fluorescence, temperature, salinity, and depth. From bottle samples at discrete depths (every 10 m from 0–100 m), we obtained nitrate (NO_3) and silicic acid (H_4SiO_4) concentrations, which were analyzed using a colorimetric assay (Armstrong et al., 1967).

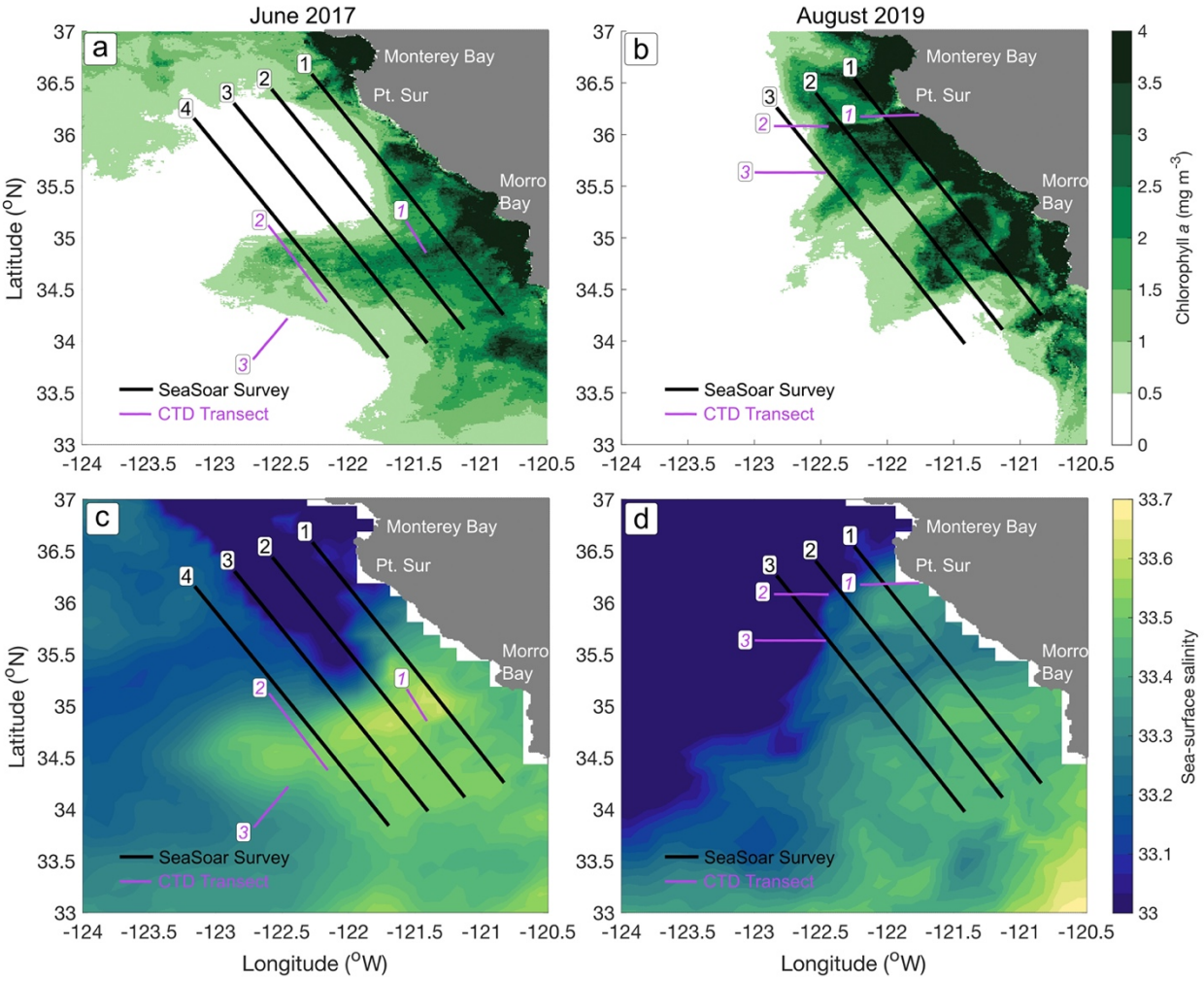

Figure 3.1: Spatiotemporal patchiness in satellite-derived sea-surface Chl (a, b) and salinity (c, d) of the central California coast during the CCE LTER P1706 cruise (a, c) and P1908 cruise (b, d). The geographic locations of the alongshore SeaSoar surveys and cross-filament CTD transects are shown in black and purple, respectively. Sea-surface Chl and salinity are averaged over the month of June 2017 for P1706, and over 1–14 August 2019 for P1908.

We also obtained Chl concentrations (in µg L^{-1}) through shipboard filtration and fluorometer readings. Using the CHEMTAX V1.95 program, we analyzed taxon-specific pigments measured by HPLC from surface bottle samples of all six transects; this provided the

proportion of total Chl attributed to eight phytoplankton taxa: dinoflagellates, diatoms, prymnesiophytes, prasinophytes, chlorophytes, cryptophytes, chrysophytes, and cyanobacteria (González-Silvera et al., 2020).

We obtained 1-km, daily sea-surface Chl data from a merged satellite ocean data product (Kahru et al., 2012) and sea-surface salinity data from a merged in situ and satellite observation data product (Droghei et al., 2016).

3.3.2 Chlorophyll data calibration

The Chl fluorescence measurements from each SeaSoar survey were calibrated using underway samples collected from the ship seawater intake system. These samples were filtered and cold-extracted in 90% acetone for approximately 24 hours. Chl concentrations were then measured with a shipboard Turner fluorometer, using the acidification technique (Lorenzen, 1967). We then compared these Chl concentrations to Chl fluorescence measurements when the SeaSoar was within 5 m of the surface. Due to the effect of nonphotochemical quenching of Chl fluorescence (Krause & Weis, 1991), we omitted daytime samples (06:00–20:00 PDT) and applied linear regressions to nighttime-only measurements to calibrate the entire SeaSoar Chl fluorescence data set (Supplemental Figure 3.1).

3.3.3 Si_{ex} calculation

From all samples with NO_3 and H_4SiO_4 measurements, we calculated Si_{ex}, a tracer equal to $[H_4SiO_4] - [NO_3] \times R_{Si:N}$, where $R_{Si:N}$ is the $[H_4SiO_4]/[NO_3]$ of upwelled water. $R_{Si:N}$ is approximately equal to 1 in the CCE (Hogle et al., 2018; King & Barbeau, 2011; Stukel et al., 2017; Stukel & Barbeau, 2020). In general, $Si_{ex} > 0$ in iron-replete conditions for silicifying organisms, while $Si_{ex} < 0$ in iron-limited conditions.

3.3.4 Nitrate climatology

We obtained salinity, σ_θ (potential density anomaly at potential temperature θ), and bottle-calibrated nitrate measurements from California Cooperative Oceanic Fisheries Investigations (CalCOFI) CTD-rosette downcast data sampled from 2003 to 2019. We used measurements from CalCOFI Lines 66.7 to 80, which cover the region from Monterey Bay to Pt. Conception, California. We used samples from all available depths for the σ_θ versus nitrate relationship and data from 0–100 m for the salinity versus nitrate relationship. We calculated mean, median, maximum, and standard deviation of nitrate concentrations within 0.05 psu salinity bins and 0.05 kg m^{-3} σ_θ bins; we used median nitrate in our subsequent analyses.

3.4 Results and Discussion

3.4.1 Maximum Observed Chlorophyll (MOC) is correlated with salinity

Waters sampled within the Morro Bay and Pt. Sur filaments and surrounding coastal regions exhibited both biological (phytoplankton) and hydrographic (salinity) patchiness in space and time (Figure 3.1). Salinity in the upper 100 m ranged from approximately 33.0 to 34.0 psu and Chl concentrations ranged from 0 to 12.8 μg L^{-1} (Figure 3.2).

When $\log_{10}$(Chl) was plotted against salinity, there was a distinct upper boundary, defining a maximum observed Chl (MOC) for a given salinity (Figure 3.2). The $\log_{10}$(MOC) increased linearly with increasing salinity (Figure 3.1), with a slope of 1.35 $\log_{10}$(μg L^{-1})/psu (R^2 = 0.91) for the combined P1706 and P1908 data set (Supplemental Figure 3.2). High-salinity waters supported exponentially higher MOC values than low-salinity waters within the salinity range of approximately 33.0 to 33.75 psu. These results therefore demonstrate that the MOC within a water parcel is positively correlated with its salinity.

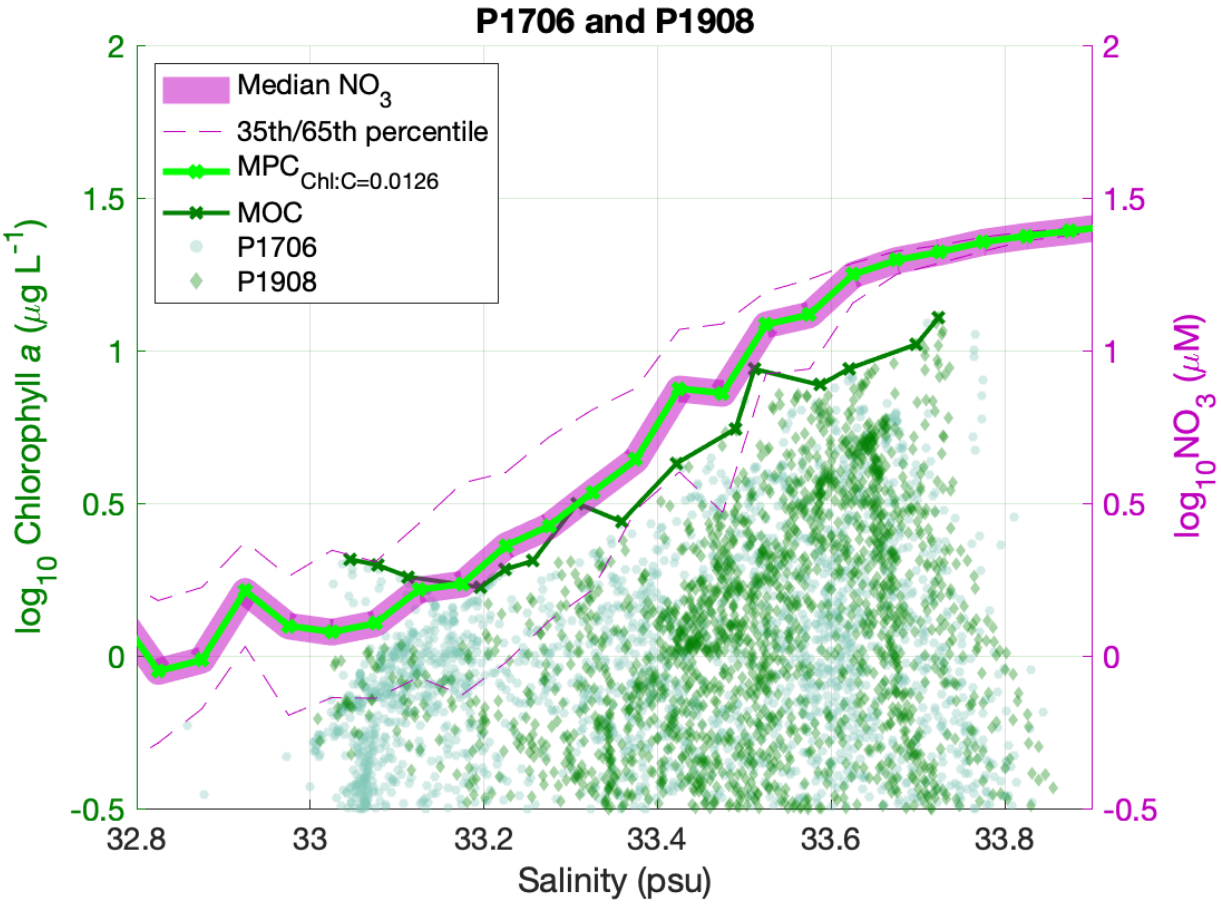

Figure 3.2: The relationship between salinity and $\log_{10}$(Chl) for waters sampled during both P1706 (light blue circles) and P1908 (green diamonds) SeaSoar surveys and transects. The maximum observed chlorophyll (MOC) boundary (solid dark green line) delineates the maximum Chl sampled in each salinity bin (0.05 psu bin width). The $\log_{10}(NO_3^{median})$ (solid magenta line) and the 35th and 65th percentiles of $\log_{10}(NO_3)$ in each 0.05-psu salinity bin (dashed magenta lines) show a positive relationship between salinity and NO_3. The maximum potential chlorophyll (MPC) boundary (solid light green line) provides the maximum Chl expected, given NO_3^{median} concentrations and a Chl:C = 0.0126 g Chl g C^{-1}.

3.4.2 Nitrate availability drives the relationship between salinity and maximum chlorophyll

It is unlikely that the relationship between MOC and salinity was driven by salinity itself. Therefore, we hypothesized that NO_3, given its potential for limiting phytoplankton growth and biomass, was a dominant driver of the observed relationship between MOC and salinity. We assumed that high NO_3 concentrations in waters upwelled from below the euphotic zone could support similarly high phytoplankton concentrations. This would require NO_3 concentrations to

exhibit an overall positive relationship with salinity, similar to MOC and salinity. To assess this, we defined "initial" NO_3 as the climatological median concentration of NO_3 (NO_3^{median}) in a water parcel; this value reflects the amount of NO_3 that would have been available to phytoplankton as a water parcel entered the euphotic zone. We found that initial NO_3 increased with salinity (slope = 1.55 $\log_{10}(\mu M)$/psu, $R^2 = 0.96$) (Figure 3.2 and Supplemental Figure 3.2). This relationship, resulting from remineralization below the euphotic zone and source-water variability in preformed NO_3 (Supplemental Figure 3.3), is well-known in this region (Bograd et al., 2019; Jacox et al., 2015; Lynn & Simpson, 1987). The strong salinity-nitrate relationship is approximately parallel to the salinity-MOC relationship, supporting the hypothesis that nitrate availability is a dominant determinant of the maximum Chl concentration in a water parcel. This salinity-nitrate relationship drives the link between hydrographic and biological patchiness, with high-salinity and high-Chl patches collocated in space and time (Figure 3.1).

3.4.3 Defining the nitrate-controlled Maximum Potential Chlorophyll (MPC)

While the MOC is a function of salinity and correlated with regional climatological NO_3, its values reflect only the waters sampled. Thus, we sought to quantify the maximum *potential* chlorophyll (MPC) that could be achieved within a water parcel of a given salinity. We defined the MPC as a quantity that would reflect regional biogeochemical patterns but would not necessarily depend on local processes (e.g., timing of bloom dynamics, etc.), as the MOC does.

Given the strong correlations between the MOC, initial NO_3, and salinity, we defined the MPC based on initial NO_3 (NO_3^{median}) concentrations as a function of salinity:

$$MPC(salinity) = Chl{:}C \times m_c \times C{:}N_{Redfield} \times NO_3^{median}(salinity) \qquad (3.1)$$

We used a constant Chl:C (in g Chl g C^{-1}), the atomic mass of carbon (12 g mol^{-1} C), and the Redfield ratio of carbon to nitrogen (106 mol C:16 mol N). Equation 3.1 provides a conversion from an initial NO_3 value (represented by NO_3^{median} in µmol L^{-1}) to the MPC (in µg Chl L^{-1}) for

that salinity. We applied Equation 3.1 using a Chl:C of 0.0126 g Chl g C^{-1}; this Chl:C value generated an MPC that is equal in magnitude to the NO_3^{median} for all salinities (Figure 3.2). Therefore, we defined a statistical MPC boundary that reflects regional NO_3 availability, positively correlates with salinity, and forms an upper envelope for most of the observed Chl and MOC data.

3.4.4 Sources of variability in Chl:C and MPC

The MPC is sensitive to Chl:C variability (Supplemental Figure 3.4). While we expect the Chl:C to be nonuniform across salinities, and to vary with factors such as light availability, nutrient limitation, and community structure (Li et al., 2010; Wang et al., 2009), we did not have adequate data to include these effects. We found the value of 0.0126 g Chl g C^{-1} representative of the mixed phytoplankton (diatom and non-diatom) communities sampled within our study region and across cruises. This value is also within the range of documented Chl:C for waters with various nutrient concentrations, depths, and community compositions. Li et al. (2010) reported minimum and maximum Chl:C of 0.005 g Chl g C^{-1} and 0.052 g Chl g C^{-1}, respectively, in this region. While we present the MPC as a function of salinity and NO_3, micronutrient limitation, light limitation, and grazing could all reduce the MPC. For instance, the MOC is often reduced with increasing depth (decreasing light) levels (Supplemental Figure 3.5). Because these processes often co-occur and exhibit nonlinear relationships with depth and salinity (Supplemental Figure 3.6), it is difficult to disentangle these mechanisms when defining the MPC. Thus, we present a simple form for the MPC based on a constant Chl:C. Future studies with more high-resolution growth, grazing, nutrient concentration, and light data could include parameterizations of Chl:C in the MPC.

3.4.5 Salinity is an indicator of phytoplankton community structure

Many studies have noted correlations of phytoplankton community composition with total Chl. Large phytoplankton, such as diatoms, usually dominate high-Chl communities; small phytoplankton, such as cyanobacteria, tend to dominate low-Chl communities (Cermeño et al., 2005; Chisholm, 1992; Goericke, 2011a, 2011b; Marañón et al., 2007). Our data was consistent with this well-known pattern, but we also showed that changes in community structure were also correlated with salinity (Figure 3.3).

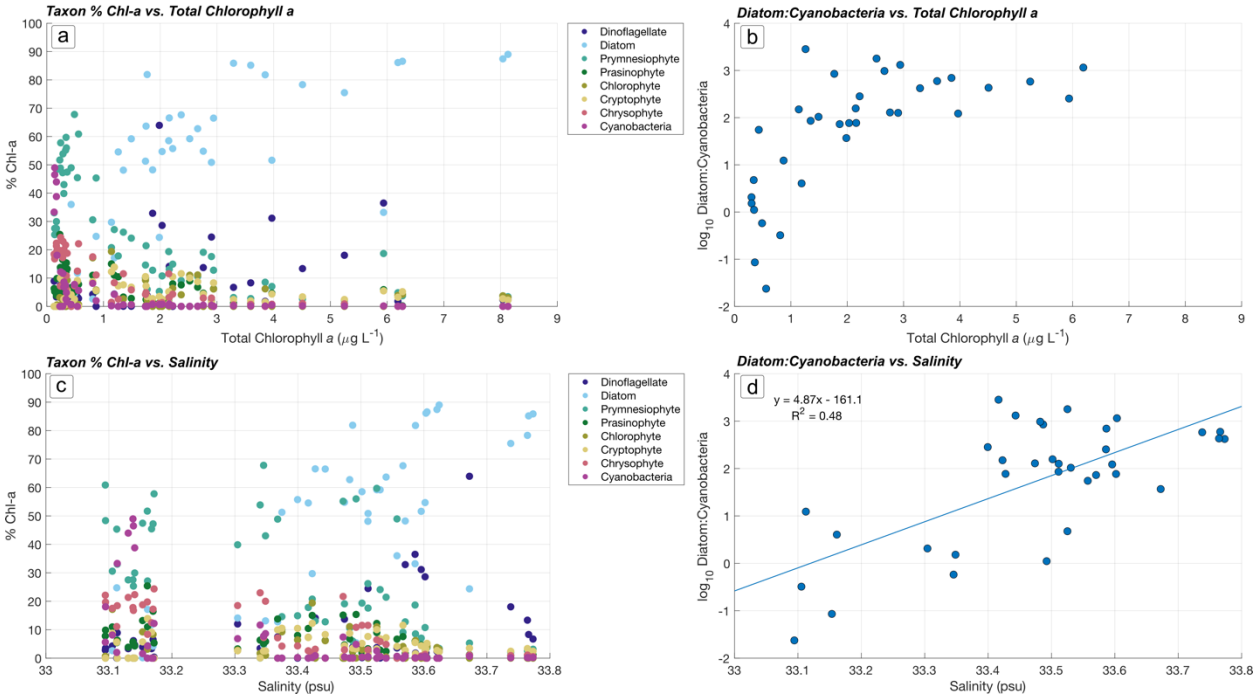

Figure 3.3: Phytoplankton size and community structure relationships with total Chl-a (in µg L^{-1}), summed for the 8 taxa represented here (dinoflagellates, diatoms, prymnesiophytes, prasinophytes, chlorophytes, cryptophytes, chrysophytes, and cyanobacteria), and salinity. The proportion (%) of the summed total Chl-a of each phytoplankton taxon (colored markers in panels a and c) indicate the dominance of diatoms in high-chlorophyll and high-salinity waters (a, c). The $\log_{10}$ of the diatom:cyanobacteria ratios show a positive relationship with increasing total chlorophyll (b) and increasing salinity ($R^2 = 0.48$ for linear fit) (d).

We found that waters with high Chl, salinity, and initial NO_3 concentrations supported a higher proportion of large phytoplankton than waters with relatively low Chl, salinity, and initial

NO_3 concentrations (Figure 3.3). The fraction of total Chl in diatoms increased with total Chl, while the fraction of Chl in prymnesiophytes (2–20 μm size range) and cyanobacteria decreased with total Chl (Figure 3.3). Consistent with the trend of increasing MPC with increasing salinity, diatoms dominated waters in the 33.4–33.8 psu high-salinity range, while cyanobacteria and prymnesiophytes dominated in the 33.1–33.2 psu low-salinity range. These patterns in phytoplankton community composition provide further evidence that, because of its relationship with sub-euphotic zone nitrate concentrations, salinity can serve as a diagnostic of phytoplankton community structure in this region.

3.4.6 Departures of observed chlorophyll values from the MPC

Given our definition of the MPC as the *maximum* Chl concentration potentially achieved by a water parcel given its NO_3^{median} concentration, statistically we would expect to find values below the MPC. Indeed, most (99%) of the observed Chl concentrations were below the MPC (Figure 3.2), and for the combined cruise data we found significant departures of the MOC from the MPC, particularly at low salinities (33.0–33.2 psu) and high salinities (> 33.5 psu).

We determined that the timing of phytoplankton bloom dynamics as well as micronutrient and light limitation were likely significant mechanisms driving the departures of MOC and other observed Chl values, from the MPC. For instance, the temporal lag in phytoplankton growth can lead to waters being sampled pre-bloom, before Chl concentrations reached their maximum, giving Chl values below the MPC. Grazing by zooplankton, sinking, or mortality, such as through viral lysis (Kolody et al., 2019), could also reduce Chl concentrations relative to their predicted MPC. In addition, iron (Fe) limitation in the CCS is known to result in waters with reduced phytoplankton biomass despite high nitrate concentrations (Bruland et al., 2005; Hogle et al., 2018; Hutchins et al., 1998; King & Barbeau, 2011). Light availability also

limits or co-limits phytoplankton biomass, particularly below the euphotic zone (Johnson et al., 2010).

Here, we tested the influence of these processes in driving departures from the MPC (Figure 3.4). We used Si_{ex} to diagnose Fe-limited conditions, when diatoms preferentially take up H_4SiO_4 over NO_3, resulting in waters with negative Si_{ex} values. We estimated the effect of light limitation through the decrease in light availability with increasing depth. Furthermore, when departures of observed Chl from the MPC could not be explained by Si_{ex} or depth, we used measured (residual) NO_3 concentrations to estimate phytoplankton bloom stage. We assumed that low residual NO_3 indicated peak- or post-bloom conditions when phytoplankton had taken up most of the available NO_3. In contrast, we assumed that high residual NO_3 indicated pre-bloom conditions when phytoplankton had not yet depleted the NO_3. Because these processes can co-occur, these diagnostics serve as potential—not definitive—explanations for the observed Chl patterns.

The striking departure of the MOC from the MPC at salinities > 33.5 psu (Figure 3.2) likely resulted from Fe-limitation dynamics within the Morro Bay filament, sampled by P1706 (Figure 3.4a,c,e), and phytoplankton communities caught pre-bloom or during-bloom within the Pt. Sur filament, sampled by P1908 (Figure 3.4b,d,f). The high-salinity waters in P1706, with Chl concentrations approaching the MOC but not MPC, exhibited strongly negative Si_{ex} values, indicating an Fe-limited diatom community (Figure 3.3c). This conclusion is supported by the Fe grow-out incubation experiments conducted by Forsch et al. (2023), which demonstrated strong Fe-limitation within the Morro Bay filament. These findings suggest that, if supplied with additional dissolved Fe, these waters may have reached even higher Chl concentrations—perhaps taking up the remaining NO_3 and meeting the MPC. The high-salinity waters of P1908, with Chl

concentrations near the MOC, also exhibited high (> 4 μM) residual NO_3 concentrations (Figure 3.4b), indicating that phytoplankton in these waters were pre-bloom or actively blooming, with sufficient NO_3 available to continue growing. These Pt. Sur filament waters were likely upwelled from a source depth or water mass with high preformed NO_3—and likely high dissolved Fe concentrations (Forsch et al., 2023). Another significant departure of the MOC from the MPC occurred at low salinities (33.0–33.2 psu). However, in this case, Chl concentrations exceeded the MPC (Figure 3.2). These waters were sampled by the P1706 SeaSoar survey; therefore, we did not have nutrient measurements aligned with these samples. We hypothesize, however, that local nutrient injections along the water-parcels' trajectories could have led to this elevated Chl signal. For example, at (sub)mesoscale density fronts, which are often associated with filaments and eddies in this region (Taylor et al., 2012; Zaba et al., 2021), enhanced vertical mixing generates upward nitrate fluxes, leading to elevated phytoplankton biomass (Levy et al., 2018; Li et al., 2012; Mahadevan, 2016).

Finally, all other waters—other than those that met the MPC directly—had observed Chl concentrations below the MPC. Some of these waters, such as those with salinities of 33.0–33.2 psu for P1706 and 33.2–33.6 psu for P1908 (Figure 3.4), were probably captured post-bloom and had experienced significant grazing, sinking, and (or) mortality, resulting in both low NO_3 and Chl concentrations. Notably, some of these low-salinity waters in P1706 were found below 50 m depth (Figure 3.4e) and with very positive Si_{ex} values (Figure 3.4c), supporting the notion that these waters may have had very low initial NO_3 and a high Si:N, which is characteristic of offshore-originating oligotrophic waters that would not have supported a diatom bloom (Bograd et al., 2015; Brzezinski et al., 2015). In contrast, the low-NO_3 and low-chlorophyll waters of

P1908 exhibited weakly negative Si_{ex} values (Figure 3.4d), indicating some degree of Fe-limitation that limited phytoplankton biomass.

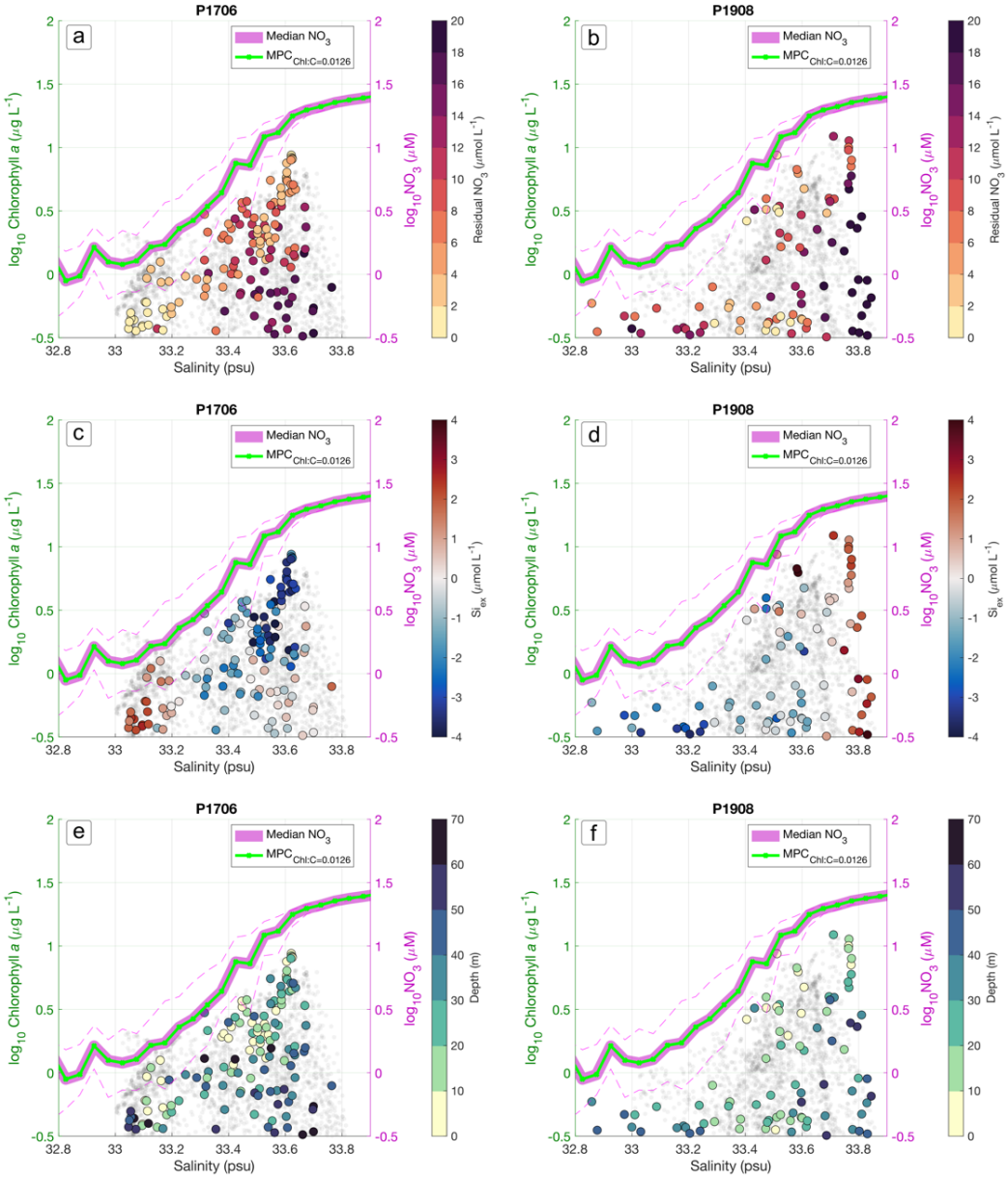

Figure 3.4: Waters sampled in the cross-filament CTD-rosette transects (colored markers) and SeaSoar surveys (gray circles in background) for P1706 (left column) and P1908 (right column). Markers were colored by (a, b) residual (in situ) NO_3 concentrations, (c, d) the iron-limitation diagnostic Si_{ex} (blue for negative Si_{ex}, red for positive Si_{ex}), and (e, f) depth. The MPC (light green line) is derived from the climatological median NO_3 (solid magenta line) and Chl:C = 0.0126 g Chl g C^{-1} (as in Figure 3.2). The 35th and 65th percentiles of NO_3 are shown (dashed magenta lines).

At high salinities in both cruises (salinity >33.4 psu for P1706 and >33.6 psu for P1908) and low salinities (32.8–33.2 psu) particularly in P1908 (Figure 3.4), we also detected waters that were consistent with a pre-bloom stage: relatively high residual NO_3 (> 4 μM). Some of these high-salinity filament waters were deeper, and likely light limited (Figure 3.4e–f). In contrast, the low-salinity, high-NO_3 waters in P1908 were sampled at depths < 50 m but exhibited negative Si_{ex} values, indicating that both light and low Fe availability may have limited diatom growth, locally depressing the MOC.

3.5 Conclusion

We showed that, through its relationship with nitrate, salinity is a robust diagnostic of MOC, MPC, and phytoplankton community structure in this region—and potentially other EBUSs. Our theoretical framework thus allows us to estimate the maximum chlorophyll concentration we would expect to find in a water parcel based solely on a measurement of its salinity. Departures of observed Chl values from the MPC can be explained through the timing of phytoplankton bloom dynamics, and regulation by micronutrient and light availability. Iron limitation, particularly within high-salinity waters, played a significant role in depressing the MOC relative to the MPC, while light limitation and pre- or post-bloom phytoplankton communities resulted in Chl concentrations below the MPC and MOC. Using salinity to quantify the MOC and how it varies in space and time relative to the MPC, will improve our ability to predict the locations and magnitudes of ecological hot spots, feeding grounds, and sites of organic carbon transport (Chenillat et al., 2016; Fiechter et al., 2020; Messié et al., 2022; Stukel et al., 2017). We encourage applying this salinity-MPC framework (Figure 3.5) as a method of synthesizing nutrient data, phytoplankton growth and grazing rates, and size-dependent plankton community dynamics —or for use when such measurements are lacking. Our work motivates long-term hydrographic and biogeochemical sampling to elucidate ecological patterns that are

intrinsically linked to—and often diagnosable by—easily measured water-mass properties such as salinity.

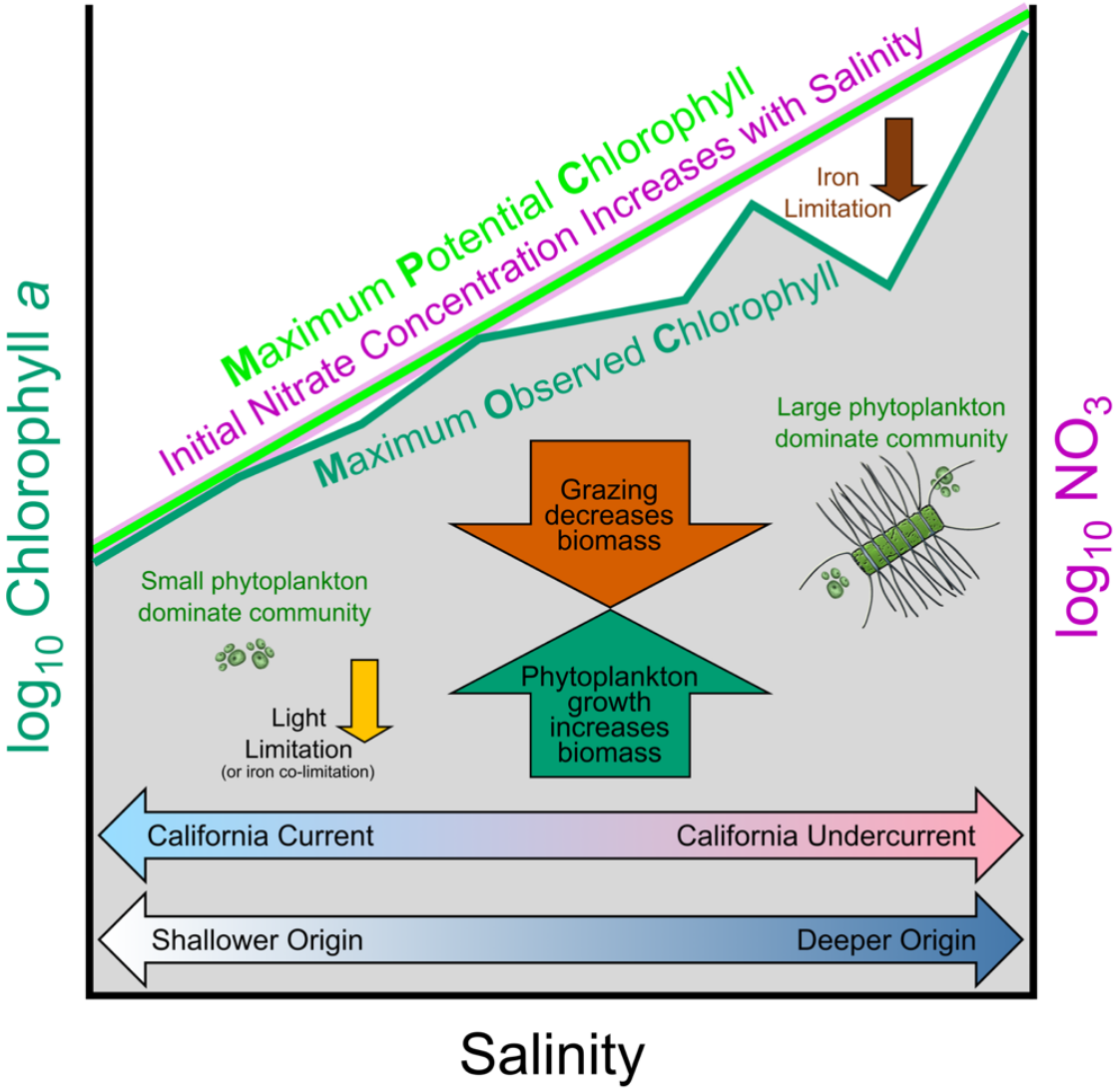

Figure 3.5: Conceptual diagram illustrating the relationships between salinity, chlorophyll *a*, initial nitrate, light, and dissolved iron availability in the California Current System. These relationships drive and set the maximum observed chlorophyll (MOC) and maximum potential chlorophyll (MPC) boundaries, which show positive linear slopes on salinity-$\log_{10}$(Chl) axes. Upwelling origin depth and source water masses result in salinity variability in the upper 100 m. Phytoplankton growth increases Chl, and higher Chl communities contain a higher fraction of larger phytoplankton (e.g., diatoms). Initial nitrate concentrations, defined as the nitrate concentration in waters upwelled into the euphotic zone, also increases with salinity, allowing for a greater maximum Chl (MOC and MPC) in high-salinity waters than low-salinity waters. Chl concentrations can be decreased by grazing, and iron and light limitation can result in Chl values below the MPC. Illustration (icons): Freya Hammar.

Data Availability

Data are available in the Environmental Data Initiative repository at https://doi.org/10.6073/pasta/1534db121199a8c66ba3e9db85f3deb1.

Acknowledgments

The authors acknowledge CCE LTER, CalCOFI, Mark Ohman, Michael Stukel, Michael Landry, Ralf Goericke, Carl Mattson, Shonna Dovel, Mati Kahru, and Katherine Zaba for assisting with data collection and processing. The authors also thank the captain and crew on the CCE LTER P1706 and P1908 cruises. CCE LTER was supported by NSF Award OCE-1637632 and OCE-2224726. S. Gangrade and K. O. Forsch were supported by the NSF Graduate Research Fellowship and Scripps Institution of Oceanography, and K. O. Forsch was supported by the NSF Postdoctoral Fellowship (OCE-2126562).

Chapter 3, in full, has been submitted for publication of the material as it may appear in *Limnology & Oceanography Letters*, 2024. Gangrade, Shailja; Franks, Peter J. S.; Forsch, Kiefer O.; Barbeau, Katherine A., 2024. The dissertation author was the primary researcher and author of this material.

Supplemental Information

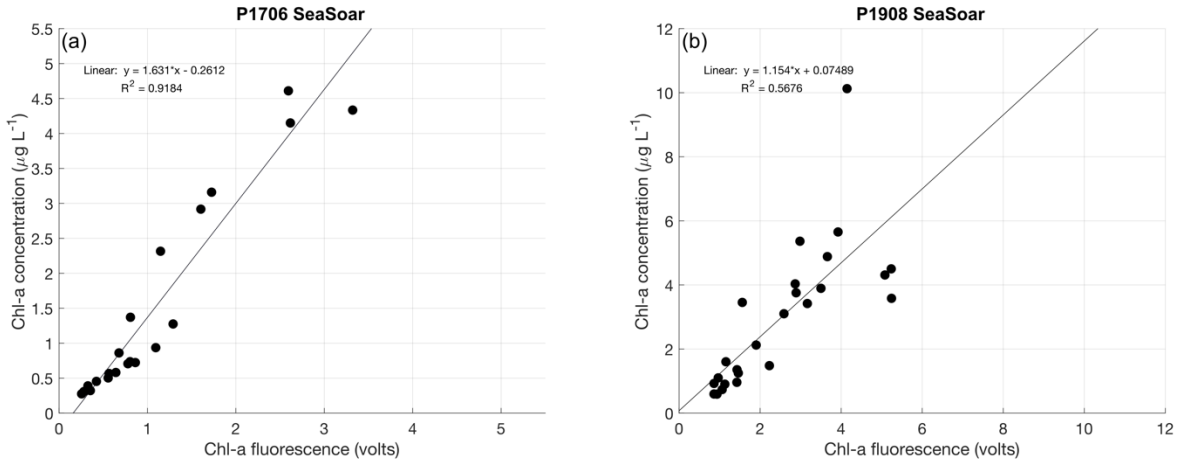

Supplemental Figure 3.1: The linear relationship between *in vivo* Chl fluorescence for near-surface SeaSoar profile data and the concurrent Chl concentrations from the near-surface seawater intake system, obtained from filtration, for (a) P1706 SeaSoar Survey 1 and (b) P1908 SeaSoar Survey 1. Linear regressions, which indicate significant positive correlations, were used to calibrate all SeaSoar survey samples within each cruise.

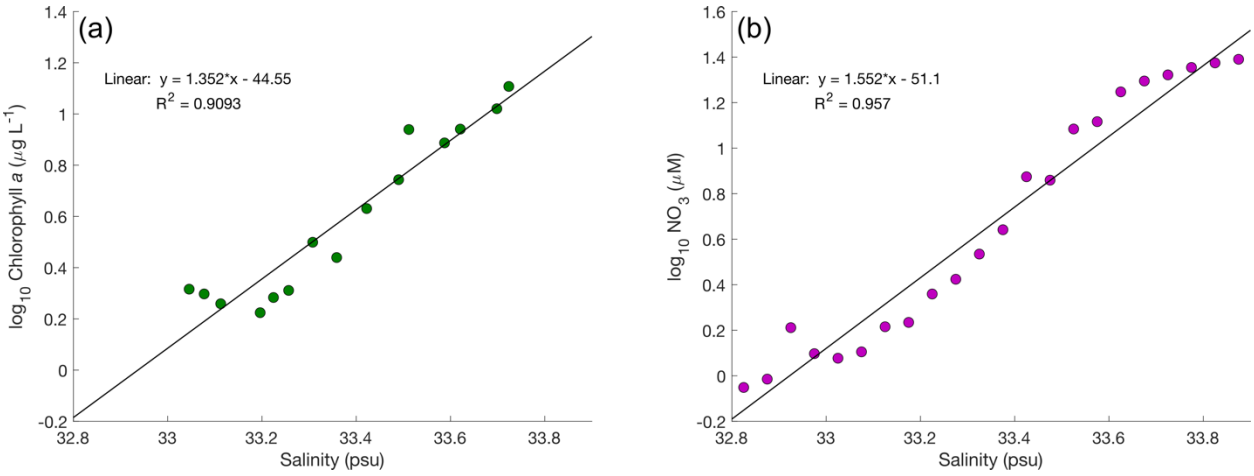

Supplemental Figure 3.2: Linear regression relationships (equations and R^2) for the (a) salinity-MOC and (b) salinity-NO_3^{median} relationships. These positive correlations indicate a significant relationship between salinity and Chl that is driven by the relationship between salinity and NO_3.

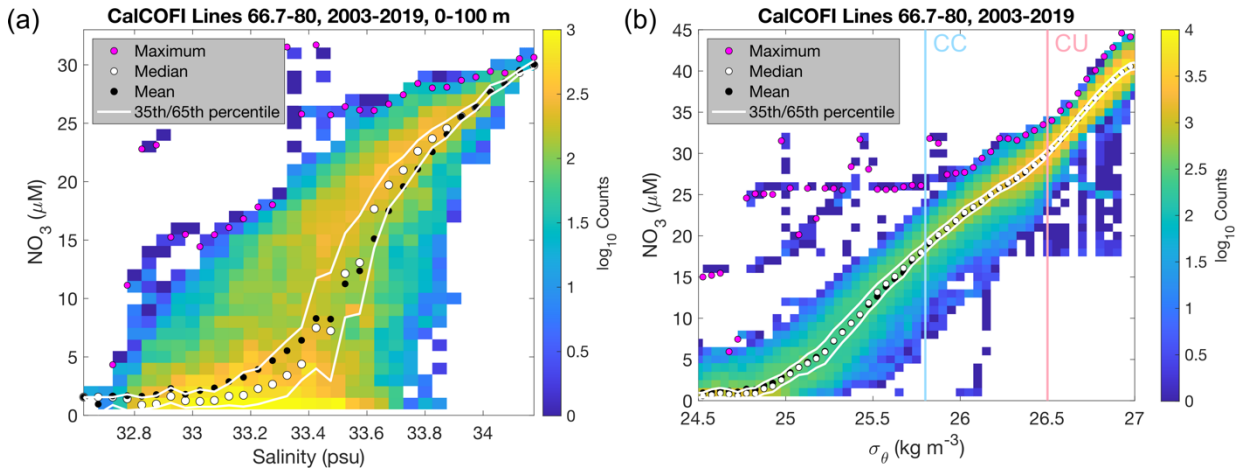

Supplemental Figure 3.3: Two-dimensional histograms (heatmaps) indicating the positive relationship between nitrate and salinity (a), and nitrate and density (σ_θ) (b). The maximum, median, and mean nitrate values within each 0.05 psu salinity bin and 0.05 kg m^{-3} σ_θ bin are highlighted in magenta, white, and red markers respectively. The blue and pink vertical lines in (b) indicate that mean NO_3 at σ_θ= 25.8 kg m^{-3} is greater than mean NO_3 at σ_θ= 26.5 kg m^{-3}. These density surfaces are representative of the California Current (CC) and California Undercurrent (CU) water masses, respectively, as described in Bograd et al. (2015).

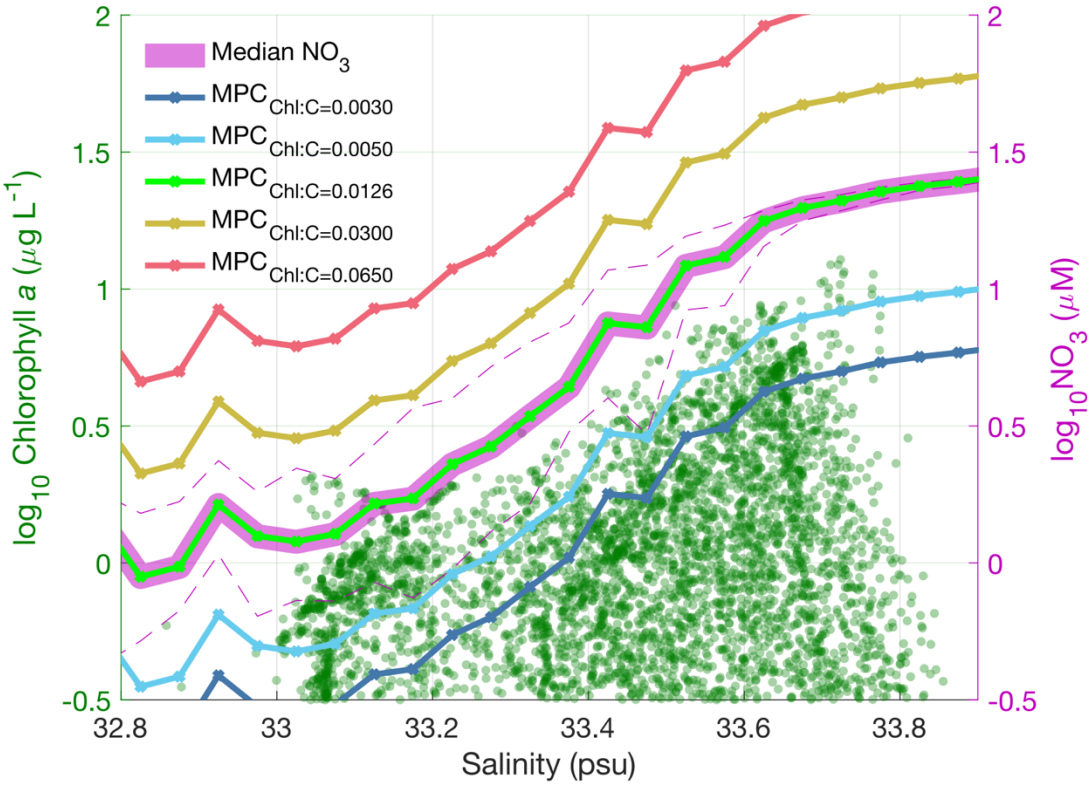

Supplemental Figure 3.4: The relationship between salinity versus $\log_{10}$(Chl) for waters sampled during both P1706 and P1908 SeaSoar surveys and transects (dark green circles). The $\log_{10}$ of the NO_3^{median} (solid magenta line) and the 35th and 65th percentiles of NO_3 in each 0.05-psu salinity bin (dashed magenta lines) demonstrate a positive relationship between salinity and NO_3. The various colored lines indicate different maximum potential chlorophyll values given NO_3^{median} concentrations and different Chl:C (dark blue for Chl:C = 0.003 g Chl g C^{-1}, light blue for Chl:C = 0.005 g Chl g C^{-1}, light green for Chl:C = 0.0126 g Chl g C^{-1}, yellow for Chl:C = 0.05 g Chl g C^{-1}, red for Chl:C = 0.065 g Chl g C^{-1}). These Chl:C values represent a range of observed Chl:C for non-diatom and diatom communities (Li et al., 2010).

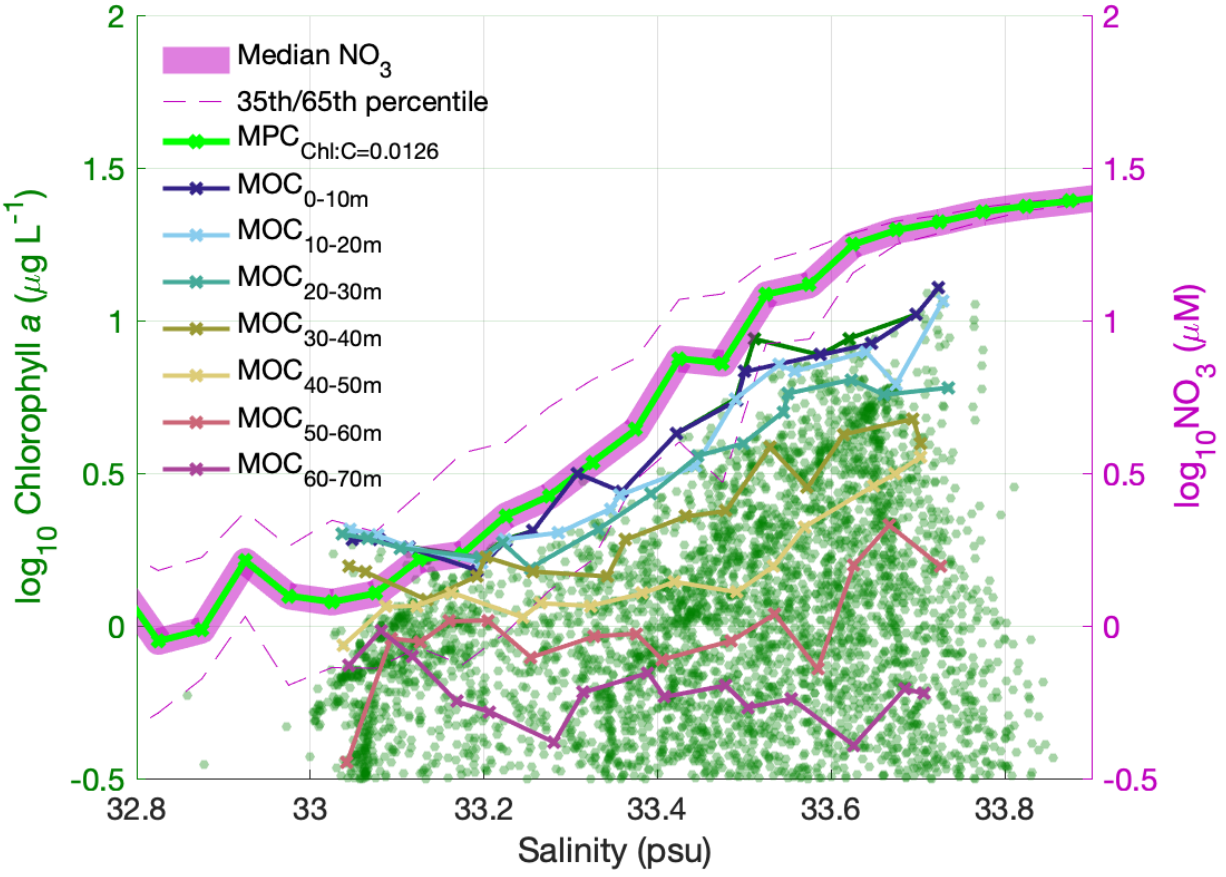

Supplemental Figure 3.5: The relationship between salinity versus $\log_{10}$(Chl) for waters sampled during the P1706 and P1908 surveys (dark green circles), with the MPC derived from $\log_{10}(NO_3^{median})$ (solid magenta line) and a Chl:C = 0.0126 g Chl g C^{-1} shown as a thick light green line. The 35th and 65th percentiles of NO_3 in each 0.05-psu salinity bin are shown as dashed magenta lines. The various colored lines indicate different maximum observed chlorophyll (MOC) values for specific 10-m depth bins (from 0 to 70 m).

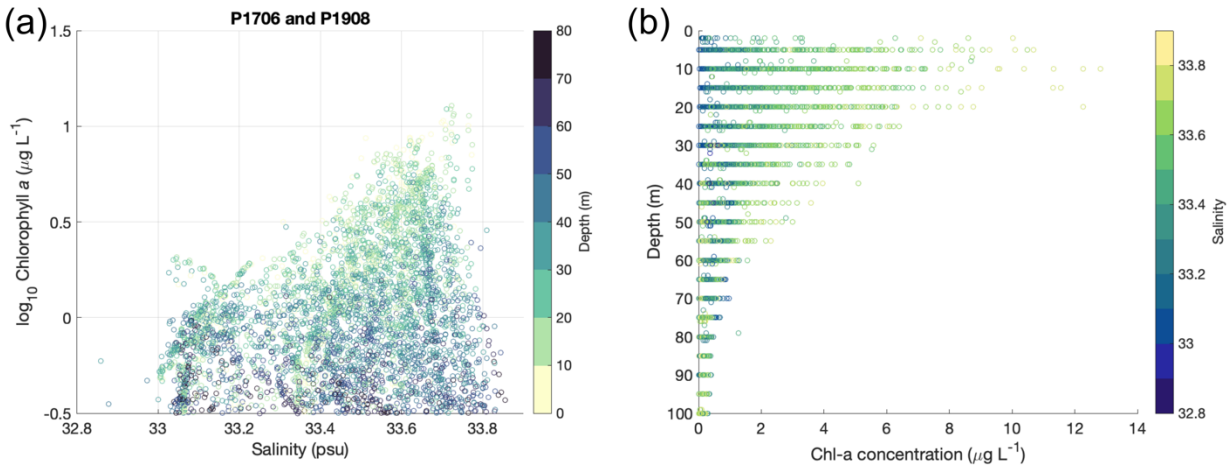

Supplemental Figure 3.6: (a) The $\log_{10}$(Chl) versus salinity relationship for waters sampled during the P1706 and P1908 surveys, colored by the depth of the sample. (b) The relationship between depth and Chl concentration for the same observations, colored by salinity.

Chapter 4: A salinity-age framework for describing variability in phytoplankton community structure and photophysiology within coastal upwelling filaments

4.1 Abstract

Coastal upwelling filaments in the California Current System transport biologically productive waters away from the coast into oligotrophic offshore regions. Previous studies have shown that the distribution of planktonic communities in these filaments is patchy—often in association with water-mass properties such as salinity. However, we lack a detailed understanding of the controls on biological patchiness across and along upwelling filaments. Because these filaments play a significant role in structuring cross-shore gradients in phytoplankton production and carbon export, we seek to characterize hydrographic and biogeochemical patchiness of waters associated with upwelling filaments—and the controls on this patchiness. Here, we use in situ and satellite observations of two coastal upwelling filaments sampled off the California coast. We analyze how phytoplankton community structure, photophysiology, and chlorophyll *a* (Chl-a) varied with water-mass type, nutrient concentration, and water-parcel age predicted from particle backtracking. We demonstrate that across-filament phytoplankton patchiness resulted from the convergence of disparate water-mass types that had different initial nitrate conditions and thus supported distinct phytoplankton communities. We also show that variability in phytoplankton communities along the filaments was consistent with upstream, source-water nutrient fluctuations and along-trajectory growth-grazing processes, which sometimes involved the development of iron limitation. We use a salinity-age framework to describe how such Lagrangian, along-trajectory changes in phytoplankton communities might also result in conditions associated with carbon export (declining Chl-a and photochemical efficiency). Our findings emphasize that filaments are fundamentally non-uniform, and we

provide a replicable pseudo-Lagrangian strategy to diagnose critical ecological patterns in this dynamic region.

4.2 Introduction

The California Current System (CCS), an Eastern Boundary Upwelling System, has a strong cross-shore gradient in biological productivity (Giddings et al., 2022; Gruber et al., 2006). At the coast, upwelling driven by equatorward winds delivers cold, nutrient-rich waters to the sunlit euphotic layer. These upwelled waters stimulate new production of phytoplankton, fueling production of higher trophic levels, such as fishes, seabirds, and marine mammals (Checkley & Barth, 2009; Huyer, 1983; Rykaczewski & Checkley, 2008). The major water-mass features in this system include the equatorward-flowing California Current, which transports low-salinity and nutrient-poor waters from subarctic origins, and the poleward-flowing California Undercurrent, which—found more inshore—transports high-salinity and nutrient-rich waters northward from subtropical origins (Bograd et al., 2015; Bograd et al., 2019; Lynn & Simpson, 1987).

Broad shifts in ecosystem dynamics are found across shore in the CCS: in the offshore, new production and export production are balanced, but in nearshore regions (> 300 km from the coast), export production exceeds new production (Chabert et al., 2021; Plattner et al., 2005; Stukel et al., 2011). Horizontal stirring features, such as eddies and filaments, that circulate waters away from the coast are hypothesized to mediate this spatial decoupling between new and export production (Nagai et al., 2015; Rossi et al., 2009). Mesoscale upwelling filaments, which intermittently develop in the summertime (May to August), typically around coastal headlands (Abbott & Barksdale, 1991), are particularly important in carrying upwelled waters with high nutrient and biomass concentrations offshore (Abbott et al., 1990; Hood et al., 1991; Strub et al., 1991).

Previous studies have found that the structure and distribution of phytoplankton communities transported within upwelling filaments are not homogeneous. In these filaments, phytoplankton concentrations often vary with water-mass properties, such as temperature and salinity, which are also nonuniform along and across a filament (Zaba et al., 2021). Furthermore, the composition of macro- and micro-nutrients are heterogeneous within and across different filaments, controlling gradients in phytoplankton biomass and community structure (Forsch et al., 2023). Filaments can also act as boundaries between distinct phytoplankton communities, typically separating coastal communities dominated by diatoms in the filament from oceanic communities outside the filament that are dominated by small phytoplankton (e.g., cyanobacteria, coccolithophores, and small flagellates) (Chavez et al., 1991; Taylor & Landry, 2018).

In this region, variability in phytoplankton photophysiology, often measured using the ratio of variable fluorescence to maximal fluorescence (F_v/F_m) has also been linked to gradients in phytoplankton biomass and community structure (Chekalyuk et al., 2012). Large phytoplankton, such as diatoms, are known to exhibit greater values of F_v/F_m compared to small phytoplankton, such as cyanobacteria (Suggett et al., 2009), which contain phycobiliproteins that result in reduced variable fluorescence (Campbell et al., 1998). Decreases in F_v/F_m are also sometimes indicative of iron-limited phytoplankton communities (Falkowski et al., 2004; Greene et al., 1992), which have been detected in upwelling filaments (Forsch et al., 2023) and potentially play a significant role in organic matter export from the euphotic zone (Brzezinski et al., 2015). The “disappearance” of phytoplankton communities along filaments, which has been linked to subduction (Washburn et al., 1991) and export (Abbott et al., 1990), also has potentially critical impacts on offshore ecosystems.

Previous studies have attributed much of the patchiness in the distribution and structure of planktonic communities within filaments to variability in mesoscale circulation and upstream source waters (Chavez et al., 1991; Gangrade & Franks, 2023; Keister et al., 2009). The use of Lagrangian sampling and analysis techniques has also shown that water parcels carry distinct planktonic communities that undergo transformations as they are stirred; thus upstream and along-trajectory dynamics must be considered when characterizing ecosystem patchiness (d'Ovidio et al., 2010; Gangrade & Mangolte, 2024). This is particularly important when considering transit times of water parcels along filaments relative to the timescales for major biological changes (i.e., growth, grazing, community shifts).

Here, we investigate patchiness in planktonic communities within two upwelling filaments, for which the drivers of across- and along-filament variability have not yet been fully characterized. We assess variability in hydrographic and biogeochemical properties, including phytoplankton community structure, photophysiology and chlorophyll *a* (Chl-a), associated with these two filaments, which were sampled off the coast of Morro Bay and Point Sur, California during 2017 and 2019, respectively. Using Lagrangian backtracking, we also predicted the ages of water parcels in and around these filaments, identifying the time elapsed between their origins at the coast and their sampling. We find that these filaments contributed to offshore transport of organic material (e.g. phytoplankton and particulate organic carbon), but these contributions were patchy in space and intermittent in time. We demonstrate that across-filament patchiness in phytoplankton community structure, photophysiology, and Chl-a resulted from the horizontal convergence of California Current and California Undercurrent water masses—distinguished by salinity (a conservative water-mass tracer)—that had different initial nitrate concentrations and thus supported distinct phytoplankton communities. We also show that patterns in variability in

phytoplankton communities along the filaments were consistent with upstream nutrient fluctuations and along-trajectory development mediated by growth and grazing. In some cases, our observations of reduced phytoplankton photochemical efficiency were consistent with the time- and source-dependent dynamics of iron limitation. To synthesize our view of upstream water-mass and along-trajectory controls on patchiness, we present a salinity-age framework, which we used to analyze how phytoplankton communities change as they age along the filaments (i.e. along their trajectories). We describe along-trajectory changes in Chl-a and F_v/F_m and show how these changes vary based on their initial condition—the salinity of a water parcel when it is upwelling into the euphotic zone. Finally, we discuss the potential role of high-salinity, nutrient-rich waters in contributing to carbon export in this region. From these analyses, we elucidate the fundamental controls on ecological patterns in this region, identifying the mediation of biological patchiness by water masses that experience upstream fluctuations and along-trajectory processes as they are transported within dynamic mesoscale filaments.

4.3 Materials and methods

Hydrographic and biogeochemical measurements were collected during two different California Current Ecosystem Long-Term Ecological Research (CCE LTER) process cruises: P1706 (June 1–July 2, 2017) and P1908 (August 5–September 6, 2019). The P1706 cruise sampled the California coastal region during the occurrence of an upwelling filament offshore of Morro Bay, California (the "Morro Bay filament"). The P1908 cruise sampled the California coastal region during the occurrence of an upwelling filament offshore of Point Sur, California (the "Pt. Sur filament"). These filaments were found to transport coastal waters offshore (away from the coast) throughout the duration of each cruise, with the flow of the Morro Bay filament extending westward and the flow of the Pt. Sur filament extending southwestward (Forsch et al., 2023).

4.3.1 Underway measurements

For the duration of each cruise, underway samples of near-surface seawater were analyzed for temperature, salinity, and Chl-a fluorescence. Meteorological data from the ship also provided photosynthetically active radiation (PAR). Underway Chl-a samples were taken on the ship, filtered onto GF/F filters, extracted with 90% acetone for 24 hours, then quantified using a calibrated Turner Designs fluorometer before and after acidification (Lorenzen, 1967). Underway measurements of meridional and zonal current velocities were made by a shipboard 75 kHz Acoustic Doppler Current Profiler (ADCP) every 15 minutes during the entirety of each cruise. These velocity data were averaged into 5-km horizontal and 16-m vertical bins; zonal velocities were rotated to the direction perpendicular to the SeaSoar survey sections.

4.3.1.1 Phytoplankton fluorescence and photochemical efficiency

From continuous underway measurements of surface waters by an Advanced Laser Fluorometer (ALF) (Chekalyuk & Hafez, 2008), we obtained fluorescence of three different spectral types of phycoerythrin (PE) and phytoplankton $F_v/F_{m.}$ The ALF provided a spectral deconvolution analysis of laser-stimulated emission excited at 405 nm and 510/532 nm (Chekalyuk et al., 2012). Type 1 phycoerythrin (PE1) is indicative of blue-water, offshore cyanobacteria (*Synechococcus*) (Wood et al., 1985); type 2 phycoerythrin (PE2) is indicative of green-water, coastal cyanobacteria (*Synechococcus*) (Wood et al., 1985); type 3 phycoerythrin (PE3) is indicative of cryptophytes, which are often abundant in coastal environments (Cowles et al., 1993; Exton et al., 1983; Sciandra et al., 2000). Measurements of F_v/F_m, were made actively using pump-during-probe measurements of Chl-a fluorescence induction and were corrected for background fluorescence (Chekalyuk & Hafez, 2008). These corrected F_v/F_m values represented the maximum quantum yield of photosystem II (PSII) and thus bulk phytoplankton photochemical efficiency.

4.3.2 SeaSoar surveys

From a towed SeaSoar vehicle, equipped with a conductivity-temperature-depth (CTD) sensor, beam transmissometer (WET Labs C-Star), and fluorometer (Seapoint), we obtained measurements of salinity, temperature, depth, beam attenuation coefficient from transmission, and Chl-a fluorescence. The SeaSoar undulated between the surface and approximately 250 m depth during three to four consecutive alongshore transects during each cruise (Figure 4.1). We multiplied transmissometer-derived beam attenuation coefficients (m^{-1}) by a conversion factor of 27 μM m^{-1} to calculate particulate organic carbon (POC) concentrations (μM) (Bishop & Wood, 2008).

Across-track geostrophic velocities along the SeaSoar sections were calculated from dynamic height anomaly and referenced at 250 dbar using underway ADCP velocities (Comas-Rodríguez et al., 2010). We obtained Chl-a concentrations during the SeaSoar surveys by calibrating Chl-a fluorescence measurements using night-only underway surface samples that were extracted and fluorometrically analyzed on the ship. Because the SeaSoar was not equipped with a nitrate (NO_3) sensor, we derived dissolved inorganic NO_3 concentrations from CTD measurements of in situ temperature using a relationship (Lilly et al., 2019) calculated from regional climatological data (Supplemental Figure 4.1). All climatological data used for assessing NO_3 relationships (e.g., with temperature and salinity) were obtained from California Cooperative Oceanic Fisheries Investigations (CalCOFI) CTD casts from 2003 to 2019 at CalCOFI Lines 66.7 through 90, which span the coastal region Monterey Bay to from Point Conception, California.

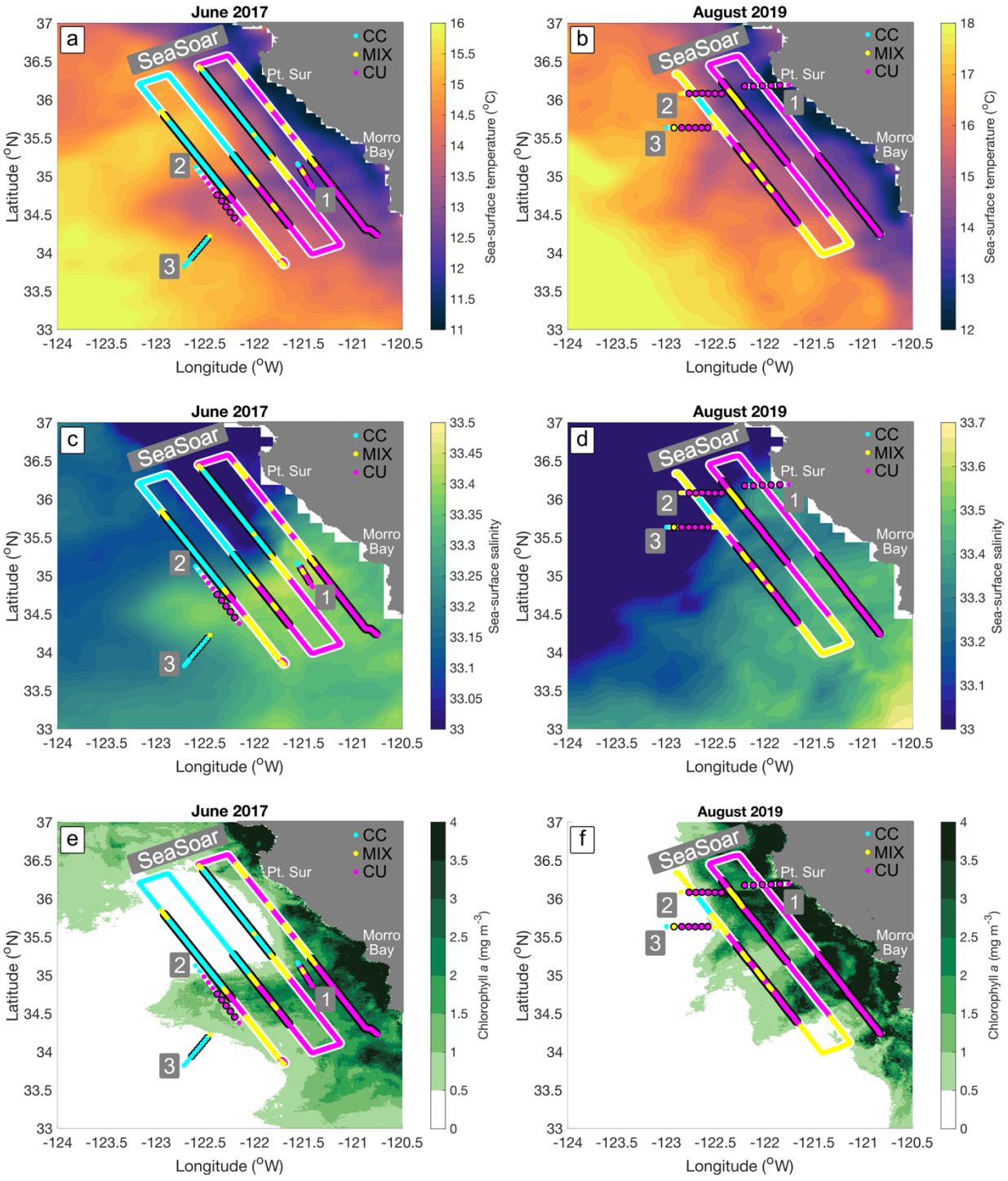

Figure 4.1: Maps of sea-surface temperature (a–b), salinity (c–d), and Chl-a (e–f) during the CCE LTER P1706 (Morro Bay filament cruise; left column) and P1908 (Pt. Sur filament cruise; right column), showing sampling locations during SeaSoar Survey 1 and three CTD-rosette transects during each cruise. Markers are colored by surface water-mass types (cyan for California Current [CC]; magenta for California Undercurrent [CU]; yellow for Mixed [MIX]) and are outlined in black if sampled during nighttime (21:00–06:00 PDT).

All SeaSoar depth profile data were then objectively mapped as in Zaba et al. (2021): we assumed a Gaussian covariance with a horizontal decorrelation length scale of 15 km and noise-to-signal ratio of 0.1. This resulted in maps with 5 km along track and 5 m vertical resolution of cross-track velocities, salinity, temperature, Chl-a, POC, and NO_3. We only used points with normalized mean squared error less than 0.3.

4.3.3 CTD-rosette transects

We obtained hydrographic, nutrient, and phytoplankton community structure data from six CTD-rosette transects (3 per cruise) with 3–8 km horizontal resolution between discrete stations (Figure 4.1). From the CTD downcasts, we obtained measurements of Chl-a fluorescence, temperature, salinity, and depth with 1 m vertical resolution down to 300 m. From bottle samples at discrete depths (approximately every 10 m from the surface to 100 m), we measured Chl-a concentrations through shipboard extraction and fluorometric analysis, as well as NO_3 and silicic acid (H_4SiO_4) concentrations, which were analyzed using a colorimetric assay (Armstrong et al., 1967).

4.3.3.1 Si_{ex} calculation

Using the NO_3 and silicic acid concentrations, we calculated Si_{ex}, a tracer equal to $[H_4SiO_4] - [NO_3] \times R_{Si:N}$ where $R_{Si:N}$ is the $[H_4SiO_4]/[NO_3]$ of upwelled water. $R_{Si:N}$ is approximately equal to 1 in the CCE region (Hogle et al., 2018; King & Barbeau, 2011; Stukel et al., 2017; Stukel & Barbeau, 2020). Si_{ex} is used as a diagnostic for iron (Fe) limitation when silicifying organisms, such as diatoms, are present. Values of $Si_{ex} > 0$ are indicative of Fe-replete conditions, and values of $Si_{ex} < 0$ are indicative of Fe-limited conditions.

4.3.3.2 Phytoplankton taxon-specific pigment analysis

Samples from surface rosette bottles were concentrated on GF/F filters and stored in liquid nitrogen during the cruise. Pigments were later extracted in acetone and analyzed by

reverse-phase high performance liquid chromatography (HPLC). Using the software CHEMTAX v1.95, we analyzed taxon-specific pigments to obtain phytoplankton community structure. This provided the proportion of total Chl-a attributed to the following phytoplankton taxa: dinoflagellates, diatoms, prymnesiophytes, prasinophytes, chlorophytes, cryptophytes, chrysophytes, and cyanobacteria (González-Silvera et al., 2020).

4.3.4 Eliminating non-photochemical quenching effects

Chl-a fluorescence, phycoerythrin fluorescence, and F_v/F_m show diel periodicity, with reduced values during daylight hours (Supplemental Figure 4.2) caused by non-photochemical quenching (NPQ) (Krause & Weis, 1991; Schuback et al., 2021). To eliminate this effect, we used only nighttime measurements (21:00 to 06:00 PDT) of all fluorescence variables in our analyses. This approach was warranted due to the strong nonlinear and asymmetric effects of NPQ on phytoplankton photophysiology and our inability to know whether sampled waters had similar phytoplankton communities within and across surveys.

4.3.5 Satellite-derived measurements

We obtained 1-km, daily sea-surface Chl-a data from a merged satellite ocean data product (Kahru et al., 2012) for the California coast (https://spg-satdata.ucsd.edu/). We obtained daily average sea-surface temperature (SST) at 0.05-degee spatial resolution (Good et al., 2020) from the European Space Agency global SST reprocessed product (https://doi.org/10.48670/moi-00169) and daily sea-surface salinity (Droghei et al., 2016) at 0.0125-degree spatial resolution from a merged in situ and satellite observation data product (https://doi.org/10.48670/moi-00051).

4.3.6 Water-mass classification

We classified water masses sampled by the SeaSoar, underway seawater intake system, and CTD-rosettes as California Current (CC) or California Undercurrent (CU) from their

measured potential temperature (θ) and salinity (S). Using the criteria defined in Zaba et al. (2021), we identified the boundaries of CC and CU waters in θ-S space using climatological measurements from the California Underwater Glider Network. Waters that were fresher than the CC threshold in θ-S space were classified as CC; waters that were saltier than the CU threshold in θ-S space were classified as CU. Waters that had intermediate θ-S values were classified as MIX (Supplemental Figure 4.3).

4.3.7 Water-parcel backtracking

We advected water parcels sampled during the SeaSoar surveys and CTD-rosette transects backward in time from their initial locations (i.e. underway sampling coordinates during SeaSoar survey and transect stations). We used the following equations:

$$x(t + \Delta t) = x(t) + u(x, y, t) \times \Delta t \quad (4.1)$$

$$y(t + \Delta t) = y(t) + v(x, y, t) \times \Delta t \quad (4.2)$$

Using a Δt = –1 day, we computed water-parcel locations (x, y) for approximately 2 months preceding each sampling date (Gangrade & Mangolte, 2024). We used surface zonal and meridional velocities $(u(x, y, t), v(x, y, t))$ that included a geostrophic component, derived from satellite altimetry, and a wind-driven Ekman component at 15-m depth derived from the ERA5 reanalysis wind stress (Rio et al., 2014). This velocity product (https://doi.org/10.48670/mds-00327) had a 1-day temporal resolution and 0.25-degree spatial resolution. For CTD transect stations, which were sampled < 10 km apart from each other, we performed backtracking for 100 parcels seeded randomly within a 0.0625-degree (approximately 5-km) radius of each station. During the backtracking, we assumed that the water parcels remained at a constant depth. Therefore, we obtained daily horizontal locations of each seeded water parcel and estimated the number of days prior to sampling a water parcel was last within

the coastal upwelling region, which we defined as within 25 km of the coastline (Huyer, 1983). We considered this the water parcel's "age since coast" in days.

4.3.8 Coastal upwelling conditions

We used the Coastal Upwelling Transport Index (CUTI) and Biologically Effective Upwelling Transport Index (BEUTI) (Jacox et al., 2018), which are defined in 1-degree latitudinal bands along the US West Coast, to estimate the intensity of upwelling experienced by coastally associated water parcels. We used the backtracked locations (latitudes) and dates when water parcels were last at the coast to find the CUTI when they were upwelled. We assumed a water parcel was upwelled if CUTI > 0 $m^2 s^{-1}$ at its origin.

4.4 Results

4.4.1 Hydrographic and biological properties within upwelling filaments

The Morro Bay and Pt. Sur filaments exhibited both along- and across-filament patchiness in hydrographic and biological properties (Figures 4.1–4.3). The Morro Bay filament had a significantly heterogeneous water-mass composition (both CU and CC waters) as it extended offshore, with relatively cold, high-NO_3, CU waters forming the southern portion of the filament and relatively warm, CC waters forming the northern portion of the filament (Figure 4.2). The Pt. Sur filament was composed mostly of CU waters until the most offshore transect, in which we observed some CC waters at the northern boundary of the offshore-flowing filament (Figure 4.3). In the core of the Pt. Sur filament, surface waters were relatively warm with low NO_3 concentrations across the width of the filament. However, there were cold, high-NO_3 waters 25–50 m below the surface of the Pt. Sur filament.

Along the SeaSoar surveys sections, we observed elevated Chl-a and POC concentrations in CU waters relative to CC waters (Figures 4.2–4.3). We also found peak Chl-a and POC

concentrations along the southern portion of each filament, extending even farther south beyond each filament's width as defined by the across-filament extent of offshore-directed velocities.

Across the SeaSoar survey sections, from nearshore to offshore, we observed along-filament variability in salinity, Chl-a, POC, and NO_3. Generally, we found higher-salinity waters in the filaments in the nearshore sections compared to the offshore. The concentrations of POC, and NO_3 changed nonlinearly along the filaments. The widths of both filaments, defined by the horizontal (along-track) extent of offshore flow, increased with distance from shore.

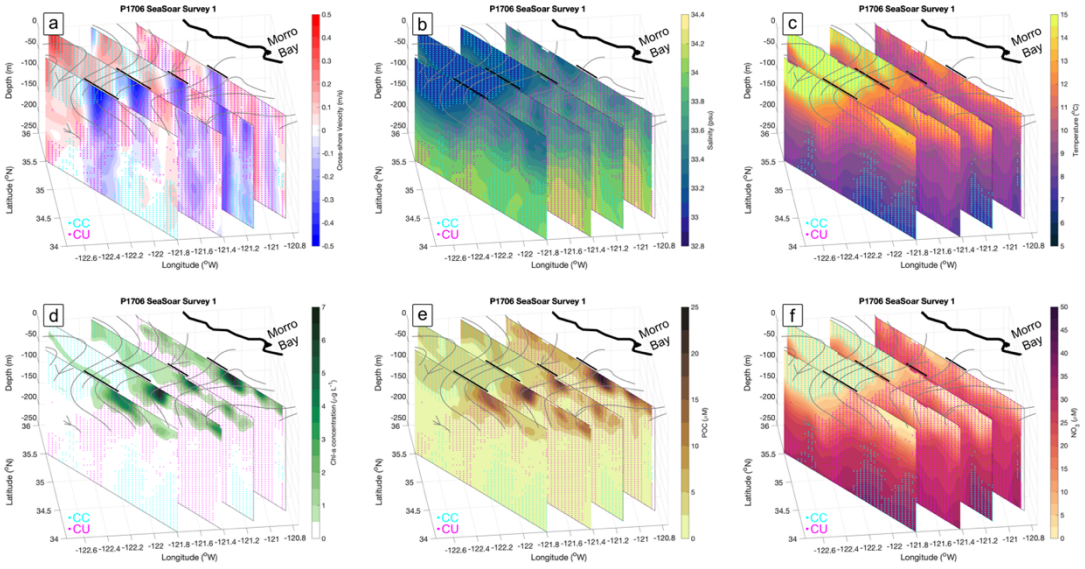

Figure 4.2: Depth-resolved sections from 0–250 m of P1706 (Morro Bay filament cruise) SeaSoar Survey 1 cross-shore velocities (a), salinity (b), temperature (c), Chl-a (d), particulate organic carbon (e), and temperature-derived nitrate concentration (f). Water-masses were classified as California Current (CC; cyan) and California Undercurrent (CU; magenta). Streamlines calculated from satellite-derived geostrophic velocities (with an added modeled 15-m Ekman velocity component) are shown as grey lines.

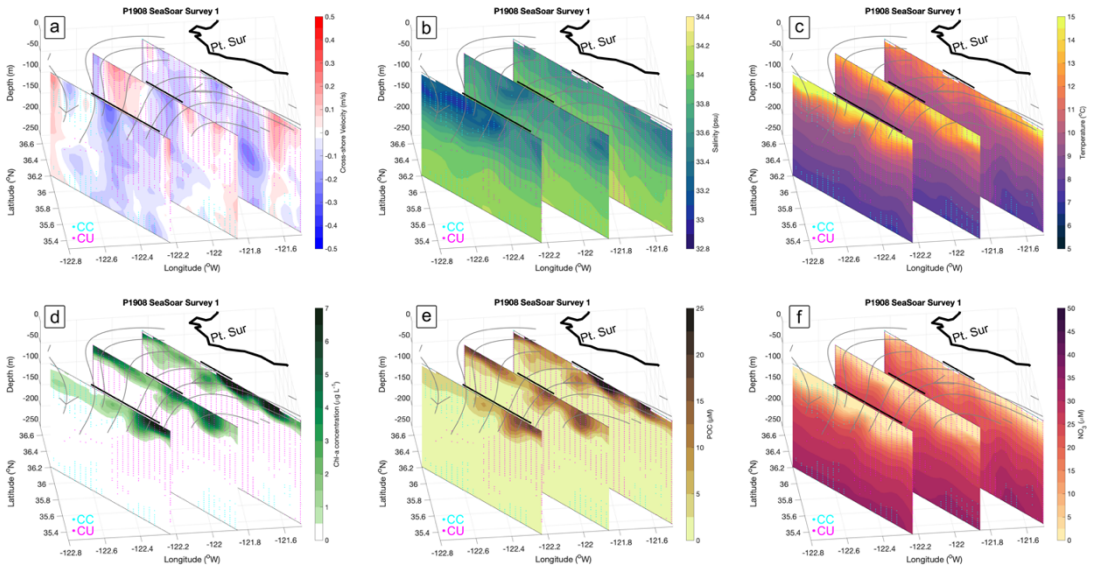

Figure 4.3: Depth-resolved sections from 0–250 m of P1908 (Pt. Sur filament cruise) SeaSoar Survey 1 cross-shore velocities (a), salinity (b), temperature (c), Chl-a (d), particulate organic carbon (e), and temperature-derived nitrate concentration (f). Water-masses were classified as California Current (CC; cyan) and California Undercurrent (CU; magenta). Streamlines calculated from satellite-derived geostrophic velocities (with an added modeled 15-m Ekman velocity component) are shown as grey lines.

4.4.2 Climatological salinity-nitrate relationship

Using regional climatological data, we found that NO_3 concentration was positively correlated with salinity (Figure 4.4). At depths > 100 m, high-salinity, CU waters showed higher median NO_3 (NO_3^{median}) concentrations than the low-salinity, CC waters. This climatological salinity-NO_3 relationship was also found within the Morro Bay and Pt. Sur filaments, where high-NO_3 concentrations were found in high-salinity waters, particularly along the southern flanks of the filaments (Figures 4.2–4.3). Notably, in surface (upper 5–10 m) waters, NO_3 concentrations were generally low (< 0.5 µM) regardless of salinity. At high salinities (> 33.4 psu), surface NO_3 concentrations were frequently found to be below the 35th percentile of NO_3 data (Figure 4.4a).

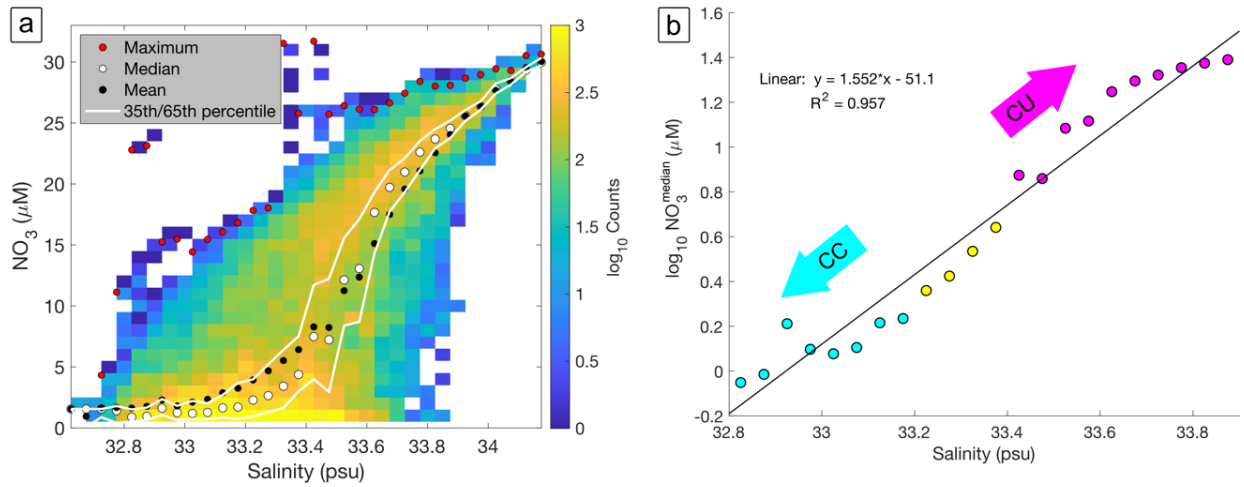

Figure 4.4: Regional climatological relationship between (a) salinity and dissolved inorganic nitrate (NO_3) from California Oceanic Cooperative Oceanic Fisheries Investigations (CalCOFI) sampling from 2003–2019 and Lines 66.7–80 (Monterey Bay to Pt. Conception, California). Maximum, median, and mean NO_3 in 0.05-psu salinity bins are shown in red, white, and black filled circles, respectively. White lines indicate the 35th and 65th percentiles of NO_3. (b) There is a significant linear relationship (slope = 1.552 µM psu^{-1}, R^2 = 0.957) between salinity and $\log_{10}(NO_3^{median})$. Points are colored by water-mass type based on salinity: cyan for California Current (CC), magenta for California Undercurrent (CU), and yellow for Mixed (MIX).

In this study, we consider the initial NO_3 concentration of a water parcel, which we define as the NO_3 concentration when a water parcel was upwelled into the euphotic zone, prior to biological uptake. We estimate the initial NO_3 as the NO_3^{median} for a given salinity. We obtained the following regression equation to estimate the initial NO_3 concentration (µM) of a water parcel given its salinity *(S)*:

$$log_{10}(Initial\ NO_3) = 1.552 \times S - 51.1 \quad (4.3)$$

4.4.3 Variability in phytoplankton community structure

Phytoplankton community structure and Chl-a varied with water-mass type (Figure 4.5). We found that CU waters were associated with high Chl-a and low *Synechococcus* abundance (low PE1 and PE2 fluorescence), and high (but variable) cryptophyte abundance (PE3 fluorescence). In contrast, CC waters were associated with low Chl-a and high *Synechococcus*

abundance (high PE1 and high but variable PE2 fluorescence), and low cryptophyte abundance (PE3 fluorescence). MIX waters were associated with intermediate values of all these variables (Figure 4.5).

We also found that the relative proportion of diatoms was higher in surface CU waters (up to 90% of total Chl-a) than in surface CC waters, while the relative proportion of cyanobacteria was higher in surface CC waters and MIX waters (up to 50% of total Chl-a) than in surface CU waters (Figure 4.6). Generally, diatoms dominated in nearshore surface waters (Transects 1 and 2 for both filaments. In offshore regions (Transect 3 in both cruises), cyanobacteria and (or) prymnesiophytes were abundant.

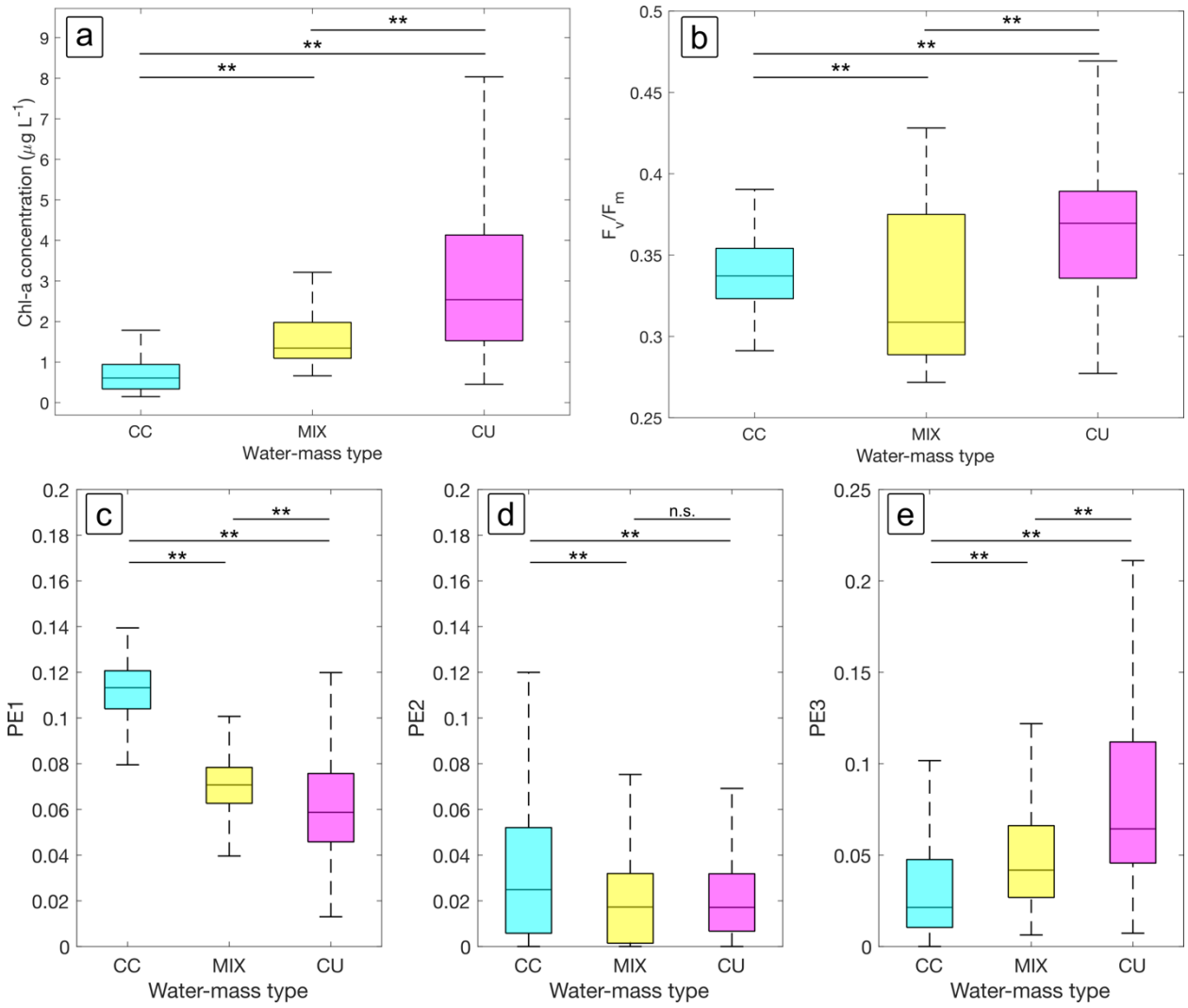

Figure 4.5: Boxplots of the relationship between water-mass type and Chl-a concentration (a), F_v/F_m (b), and phycoerythrin (PE) type 1 (c), type 2 (d), and type 3 (e) for surface water samples during P1706 (Morro Bay filament cruise) SeaSoar Survey 1 and P1908 (Pt. Sur filament cruise) SeaSoar Survey 1. Statistically significant Kruskal-Wallis tests had *p*-values < 0.01 (shown as **) and not significant Kruskal-Wallis tests (shown as n.s.) had *p*-values > 0.05.

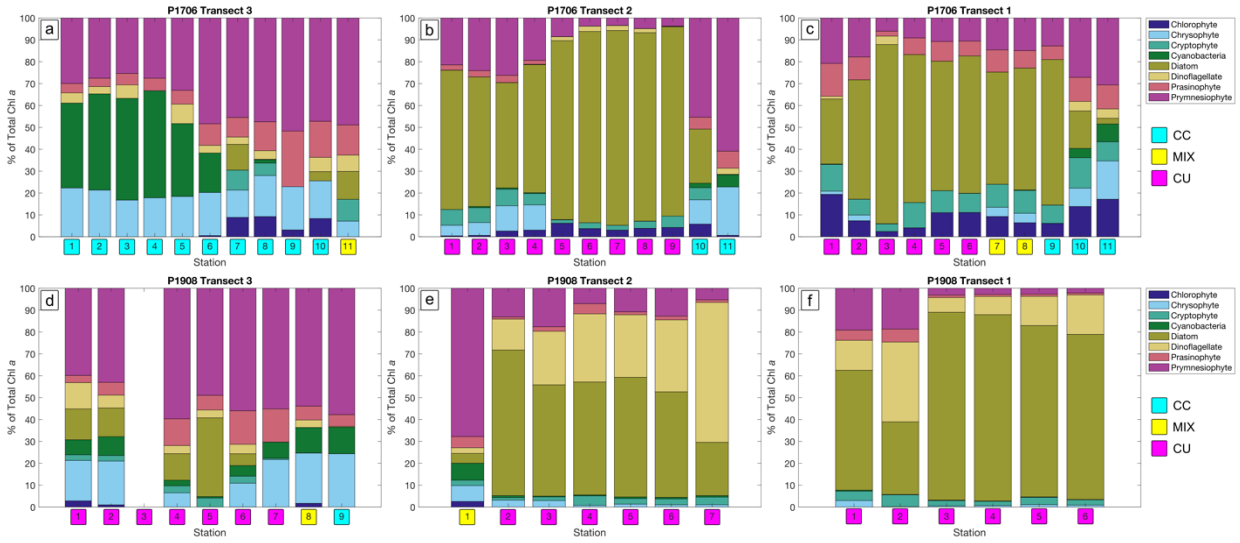

Figure 4.6: Stacked bar chart showing the HPLC-derived relative proportion (%) of total Chl-a attributed to each of the following phytoplankton taxa: chlorophytes (dark purple), chrysophytes (light blue) cryptopyhtes (teal), cyanobacteria (dark green), diatom (light green), dinoflagellate (yellow), prasinophytes (reddish pink), prymnesiophytes (dark magenta). Community structure was enumerated in surface waters sampled at each station of each CTD-rosette transect from P1706 (Morro Bay filament cruise; top row) and P1908 (Pt. Sur filament cruise; bottom row). During each cruise, Transect 3 (left column) was sampled most offshore, Transect 2 (middle column) was sampled at an intermediate cross-shore distance, and Transect 1 (right column) was sampled most nearshore. Station numbers are colored by surface water-mass type (cyan for California Current [CC], yellow for Mixed [MIX], and magenta for California Undercurrent [CU]).

4.4.4 Variability in phytoplankton photophysiology

We found that phytoplankton F_v/F_m varied by water-mass type: CU waters had relatively high F_v/F_m, CC waters had relatively low F_v/F_m, and MIX waters had intermediate values of F_v/F_m (Figure 4.5). Also, F_v/F_m was positively and linearly correlated with salinity (Figure 4.7). This relationship varied between cruises, with a steeper slope for P1908 than P1706 waters. We also observed that waters of similar salinities sometimes had different F_v/F_m values (Figure 4.8a–b), with F_v/F_m varying up to ~0.2 units for a given salinity. F_v/F_m also varied in association with measured NO_3 concentrations and diatom fraction of total Chl-a, increasing in waters with higher measured NO_3 and greater diatom fraction (Figure 4.8c–f).

The relationship between F_v/F_m and Si_{ex} was not consistent between cruises. For P1706 transect waters, there was a peak in F_v/F_m at $S_{iex} \sim 0$ μM (Figure 4.8i–j). In contrast, for P1908 transect waters, there was a somewhat positive relationship, with F_v/F_m increasing with Si_{ex} for most points, except for one water parcel with high F_v/F_m and low (negative) Si_{ex}.

We also found that F_v/F_m had a negative relationship with estimated water-parcel age (Figure 4.8k–l). Waters varied in age from about 10–50 days for P1706 waters, and 0–35 days for P1908 waters. The "youngest" water parcels were the most nearshore waters (Transect 1) from each cruise, while the "oldest" water parcels were the most offshore waters (Transect 3). The P1908 cruise sampled several waters with ages < 20 days and these waters exhibited F_v/F_m values that were strongly negatively correlated with age. The negative relationship between F_v/F_m and age was less pronounced in Morro Bay filament waters than Pt. Sur filament waters.

There were also cross-shore differences in F_v/F_m. In general, Transect 1 waters (most nearshore) of each cruise were associated with the highest F_v/F_m across CTD Transects. Transect 3 waters (most offshore) were associated with intermediate F_v/F_m for P1706 and the lowest F_v/F_m

for P1908. Transect 2 waters in P1706, which crossed the Morro Bay filament approximately 150 km offshore, exhibited the lowest F_v/F_m within that cruise.

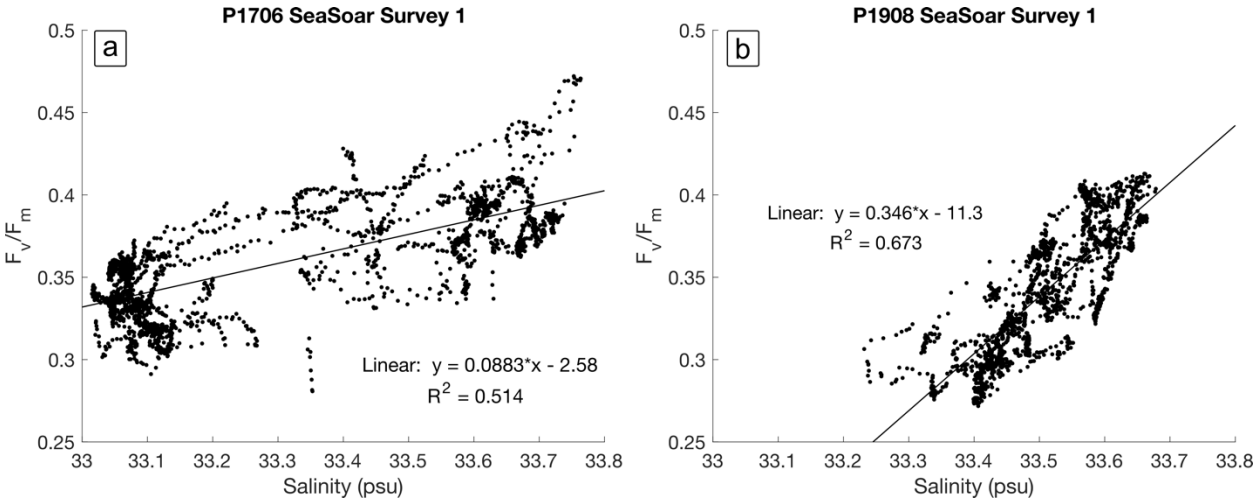

Figure 4.7: The positive linear relationship between salinity and F_v/F_m for surface waters sampled in P1706 (Morro Bay filament cruise) SeaSoar Survey 1 (a) and P1908 (Pt. Sur filament cruise) SeaSoar Survey 1 (b). The P1706 relationship has a slope of 0.0883 psu^{-1} and R^2 of 0.514; the P1908 relationship has a slope of 0.346 psu^{-1} and R^2 of 0.673.

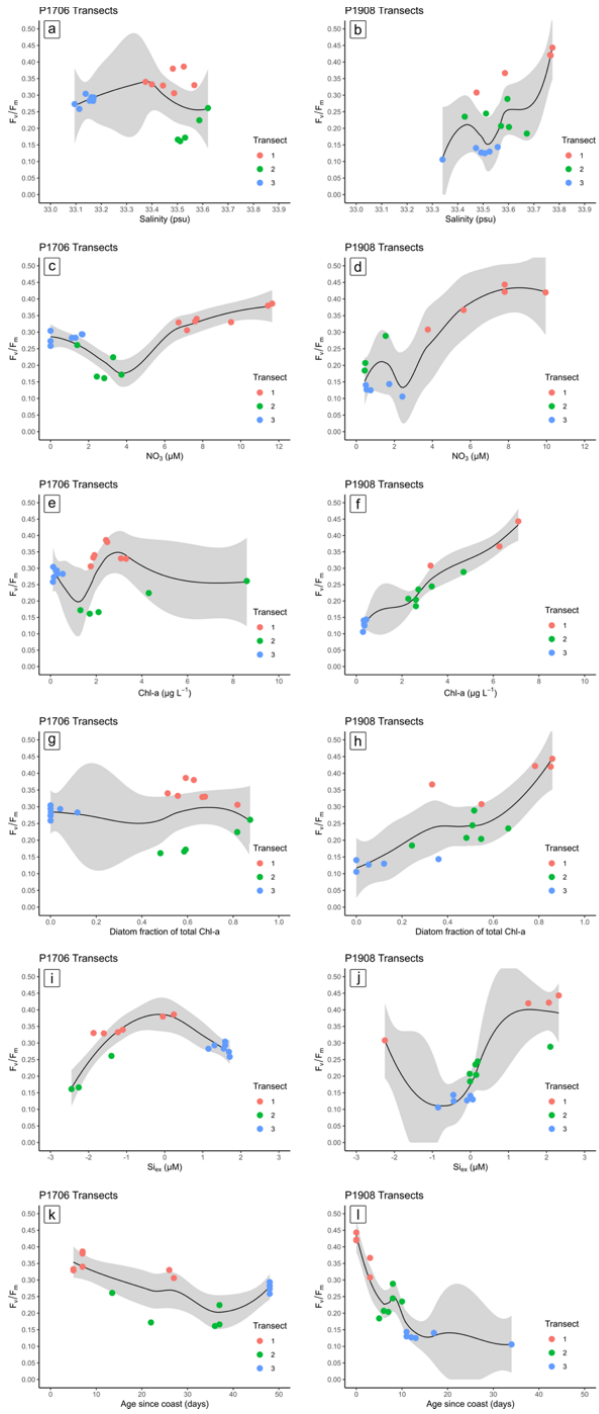

Figure 4.8: Relationships between F_v/F_m and salinity (a–b), measured NO_3 (c–d), Chl-a (e–f), diatom fraction of total Chl-a (g–h), Si_{ex} (i–j), and age since coast (k–l) for the CTD-rosette transects sampled during P1706 (Morro Bay filament cruise; left column) and P1908 (Pt. Sur filament cruise; right column). Transect 1 (most nearshore), Transect 2, and Transect 3 during are shown in red, green, and blue respectively. The grey shaded region represented the 95% confidence intervals of the locally estimated scatterplot smoothing (loess) function (black lines; applied to the data with span = 0.75).

4.5 Discussion

Our results demonstrate that upwelling filaments, despite having somewhat geostationary velocity signatures for several weeks, transport water masses with heterogeneous hydrographic (i.e., temperature and salinity) and biological properties. In particular, filaments exhibit both across-filament and along-filament patchiness in water masses and phytoplankton communities. Here, we describe this across- and along-filament patchiness and investigate how nutrient conditions drive variability in phytoplankton community structure, photophysiology, and Chl-a. We found that across-filament phytoplankton patchiness is associated with a confluence of streams of CU and CC water masses, both of which are entrained in offshore-flowing filaments and form distinct "branches." Because CU water masses have higher initial nutrient concentrations than CC waters, the southern, CU-branch waters support phytoplankton communities with relatively higher Chl-a, dominated by large phytoplankton that exhibit high F_v/F_m. We also found that along-filament patchiness in phytoplankton communities was consistent with the following mechanism: fluctuations in initial (coastal) nutrient conditions are driven by pulsatile wind-driven coastal upwelling, these water parcels with different nutrient and phytoplankton properties are advected along the filament, and the planktonic communities develop —mediated by growth, grazing, and sometimes Fe-limitation—along Lagrangian trajectories. Finally, we will show that by knowing the salinity and age of a water parcel, we can predict its Chl-a concentration and F_v/F_m. This framework can facilitate our understanding of how planktonic communities develop along Lagrangian trajectories and helps us diagnose conditions in which carbon export, through phytoplankton cell sinking and grazer fecal-pellet production, occurs. In the following sections, we discuss these controls on patchiness and their implications.

4.5.1 Across-filament patchiness

Here, we describe how the nonuniformities of water-mass and biological properties across the axes of the filaments and identify the mechanisms generating this heterogeneity. We found that upwelling filaments were composed of distinct water masses, with distinct biological communities. Therefore, not all water masses in such filaments contain high-Chl-a and large phytoplankton.

4.5.1.1 Convergence of CU and CC water masses

Offshore-flowing filaments, while relatively smooth and stationary in velocity structure, are composed of distinct water masses—with distinct temperature-salinity properties—that converge in the offshore-flowing features. The convergence of these waters within a filament generates across-filament patchiness in water masses that is not associated with similar patchiness of the velocity field. Across the axis of the Morro Bay and Pt. Sur filaments, we observed CU and CC waters masses adjacent to each other, both flowing offshore (Figures 4.2–4.3). Often, there was a sharp abutment of CU and CC waters across the filaments, which Zaba et al. (2021) characterized as a strong CU-CC front in the Morro Bay filament. We observed a similar front in the most offshore SeaSoar survey section across the Pt. Sur filament (Figure 4.3). This suggests that, in the CCE, filaments are often a patchwork of CU and CC waters.

The locations of CU and CC water masses within the filaments were mediated by the surrounding mesoscale circulation (e.g., lateral flows, eddies, etc.). Most of the CU waters originated at the coast and were rapidly entrained into the southern flanks of the offshore-flowing filament (Supplemental Figure 4.4). In contrast, most of the CC waters we sampled were entrained from the north or from offshore regions before recirculating and being directed across shore (nearshore to offshore) in the northern flank of the filament (Supplemental Figure 4.4).

This entrainment of both CU and CC waters masses into filaments generates spatial patchiness in temperature-salinity properties across the axes of filaments.

4.5.1.2 Nitrate availability drives distinct CU and CC phytoplankton communities

Here, we show that CU and CC water masses contain varying initial nitrate concentrations, and consequently support distinct phytoplankton communities with different amounts of Chl-a and photochemical efficiencies (F_v/F_m). Many previous studies in this region have found that phytoplankton community structure and Chl-a are correlated with nutrient concentrations: high nutrient availability drives high-Chl-a phytoplankton communities that are dominated by large phytoplankton, such as diatoms (Gangrade et al., in review; Goericke, 2011a, 2011b; Van Oostende et al., 2015). Also, variability in phytoplankton F_v/F_m is correlated with changes in community structure. High-Chl-a, diatom communities, not under nutrient stress conditions, typically exhibit high F_v/F_m (Figure 4.8), while cyanobacteria exhibit low F_v/F_m (Campbell et al., 1998; Chekalyuk et al., 2012; Suggett et al., 2009).

Our observations are entirely consistent with these patterns in phytoplankton community composition, Chl-a, and F_v/F_m. We found that high-salinity CU waters had higher initial nitrate concentrations than low-salinity CC waters (Figure 4.4). Subsequently, CU waters developed relatively high F_v/F_m, high Chl-a and large phytoplankton (cryptophytes), while CC waters had relatively low F_v/F_m, low Chl-a, and cyanobacteria (*Synechococcus*) (Figure 4.5). These differences in phytoplankton community structure, driven by initial NO_3, generated the overall positive correlation between salinity and F_v/F_m: large phytoplankton with high F_v/F_m were found in high-salinity waters, while small phytoplankton with low F_v/F_m were found in low-salinity waters (Figures 4.5–4.7). Thus, the observed patchiness of phytoplankton communities across the Morro Bay and Pt. Sur filaments was due to their associations with CU and CC water masses.

4.5.2 Along-filament patchiness

We observed along-filament variability in phytoplankton community structure, photophysiology, and Chl-a. Here, we explore some physical and biogeochemical mechanisms that contributed to this variability.

4.5.2.1 Upstream fluctuations in nutrient conditions

Patterns in along-filament variability in salinity, as well as phytoplankton community structure, photophysiology, and Chl-a, were consistent with upstream fluctuations in wind-driven upwelling, which modulated the initial nutrient conditions. In particular, pulses of coastal wind-driven upwelling result in waters with varying salinities and initial nitrate concentrations that are subsequently transported along filaments (Gangrade & Franks, 2023; He & Mahadevan, 2021; Jacox et al., 2018). This leads to water parcels with distinct phytoplankton communities and varying Chl-a concentrations along the filament jets (Gangrade & Franks, 2023). Through this mechanism, the Morro Bay and Pt. Sur filaments likely contained several different water parcels along the filament's axis, with distinct phytoplankton communities resulting from varying initial nutrient conditions. These parcels advected along each filament and were captured at discrete time points by our cross-filament sampling.

If the intensity of coastal wind-driven upwelling is correlated with the amount of nitrate advected vertically into the euphotic zone—thus setting the amount of new production of phytoplankton—we would expect high upwelling intensities to be correlated with water masses containing high phytoplankton biomass—or high Chl-a. We indeed observed such a relationship between upwelling intensity—as measured by CUTI and BEUTI—and Chl-a, but this relationship was nonlinear (Supplemental Figure 4.5). These findings suggest that variability in Chl-a along the filament is consistent with fluctuations in upwelling intensity; however, the CUTI or BEUTI metrics, are perhaps too spatially and temporally coarse to describe this relationship in detail.

In summary, we find that observed along-filament patchiness in phytoplankton is consistent with variability in upstream nutrient conditions, which is driven by fluctuations in wind-driven coastal upwelling. This leads to water parcels with distinct nutrient and phytoplankton properties being advected along filaments.

4.5.2.2 Planktonic community development along Lagrangian trajectories

Along-filament variability in Chl-a is also consistent with planktonic community development—primarily mediated by phytoplankton growth and grazing—occurring along Lagrangian trajectories of water parcels. Phytoplankton blooms occur in water parcels in response to initial upwelled nutrient concentrations; doubling times of phytoplankton populations are typically days to weeks in the CCE (Landry et al., 2009; Li et al., 2012). Thus, on these timescales, we would expect Chl-a concentrations in a water parcel to increase and reach a maximum. After some days to weeks, we would expect Chl-a to decline as nutrients are used up and as phytoplankton are grazed down and (or) sink out of the euphotic zone. In the CCE, microzooplankton and mesozooplankton grazing is responsible for a significant proportion (> 90%) of phytoplankton loss (Landry et al., 2009; Stukel et al., 2011; Stukel et al., 2013). Peaks in phytoplankton abundance in a water parcel are thus followed by increased abundances of zooplankton grazers, which also eventually peak and then decline (Gangrade & Mangolte, 2024; Messié & Chavez, 2017; Messié et al., 2022). These biological transformations in a water parcel occur as it is being advected along the filament. Thus, distinct water parcels—at different stages in their planktonic ecosystem development—can be found along filament jets at the same time (Gangrade & Mangolte, 2024).

By examining changes in Chl-a in a water parcel in relation to its salinity and its age (calculated through particle backtracking), we can reveal the planktonic community development along pseudo-Lagrangian trajectories (Figures 4.9 and 4.10). Using this salinity-age framework,

we showed that along the trajectories of high-salinity (≥ 33.4 psu) water parcels, Chl-a concentration peaked at approximately 10–15 days (Figure 4.9 a–b). Along the trajectories of low-salinity (< 33.4 psu) water parcels, peaks in Chl-a occurred on a similar timescale, but the magnitudes of the Chl-a peaks were much lower than those of high-salinity waters. Furthermore, in low-salinity waters, Chl-a did not vary as much with age as it did in high-salinity waters. These results are consistent with our conclusion that low-salinity waters had relatively lower initial NO_3 concentrations than high-salinity waters, and were therefore not able to support high-Chl-a concentrations or blooms of the large phytoplankton which are often associated with high-Chl-a. This salinity-age framework reveals that high-Chl-a phytoplankton blooms predominantly occur in high-salinity (> 33.4 psu) waters, with Chl-a peaking within 10–15 days of a water parcel originating at the coast. Grazing-mediated declines in Chl-a subsequently occur in water parcels as they are advected offshore.

In summary, we find that along-trajectory planktonic community development begins with phytoplankton blooms that are subsequently grazed down, resulting in peaks in Chl-a in water parcels as they age and are advected along filaments. Thus, if a water parcel were to be resampled throughout its along-filament trajectory, we would observe a peak and then decline in Chl-a along the filament, which would result in along-filament Chl-a patchiness. This patchiness is further complicated by water parcels with distinct salinities, initial nutrient concentrations, and ages, which occur simultaneously along the filaments at different stages in their planktonic ecosystem developments.

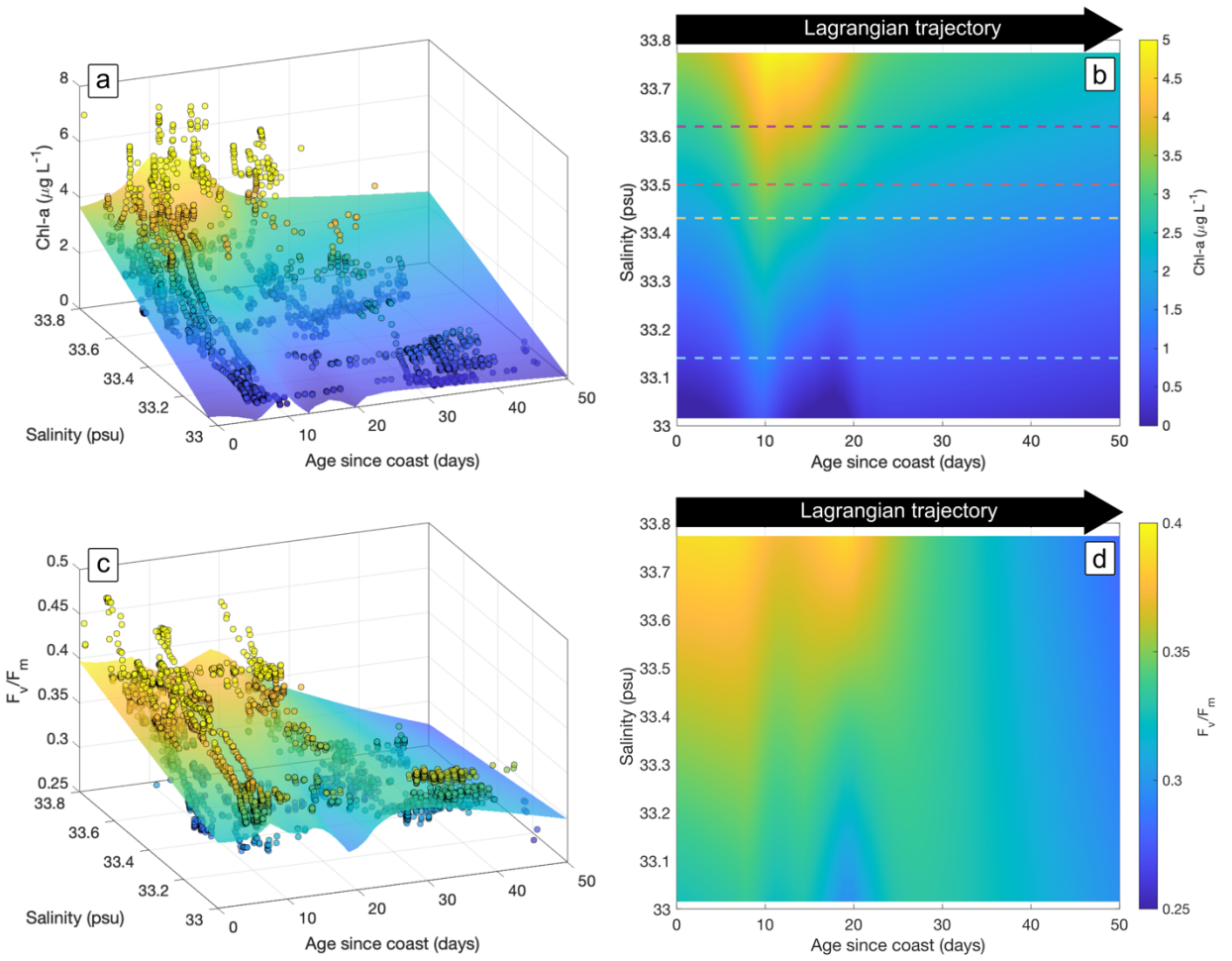

Figure 4.9: The three-dimensional relationships between salinity, age since coast, and Chl-a (a) and between salinity, age since coast, and F_v/F_m (c)—also shown as a 2-dimensional heatmaps (b ,d) —represent changes in Chl-a and F_v/F_m along Lagrangian trajectories. Data are combined from both P1706 (Morro Bay filament cruise) and P1908 (Pt. Sur filament cruise). The smoothed surfaces display the outputs from a locally weighted scatterplot smoothing function (span = 0.55; $R^2 = 0.52$ for Chl-a and $R^2 = 0.30$ for F_v/F_m). The color scale represents the relative magnitude of the Chl-a (a, b) and F_v/F_m (b). Dashed lines in (b) correspond to different salinity values used in Figure 4.10.

4.5.2.3 A special case: the development of Fe-limitation

Within diatom-dominated communities that are typically found in the CU "branch" of filaments, observed decreases in F_v/F_m and Si_{ex} in water parcels of ages > 10 days were consistent with the development of Fe-limitation. The occurrence of Fe-limitation could also be patchy along a filament due to variability in water-mass origins that result in differences in initial

Fe concentrations. This legacy of initial Fe-concentration conditions and the subsequent along-trajectory development of Fe-limitation can exacerbate along-filament phytoplankton patchiness.

We predicted that Fe-limitation would be diagnosed by both Si_{ex} and F_v/F_m. Due to the preferential uptake of H_4SiO_4 relative to NO_3 by Fe-limited diatoms, we expected a negative Si_{ex} signal (Brzezinski et al., 2015; Hogle et al., 2018), as well as low F_v/F_m (Greene et al., 1992) to be associated with Fe-limited phytoplankton communities. In contrast, we expected a positive Si_{ex} signal and elevated F_v/F_m in Fe-replete phytoplankton communities.

Nearshore (Transect 1), we found positive Si_{ex} and elevated F_v/F_m. These waters were mostly young (ages < 10 days), recently upwelled, with a high proportion of diatoms that were likely actively blooming, given relatively high measured (residual) NO_3 concentrations (Figure 4.8c–f). It is unlikely these waters were experiencing Fe-limitation, as they had generally neutral or positive Si_{ex} values (and elevated F_v/F_m) (Figure 4.8g–h). Farther offshore (P1706 Transect 2 and P1908 Transect 3) in water parcels with ages > 10 days, we observed negative Si_{ex} and low F_v/F_m. We also observed low NO_3 in these waters, consistent with diatom communities continuing to mature along the filaments ultimately becoming Fe-limited and less photochemically efficient.

Our detection of water-mass patches consistent with Fe-limitation is supported by other studies of these upwelling filaments in the CCE. For example, our observation of reduced F_v/F_m across shore (i.e. along the filaments) with aging water parcels is supported by measurements made by Kranz et al. (2020), who found decreases in nighttime F_v/F_m values from nearshore to offshore Morro Bay filament waters. Furthermore, Forsch et al. (2023), using Fe grow-out incubation experiments, measured significant Fe-limitation of diatom communities in both the Morro Bay and Pt. Sur filament waters. These experiments also revealed that phytoplankton

communities in the Morro Bay filament experienced a greater degree of Fe-limitation than the Pt. Sur filament. Our results are consistent with this finding, as we observed lower (more negative) Si_{ex} values in Morro Bay filament (Transect 2) than in the Pt. Sur filament (Transect 3).

Variability in upstream Fe supply could have also resulted in the patchy distribution of Fe-limitation along the filaments: some waters that advected along the filaments may have had high initial Fe supply, while others did not, eventually becoming Fe-limited. Moreover, Fe supply to filament waters could vary based on where a filament developed along the coast. This is because sources of Fe to upwelling filaments are highly variable in space and time. This variability in dissolved Fe supply depends on factors such as riverine inputs, benthic boundary layer dynamics, fluctuations in Fe-solubility with dissolved oxygen, and enhanced sediment resuspension at coastal headlands (Chase et al., 2007; Elrod et al., 2004; Forsch et al., 2023). Therefore, the observed patchiness in Fe-limitation within and across the Morro Bay and Pt. Sur filaments could have resulted from fluctuations in upstream Fe supply, which is dependent on many physical, geological, and chemical factors.

We also observed that other processes, such as changes in phytoplankton community structure, were also correlated with changes in F_v/F_m (Figure 4.8). Unfortunately, we did not have the appropriate data to fully characterize such controls on F_v/F_m variability, which are spatially and temporally complex (Behrenfeld & Milligan, 2013). However, the patterns we observed were indeed consistent with Fe-limitation in some regions within both filaments: negative Si_{ex} and low F_v/F_m were observed in offshore transects of the filaments. Therefore, along-trajectory development of the plankton community can—in some cases—include the development of Fe-limitation. Moreover, whether Fe-limitation occurs along a filament and to

what degree it occurs is highly dependent on how much dissolved Fe is supplied to filament waters at their origins.

4.5.2.4 Other mechanisms of along-filament patchiness

There are mechanisms other than changes in initial conditions and the advection of transforming water parcels that could have driven along-filament patchiness in phytoplankton. These include local, in-filament processes, such as vertical advection and mixing associated with submesoscale density fronts. In these features, which can occur along filaments, vertical nutrient fluxes can stimulate phytoplankton growth (Li et al., 2012; Lévy et al., 2012). Such submesoscale interactions occurring along the trajectories of water parcels could stimulate the development high-Chl-a phytoplankton patches along the filaments, independent of their initial conditions.

Another mechanism generating along-filament changes in phytoplankton is subduction, which would result in decreases in surface Chl-a concentrations from nearshore to offshore. While subduction of phytoplankton-rich waters has been previously documented in filaments within the CCS (Hood et al., 1991; Kadko et al., 1991), we did not find evidence of this in the Morro Bay and Pt. Sur filaments. While localized along-filament (i.e., non-initial condition derived) injections of nutrients or physical subduction of phytoplankton could have occurred, creating additional along-filament patchiness in Chl-a, we did not observe these processes in our data.

4.5.2.5 Summary of along-filament patchiness

In summary, we demonstrate that the observed along-filament patchiness of water masses and phytoplankton communities were consistent with the along-filament advection of initial fluctuations of NO_3 and Fe concentrations at the coast driven by fluctuating wind-driven coastal

upwelling. Waters with different initial conditions support distinct phytoplankton communities; these communities develop as they advect along filaments: phytoplankton take up nutrients, bloom, and then are grazed on by zooplankton. Depending on initial conditions, these phytoplankton may become Fe-limited over time as they are transported along the filaments, exhibiting reduced photochemical efficiency and preferential Si uptake.

The temporal and spatial sampling patterns captured water parcels at different time points in their advective and biological histories that reflect the legacy of their initial nutrient conditions and subsequent ecosystem interactions. When we sampled these distinct water parcels within an Eulerian framework (i.e. transects), we thus captured a range of ecosystem states (Figure 4.10) that reflected both their ages and their initial conditions. These processes resulted in the observed along-filament patchiness in phytoplankton communities.

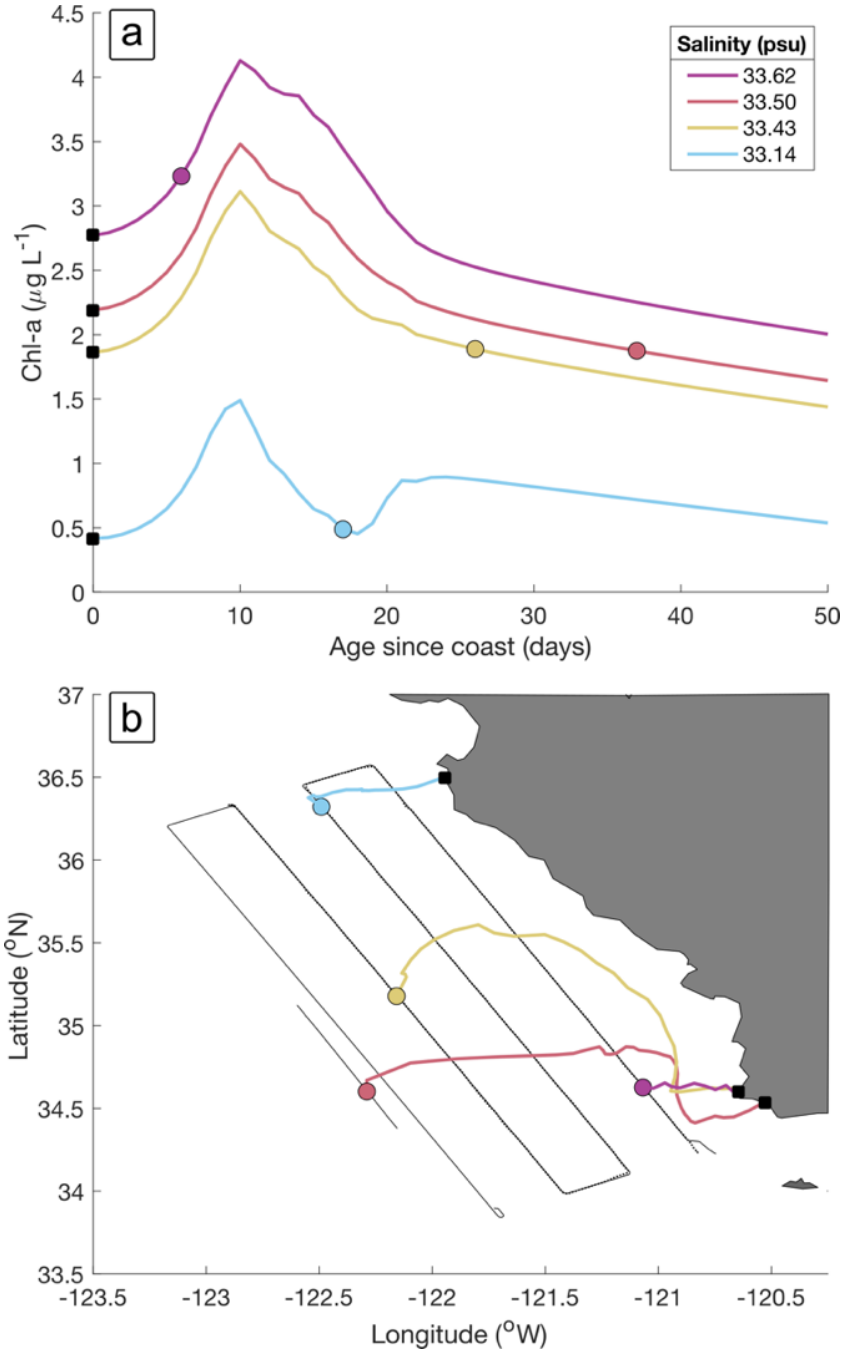

Figure 4.10: (a) Time-dependent, along-trajectory changes in Chl-a of four different water parcels with distinct salinities (33.62 psu in purple, 33.50 psu in red, 33.43 in yellow, and 33.14 psu in blue). Each water parcel was sampled at different time points shown by locations of scatter points in (a) along the *x*-axis. (b) Map of the sampling locations of the four different water parcels and their trajectory pathlines, which indicate their locations prior to sampling. Black lines indicate SeaSoar Survey and Transect sampling locations from both P1706 (Morro Bay filament cruise) and P1908 (Pt. Sur filament cruise). Black squares indicate beginning of Lagrangian trajectories at age = 0 days in (a) and their geographic origins on the coast in (b).

4.5.3 Salinity-age framework: Implications for cross-shore carbon export

Here, we use a salinity-age framework to describe changes in Chl-a and F_v/F_m along Lagrangian trajectories. We assume that post-bloom declines in Chl-a and F_v/F_m are consistently associated with high export production (relative to new production), through grazing and sinking which is enhanced by Fe-limitation. Using this assumption, we can use the age of water parcels to identify the distance offshore at which these "export conditions" are likely to occur in the CCE.

Phytoplankton cell sinking and fecal-pellet production by mesozooplankton grazers drive the export of particulate organic carbon from the euphotic zone (Landry et al., 2009; Stukel et al., 2011). Furthermore, Fe-limited conditions lead to increased silicification by diatoms, creating heavily ballasted diatom cells and grazer fecal pellets that dramatically increase sinking POC (Brzezinski et al., 2015; Stukel et al., 2017). We expect that grazing of phytoplankton and cell sinking would be associated with decreases in Chl-a, and we would expect Fe-limited conditions would be associated with decreases in, or low values of, F_v/F_m. Therefore, we used the observed declines in Chl-a and F_v/F_m along water-parcel trajectories (Figure 4.9), to identify when (at what age) and where (distance offshore) these "export conditions" could have occurred.

We found that declines in Chl-a and F_v/F_m in high-salinity ($\geq$ 33.4 psu) water parcels—those with high predicted export relative to new production—occurred approximately 15–25 days after a water parcel originated at the coast (Figure 4.9). These high-salinity water parcels aged 15–25 days were found at a median offshore distance of ~115 km, and 80% of these waters were found between approximately 55–130 km offshore (Figure 4.11). These results show that water parcels exhibiting "export conditions"—inferred from decreasing Chl-a and F_v/F_m—are advected offshore, consistently reaching distances of over 100 km offshore.

Cross-shore variability in productivity and export has been detected by several previous studies conducted in the CCE. Our observations are consistent with these previous findings. Both Kranz et al. (2020) and Bourne et al. (2021) found high export fluxes associated with Morro Bay filament waters at approximately 110 km from shore. Some of this export flux was attributed to fast-sinking ovoid fecal pellets (Bourne et al., 2021). We observed that waters parcels with declining Chl-a and F_v/F_m along their trajectories were found at similar distances offshore (~115 km), and so these studies support our hypothesis that "export conditions" were likely to occur at these cross-shore distances. On a regional scale, in the CCE, magnitudes of net primary productivity typically decrease with distance offshore (Kranz et al., 2020; Landry et al., 2009). And while magnitudes of export fluxes (both passive fluxes and active transport) also decrease with distance offshore (Kranz et al., 2020; Stukel et al., 2013), the *e*-ratio (the ratio of export to total production, also known as export efficiency) increases with cross-shore distance (Kelly et al., 2018; Stukel et al., 2011). The *e*-ratio is also related to water-parcel age: higher export efficiencies are typically found in older, offshore waters than in younger, nearshore waters (Kelly et al., 2018). Our observations of water parcels with "export conditions" being found approximately 115 km offshore provides a mechanism that would drive the observed nearshore-to-offshore gradient in *e*-ratios. Similarly, Chabert et al. (2021) found that surface nutrient concentrations, net primary productivity, and the ratio of new production to carbon export all rapidly decreased within the first 20 days of a water parcel leaving the coast. While the locations of these water parcels after 20 days were measured, there were no consistent patterns in their cross-shore extents.

In summary, we find that our salinity-age framework is useful in identifying how planktonic communities develop along Lagrangian trajectories and in diagnosing conditions (i.e.

through declines in Chl-a and F_v/F_m) that are consistent with high export relative to new production. We estimated that these "export conditions" occurred in high-salinity waters parcels at timescales of 15–25 days after upwelling at the coast, and distances offshore of approximately 115 km; these scales were consistent with other regional studies.

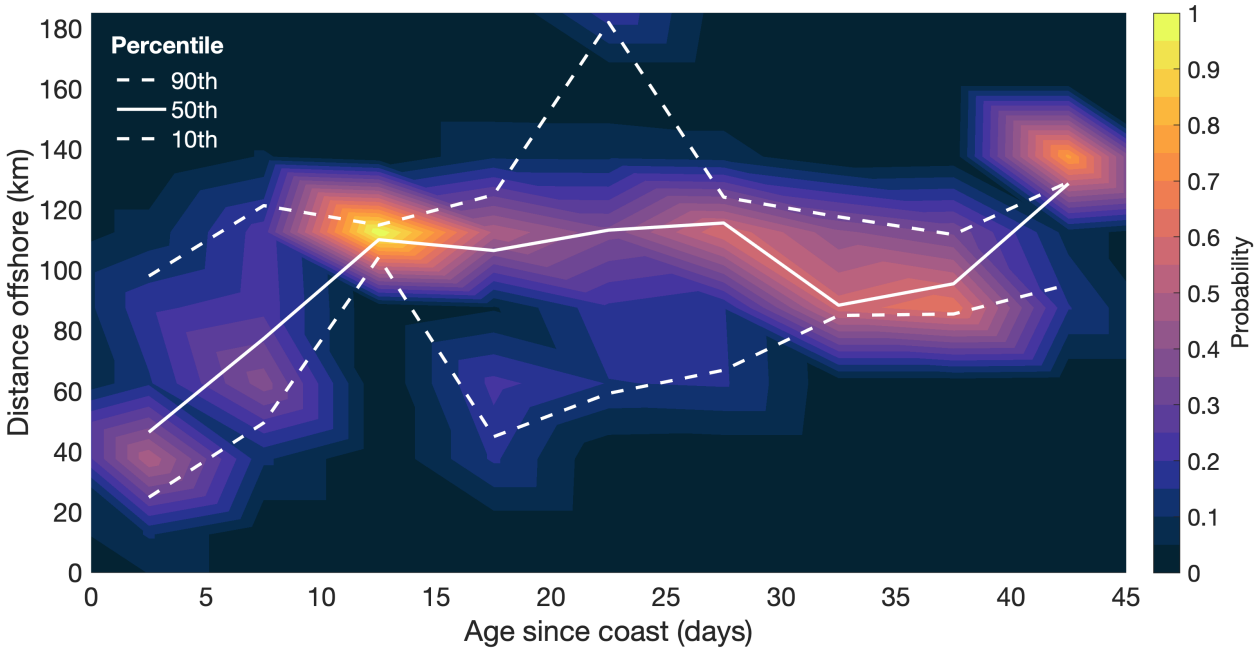

Figure 4.11: Probability heatmap of distance offshore versus age of high-salinity (≥ 33.4 psu) water parcels. Probabilities were calculated for data in 5-day age and 25-km distance bins for all waters parcels sampled during P1706 (Morro Bay filament cruise) SeaSoar Survey 1 and P1908 (Pt. Sur filament cruise) SeaSoar Survey 1. Probabilities were calculated for each age bin (i.e., probabilities along *y*-axis sum to 1). White solid line represents median (50th percentile) of data in each age bin, and white dashed lines represent 10th and 90th percentiles of data in each age bin.

4.6 Conclusion

In this study, we observed that waters associated with upwelling filaments exhibited significant hydrographic and biological patchiness. We found that across-filament patchiness in phytoplankton community structure, photophysiology, and Chl-a resulted from the horizontal convergence of water masses with distinct phytoplankton communities: only a portion of the filaments (as defined by their slowly changing velocity structure) contained communities with

high Chl-a and large phytoplankton. Along the filaments, we observed variability in phytoplankton community structure, photophysiology, and Chl-a that was associated with fluctuating initial conditions at the coast and the subsequent along-filament advection of water parcels with distinct hydrographic and biogeochemical properties. We also found that planktonic communities changed along their trajectories as they transited the filaments, in association with growth-grazing dynamics. Some water parcels showed reductions in phytoplankton photochemical efficiency consistent with the time-dependent development of Fe-limitation, which was likely related to initial nutrient supplies. Finally, we demonstrated that a salinity-age framework of tracking changes in biological properties can be used as a pseudo-Lagrangian system. Using this framework, we predicted that phytoplankton communities with declining Chl-a and F_v/F_m had enhanced organic carbon export. These communities were often found within 15–25 days of originating at the coast and approximately 115 km from shore. Together, these findings indicate that filaments are heterogeneous and fundamentally non-uniform in physical, biological, and chemical properties. Therefore, purely physical descriptions of filaments, such as defining them as simple horizontal density extrema (McWilliams et al., 2009), are not sufficient for characterizing the hydrographic and biological variability that occurs both across and along their axes.

We also emphasize that interpreting biological patchiness in filaments within a Lagrangian framework (Forsch et al., 2023; Kranz et al., 2020; Wang et al., 2020) is critical to elucidating the time- and source-dependent controls and dynamics. In this study, we showed that Lagrangian trajectories (and the associated water-parcel histories) can be inferred from Eulerian measurements and spatially and temporally resolved velocity fields. This method allows us to understand planktonic ecosystem changes along water-parcel trajectories, which allows the

estimation of ecosystem-wide impacts. For example, identifying where and when phytoplankton communities potentially bloom, degrade, and are exported is important for understanding how primary production shapes patterns in the distribution of higher trophic levels, such as zooplankton (Lilly et al., 2022), seabirds (Ballance et al., 1997), and cetaceans (Barlow et al., 2008; Tynan et al., 2005)—as well as benthic ecosystems (Rathburn et al., 2001; Tecchio et al., 2013). The mechanistic salinity-age framework we describe therefore has the potential to allow identification and characterization of critical ecological patterns within a dynamic mesoscale flow field.

Data Availability

All cruise data are available from download from the CCE LTER Datazoo website (https://oceaninformatics.ucsd.edu/datazoo/catalogs/ccelter/datasets), and data stored in the CCE LTER Environmental Data Initiative (EDI) repository are searchable at https://ccelter.ucsd.edu/data/. CalCOFI data are available for download at https://calcofi.org/data/. Sea surface temperature data (https://doi.org/10.48670/moi-00169) and salinity data (https://doi.org/10.48670/moi-00051) are available for download at Copernicus Marine Environmental Monitoring Service website. Sea surface chlorophyll data are available for download at https://spg-satdata.ucsd.edu. California Underwater Glider Network data are available for download at https://spraydata.ucsd.edu/projects/cugn/.

Acknowledgments

The authors acknowledge Katherine Zaba, Kiefer Forsch, Sven Kranz, Mark Ohman, Kathy Barbeau, Mike Stukel, Shonna Dovel, Ralf Goericke, Mati Kahru, and Alexander Chekalyuk for their feedback and/or help with supplying/processing data. The authors also thank the captain and crew on the CCE LTER P1706 and P1908 cruises. CCE LTER was supported by

NSF Award OCE-1637632 and OCE-2224726. Shailja Gangrade was supported by an NSF Graduate Research Fellowship and Scripps Institution of Oceanography.

Chapter 4, in part, is currently being prepared for submission for publication of the material. Gangrade, Shailja; Franks, Peter J. S., 2024. The dissertation author was the primary researcher and author of this material.

Supplemental Information

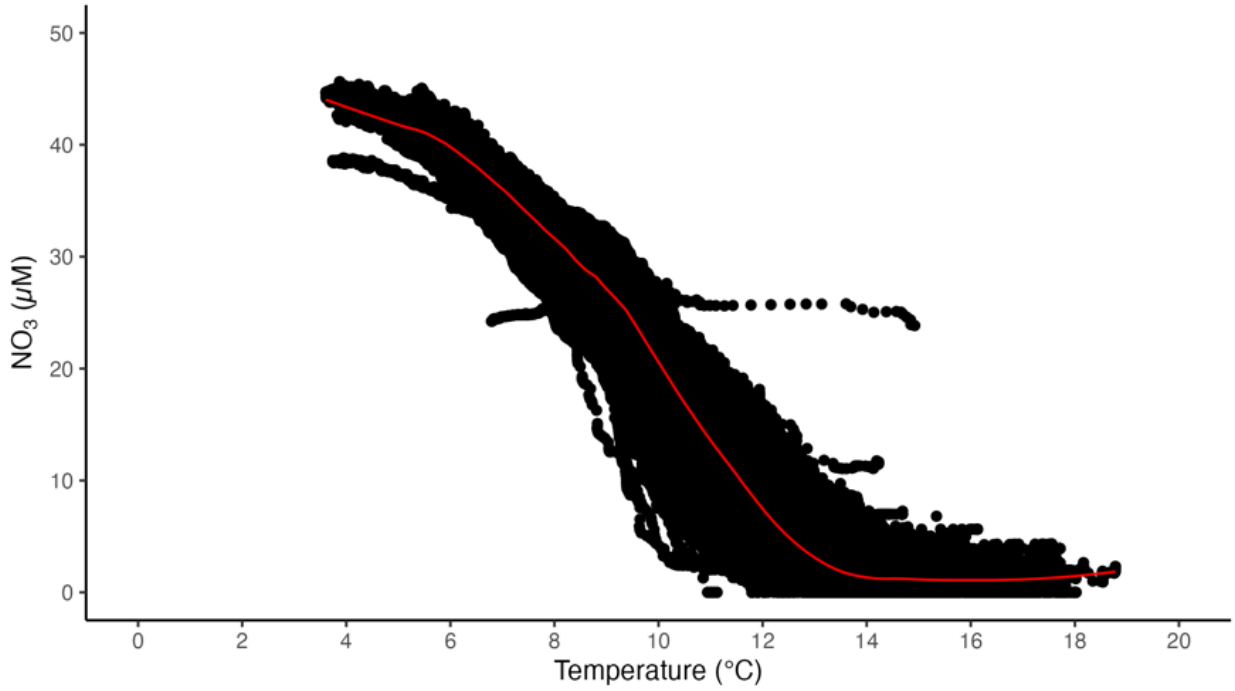

Supplemental Figure 4.1: Regional climatological relationship between dissolved inorganic nitrate (NO_3) and temperature from California Oceanic Cooperative Oceanic Fisheries Investigations (CalCOFI) sampling from 2003–2019 and Lines 66.7–80 (Monterey Bay to Pt. Conception, California). The locally estimated scatterplot smoothing function (span = 0.1) is shown in red; this relationship was used to derive NO_3 from measured temperature for the depth-dependent data of P1706 (Morro Bay filament cruise) and P1908 (Pt. Sur filament cruise) SeaSoar Survey 1.

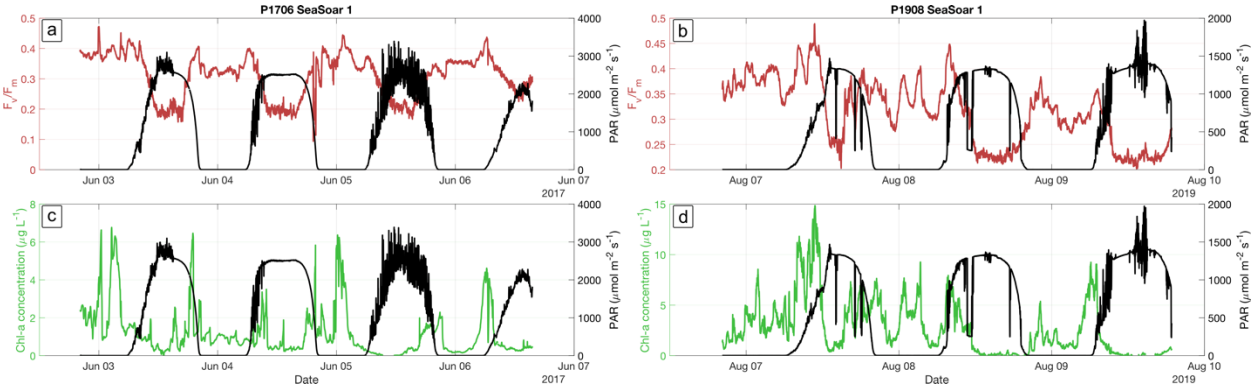

Supplemental Figure 4.2: Diel periodicity (due to nonphotochemical quenching) and asymmetry of F_v/F_m (red lines in a–b) and Chl-a concentration (green lines in c–d) with photosynthetically active radiation (PAR; black lines) for surface waters sampled during P1706 (Morro Bay filament cruise) SeaSoar Survey 1 (left column) and P1908 (Pt. Sur filament cruise) SeaSoar Survey 1 (right columns).

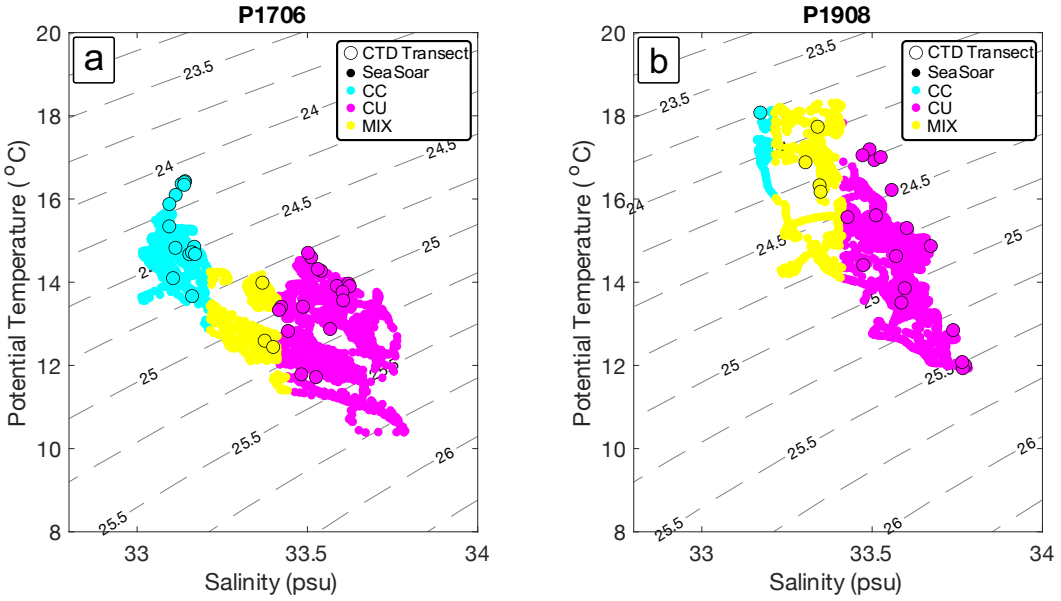

Supplemental Figure 4.3: Diagrams of potential temperature versus salinity for P1706 (Morro Bay filament cruise; left) and P1908 (Pt. Sur filament cruise; right) sampling (both SeaSoar Survey 1 and CTD-rosette transects). Water masses identified as California Current (CC), California Undercurrent (CU), and Mixed (MIX) are shown in cyan, magenta, and yellow filled circles respectively. Waters sampled during the CTD-rosette transects are shown as filled circles outlined in black. Potential density anomalies at conservative temperature (σ_Θ) are shown as dashed contours.

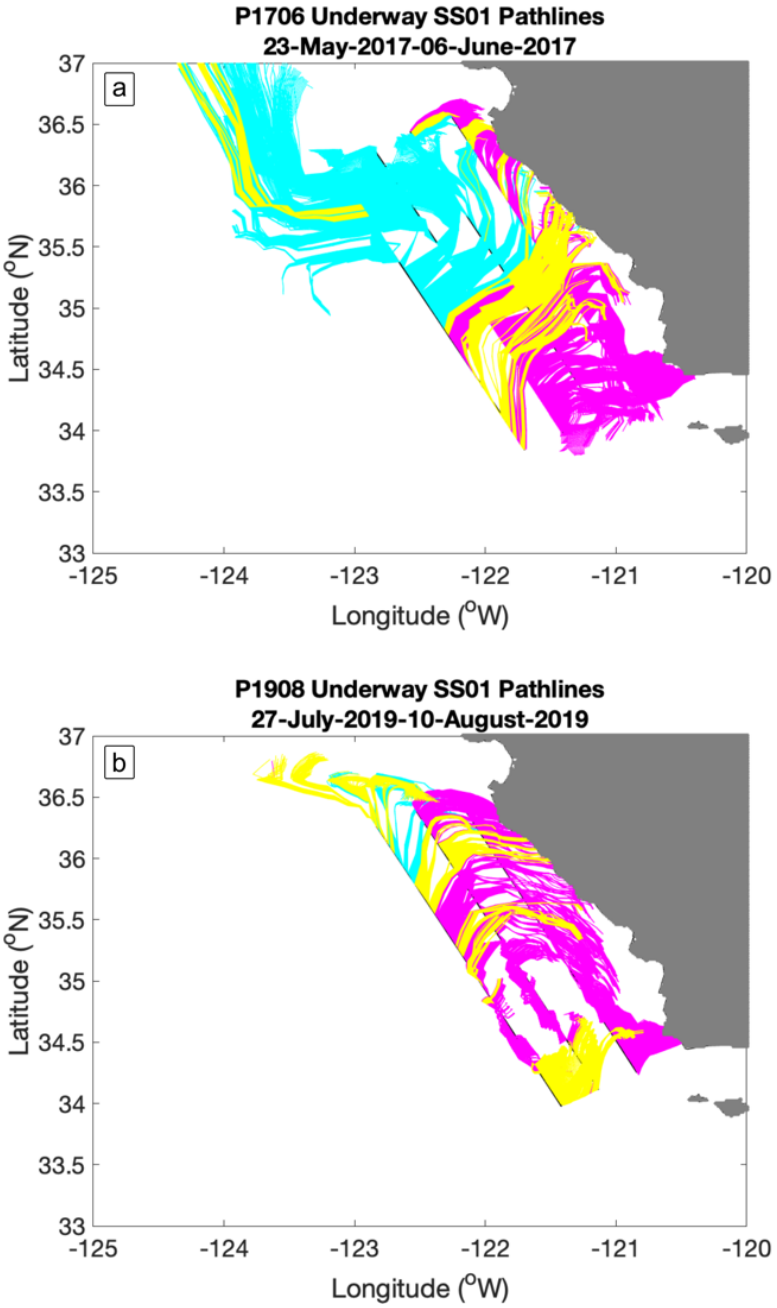

Supplemental Figure 4.4: Maps of the pathlines of backtracked water parcels from the underway P1706 and P1908 SeaSoar Survey 1 sampling locations. Pathlines are drawn for tracked locations from 14 days prior to the last date of sampling of each survey (May 23, 2017, during P1706 and July 27, 2019, during P1908) until the day the water parcels were sampled by the SeaSoar (June 3–6, 2017 for P1706 and August 8–9, 2019 for P1908). Pathlines are colored by water-mass type of sample (cyan for California Current [CC], magenta for California Undercurrent [CU], and yellow for Mixed [MIX]). Black lines indicate the alongshore SeaSoar survey lines upon which depth-resolved data were objectively mapped. Water parcels were backtracked using daily geostrophic plus 15-m Ekman velocities.

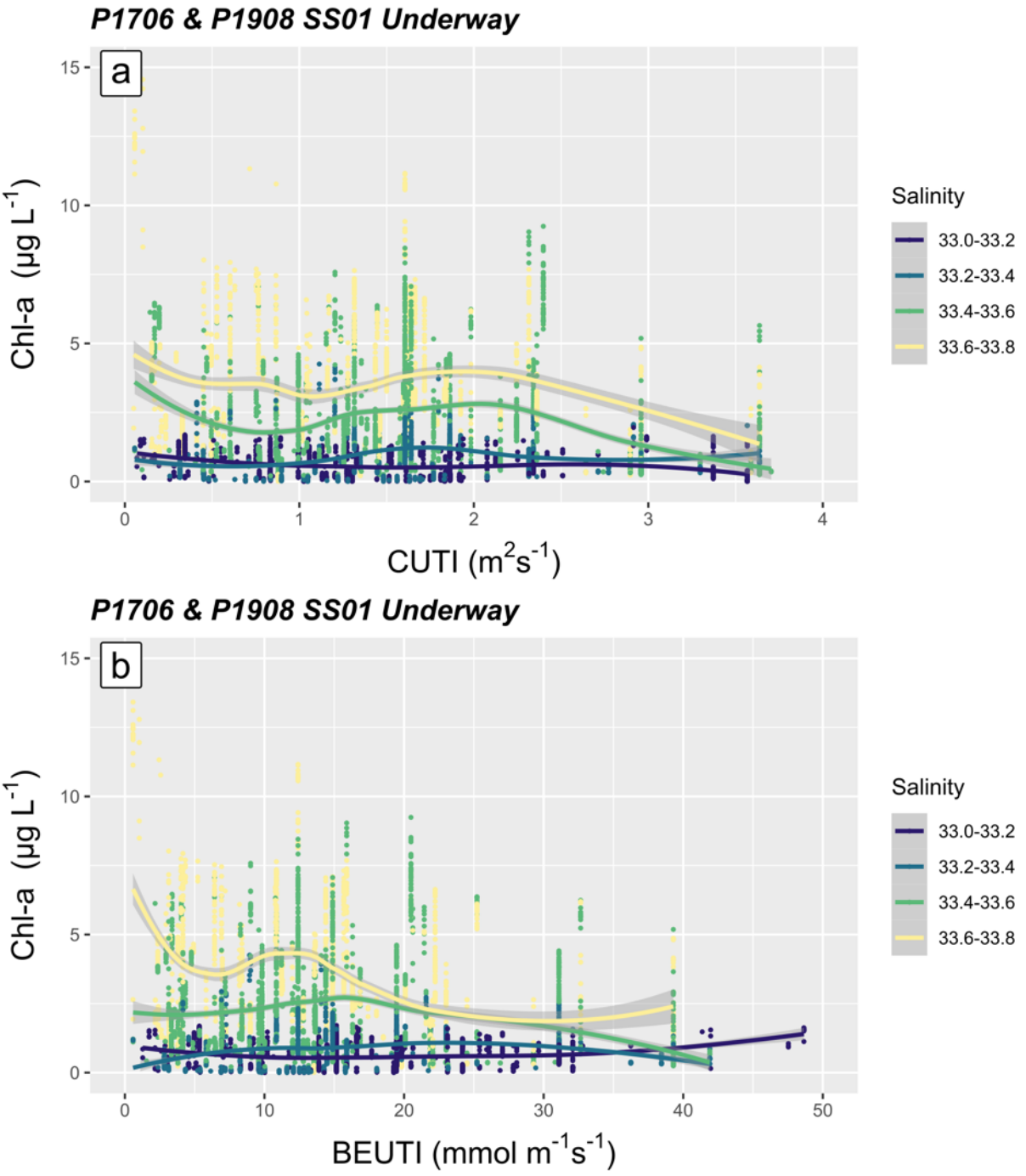

Supplemental Figure 4.5: The relationship between Coastal Upwelling Transport Index (CUTI) (a) and Chl-a and Biologically Effective Upwelling Transport Index (BEUTI) (b) and Chl-a for P1706 (Morro Bay filament cruise) and P1908 (Pt. Sur filament cruise) SeaSoar Survey 1 surface waters. Data were binned into salinity ranges (33.0–33.2 psu, 33.2–33.4 psu, 33.4–33.6 psu, and 33.6–33.8 psu); the colors of the lines and scatter points reflect the data within these ranges. The lines represent fits from the locally estimated scatterplot smoothing function (span = 0.75) and the grey shaded regions represent the 95% confidence intervals of these fits.

CONCLUSION

Summary

The main objectives of this dissertation were to characterize spatiotemporal patterns in hydrographic and plankton patchiness at mesoscale fronts and filaments in the California Current System, and to investigate the physical and biological forcing mechanisms that structure this patchiness. The main findings of this dissertation were that mesoscale fronts and filaments are highly advective systems that act as conduits of different water masses with distinct planktonic communities. Distinct "plankton patches", with nonuniform community structure and biomass, are shaped by upstream and source-water nutrient properties, as well as biological processes that occur along Lagrangian trajectories. These plankton patches become entrained into fronts or filaments, where they can converge with other patches and advect along a jet.

Initial, upstream, nutrient conditions can be predicted by the salinities of regional water-mass types (California Current or California Undercurrent), combined with the intensity and source depth of wind-driven coastal upwelling. Waters from the high-salinity California Undercurrent can support phytoplankton communities with higher Chl-a than the lower-salinity California Current waters. Also, even small-magnitude differences in salinity within CU waters, consistent with modulations in upwelling intensity at the coast, are correlated with incremental differences in Chl-a. Phytoplankton communities in CU waters are typically dominated by diatoms and have relatively high proportions of cryptophytes, dinoflagellates, and other eukaryotic phytoplankton. These communities exhibit relatively high F_v/F_m, especially in nutrient-replete conditions. In contrast, phytoplankton communities in CC waters are typically dominated by cyanobacteria and sometimes prymnesiophytes; these communities exhibit consistently low F_v/F_m. Unlike phytoplankton, zooplankton community composition does not show consistent patterns with water-mass type. Instead, the abundances of some zooplankton

taxa (e.g., copepods, rhizarians, and appendicularians) exhibit strong relationships with the age of a water parcel (the time since upwelling at the coast), indicating that the zooplankton community changes in water parcels as they are advected.

Thus, plankton patches undergo biological transformations (in terms of community structure and biomass) along Lagrangian trajectories, as water parcels transit fronts and filaments. These transformations are the result of ecosystem dynamics, such as growth, grazing, and iron limitation. Because grazing and iron limitation are both coupled with export processes (i.e., sinking of phytoplankton cells and fecal pellets), we can diagnose potential high-export waters based on declines in Chl-a and F_v/F_m. These declines are associated with grazing and sinking enhanced by iron limitation, respectively. In congruence with previous studies, I found the cross-shore decoupling of productivity and export to be mediated by the strong offshore advection of plankton patches in the frontal and filament jets that may persistently form off Pt. Conception, Morro Bay, and Pt. Sur, California.

Due to the patterns and processes associated with the strong advection of plankton patches, the way we sample dynamic mesoscale fronts and filaments is critically important. For example, the direction of successive transects across a front or filament could yield either a snapshot of one patch that gets resampled or a snapshot containing several distinct patches. While biological gradients along the axis of flow might look similar in both cases, each situation has different ecological implications that depend on the nutrient and plankton properties contained in the patches.

The results of this dissertation ultimately support the Boundary Condition Hypothesis (including the Pulsatile Patch Hypothesis) and Lagrangian Reaction Hypothesis and reject the Stationary Patch Hypothesis. In Chapter 1, I demonstrated that fluctuations in upstream boundary

conditions, associated with modulations in wind-driven upwelling intensity, generated distinct phytoplankton patches that transited along a front. In Chapter 2 and Chapter 3, I demonstrated that boundary conditions varied geographically, and initial nutrients conditions were correlated with water-mass type. In Chapter 2 and Chapter 4, I demonstrated that phytoplankton growth and grazing reactions occur during Lagrangian trajectories, and in some cases iron limitation can lead to changes in phytoplankton photophysiology (Chapter 4) as well as suppress phytoplankton growth (Chapter 3). I conclude that a combined Eulerian-Lagrangian approach is needed to appropriately characterize and interpret planktonic patchiness in mesoscale fronts and filaments, which are fundamentally non-steady-state systems.

Implications and future directions

In this dissertation, I presented several frameworks that can be used to diagnose patterns in planktonic community distribution and composition in the CCS: the SSH-PPH framework (Chapter 1), the Lagrangian history framework (Chapter 2), the salinity-MPC framework (Chapter 3), and the salinity-age framework (Chapter 4). Using these frameworks, we can begin to identify patterns in biological diversity, ecological hotspots, and carbon export in EBUSs; however, future work is needed to augment these frameworks and increase their diagnostic and predictive power.

Biological diversity

In this dissertation, I showed that the taxonomic composition of phytoplankton and zooplankton communities could be diagnosed by combined patterns in salinity (i.e., water masses) and advection. Therefore, by knowing the water-mass type, which is correlated with initial nutrient supply, and the advection history of a water parcel, we can potentially predict planktonic community composition and how it changes. This has important implications for describing spatial and temporal patterns and controls of biological diversity.

In the CCS, cross-shore patterns in microbial diversity are strongly correlated with nutrient supply across both seasonal and interannual timescales (James et al., 2022). Future work using the Lagrangian framework presented in this dissertation combined with highly resolved taxonomic information could help contextualize this broad regional gradient. This framework could help evaluate where, when, and why waters are more biologically diverse than others—and how diversity might change along Lagrangian trajectories. Different planktonic species or functional types exhibit different responses to changes in oceanic conditions, such as short-term shifts in nutrient supply during upwelling cycles (Lampe et al., 2021), multi-year climate oscillations (Bode et al., 2013; Lilly & Ohman, 2021), or long-term shifts in temperature (Anderson et al., 2021). Therefore, identifying the occurrence and distribution of plankton, in tandem with community composition and diversity, can help to characterize multiscale planktonic ecosystem responses.

Ecological hotspots

In this dissertation, phytoplankton (Chl-a) concentrations were diagnosed by patterns in water masses and the ages of water parcels: the biological potential of a water parcel, when controlled from the bottom-up by phytoplankton, is predictable. Using the salinity-MPC framework as a guide, we may be able to identify locations where phytoplankton biomass meets its maximum potential concentration, thereby identifying ecological hotspots.

Future work could further investigate coastal regions off California that are suspected to be hotspots for marine mammals and seabirds; one such region is the Santa Lucia Escarpment, located offshore of Morro Bay (Russell et al., in prep). The drivers of potentially enhanced biological activity at this site are unknown. Strikingly, CCE LTER sampling (used in Chapter 3 and Chapter 4) in 2017 included this region, which is now part of the newly formed and culturally important Chumash Heritage National Marine Sanctuary. The results of this

dissertation bolster the hypothesis that biological productivity in the Santa Lucia region is fueled by the advective delivery of Chl-a-rich waters along persistent upwelling filaments. Characterizing patterns in salinity, MPC, and observed Chl-a in this region using long-term datasets could help identify the roles of bottom-up processes in generating and maintaining an ecological hotspot. Importantly, because hotspots of zooplankton and marine predators may be decoupled in space and time from regions of high phytoplankton biomass (Fiechter et al., 2020; Messié & Chavez, 2017), Lagrangian studies to characterize the role of advection in structuring the timing and occurrence of such hotspots are needed. Furthermore, the use of salinity as a diagnostic of Chl-a concentration also allows for the analysis of phytoplankton patterns in regions that have historically lacked observations or long-term monitoring.

Carbon export

In this dissertation, by using diagnostic metrics and qualitative analyses, I associated time-dependent declines in Chl-a with grazing and—in some cases—sinking enhanced by iron limitation. I then qualitatively linked grazing and iron limitation processes to the export of phytoplankton from the euphotic zone—through direct phytoplankton cell sinking and zooplankton fecal-pellet production (Stukel et al., 2011). These analyses would benefit from being augmented with quantitative measurements to enhance the prediction of patterns in carbon export.

Specifically, future work incorporating grazing and export rates (e.g., sinking particle fluxes) into the salinity-age framework could improve the identification of when and where waters contribute to high export production. Importantly, export rates are highly influenced by particle sinking speeds, which vary based on many factors that also depend on planktonic community composition. These factors include phytoplankton cell size, degree of silicification in diatoms, fecal origins, and pellet shapes and sizes (Buesseler et al., 2007; Gowing et al., 2001;

Small & Ellis, 1992; Smayda, 1970; Wilson et al., 2008). Therefore, understanding how planktonic community composition changes along Lagrangian trajectories could help constrain export estimates in this region.

Long-term changes in hydrography and circulation

In this dissertation, I described how biological patchiness is fundamentally linked to hydrographic patchiness, and so patterns in biological properties are correlated with salinity and water-mass type. However, water properties in the CCS are variable and changing over time, and this could drive biological variability.

Long-term water-mass variability off the coast of southern California has been attributed to modifications in source waters (Bograd et al., 2015). These modulations have led to anomalous salinity changes in the California Current (Ren & Rudnick, 2021) and a long-term increase in temperature and salinity in the California Undercurrent (Meinvielle & Johnson, 2013). Upwelling source waters have also changed over time, based on fluctuations in the upwelling cell forced by the Pacific Decadal Oscillation (Chhak & Di Lorenzo, 2007; Song et al., 2011). The nitrate concentrations of upwelled waters are projected to decline in the future (Pozo Buil et al., 2021), potentially having strong consequences for biological productivity throughout the CCS (Jacox et al., 2024) and specifically off central California, where wind-driven upwelling has been increasing (García-Reyes & Largier, 2010). Examining how these long-term and decadal-scale modulations affect the salinity-nitrate and salinity-chlorophyll relationships presented in this dissertation could further elucidate long-term changes in productivity.

Additionally, long-term changes in mesoscale circulation have been altering how water masses—and biological properties associated with these water masses—are laterally distributed in the CCS. Basin-scale processes driven by the El Niño Southern Oscillation have led to changes in mesoscale energy in the CCS, with increased mesoscale activity detected during

relatively cold La Niña years (Keister & Strub, 2008). Additionally, as stratification increases due to ocean warming, eddy kinetic energy in the CCS is also increasing (Cordero-Quirós et al., 2022). Furthermore, despite a long-term increase in frontal frequency in the CCS, anomalously warm periods are associated with decreased frontal frequency which are consistent with declines in Chl-a. Therefore, changes in the energy and frequency of fronts, filaments, and eddies and increases in ocean temperature have important impacts on biological communities that are attracted to, aggregated in, or transported by these features (Abrahms et al., 2018; Brodeur et al., 2019; Hyrenbach & Veit, 2003; Koslow et al., 2017).

In summary, we cannot evaluate the links between biological and hydrographic patchiness using a static snapshot of the CCS. Instead, we must investigate biological patchiness and its controls within an evolving system that is shaped by hydrography and circulation, which are changing in response to climate oscillations and ocean warming trends.

REFERENCES

Abbott, M., & Barksdale, B. (1991). PHYTOPLANKTON PIGMENT PATTERNS AND WIND FORCING OFF CENTRAL CALIFORNIA. *JOURNAL OF GEOPHYSICAL RESEARCH-OCEANS*, *96*, 14649-14667.

Abbott, M., Brink, K., Booth, C., Blasco, D., Codispoti, L., Niler, P., & Ramp, S. (1990). OBSERVATIONS OF PHYTOPLANKTON AND NUTRIENTS FROM A LAGRANGIAN DRIFTER OFF NORTHERN CALIFORNIA. *JOURNAL OF GEOPHYSICAL RESEARCH-OCEANS*, *95*, 9393-9409.

Abrahms, B., Scales, K., Hazen, E., Bograd, S., Schick, R., Robinson, P., & Costa, D. (2018). Mesoscale activity facilitates energy gain in a top predator. *PROCEEDINGS OF THE ROYAL SOCIETY B-BIOLOGICAL SCIENCES*, *285*, Article 20181101. https://doi.org/10.1098/rspb.2018.1101

Allen, J., Brown, L., Sanders, R., Moore, C., Mustard, A., Fielding, S., Lucas, M., Rixen, M., Savidge, G., Henson, S, & Mayor, D. (2005). Diatom carbon export enhanced by silicate upwelling in the northeast Atlantic. *NATURE*, *437*, 728-732. https://doi.org/10.1038/nature03948

Amos, C. M., Castelao, R. M., & Medeiros, P. M. (2019). Offshore transport of particulate organic carbon in the California Current System by mesoscale eddies [Article]. *Nature Communications*, *10*, 8, Article 4940. https://doi.org/10.1038/s41467-019-12783-5

Anderson, S., Barton, A., Clayton, S., Dutkiewicz, S., & Rynearson, T. (2021). Marine phytoplankton functional types exhibit diverse responses to thermal change. *NATURE COMMUNICATIONS*, *12*, Article 6413. https://doi.org/10.1038/s41467-021-26651-8

Armstrong, F. A., Stearns, C. R., & Strickland, J. D. (1967). MEASUREMENT OF UPWELLING AND SUBSEQUENT BIOLOGICAL PROCESSES BY MEANS OF TECHNICON AUTOANALYZER AND ASSOCIATED EQUIPMENT [Note]. *Deep-Sea Research*, *14*(3), 381-+. https://doi.org/10.1016/0011-7471(67)90082-4

Ballance, L., Pitman, R., & Reilly, S. (1997). Seabird community structure along a productivity gradient: Importance of competition and energetic constraint. *ECOLOGY*, *78*, 1502-1518.

Barlow, J., Kahru, M., & Mitchell, B. (2008). Cetacean biomass, prey consumption, and primary production requirements in the California Current ecosystem. *MARINE ECOLOGY PROGRESS SERIES*, *371*, 285-295. https://doi.org/10.3354/meps07695

Barth, J. A., Pierce, S. D., & Cowles, T. J. (2005). Mesoscale structure and its seasonal evolution in the northern California Current System [Article]. *Deep-Sea Research Part Ii-Topical Studies in Oceanography*, *52*(1-2), 5-28. https://doi.org/10.1016/j.dsr2.2004.09.026

Barth, J. A., Pierce, S. D., & Smith, R. L. (2000). A separating coastal upwelling jet at Cape Blanco, Oregon and its connection to the California Current System [Article]. *Deep-Sea Research Part Ii-Topical Studies in Oceanography*, *47*(5-6), 783-810. https://doi.org/10.1016/s0967-0645(99)00127-7

Behrenfeld, M., & Milligan, A. (2013). Photophysiological Expressions of Iron Stress in Phytoplankton. In *ANNUAL REVIEW OF MARINE SCIENCE, VOL 5* (Vol. 5, pp. 217-246).

Belkin, I. (2021). Remote Sensing of Ocean Fronts in Marine Ecology and Fisheries. *REMOTE SENSING*, *13*, Article 883. https://doi.org/10.3390/rs13050883

Biard, T. (2015). *Diversité, biogéographie et écologie des Collodaires (Radiolaires) dans l'océan mondial* Université Pierre et Marie Curie - Paris VI].

Biard, T., & Ohman, M. (2020). Vertical niche definition of test-bearing protists (Rhizaria) into the twilight zone revealed by in situ imaging. *LIMNOLOGY AND OCEANOGRAPHY*, *65*, 2583-2602. https://doi.org/10.1002/lno.11472

Bishop, J., & Wood, T. (2008). Particulate matter chemistry and dynamics in the twilight zone at VERTIGO ALOHA and K2 sites. *DEEP-SEA RESEARCH PART I-OCEANOGRAPHIC RESEARCH PAPERS*, *55*, 1684-1706. https://doi.org/10.1016/j.dsr.2008.07.012

Bode, A., Alvarez-Ossorio, M., Miranda, A., & Ruiz-Villarreal, M. (2013). Shifts between gelatinous and crustacean plankton in a coastal upwelling region. *ICES JOURNAL OF MARINE SCIENCE*, *70*, 934-942. https://doi.org/10.1093/icesjms/fss193

Bograd, S. J., Buil, M. P., Di Lorenzo, E., Castro, C. G., Schroeder, I. D., Goericke, R., Anderson, C. R., Benitez-Nelson, C., & Whitney, F. A. (2015). Changes in source waters to the Southern California Bight [Article]. *Deep-Sea Research Part II-Topical Studies in Oceanography*, *112*, 42-52. https://doi.org/10.1016/j.dsr2.2014.04.009

Bograd, S. J., & Lynn, R. J. (2003). Long-term variability in the Southern California Current System [Article]. *Deep-Sea Research Part II: Topical Studies in Oceanography*, *50*(14-16), 2355-2370. https://doi.org/10.1016/s0967-0645(03)00131-0

Bograd, S. J., Schroeder, I. D., & Jacox, M. G. (2019). A water mass history of the Southern California current system [Article]. *Geophysical Research Letters*, *46*(12), 6690-6698. https://doi.org/10.1029/2019gl082685

Bourne, H., Bishop, J., Connors, E., & Wood, T. (2021). Carbon export and fate beneath a dynamic upwelled filament off the California coast. *BIOGEOSCIENCES*, *18*, 3053-3086. https://doi.org/10.5194/bg-18-3053-2021

Boyd, P., Jickells, T., Law, C., Blain, S., Boyle, E., Buesseler, K., Coale, K.H., Cullen, J.J., de Baar, H.J.W., Follows, M., Harvey, M., Lancelot, C., Levasseur, M., Owens, N.P.J., Pollard, R., Rivkin, R.B., Sarmiento, J., Schoemann, V., Smetacek, V., Takeda, S., Tsuda, A., Turner, S., & Watson, A. (2007). Mesoscale iron enrichment experiments 1993-2005: Synthesis and future directions. *SCIENCE*, *315*, 612-617. https://doi.org/10.1126/science.1131669

Brandao, M. C., Benedetti, F., Martini, S., Soviadan, Y. D., Irisson, J. O., Romagnan, J. B., Elineau, A., Desnos, C., Jalabert, L., Freire, A. S., Picheral, M., Guidi, L., Gorsky, G., Bowler, C., Karp-Boss, L., Henry, N., de Vargas, C., Sullivan, M. B., Stemmann, L., Lombard, F., & Tara Oceans Consortium, C. (2021). Macroscale patterns of oceanic zooplankton composition

and size structure [Article]. *Scientific Reports*, *11*(1), 19, Article 15714. https://doi.org/10.1038/s41598-021-94615-5

Brink, K. H. (1992). COLD-WATER FILAMENTS IN THE CALIFORNIA CURRENT SYSTEM [Article]. *South African Journal of Marine Science-Suid-Afrikaanse Tydskrif Vir Seewetenskap*, *12*, 53-60.

Brodeur, R. D., Auth, T. D., & Phillips, A. J. (2019). Major Shifts in Pelagic Micronekton and Macrozooplankton Community Structure in an Upwelling Ecosystem Related to an Unprecedented Marine Heatwave [Article]. *Frontiers in Marine Science*, *6*, 15, Article 212. https://doi.org/10.3389/fmars.2019.00212

Bruland, K. W., Rue, E. L., Smith, G. J., & DiTullio, G. R. (2005). Iron, macronutrients and diatom blooms in the Peru upwelling regime: brown and blue waters of Peru [Article]. *Marine Chemistry*, *93*(2-4), 81-103. https://doi.org/10.1016/j.marchem.2004.06.011

Brzezinski, M. A., Krause, J. W., Bundy, R. M., Barbeau, K. A., Franks, P., Goericke, R., Landry, M. R., & Stukel, M. R. (2015). Enhanced silica ballasting from iron stress sustains carbon export in a frontal zone within the California Current [Article]. *Journal of Geophysical Research-Oceans*, *120*(7), 4654-4669. https://doi.org/10.1002/2015jc010829

Buesseler, K. O., Antia, A. N., Chen, M., Fowler, S. W., Gardner, W. D., Gustafsson, O., Harada, K., Michaels, A. F., van der Loeff'o, M. R., Sarin, M., Steinberg, D. K, & Trull, T. (2007). An assessment of the use of sediment traps for estimating upper ocean particle fluxes. *JOURNAL OF MARINE RESEARCH*, *65*(3), 345-416. https://doi.org/10.1357/002224007781567621

Calbet, A., & Landry, M. R. (2004). Phytoplankton growth, microzooplankton grazing, and carbon cycling in marine systems [Article]. *Limnology and Oceanography*, *49*(1), 51-57. https://doi.org/10.4319/lo.2004.49.1.0051

Campbell, D., Hurry, V., Clarke, A., Gustafsson, P., & Öquist, G. (1998). Chlorophyll fluorescence analysis of cyanobacterial photosynthesis and acclimation [Review]. *MICROBIOLOGY AND MOLECULAR BIOLOGY REVIEWS*, *62*, 667-+.

Capitanio, F., & Esnal, G. (1998). Vertical distribution of maturity stages of *Oikopleura dioica* (Tunicata, Appendicularia) in the frontal system off Valdes Peninsula, Argentina. *BULLETIN OF MARINE SCIENCE*, *63*, 531-539.

Cermeño, P., Marañón, E., Rodríguez, J., & Fernández, E. (2005). Large-sized phytoplankton sustain higher carbonspecific photosynthesis than smaller cells in a coastal eutrophic ecosystem [Article]. *Marine Ecology Progress Series*, *297*, 51-60. https://doi.org/10.3354/meps297051

Chabert, P., d'Ovidio, F., Echevin, V., Stukel, M. R., & Ohman, M. D. (2021). Cross-Shore Flow and Implications for Carbon Export in the California Current Ecosystem: A Lagrangian Analysis [Article]. *Journal of Geophysical Research: Oceans*, *126*(2), 14, Article e2020JC016611. https://doi.org/10.1029/2020jc016611

Chase, Z., Strutton, P., & Hales, B. (2007). Iron links river runoff and shelf width to phytoplankton biomass along the U.S. West Coast. *GEOPHYSICAL RESEARCH LETTERS*, *34*, Article L04607. https://doi.org/10.1029/2006GL028069

Chavez, F., Barber, R., Kosro, P., Huyer, A., Ramp, S., Stanton, T., & Demendiola, B. (1991). HORIZONTAL TRANSPORT AND THE DISTRIBUTION OF NUTRIENTS IN THE COASTAL TRANSITION ZONE OFF NORTHERN CALIFORNIA - EFFECTS ON PRIMARY PRODUCTION, PHYTOPLANKTON BIOMASS AND SPECIES COMPOSITION. *JOURNAL OF GEOPHYSICAL RESEARCH-OCEANS*, *96*, 14833-14848.

Chavez, F. P., & Messié, M. (2009). A comparison of Eastern Boundary Upwelling Ecosystems [Review]. *Progress in Oceanography*, *83*(1-4), 80-96. https://doi.org/10.1016/j.pocean.2009.07.032

Checkley, D. M., & Barth, J. A. (2009). Patterns and processes in the California Current System [Review]. *Progress in Oceanography*, *83*(1-4), 49-64. https://doi.org/10.1016/j.pocean.2009.07.028

Chekalyuk, A., & Hafez, M. (2008). Advanced laser fluorometry of natural aquatic environments [Article]. *Limnology and Oceanography-Methods*, *6*, 591-609. https://doi.org/10.4319/lom.2008.6.591

Chekalyuk, A. M., Landry, M. R., Goericke, R., Taylor, A. G., & Hafez, M. A. (2012). Laser fluorescence analysis of phytoplankton across a frontal zone in the California Current ecosystem [Article]. *Journal of Plankton Research*, *34*(9), 761-777. https://doi.org/10.1093/plankt/fbs034

Chelton, D., Gaube, P., Schlax, M., Early, J., & Samelson, R. (2011). The Influence of Nonlinear Mesoscale Eddies on Near-Surface Oceanic Chlorophyll. *SCIENCE*, *334*, 328-332. https://doi.org/10.1126/science.1208897

Chelton, D. B. (1982). Large-scale response of the California Current to forcing by the wind stress curl. In (Vol. 23, pp. 130-148). California Cooperative Oceanic Fisheries Investigations Reports: California Cooperative Oceanic Fisheries Investigations

Chenillat, F., Franks, P. J. S., & Combes, V. (2016). Biogeochemical properties of eddies in the California Current System [Article]. *Geophysical Research Letters*, *43*(11), 5812-5820. https://doi.org/10.1002/2016gl068945

Chenillat, F., Franks, P. J. S., Riviere, P., Capet, X., Grima, N., & Blanke, B. (2015). Plankton dynamics in a cyclonic eddy in the Southern California Current System [Article]. *Journal of Geophysical Research: Oceans*, *120*(8), 5566-5588. https://doi.org/10.1002/2015jc010826

Chhak, K., & Di Lorenzo, E. (2007). Decadal variations in the California Current upwelling cells. *GEOPHYSICAL RESEARCH LETTERS*, *34*(14), Article L14604. https://doi.org/10.1029/2007GL030203

Chisholm, S. W. (1992). PHYTOPLANKTON SIZE [Proceedings Paper]. *Primary Productivity and Biogeochemical Cycles in the Sea*, *43*, 213-237.

Claustre, H., Kerherve, P., Marty, J. C., Prieur, L., Videau, C., & Hecq, J. H. (1994). Phytoplankton dynamics associated with a geostrophic front: Ecological and biogeochemical implications [Article]. *Journal of Marine Research*, *52*(4), 711-742. https://doi.org/10.1357/0022240943077000

Clayton, S., Dutkiewicz, S., Jahn, O., & Follows, M. J. (2013). Dispersal, eddies, and the diversity of marine phytoplankton. *Limnology and Oceanography: Fluids and Environments*, *3*(1), 182-197. https://doi.org/https://doi.org/10.1215/21573689-2373515

Cloern, J., Jassby, A., Schraga, T., Nejad, E., & Martin, C. (2017). Ecosystem variability along the estuarine salinity gradient: Examples from long-term study of San Francisco Bay [Article]. *LIMNOLOGY AND OCEANOGRAPHY*, *62*, S272-S291. https://doi.org/10.1002/lno.10537

Comas-Rodríguez, I., Hernández-Guerra, A., & Mcdonagh, E. (2010). Referencing geostrophic velocities using ADCP data at 24.5°N (North Atlantic). *SCIENTIA MARINA*, *74*, 331-338. https://doi.org/10.3989/scimar.2010.74n2331

Conomos, T. J., Smith, R. E., Peterson, D. H., Hager, S. W., & Schemel, L. E. (1979). Processes affecting seasonal distributions of water properties in the San Francisco Bay estuarine system. *San Francisco Bay: The urbanized estuary*, 115–142.

Cordero-Quirós, N., Jacox, M., Buil, M., & Bograd, S. (2022). Future Changes in Eddy Kinetic Energy in the California Current System From Dynamically Downscaled Climate Projections. *GEOPHYSICAL RESEARCH LETTERS*, *49*, Article e2022GL099042. https://doi.org/10.1029/2022GL099042

Cowles, T., Desiderio, R., & Neuer, S. (1993). INSITU CHARACTERIZATION OF PHYTOPLANKTON FROM VERTICAL PROFILES OF FLUORESCENCE EMISSION-SPECTRA. *MARINE BIOLOGY*, *115*, 217-222.

Cravo, A., Relvas, P., Cardeira, S., Rita, F., Madureira, M., & Sanchez, R. (2010). An upwelling filament off southwest Iberia: Effect on the chlorophyll a and nutrient export [Article]. *Continental Shelf Research*, *30*(15), 1601-1613. https://doi.org/10.1016/j.csr.2010.06.007

Cushman-Roisin, B., & Beckers, J.-M. (2011). Chapter 6 - Transport and Fate. In B. Cushman-Roisin & J.-M. Beckers (Eds.), *Introduction to Geophysical Fluid Dynamics: Physical and Numerical Aspects* (Vol. 101, pp. 163-202). Academic Press. https://doi.org/https://doi.org/10.1016/B978-0-12-088759-0.00006-7

d'Ovidio, F., De Monte, S., Alvain, S., Dandonneau, Y., & Levy, M. (2010). Fluid dynamical niches of phytoplankton types [Article]. *Proceedings of the National Academy of Sciences of the United States of America*, *107*(43), 18366-18370. https://doi.org/10.1073/pnas.1004620107

d'Ovidio, F., Della Penna, A., Trull, T., Nencioli, F., Pujol, M., Rio, M., Park, Y.H., Cotté, C., Zhou, M., & Blain, S. (2015). The biogeochemical structuring role of horizontal stirring: Lagrangian perspectives on iron delivery downstream of the Kerguelen Plateau. *BIOGEOSCIENCES*, *12*, 5567-5581. https://doi.org/10.5194/bg-12-5567-2015

d'Ovidio, F., Fernandez, V., Hernandez-Garcia, E., & Lopez, C. (2004). Mixing structures in the Mediterranean Sea from finite-size Lyapunov exponents [Article]. *Geophysical Research Letters*, *31*(17), 4, Article L17203. https://doi.org/10.1029/2004gl020328

de Verneil, A., & Franks, P. J. S. (2015). A pseudo-Lagrangian method for remapping ocean biogeochemical tracer data: Calculation of net Chl-a growth rates [Article]. *Journal of Geophysical Research: Oceans*, *120*(7), 4962-4979. https://doi.org/10.1002/2015jc010898

de Verneil, A., Franks, P. J. S., & Ohman, M. D. (2019). Frontogenesis and the Creation of Fine-Scale Vertical Phytoplankton Structure [Article]. *Journal of Geophysical Research: Oceans*, *124*(3), 1509-1523. https://doi.org/10.1029/2018jc014645

Deibel, D., & Lowen, B. (2012). A review of the life cycles and life-history adaptations of pelagic tunicates to environmental conditions. *ICES JOURNAL OF MARINE SCIENCE*, *69*, 358-369. https://doi.org/10.1093/icesjms/fsr159

Della Penna, A., Trull, T., Wotherspoon, S., De Monte, S., Johnson, C., & d'Ovidio, F. (2018). Mesoscale Variability of Conditions Favoring an Iron-Induced Diatom Bloom Downstream of the Kerguelen Plateau. *JOURNAL OF GEOPHYSICAL RESEARCH-OCEANS*, *123*, 3355-3367. https://doi.org/10.1029/2018JC013884

Di Lorenzo, E., & Ohman, M. (2013). A double-integration hypothesis to explain ocean ecosystem response to climate forcing. *PROCEEDINGS OF THE NATIONAL ACADEMY OF SCIENCES OF THE UNITED STATES OF AMERICA*, *110*, 2496-2499. https://doi.org/10.1073/pnas.1218022110

Dolan, J. R. (2010). Morphology and Ecology in Tintinnid Ciliates of the Marine Plankton: Correlates of Lorica Dimensions [Article]. *Acta Protozoologica*, *49*(3), 235-244.

Droghei, R., Nardelli, B., & Santoleri, R. (2016). Combining In Situ and Satellite Observations to Retrieve Salinity and Density at the Ocean Surface. *JOURNAL OF ATMOSPHERIC AND OCEANIC TECHNOLOGY*, *33*, 1211-1223. https://doi.org/10.1175/JTECH-D-15-0194.1

Dugenne, M., Freitas, F., Wilson, S., Karl, D., & White, A. (2021). Life and death of *Crocosphaera* sp. in the Pacific Ocean: Fine scale predator-prey dynamics (vol 65, pg 2603, 2021). *LIMNOLOGY AND OCEANOGRAPHY*, *66*, 3856-3856. https://doi.org/10.1002/lno.11932

Eiane, K., & Ohman, M. (2004). Stage-specific mortality of *Calanus finmarchicus*, *Pseudocalanus elongatus* and *Oithona similis* on Fladen Ground, North Sea, during a spring bloom. *MARINE ECOLOGY PROGRESS SERIES*, *268*, 183-193.

Elrod, V., Berelson, W., Coale, K., & Johnson, K. (2004). The flux of iron from continental shelf sediments: A missing source for global budgets. *GEOPHYSICAL RESEARCH LETTERS*, *31*, Article L12307. https://doi.org/10.1029/2004GL020216

Eppley, R. W., & Renger, E. H. (1986). Nitrate-based primary production in nutrient-depleted surface waters off California. *Oceanogr. Trop*, *21*(2), 229-238.

Exton, R., Houghton, W., Esaias, W., Haas, L., & Hayward, D. (1983). SPECTRAL DIFFERENCES AND TEMPORAL STABILITY OF PHYCOERYTHRIN FLUORESCENCE IN ESTUARINE AND COASTAL WATERS DUE TO THE DOMINATION OF LABILE CRYPTOPHYTES AND STABILE CYANOBACTERIA. *LIMNOLOGY AND OCEANOGRAPHY*, *28*, 1225-1230.

Falkowski, P. G., Koblfzek, M., Gorbunov, M., & Kolber, Z. (2004). Development and Application of Variable Chlorophyll Fluorescence Techniques in Marine Ecosystems. In G. C. Papageorgiou, Govindjee (Ed.), *Advances in Photosynthesis and Respiration* (Vol. 19). Springer. https://doi.org/https://doi.org/10.1007/978-1-4020-3218-9_30

Feinberg, L. R., & Dam, H. G. (1998). Effects of diet on dimensions, density and sinking rates of fecal pellets of the copepod Acartia tonsa [Article]. *Marine Ecology Progress Series*, *175*, 87-96. https://doi.org/10.3354/meps175087

Fiechter, J., & Moore, A. (2024). Physical and Biogeochemical Properties of California Current Upwelled Source Waters. *JOURNAL OF GEOPHYSICAL RESEARCH-OCEANS*, *129*, Article e2023JC020164. https://doi.org/10.1029/2023JC020164

Fiechter, J., Santora, J., Chavez, F., Northcott, D., & Messié, M. (2020). Krill Hotspot Formation and Phenology in the California Current Ecosystem. *GEOPHYSICAL RESEARCH LETTERS*, *47*, Article e2020GL088039. https://doi.org/10.1029/2020GL088039

Fiechter, J., Santora, J. A., Chavez, F., Northcott, D., & Messié, M. (2020). Krill Hotspot Formation and Phenology in the California Current Ecosystem [Article]. *Geophysical Research Letters*, *47*(13), 10, Article e2020GL088039. https://doi.org/10.1029/2020gl088039

Forsch, K. O., Fulton, K. C., Weiss, M. M., Krause, J. W., Stukel, M. R., & Barbeau, K. A. (2023). Iron Limitation and Biogeochemical Effects in Southern California Current Coastal Upwelling Filaments [Article]. *Journal of Geophysical Research-Oceans*, *128*(11), 24, Article e2023JC019961. https://doi.org/10.1029/2023jc019961

Franks, P. J. S. (1992). Sink or swim: accumulation of biomass at fronts [Article]. *Marine Ecology Progress Series*, *82*(1), 1-12. https://doi.org/10.3354/meps082001

Franks, P. J. S. (2014). Has Sverdrup's critical depth hypothesis been tested? Mixed layers vs. turbulent layers. *ICES Journal of Marine Science*, *72*(6), 1897-1907. https://doi.org/10.1093/icesjms/fsu175

Franks, P. J. S., & Walstad, L. J. (1997). Phytoplankton patches at fronts: A model of formation and response to wind events [Article]. *Journal of Marine Research*, *55*(1), 1-29. https://doi.org/10.1357/0022240973224472

Gangrade, S., & Franks, P. J. S. (2023). Phytoplankton Patches at Oceanic Fronts Are Linked to Coastal Upwelling Pulses: Observations and Implications in the California Current System [Article]. *Journal of Geophysical Research-Oceans*, *128*(3), 21, Article e2022JC019095. https://doi.org/10.1029/2022jc019095

Gangrade, S., Franks, P. J. S., Forsch, K. O., & Barbeau, K. A. (in review). Salinity is diagnostic of maximum potential chlorophyll and phytoplankton community structure in an Eastern Boundary Upwelling System. In.

Gangrade, S., & Mangolte, I. (2024). Patchiness of plankton communities at fronts explained by Lagrangian history of upwelled water parcels [Article; Early Access]. *LIMNOLOGY AND OCEANOGRAPHY*. https://doi.org/10.1002/lno.12654

García-Reyes, M., & Largier, J. (2010). Observations of increased wind-driven coastal upwelling off central California. *JOURNAL OF GEOPHYSICAL RESEARCH-OCEANS*, *115*, Article C04011. https://doi.org/10.1029/2009JC005576

Gastauer, S., & Ohman, M. (2024). Resolving abrupt frontal gradients in zooplankton community composition and marine snow fields with an autonomous *Zooglider*. *LIMNOLOGY AND OCEANOGRAPHY*. https://doi.org/10.1002/lno.12642

Gaube, P., Chelton, D., Strutton, P., & Behrenfeld, M. (2013). Satellite observations of chlorophyll, phytoplankton biomass, and Ekman pumping in nonlinear mesoscale eddies. *JOURNAL OF GEOPHYSICAL RESEARCH-OCEANS*, *118*, 6349-6370. https://doi.org/10.1002/2013JC009027

Gay, P., & Chereskin, T. (2009). Mean structure and seasonal variability of the poleward undercurrent off southern California. *JOURNAL OF GEOPHYSICAL RESEARCH-OCEANS*, *114*, Article C02007. https://doi.org/10.1029/2008JC004886

Giddings, A., Franks, P. J. S., & Baumann-Pickering, S. (2022). Monthly to Decadal Variability of Mesoscale Stirring in the California Current System: Links to Upwelling, Climate Forcing, and Chlorophyll Transport [Article]. *Journal of Geophysical Research: Oceans*, *127*(6), 20, Article e2021JC018180. https://doi.org/10.1029/2021jc018180

Goericke, R. (2011a). THE SIZE STRUCTURE OF MARINE PHYTOPLANKTON-WHAT ARE THE RULES? [Article]. *California Cooperative Oceanic Fisheries Investigations Reports*, *52*, 198-204.

Goericke, R. (2011b). THE STRUCTURE OF MARINE PHYTOPLANKTON COMMUNITIES-PATTERNS, RULES AND MECHANISMS [Article]. *California Cooperative Oceanic Fisheries Investigations Reports*, *52*, 182-197.

Goericke, R., & Montoya, J. P. (1998). Estimating the contribution of microalgal taxa to chlorophyll a in the field - variations of pigment ratios under nutrient- and light-limited growth [Article]. *Marine Ecology Progress Series*, *169*, 97-112. https://doi.org/10.3354/meps169097

González-Silvera, A., Santamaría-del-Angel, E., Camacho-Ibar, V., López-Calderón, J., Santander-Cruz, J., & Mercado-Santana, A. (2020). The Effect of Cold and Warm Anomalies on Phytoplankton Pigment Composition in Waters off the Northern Baja California Peninsula (Mexico): 2007-2016 [Article]. *JOURNAL OF MARINE SCIENCE AND ENGINEERING*, *8*, Article 533. https://doi.org/10.3390/jmse8070533

Good, S., Fiedler, E., Mao, C., Martin, M., Maycock, A., Reid, R., Roberts-Jones, J., Searle, T.,Waters, J., While, J., & Worsfold, M. (2020). The Current Configuration of the OSTIA System for Operational Production of Foundation Sea Surface Temperature and Ice Concentration Analyses. *REMOTE SENSING*, *12*, Article 720. https://doi.org/10.3390/rs12040720

Gorbunov, M., & Falkowski, P. (2022). Using Chlorophyll Fluorescence to Determine the Fate of Photons Absorbed by Phytoplankton in the World's Oceans. *ANNUAL REVIEW OF MARINE SCIENCE*, *14*, 213-238. https://doi.org/10.1146/annurev-marine-032621-122346

Gowing, M. M., Garrison, D. L., Kunze, H. B., & Winchell, C. J. (2001). Biological components of Ross Sea short-term particle fluxes in the austral summer of 1995-1996. *DEEP-SEA RESEARCH PART I-OCEANOGRAPHIC RESEARCH PAPERS*, *48*(12), 2645-2671. https://doi.org/10.1016/S0967-0637(01)00034-6

Greene, R. M., Geider, R. J., Kolber, Z., & Falkowski, P. G. (1992). IRON-INDUCED CHANGES IN LIGHT HARVESTING AND PHOTOCHEMICAL ENERGY-CONVERSION PROCESSES IN EUKARYOTIC MARINE-ALGAE. *Plant Physiology*, *100*(2), 565-575. https://doi.org/10.1104/pp.100.2.565

Gruber, N., Frenzel, H., Doney, S., Marchesiello, P., McWilliams, J., Moisan, J., Oram, J.J., Plattner, G.K., & Stolzenbach, K. (2006). Eddy-resolving simulation of plankton ecosystem dynamics in the California Current System. *DEEP-SEA RESEARCH PART I-OCEANOGRAPHIC RESEARCH PAPERS*, *53*, 1483-1516. https://doi.org/10.1016/j.dsr.2006.06.005

Haberlin, D., Raine, R., McAllen, R., & Doyle, T. (2019). Distinct gelatinous zooplankton communities across a dynamic shelf sea. *LIMNOLOGY AND OCEANOGRAPHY*, *64*, 1802-1818. https://doi.org/10.1002/lno.11152

He, J., & Mahadevan, A. (2021). How the Source Depth of Coastal Upwelling Relates to Stratification and Wind. *Journal of Geophysical Research: Oceans*, *126*(12). https://doi.org/10.1029/2021JC017621

Herman, A. W., Beanlands, B., & Phillips, E. F. (2004). The next generation of Optical Plankton Counter: the Laser-OPC [Article]. *Journal of Plankton Research*, *26*(10), 1135-1145. https://doi.org/10.1093/plankt/fbh095

Hernández-Carrasco, I., Rossi, V., Navarro, G., Turiel, A., Bracco, A., & Orfila, A. (2023). Flow Structures With High Lagrangian Coherence Rate Promote Diatom Blooms in Oligotrophic Waters. *GEOPHYSICAL RESEARCH LETTERS*, *50*, Article e2023GL103688. https://doi.org/10.1029/2023GL103688

Hogle, S. L., Dupont, C. L., Hopkinson, B. M., King, A. L., Buck, K. N., Roe, K. L., Stuart, R. K., Allen, A. E., Mann, E. L., Johnson, Z. I., & Barbeau, K. A. (2018). Pervasive iron limitation at subsurface chlorophyll maxima of the California Current [Article]. *Proceedings of the*

National Academy of Sciences of the United States of America, *115*(52), 13300-13305. https://doi.org/10.1073/pnas.1813192115

Hood, R. R., Abbott, M. R., & Huyer, A. (1991). Phytoplankton and photosynthetic light response in the Coastal Transition Zone off northern California in June 1987 [Article]. *Journal of Geophysical Research: Oceans*, *96*(C8), 14769-14780. https://doi.org/10.1029/91jc01208

Hood, R. R., Abbott, M. R., Huyer, A., & Kosro, P. M. (1990). Surface patterns in temperature, flow, phytoplankton biomass, and species composition in the Coastal Transition Zone off Northern California [Article]. *Journal of Geophysical Research: Oceans*, *95*(C10), 18081-18094. https://doi.org/10.1029/JC095iC10p18081

Hutchins, D. A., DiTullio, G. R., Zhang, Y., & Bruland, K. W. (1998). An iron limitation mosaic in the California upwelling regime [Article]. *Limnology and Oceanography*, *43*(6), 1037-1054. https://doi.org/10.4319/lo.1998.43.6.1037

Huyer, A. (1983). COASTAL UPWELLING IN THE CALIFORNIA CURRENT SYSTEM [Review]. *Progress in Oceanography*, *12*(3), 259-284. https://doi.org/10.1016/0079-6611(83)90010-1

Huyer, A., Kosro, P. M., Fleischbein, J., Ramp, S. R., Stanton, T., Washburn, L., Chavez, F. P., Cowles, T. J., Pierce, S. D., & Smith, R. L. (1991). CURRENTS AND WATER MASSES OF THE COASTAL TRANSITION ZONE OFF NORTHERN CALIFORNIA, JUNE TO AUGUST 1988 [Article]. *Journal of Geophysical Research: Oceans*, *96*(C8), 14809-14831. https://doi.org/10.1029/91jc00641

Hyrenbach, K., & Veit, R. (2003). Ocean warming and seabird communities of the southern California Current System (1987-98): response at multiple temporal scales. *DEEP-SEA RESEARCH PART II-TOPICAL STUDIES IN OCEANOGRAPHY*, *50*, 2537-2565. https://doi.org/10.1016/S0967-0645(03)00123-1

Inomura, K., Karlusich, J., Dutkiewicz, S., Deutsch, C., Harrison, P., & Bowler, C. (2023). High Growth Rate of Diatoms Explained by Reduced Carbon Requirement and Low Energy Cost of Silica Deposition. *MICROBIOLOGY SPECTRUM*, *11*. https://doi.org/10.1128/spectrum.03311-22

Jacox, M., Bograd, S., Fiechter, J., Buil, M., Alexander, M., Amaya, D., Quiros, N.C., Ding, H., & Rykaczewski, R. (2024). Linking Upwelling Dynamics and Subsurface Nutrients to Projected Productivity Changes in the California Current System. *GEOPHYSICAL RESEARCH LETTERS*, *51*, Article e2023GL108096. https://doi.org/10.1029/2023GL108096

Jacox, M. G., Bograd, S. J., Hazen, E. L., & Fiechter, J. (2015). Sensitivity of the California Current nutrient supply to wind, heat, and remote ocean forcing [Article]. *Geophysical Research Letters*, *42*(14), 5950-5957. https://doi.org/10.1002/2015gl065147

Jacox, M. G., & Edwards, C. A. (2012). Upwelling source depth in the presence of nearshore wind stress curl [Article]. *Journal of Geophysical Research: Oceans*, *117*, 8, Article C05008. https://doi.org/10.1029/2011jc007856

Jacox, M. G., Edwards, C. A., Hazen, E. L., & Bograd, S. J. (2018). Coastal Upwelling Revisited: Ekman, Bakun, and Improved Upwelling Indices for the US West Coast [Article]. *Journal of Geophysical Research: Oceans*, *123*(10), 7332-7350. https://doi.org/10.1029/2018jc014187

James, C. C., Barton, A. D., Allen, L. Z., Lampe, R. H., Rabines, A., Schulberg, A., Zheng, H. Goericke, R., Goodwin, K. D., & Allen, A. E. (2022). Influence of nutrient supply on plankton microbiome biodiversity and distribution in a coastal upwelling region (vol 13, 2448, 2022). *NATURE COMMUNICATIONS*, *13*(1), Article 2887. https://doi.org/10.1038/s41467-022-30665-1

Johnson, Z. I., Shyam, R., Ritchie, A. E., Mioni, C., Lance, V. P., Murray, J. W., & Zinser, E. R. (2010). The effect of iron- and light-limitation on phytoplankton communities of deep chlorophyll maxima of the western Pacific Ocean [Article]. *Journal of Marine Research*, *68*(2), 283-308. https://doi.org/10.1357/002224010793721433

Jönsson, B., & Watson, J. (2016). The timescales of global surface-ocean connectivity. *NATURE COMMUNICATIONS*, *7*, Article 11239. https://doi.org/10.1038/ncomms11239

Kadko, D. C., Washburn, L., & Jones, B. (1991). EVIDENCE OF SUBDUCTION WITHIN COLD FILAMENTS OF THE NORTHERN CALIFORNIA COASTAL TRANSITION ZONE [Article]. *Journal of Geophysical Research: Oceans*, *96*(C8), 14909-14926. https://doi.org/10.1029/91jc00885

Kahru, M., Kudela, R. M., Manzano-Sarabia, M., & Mitchell, B. G. (2012). Trends in the surface chlorophyll of the California Current: Merging data from multiple ocean color satellites [Article]. *Deep-Sea Research Part Ii-Topical Studies in Oceanography*, *77-80*, 89-98. https://doi.org/10.1016/j.dsr2.2012.04.007

Keister, J., & Strub, P. (2008). Spatial and interannual variability in mesoscale circulation in the northern California Current System. *JOURNAL OF GEOPHYSICAL RESEARCH-OCEANS*, *113*, Article C04015. https://doi.org/10.1029/2007JC004256

Keister, J. E., Cowles, T. J., Peterson, W. T., & Morgan, C. A. (2009). Do upwelling filaments result in predictable biological distributions in coastal upwelling ecosystems? [Review]. *Progress in Oceanography*, *83*(1-4), 303-313. https://doi.org/10.1016/j.pocean.2009.07.042

Kelly, T., Goericke, R., Kahru, M., Song, H., & Stukel, M. (2018). CCE II: Spatial and interannual variability in export efficiency and the biological pump in an eastern boundary current upwelling system with substantial lateral advection. *DEEP-SEA RESEARCH PART I-OCEANOGRAPHIC RESEARCH PAPERS*, *140*, 14-25. https://doi.org/10.1016/j.dsr.2018.08.007

Kessouri, F., Bianchi, D., Renault, L., McWilliams, J., Frenzel, H., & Deutsch, C. (2020). Submesoscale Currents Modulate the Seasonal Cycle of Nutrients and Productivity in the California Current System. *GLOBAL BIOGEOCHEMICAL CYCLES*, *34*, Article e2020GB006578. https://doi.org/10.1029/2020GB006578

King, A. L., & Barbeau, K. (2007). Evidence for phytoplankton iron limitation in the southern California Current System [Article]. *Marine Ecology Progress Series*, *342*, 91-103. https://doi.org/10.3354/meps342091

King, A. L., & Barbeau, K. A. (2011). Dissolved iron and macronutrient distributions in the southern California Current System [Article]. *Journal of Geophysical Research-Oceans*, *116*, 18, Article C03018. https://doi.org/10.1029/2010jc006324

Kolody, B. C., McCrow, J. P., Allen, L. Z., Aylward, F. O., Fontanez, K. M., Moustafa, A., Moniruzzaman, M., Chavez, F. P., Scholin, C. A., Allen, E. E., Worden, A. Z., Delong, E. F., & Allen, A. E. (2019). Diel transcriptional response of a California Current plankton microbiome to light, low iron, and enduring viral infection [Article]. *ISME Journal*, *13*(11), 2817-2833. https://doi.org/10.1038/s41396-019-0472-2

Koslow, J., McMonagle, H., & Watson, W. (2017). Influence of climate on the biodiversity and community structure of fishes in the southern California Current. *MARINE ECOLOGY PROGRESS SERIES*, *571*, 193-206. https://doi.org/10.3354/meps12095

Kosro, P. M., & Huyer, A. (1986). CTD AND VELOCITY SURVEYS OF SEAWARD JETS OFF NORTHERN CALIFORNIA, JULY 1981 AND 1982 [Article]. *Journal of Geophysical Research: Oceans*, *91*(C6), 7680-7690. https://doi.org/10.1029/JC091iC06p07680

Kranz, S., Wang, S., Kelly, T., Stukel, M., Goericke, R., Landry, M., & Cassar, N. (2020). Lagrangian Studies of Marine Production: A Multimethod Assessment of Productivity Relationships in the California Current Ecosystem Upwelling Region. *JOURNAL OF GEOPHYSICAL RESEARCH-OCEANS*, *125*, Article e2019JC015984. https://doi.org/10.1029/2019JC015984

Krause, G. H., & Weis, E. (1991). CHLOROPHYLL FLUORESCENCE AND PHOTOSYNTHESIS - THE BASICS [Review]. *Annual Review of Plant Physiology and Plant Molecular Biology*, *42*, 313-349. https://doi.org/10.1146/annurev.pp.42.060191.001525

Lampe, R., Hernandez, G., Lin, Y., & Marchetti, A. (2021). Representative Diatom and Coccolithophore Species Exhibit Divergent Responses throughout Simulated Upwelling Cycles. *MSYSTEMS*, *6*, Article e00188-21. https://doi.org/10.1128/mSystems.00188-21

Landry, M. R., Ohman, M. D., Goericke, R., Stukel, M. R., Barbeau, K. A., Bundy, R., & Kahru, M. (2012). Pelagic community responses to a deep-water front in the California Current Ecosystem: overview of the A-Front Study [Article]. *Journal of Plankton Research*, *34*(9), 739-748. https://doi.org/10.1093/plankt/fbs025

Landry, M. R., Ohman, M. D., Goericke, R., Stukel, M. R., & Tsyrklevich, K. (2009). Lagrangian studies of phytoplankton growth and grazing relationships in a coastal upwelling

ecosystem off Southern California [Review]. *Progress in Oceanography*, *83*(1-4), 208-216. https://doi.org/10.1016/j.pocean.2009.07.026

Lapeyre, G., & Klein, P. (2006). Impact of the small-scale elongated filaments on the oceanic vertical pump [Article]. *Journal of Marine Research*, *64*(6), 835-851. https://doi.org/10.1357/002224006779698369

Lara-Lopez, A. L., Davison, P., & Koslow, J. A. (2012). Abundance and community composition of micronekton across a front off Southern California [Article]. *Journal of Plankton Research*, *34*(9), 828-848. https://doi.org/10.1093/plankt/fbs016

Lavaniegos, B., & Ohman, M. (2003). Long-term changes in pelagic tunicates of the California Current. *DEEP-SEA RESEARCH PART II-TOPICAL STUDIES IN OCEANOGRAPHY*, *50*, 2473-2498. https://doi.org/10.1016/S0967-0645(03)00132-2

Legaard, K. R., & Thomas, A. C. (2006). Spatial patterns in seasonal and interannual variability of chlorophyll and sea surface temperature in the California Current. *JOURNAL OF GEOPHYSICAL RESEARCH-OCEANS*, *111*(C6), Article C06032. https://doi.org/10.1029/2005JC003282

Lehahn, Y., d'Ovidio, F., & Koren, I. (2018). A Satellite-Based Lagrangian View on Phytoplankton Dynamics. In *ANNUAL REVIEW OF MARINE SCIENCE, VOL 10* (Vol. 10, pp. 99-+).

Lehahn, Y., d'Ovidio, F., Levy, M., Amitai, Y., & Heifetz, E. (2011). Long range transport of a quasi isolated chlorophyll patch by an Agulhas ring. *GEOPHYSICAL RESEARCH LETTERS*, *38*, Article L16610. https://doi.org/10.1029/2011GL048588

Lehahn, Y., Koren, I., Sharoni, S., d'Ovidio, F., Vardi, A., & Boss, E. (2017). Dispersion/dilution enhances phytoplankton blooms in low-nutrient waters. *NATURE COMMUNICATIONS*, *8*, Article 14868. https://doi.org/10.1038/ncomms14868

Levin, S., & Segel, L. (1976). HYPOTHESIS FOR ORIGIN OF PLANKTONIC PATCHINESS. *NATURE*, *259*, 659-659.

Levy, M., Franks, P. J. S., & Smith, K. S. (2018). The role of submesoscale currents in structuring marine ecosystems [Review]. *Nature Communications*, *9*, 16, Article 4758. https://doi.org/10.1038/s41467-018-07059-3

Lewandowska, A., Striebel, M., Feudel, U., Hillebrand, H., & Sommer, U. (2015). The importance of phytoplankton trait variability in spring bloom formation. *ICES JOURNAL OF MARINE SCIENCE*, *72*, 1908-1915. https://doi.org/10.1093/icesjms/fsv059

Li, Q. P., Franks, P. J. S., Ohman, M. D., & Landry, M. R. (2012). Enhanced nitrate fluxes and biological processes at a frontal zone in the southern California current system [Article]. *Journal of Plankton Research*, *34*(9), 790-801. https://doi.org/10.1093/plankt/fbs006

Lilly, L., Cornuelle, B., & Ohman, M. (2022). Using a Lagrangian particle tracking model to evaluate impacts of El Nin tilde o-related advection on euphausiids in the southern California Current System. *DEEP-SEA RESEARCH PART I-OCEANOGRAPHIC RESEARCH PAPERS*, *187*, Article 103835. https://doi.org/10.1016/j.dsr.2022.103835

Lilly, L., Send, U., Lankhorst, M., Martz, T., Feely, R., Sutton, A., & Ohman, M. (2019). Biogeochemical Anomalies at Two Southern California Current System Moorings During the 2014-2016 Warm Anomaly-El Nino Sequence. *JOURNAL OF GEOPHYSICAL RESEARCH-OCEANS*, *124*, 6886-6903. https://doi.org/10.1029/2019JC015255

Lilly, L. E., & Ohman, M. D. (2021). Euphausiid spatial displacements and habitat shifts in the southern California Current System in response to El Nino variability. *PROGRESS IN OCEANOGRAPHY*, *193*, Article 102544. https://doi.org/10.1016/j.pocean.2021.102544

Lindegren, M., Checkley, D. M., Koslow, J. A., Goericke, R., & Ohman, M. D. (2018). Climate-mediated changes in marine ecosystem regulation during El Nino [Article]. *Global Change Biology*, *24*(2), 796-809. https://doi.org/10.1111/gcb.13993

Longhurst, A. R. (2007). Chapter 7 - PROVINCES: THE SECONDARY COMPARTMENTS. In A. R. Longhurst (Ed.), *Ecological Geography of the Sea (Second Edition)* (pp. 103-114). Academic Press. https://doi.org/https://doi.org/10.1016/B978-012455521-1/50008-5

Lopez, E., & Anadon, R. (2008). Copepod communities along an Atlantic Meridional Transect: Abundance, size structure, and grazing rates [Article]. *Deep-Sea Research Part I-Oceanographic Research Papers*, *55*(10), 1375-1391. https://doi.org/10.1016/j.dsr.2008.05.012

Lorenzen, C. (1967). DETERMINATION OF CHLOROPHYLL AND PHEO-PIGMENTS - SPECTROPHOTOMETRIC EQUATIONS [Note]. *LIMNOLOGY AND OCEANOGRAPHY*, *12*, 343-&.

Lynn, R. J., & Simpson, J. J. (1987). THE CALIFORNIA CURRENT SYSTEM - THE SEASONAL VARIABILITY OF ITS PHYSICAL CHARACTERISTICS [Article]. *Journal of Geophysical Research-Oceans*, *92*(C12), 12947-&. https://doi.org/10.1029/JC092iC12p12947

Lévy, M., Ferrari, R., Franks, P. J. S., Martin, A. P., & Rivière, P. (2012). Bringing physics to life at the submesoscale. *GEOPHYSICAL RESEARCH LETTERS*, *39*, Article L14602. https://doi.org/10.1029/2012GL052756

Lévy, M., Franks, P. J. S., & Smith, K. S. (2018). The role of submesoscale currents in structuring marine ecosystems [Review]. *Nature Communications*, *9*, 16, Article 4758. https://doi.org/10.1038/s41467-018-07059-3

Lévy, M., Jahn, O., Dutkiewicz, S., Follows, M. J., & d'Ovidio, F. (2015). The dynamical landscape of marine phytoplankton diversity [Article]. *Journal of the Royal Society Interface*, *12*(111), 11, Article 20150481. https://doi.org/10.1098/rsif.2015.0481

Mackas, D. L., & Coyle, K. O. (2005). Shelf-offshore exchange processes, and their effects on mesozooplankton biomass and community composition patterns in the northeast Pacific. *DEEP-*

SEA RESEARCH PART II-TOPICAL STUDIES IN OCEANOGRAPHY, *52*(5-6), 707-725. https://doi.org/10.1016/j.dsr2.2004.12.020

Mahadevan, A. (2016). The Impact of Submesoscale Physics on Primary Productivity of Plankton. In C. A. Carlson & S. J. Giovannoni (Eds.), *Annual Review of Marine Science, Vol 8* (Vol. 8, pp. 161-184). Annual Reviews. https://doi.org/10.1146/annurev-marine-010814-015912

Mahadevan, A., D'Asaro, E., Lee, C., & Perry, M. J. (2012). Eddy-Driven Stratification Initiates North Atlantic Spring Phytoplankton Blooms. *Science*, *337*(6090), 54-58. https://doi.org/10.1126/science.1218740

Mangolte, I., Lévy, M., Dutkiewicz, S., Clayton, S., & Jahn, O. (2022). Plankton community response to fronts: winners and losers. *JOURNAL OF PLANKTON RESEARCH*, *44*, 241-258. https://doi.org/10.1093/plankt/fbac010

Mangolte, I., Lévy, M., Haëck, C., & Ohman, M. D. (2023). Sub-frontal niches of plankton communities driven by transport and trophic interactions at ocean fronts [Article]. *Biogeosciences*, *20*(15), 3273-3299. https://doi.org/10.5194/bg-20-3273-2023

Marañón, E., Cermeño, P., Rodríguez, J., Zubkov, M. V., & Harris, R. P. (2007). Scaling of phytoplankton photosynthesis and cell size in the ocean [Article]. *Limnology and Oceanography*, *52*(5), 2190-2198. https://doi.org/10.4319/lo.2007.52.5.2190

Marchesiello, P., McWilliams, J. C., & Shchepetkin, A. (2003). Equilibrium structure and dynamics of the California Current System [Article]. *Journal of Physical Oceanography*, *33*(4), 753-783. https://doi.org/10.1175/1520-0485(2003)33<753:esadot>2.0.co;2

Marra, J., Houghton, R. W., & Garside, C. (1990). Phytoplankton growth at the shelf-break front in the Middle Atlantic Bight [Article]. *Journal of Marine Research*, *48*(4), 851-868. https://doi.org/10.1357/002224090784988665

Martin, A. (2003). Phytoplankton patchiness: the role of lateral stirring and mixing. *PROGRESS IN OCEANOGRAPHY*, *57*, 125-174. https://doi.org/10.1016/S0079-6611(03)00085-5

Matthews, S., & Ohman, M. (2023). A space-for-time framework for forecasting the effects of ocean stratification on zooplankton vertical habitat use and trait composition. *LIMNOLOGY AND OCEANOGRAPHY*, *68*, 2688-2702. https://doi.org/10.1002/lno.12450

McGillicuddy, D., & Franks, P. (2019). *Models of Plankton Patchiness*. https://doi.org/10.1016/B978-0-12-409548-9.11610-0

McGowan, J. A., Bograd, S. J., Lynn, R. J., & Miller, A. J. (2003). The biological response to the 1977 regime shift in the California Current [Article]. *Deep-Sea Research Part II: Topical Studies in Oceanography*, *50*(14-16), 2567-2582. https://doi.org/10.1016/s0967-0645(03)00135-8

McWilliams, J. (2016). Submesoscale currents in the ocean. *PROCEEDINGS OF THE ROYAL SOCIETY A-MATHEMATICAL PHYSICAL AND ENGINEERING SCIENCES*, *472*, Article 20160117. https://doi.org/10.1098/rspa.2016.0117

McWilliams, J. C., Colas, F., & Molemaker, M. J. (2009). Cold filamentary intensification and oceanic surface convergence lines [Article]. *Geophysical Research Letters*, *36*, 5, Article L18602. https://doi.org/10.1029/2009gl039402

McWilliams, J. C., & Fox-Kemper, B. (2013). Oceanic wave-balanced surface fronts and filaments [Article]. *Journal of Fluid Mechanics*, *730*, 464-490. https://doi.org/10.1017/jfm.2013.348

Meinvielle, M., & Johnson, G. C. (2013). Decadal water-property trends in the California Undercurrent, with implications for ocean acidification. *JOURNAL OF GEOPHYSICAL RESEARCH-OCEANS*, *118*(12), 6687-6703. https://doi.org/10.1002/2013JC009299

Melton, C., Washburn, L., & Gotschalk, C. (2009). Wind relaxations and poleward flow events in a coastal upwelling system on the central California coast [Article]. *Journal of Geophysical Research: Oceans*, *114*, 18, Article C11016. https://doi.org/10.1029/2009jc005397

Messié, M., Sancho-Gallegos, D. A., Fiechter, J., Santora, J. A., & Chavez, F. P. (2022). Satellite-Based Lagrangian Model Reveals How Upwelling and Oceanic Circulation Shape Krill Hotspots in the California Current System [Article]. *Frontiers in Marine Science*, *9*, 19, Article 835813. https://doi.org/10.3389/fmars.2022.835813

Messié, M., & Chavez, F. P. (2017). Nutrient supply, surface currents, and plankton dynamics predict zooplankton hotspots in coastal upwelling systems. *GEOPHYSICAL RESEARCH LETTERS*, *44*(17), 8979-8986, Article L074322. https://doi.org/10.1002/2017GL074322

Messié, M., Sancho-Gallegos, D. A., Fiechter, J., Santora, J. A., & Chavez, F. P. (2022). Satellite-Based Lagrangian Model Reveals How Upwelling and Oceanic Circulation Shape Krill Hotspots in the California Current System [Article]. *Frontiers in Marine Science*, *9*, 19, Article 835813. https://doi.org/10.3389/fmars.2022.835813

Messié, M., Sherlock, R., Huffard, C., Pennington, J., Choy, C., Michisaki, R., Gomes, K., Chavez, F.P., Robison, B.H., & Smith, K. (2023). Coastal upwelling drives ecosystem temporal variability from the surface to the abyssal seafloor. *PROCEEDINGS OF THE NATIONAL ACADEMY OF SCIENCES OF THE UNITED STATES OF AMERICA*, *120*, Article e2214567120. https://doi.org/10.1073/pnas.2214567120

Mousing, E., Richardson, K., Bendtsen, J., Cetinic, I., & Perry, M. (2016). Evidence of small-scale spatial structuring of phytoplankton alpha- and beta-diversity in the open ocean. *JOURNAL OF ECOLOGY*, *104*, 1682-1695. https://doi.org/10.1111/1365-2745.12634

Nagai, T., Gruber, N., Frenzel, H., Lachkar, Z., McWilliams, J. C., & Plattner, G. K. (2015). Dominant role of eddies and filaments in the offshore transport of carbon and nutrients in the California Current System [Article]. *Journal of Geophysical Research: Oceans*, *120*(8), 5318-5341. https://doi.org/10.1002/2015jc010889

O'Loughlin, J., Bernard, K., Daly, E., Zeman, S., Fisher, J., Brodeur, R., & Hurst, T. (2020). Implications of *Pyrosoma atlanticum* range expansion on phytoplankton standing stocks in the

Northern California Current. *PROGRESS IN OCEANOGRAPHY*, *188*, Article 102424. https://doi.org/10.1016/j.pocean.2020.102424

Ohman, M. D. (1990). THE DEMOGRAPHIC BENEFITS OF DIEL VERTICAL MIGRATION BY ZOOPLANKTON. *ECOLOGICAL MONOGRAPHS*, *60*, 257-281.

Ohman, M. D., Barbeau, K., Franks, P. J. S., Goericke, R., Landry, M. R., & Miller, A. J. (2013). Ecological Transitions in a Coastal Upwelling Ecosystem [Article]. *Oceanography*, *26*(3), 210-219. https://doi.org/10.5670/oceanog.2013.65

Ohman, M. D., Powell, J. R., Picheral, M., & Jensen, D. W. (2012). Mesozooplankton and particulate matter responses to a deep-water frontal system in the southern California Current System [Article]. *Journal of Plankton Research*, *34*(9), 815-827. https://doi.org/10.1093/plankt/fbs028

Palacios, D. M., Bograd, S. J., Foley, D. G., & Schwing, F. B. (2006). Oceanographic characteristics of biological hot spots in the North Pacific: A remote sensing perspective. *DEEP-SEA RESEARCH PART II-TOPICAL STUDIES IN OCEANOGRAPHY*, *53*(3-4), 250-269. https://doi.org/10.1016/j.dsr2.2006.03.004

Pauly, D., & Christensen, V. (1995). PRIMARY PRODUCTION REQUIRED TO SUSTAIN GLOBAL FISHERIES (VOL 374, PG 255, 1995) [Correction, Addition]. *Nature*, *376*(6537), 279-279. https://doi.org/10.1038/376279b0

Peterson, D. H., Conomos, T. J., Broenkow, W. W., & Doherty, P. C. (1975). Location of the non-tidal current null zone in northern San Francisco Bay. *Estuarine and Coastal Marine Science*, *3*(1), 1-11. https://doi.org/https://doi.org/10.1016/0302-3524(75)90002-X

Pickett, M. H., & Paduan, J. D. (2003). Ekman transport and pumping in the California Current based on the U.S. Navy's high-resolution atmospheric model (COAMPS) [Article]. *Journal of Geophysical Research: Oceans*, *108*(C10), 10, Article 3327. https://doi.org/10.1029/2003jc001902

Plattner, G. K., Gruber, N., Frenzel, H., & McWilliams, J. C. (2005). Decoupling marine export production from new production [Article]. *Geophysical Research Letters*, *32*(11), 4, Article L11612. https://doi.org/10.1029/2005gl022660

Powell, J. R., & Ohman, M. D. (2015). Changes in zooplankton habitat, behavior, and acoustic scattering characteristics across glider-resolved fronts in the Southern California Current System [Review]. *Progress in Oceanography*, *134*, 77-92. https://doi.org/10.1016/j.pocean.2014.12.011

Pozo Buil, M., Jacox, M., Fiechter, J., Alexander, M., Bograd, S., Curchitser, E., Edwards, C.A., Rykaczewski, R.R., & Stock, C. (2021). A Dynamically Downscaled Ensemble of Future Projections for the California Current System. *FRONTIERS IN MARINE SCIENCE*, *8,* Article 612874. https://doi.org/10.3389/fmars.2021.612874

Prants, S. (2022). Marine life at Lagrangian fronts. *PROGRESS IN OCEANOGRAPHY*, *204*, Article 102790. https://doi.org/10.1016/j.pocean.2022.102790

Rathburn, A., Perez, M., & Lange, C. (2001). Benthic-pelagic coupling in the Southern California Bight: Relationships between sinking organic material, diatoms and benthic foraminifera. *MARINE MICROPALEONTOLOGY*, *43*, 261-271.

Ren, A., & Rudnick, D. (2021). Temperature and salinity extremes from 2014-2019 in the California Current System and its source waters. *COMMUNICATIONS EARTH & ENVIRONMENT*, *2*, Article 62. https://doi.org/10.1038/s43247-021-00131-9

Rio, M. H., Mulet, S., & Picot, N. (2014). Beyond GOCE for the ocean circulation estimate: Synergetic use of altimetry, gravimetry, and in situ data provides new insight into geostrophic and Ekman currents [Article]. *Geophysical Research Letters*, *41*(24), 8918-8925. https://doi.org/10.1002/2014gl061773

Robinson, J., Popova, E. E., Yool, A., Srokosz, M., Lampitt, R. S., & Blundell, J. R. (2014). How deep is deep enough? Ocean iron fertilization and carbon sequestration in the Southern Ocean. *Geophysical Research Letters*, *41*(7), 2489-2495. https://doi.org/https://doi.org/10.1002/2013GL058799

Rossi, V., Garçon, V., Tassel, J., Romagnan, J., Stemmann, L., Jourdin, F., Morin, P., & Morel, Y. (2013). Cross-shelf variability in the Iberian Peninsula Upwelling System: Impact of a mesoscale filament. *CONTINENTAL SHELF RESEARCH*, *59*, 97-114. https://doi.org/10.1016/j.csr.2013.04.008

Rossi, V., López, C., Hernández-García, E., Sudre, J., Garçon, V., & Morel, Y. (2009). Surface mixing and biological activity in the four Eastern Boundary Upwelling Systems. *NONLINEAR PROCESSES IN GEOPHYSICS*, *16*, 557-568.

Rossi, V., Ser-Giacomi, E., López, C., & Hernández-García, E. (2014). Hydrodynamic provinces and oceanic connectivity from a transport network help designing marine reserves. *Geophysical Research Letters*, *41*(8), 2883-2891. https://doi.org/https://doi.org/10.1002/2014GL059540

Rudnick, D., Zaba, K., Todd, R., & Davis, R. (2017). A climatology of the California Current System from a network of underwater gliders. *PROGRESS IN OCEANOGRAPHY*, *154*, 64-106. https://doi.org/10.1016/j.pocean.2017.03.002

Russell, T. M. (2024). *Spatiotemporal trends of Seabirds in the California Current Ecosystem* University of California San Diego].

Ryan, J., Chavez, F., & Bellingham, J. (2005). Physical-biological coupling in Monterey Bay, California: topographic influences on phytoplankton ecology. *MARINE ECOLOGY PROGRESS SERIES*, *287*, 23-32.

Rykaczewski, R. R., & Checkley, D. M. (2008). Influence of ocean winds on the pelagic ecosystem in upwelling regions [Article]. *Proceedings of the National Academy of Sciences of the United States of America*, *105*(6), 1965-1970. https://doi.org/10.1073/pnas.0711777105

Ryther, J. H. (1969). Photosynthesis and fish production in the sea. *Science*, *166*(3901), 72-76. https://doi.org/10.1126/science.166.3901.72

Sarthou, G., Timmermans, K., Blain, S., & Tréguer, P. (2005). Growth physiology and fate of diatoms in the ocean:: a review. *JOURNAL OF SEA RESEARCH*, *53*, 25-42. https://doi.org/10.1016/j.seares.2004.01.007

Schmid, M., Sponaugle, S., Thompson, A., Sutherland, K., & Cowen, R. (2023). Drivers of plankton community structure in intermittent and continuous coastal upwelling systems-from microbes and microscale in-situ imaging to large scale patterns. *FRONTIERS IN MARINE SCIENCE*, *10*, Article 1166629. https://doi.org/10.3389/fmars.2023.1166629

Schuback, N., Tortell, P., Berman-Frank, I., Campbell, D., Ciotti, A., Courtecuisse, E., Erickson, Z. K .K., Fujiki, T., Halsey, K., Hickman, A. E. E., Huot, Y., Gorbunov, M. Y. Y., Hughes, D. J. J., Kolber, Z. S. S., Moore, C. M., Oxborough, K., Prásil, O., Robinson, C. M. M., Ryan-Keogh, T. J. J., Silsbe, G., Simis, S., Suggett, D. J. J., Thomalla, S., & Varkey, D. (2021). Single-Turnover Variable Chlorophyll Fluorescence as a Tool for Assessing Phytoplankton Photosynthesis and Primary Productivity: Opportunities, Caveats and Recommendations. *FRONTIERS IN MARINE SCIENCE*, *8*, Article 690607. https://doi.org/10.3389/fmars.2021.690607

Sciandra, A., Lazzara, L., Claustre, H., & Babin, M. (2000). Responses of growth rate, pigment composition and optical properties of *Cryptomonas* sp to light and nitrogen stresses. *MARINE ECOLOGY PROGRESS SERIES*, *201*, 107-120.

Ser-Giacomi, E., Martinez-Garcia, R., Dutkiewicz, S., & Follows, M. (2023). A Lagrangian model for drifting ecosystems reveals heterogeneity-driven enhancement of marine plankton blooms. *NATURE COMMUNICATIONS*, *14*, Article 6092. https://doi.org/10.1038/s41467-023-41469-2

Sergi, S., Baudena, A., Cotté, C., Ardyna, M., Blain, S., & d'Ovidio, F. (2020). Interaction of the Antarctic Circumpolar Current With Seamounts Fuels Moderate Blooms but Vast Foraging Grounds for Multiple Marine Predators. *FRONTIERS IN MARINE SCIENCE*, *7*, Article 416. https://doi.org/10.3389/fmars.2020.00416

Small, L. F., & Ellis, S. G. (1992). FECAL CARBON PRODUCTION BY ZOOPLANKTON IN SANTA-MONICA BASIN - THE EFFECTS OF BODY SIZE AND CARNIVOROUS FEEDING. *PROGRESS IN OCEANOGRAPHY*, *30*(1-4), 197-221. https://doi.org/10.1016/0079-6611(92)90013-P

Smayda, T. J. (1970). The suspension and sinking of phytoplankton in the sea. *Oceanography and Marine Biology*, *8*, 353-414.

Smith, C., Hoover, D., Doan, S., Pope, R., Demaster, D., Dobbs, F., & Altabet, M. (1996). Phytodetritus at the abyssal seafloor across 10 degrees of latitude in the central equatorial Pacific. *DEEP-SEA RESEARCH PART II-TOPICAL STUDIES IN OCEANOGRAPHY*, *43*, 1309-1338.

Song, H., Miller, A., Cornuelle, B., & Di Lorenzo, E. (2011). Changes in upwelling and its water sources in the California Current System driven by different wind forcing. *DYNAMICS OF ATMOSPHERES AND OCEANS*, *52*, 170-191. https://doi.org/10.1016/j.dynatmoce.2011.03.001

Stephens, B. M., Porrachia, M., Dovel, S., Roadman, M., Goericke, R., & Aluwihare, L. I. (2018). Nonsinking Organic Matter Production in the California Current [Article]. *Global Biogeochemical Cycles*, *32*(9), 1386-1405. https://doi.org/10.1029/2018gb005930

Stolte, W., McCollin, T., Noordeloos, A. A. M., & Riegman, R. (1994). Effect of nitrogen-source on the size distribution within marine-phytoplankton populations [Article]. *Journal of Experimental Marine Biology and Ecology*, *184*(1), 83-97. https://doi.org/10.1016/0022-0981(94)90167-8

Strub, P. T., Kosro, P. M., & Huyer, A. (1991). THE NATURE OF THE COLD FILAMENTS IN THE CALIFORNIA CURRENT SYSTEM [Article]. *Journal of Geophysical Research: Oceans*, *96*(C8), 14743-14768. https://doi.org/10.1029/91jc01024

Stukel, M. R., Aluwihare, L. I., Barbeau, K. A., Chekalyuk, A. M., Goericke, R., Miller, A. J., Ohman, M. D., Ruacho, A., Song, H., Stephens, B. M., & Landry, M. R. (2017). Mesoscale ocean fronts enhance carbon export due to gravitational sinking and subduction [Article]. *Proceedings of the National Academy of Sciences of the United States of America*, *114*(6), 1252-1257. https://doi.org/10.1073/pnas.1609435114

Stukel, M. R., & Barbeau, K. A. (2020). Investigating the Nutrient Landscape in a Coastal Upwelling Region and Its Relationship to the Biological Carbon Pump [Article]. *Geophysical Research Letters*, *47*(6), 11, Article e2020GL087351. https://doi.org/10.1029/2020gl087351

Stukel, M. R., Landry, M. R., Benitez-Nelson, C. R., & Goericke, R. (2011). Trophic cycling and carbon export relationships in the California Current Ecosystem [Article]. *Limnology and Oceanography*, *56*(5), 1866-1878. https://doi.org/10.4319/lo.2011.56.5.1866

Stukel, M. R., Ohman, M. D., Benitez-Nelson, C. R., & Landry, M. R. (2013). Contributions of mesozooplankton to vertical carbon export in a coastal upwelling system [Article]. *Marine Ecology Progress Series*, *491*, 47-+. https://doi.org/10.3354/meps10453

Suggett, D., Moore, C., Hickman, A., & Geider, R. (2009). Interpretation of fast repetition rate (FRR) fluorescence: signatures of phytoplankton community structure versus physiological state. *MARINE ECOLOGY PROGRESS SERIES*, *376*, 1-19. https://doi.org/10.3354/meps07830

Taylor, A., Goericke, R., Landry, M., Selph, K., Wick, D., & Roadman, M. (2012). Sharp gradients in phytoplankton community structure across a frontal zone in the California Current Ecosystem [Article]. *JOURNAL OF PLANKTON RESEARCH*, *34*, 778-789. https://doi.org/10.1093/plankt/fbs036

Taylor, A., & Landry, M. (2018). Phytoplankton biomass and size structure across trophic gradients in the southern California Current and adjacent ocean ecosystems. *MARINE ECOLOGY PROGRESS SERIES*, *592*, 1-17. https://doi.org/10.3354/meps12526

Tecchio, S., van Oevelen, D., Soetaert, K., Navarro, J., & Ramírez-Llodra, E. (2013). Trophic Dynamics of Deep-Sea Megabenthos Are Mediated by Surface Productivity. *PLOS ONE*, *8*, Article e63796. https://doi.org/10.1371/journal.pone.0063796

Thomson, R., & Krassovski, M. (2010). Poleward reach of the California Undercurrent extension. *JOURNAL OF GEOPHYSICAL RESEARCH-OCEANS*, *115*, Article C09027. https://doi.org/10.1029/2010JC006280

Till, C., Solomon, J., Cohen, N., Lampe, R., Marchetti, A., Coale, T., & Bruland, K. (2019). The iron limitation mosaic in the California Current System: Factors governing Fe availability in the shelf/near-shelf region. *LIMNOLOGY AND OCEANOGRAPHY*, *64*, 109-123. https://doi.org/10.1002/lno.11022

Tilman, D. (1977). Resource Competition between Plankton Algae: An Experimental and Theoretical Approach. *Ecology*, *58*(2), 338-348. https://doi.org/10.2307/1935608

Todd, R., Rudnick, D., Mazloff, M., Davis, R., & Cornuelle, B. (2011). Poleward flows in the southern California Current System: Glider observations and numerical simulation. *JOURNAL OF GEOPHYSICAL RESEARCH-OCEANS*, *116*, Article 116. https://doi.org/10.1029/2010JC006536

Tomczak, M., & Godfrey, J. S. (2003). *Regional oceanography: an introduction*. Daya books.

Turner, J. T. (2015). Zooplankton fecal pellets, marine snow, phytodetritus and the ocean's biological pump [Review]. *Progress in Oceanography*, *130*, 205-248. https://doi.org/10.1016/j.pocean.2014.08.005

Tynan, C., Ainley, D., Barth, J., Cowles, T., Pierce, S., & Spear, L. (2005). Cetacean distributions relative to ocean processes in the northern California Current System. *DEEP-SEA RESEARCH PART II-TOPICAL STUDIES IN OCEANOGRAPHY*, *52*, 145-167. https://doi.org/10.1016/j.dsr2.2004.09.024

Tzortzis, R., Doglioli, A., Barrillon, S., Petrenko, A., d'Ovidio, F., Izard, L., Thyssen, M., Pascual, A., Barceló-Llull, B., Cyr, F., Tedetti, M., Bhairy, N., Garreau, P., Dumas, F., & Gregori, G. (2021). Impact of moderately energetic fine-scale dynamics on the phytoplankton community structure in the western Mediterranean Sea. *BIOGEOSCIENCES*, *18*, 6455-6477. https://doi.org/10.5194/bg-18-6455-2021

Van Oostende, N., Dunne, J., Fawcett, S., & Ward, B. (2015). Phytoplankton succession explains size-partitioning of new production following upwelling-induced blooms. *JOURNAL OF MARINE SYSTEMS*, *148*, 14-25. https://doi.org/10.1016/j.jmarsys.2015.01.009

van Sebille, E., Griffies, S. M., Abernathey, R., Adams, T. P., Berloff, P., Biastoch, A., Blanke, B., Chassignet, E. P., Cheng, Y., Cotter, C. J., Deleersnijder, E., Doos, K., Drake, H. F., Drijfhout, S., Gary, S. F., Heemink, A. W., Kjellsson, J., Koszalka, I. M., Lange, M., Lique, C., MacGilchrist, G. A., Marsh, R., Adame, C. G. M., McAdam, R., Nencioli, F., Paris, C. B., Piggott, M. D., Polton, J. A., Ruhs, S., Shah, Sham, Thomas, M. D., Wang, J. B., Wolfram, P. J., Zanna, L., & Zika, J. D. (2018). Lagrangian ocean analysis: Fundamentals and practices [Review]. *Ocean Modelling*, *121*, 49-75. https://doi.org/10.1016/j.ocemod.2017.11.008

Venrick, E. L. (2002). Floral patterns in the California current system off southern California: 1990-1996 [Article]. *Journal of Marine Research*, *60*(1), 171-189. https://doi.org/10.1357/002224002762341294

Wang, S., Kranz, S. A., Kelly, T. B., Song, H., Stukel, M. R., & Cassar, N. (2020). Lagrangian Studies of Net Community Production: The Effect of Diel and Multiday Nonsteady State Factors and Vertical Fluxes on O_2/Ar in a Dynamic Upwelling Region. *JOURNAL OF GEOPHYSICAL RESEARCH-BIOGEOSCIENCES*, *125*(6), Article e2019JG005569. https://doi.org/10.1029/2019JG005569

Washburn, L., Kadko, D. C., Jones, B. H., Hayward, T., Kosro, P. M., Stanton, T. P., Ramp, S., & Cowles, T. (1991). WATER MASS SUBDUCTION AND THE TRANSPORT OF PHYTOPLANKTON IN A COASTAL UPWELLING SYSTEM [Article]. *Journal of Geophysical Research: Oceans*, *96*(C8), 14927-14945. https://doi.org/10.1029/91jc01145

Whitmore, B., & Ohman, M. (2021). *Zooglider*-measured association of zooplankton with the fine-scale vertical prey field. *LIMNOLOGY AND OCEANOGRAPHY*, *66*, 3811-3827. https://doi.org/10.1002/lno.11920

Wilkins, D., van Sebille, E., Rintoul, S., Lauro, F., & Cavicchioli, R. (2013). Advection shapes Southern Ocean microbial assemblages independent of distance and environment effects. *NATURE COMMUNICATIONS*, *4*, Article 2457. https://doi.org/10.1038/ncomms3457

Wilson, S. E., Steinberg, D. K., & Buesseler, K. O. (2008). Changes in fecal pellet characteristics with depth as indicators of zooplankton repackaging of particles in the mesopelagic zone of the subtropical and subarctic North Pacific Ocean. *DEEP-SEA RESEARCH PART II-TOPICAL STUDIES IN OCEANOGRAPHY*, *55*(14-15), 1636-1647. https://doi.org/10.1016/j.dsr2.2008.04.019

Wood, A., Horan, P., Muirhead, K., Phinney, D., Yentsch, C., & Waterbury, J. (1985). DISCRIMINATION BETWEEN TYPES OF PIGMENTS IN MARINE SYNECHOCOCCUS SPP BY SCANNING SPECTROSCOPY, EPIFLUORESCENCE MICROSCOPY, AND FLOW-CYTOMETRY. *LIMNOLOGY AND OCEANOGRAPHY*, *30*, 1303-1315.

Yoder, J. A., Ackleson, S. G., Barber, R. T., Flament, P., & Balch, W. M. (1994). A line in the sea [Article]. *Nature*, *371*(6499), 689-692. https://doi.org/10.1038/371689a0

Zaba, K., Rudnick, D., Cornuelle, B., Gopalakrishnan, G., & Mazloff, M. (2018). Annual and Interannual Variability in the California Current System: Comparison of an Ocean State Estimate with a Network of Underwater Gliders. *JOURNAL OF PHYSICAL OCEANOGRAPHY*, *48*, 2965-2988. https://doi.org/10.1175/JPO-D-18-0037.1

Zaba, K. D., Franks, P. J. S., & Ohman, M. D. (2021). The California Undercurrent as a Source of Upwelled Waters in a Coastal Filament [Article]. *Journal of Geophysical Research: Oceans*, *126*(2), 13, Article e2020JC016602. https://doi.org/10.1029/2020jc016602